

# **Pore pressure estimation from single and repeated seismic data sets**

by

**Øyvind Kvam**

**A dissertation for the partial fulfilment of requirements for the degree Doktor Ingeniør at the Department of Petroleum Engineering and Applied Geophysics, Norwegian University of Science and Technology**

**January, 2005**



# Preface

This thesis was completed as a part of my Doktor Ingeniør project at the Norwegian University of Science and Technology. The work has been funded by the Norwegian Research Council under the PetroForsk program.

I acknowledge the following people for their support and assistance

My advisor, Professor Martin Landrø for his valuable recommendations and advice. His expertise and experience has been a source of inspiration, and through our discussions I have gained invaluable knowledge. I also wish to thank him for his support and encouragement, which has been most appreciated.

Dr. Jesper Spetzler, who I learned to know during a six month stay at the Technical University of Delft, the Netherlands. Our collaboration has been very useful, as proven by this thesis, and we have had many interesting discussions. I also wish to thank Jesper for making my stay in Delft a pleasant one.

The teaching staff at the Department of Petroleum Engineering and Applied Geophysics for useful advice and support.

My friends and colleagues at the Department of Petroleum Engineering and Applied Geophysics for discussions and support.

My parents for their support through many years.

Finally, I want to thank my wife, Therese, for her patience and for her invaluable support.



# Contents

<b>1</b>	<b>Introductory part</b>	<b>1</b>
1	Introduction . . . . .	1
2	Basic concepts . . . . .	3
3	Seismic pore pressure prediction . . . . .	5
4	Motivation for the thesis . . . . .	6
5	Organisation of the thesis . . . . .	8
<b>2</b>	<b>Seismic amplitudes in pore pressure prediction</b>	<b>11</b>
1	Theory . . . . .	13
2	AVO modeling . . . . .	14
2.1	Pore pressure . . . . .	17
2.2	Fluid saturation . . . . .	19
2.3	Anisotropy . . . . .	20
2.4	Attenuation . . . . .	20
3	Results . . . . .	21

4	Discussion and conclusions . . . . .	24
A	Modeling results . . . . .	25
<b>3</b>	<b>Pore pressure sensitivities tested with time-lapse seismic data</b>	<b>39</b>
1	Introduction . . . . .	40
2	Theory . . . . .	41
3	Seismic modeling of an overpressured zone . . . . .	47
3.1	Velocity analysis . . . . .	49
3.2	AVO analysis . . . . .	52
4	Velocity analysis on real data . . . . .	53
5	AVO analysis on real data . . . . .	55
6	Discussion . . . . .	64
7	Conclusions . . . . .	65
8	Acknowledgements . . . . .	66
<b>4</b>	<b>Pore pressure estimation from seismic data on Haltenbanken</b>	<b>67</b>
1	Introduction . . . . .	67
2	Study area . . . . .	68
3	A model for pore pressure prediction at Haltenbanken . . . . .	70
3.1	Effective pressure . . . . .	70
3.2	Known methods for pore pressure prediction . . . . .	71

3.3	Pressure dependent velocities at Haltenbanken . . . . .	73
3.4	Porosity trends on Haltenbanken . . . . .	76
3.5	Modified Herz-Mindlin theory for pore pressure prediction . . . .	77
4	Seismic data analysis at Haltenbanken . . . . .	83
4.1	Velocity analysis . . . . .	83
4.2	Amplitude analysis . . . . .	90
5	Discussion . . . . .	96
6	Conclusions . . . . .	99
<b>5</b>	<b>Pore pressure estimation - what can we learn from 4D?</b>	<b>101</b>
1	Introduction . . . . .	102
2	The Hertz-Mindlin model: an attempt to relate velocity to pressure . . . .	102
3	Simple equations for overpressure detection based on Hertz-Mindlin theory	105
4	Fluid effects . . . . .	107
5	PS-converted data . . . . .	107
6	A 4D example: Velocity changes caused by a pore pressure increase . . .	109
7	What about seismic effects caused by pore pressure decrease? . . . . .	110
7.1	Conventional velocity analysis, is it accurate enough to detect a pressure increase of 6 MPa at 2000 m reservoir depth? . . . . .	112
8	Discussion . . . . .	113
9	Conclusion . . . . .	114

<b>6</b>	<b>A spectral ratio approach to time-lapse seismic monitoring on the Gullfaks Field</b>	<b>115</b>
1	Introduction . . . . .	116
2	Theory . . . . .	117
2.1	From amplitude ratios to seismic parameters . . . . .	126
3	Results . . . . .	127
3.1	Synthetic study . . . . .	127
3.2	Gullfaks data . . . . .	135
4	Discussion . . . . .	140
5	Conclusions . . . . .	141
6	Acknowledgements . . . . .	142
<b>7</b>	<b>Discrimination between Phase and Amplitude Attributes in Time-Lapse Seismic Streamer Data</b>	<b>143</b>
1	Introduction . . . . .	144
2	Time-lapse changes in phase and amplitude attributes of reflected wave-fields . . . . .	145
2.1	Discrimination between phase and amplitude . . . . .	146
2.2	Correction for source-receiver response and overburden differences	148
2.3	Limitation of time-lapse monitoring algorithm . . . . .	150
2.4	The effect of mispositioning on the travelttime shift and reflectivity ratio . . . . .	150
3	Synthetic modelling of a time-lapse marine experiment . . . . .	152



---

3.1	Petrophysical time-lapse model . . . . .	152
3.2	Forward modelling of time-lapse streamer experiment . . . . .	154
3.3	Preprocessing of synthetic time-lapse streamer data . . . . .	155
3.4	Result of synthetic time-lapse monitoring . . . . .	158
4	Example of time-lapse monitoring of a real streamer time-lapse data set .	162
5	Conclusions and discussion . . . . .	163
6	Acknowledgements . . . . .	167
A	The effect of mispositioning on traveltimes and reflectivity changes . . . .	168
<b>8</b>	<b>Closing remarks</b>	<b>171</b>

# Chapter 1

## Introductory part

### 1 Introduction

Pore pressure is defined as the fluid pressure in the pore space of the rock matrix. In a geologic setting with perfect communication between the pores, the pore pressure is the hydrostatic pressure due to the weight of the fluid. The pore pressure at depth  $z$  can then be computed as

$$p(z) = \int_{z_0}^z \rho(z) g z \, dz + p_0, \quad (1)$$

where  $\rho(z)$  is the fluid density and  $g$  is the gravitational constant.  $p_0$  is the pressure at depth  $z_0$ , usually atmospheric pressure.

Hydrostatic pressure is often referred to as normal pressure conditions. Conditions that deviate from normal pressure are said to be either overpressured or underpressured, depending on whether the pore pressure is greater than or less than the normal pressure. The term “geopressure” is often used to describe abnormally high pore fluid pressures.

The concept of abnormal pressure, especially geopressure, is most important in hydrocarbon exploration and production. Drilling through geopressured zones is challenging, and requires extra care. As fields have matured, there is a rising demand in the industry to explore areas that previously were regarded as too technically challenging. This includes deepwater areas, which are often associated with high pore pressures. Dutta (2002b) reports that the industry will spend about \$100 billion in hydrocarbon exploration and production in deepwater areas over a five-year period, beginning in 2001. In the North sea it is estimated that each deep-drilled well (high-temperature high-pressure well) on average gives 2 kicks related to high pore pressures.

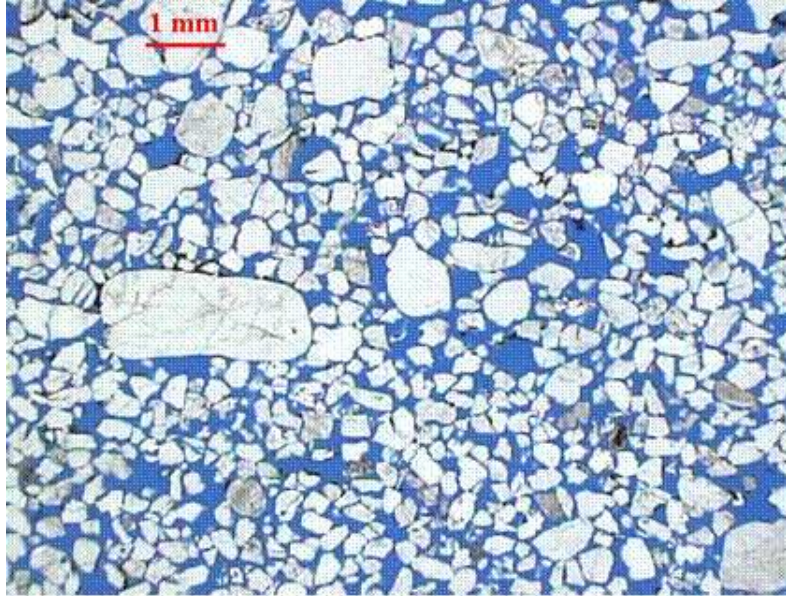


**Figure 1:** Thin section of sandstone. The pore pressure is the pressure in the pore space (blue color).

Knowledge of the pore pressure in an area is important for several reasons. In overpressured zones, there is often little difference between the fluid pressure and the reservoir fracture pressure. In order to maintain a safe and controlled drilling, the mud weight must lie in this interval (i.e. between fluid pressure and fracture pressure). If a too low mud weight is used (underbalanced drilling) while drilling through high pressure zones, there is danger of well kicks. In rare cases one might encounter dangerous blowouts, although the risk of this is significantly reduced the last decade thanks to modern equipment. If the mud weight is too high, the fracture pressure is exceeded, and the drill pipe may be stuck. In either case, valuable operation time is lost. On average a well kick will slow down the drilling operation by 2 days, resulting economic loss. It is estimated that 50 % of the well kicks encountered worldwide is due to high pressure (personal communication with Pål Skalle, 2003).

Worldwide, about 1 in 100 kicks will give an uncontrolled blowout. This is clearly worse than kicks that can be controlled with a proper blowout preventing equipment (BOP's), since it represents a direct health hazard to the drilling personel, and also a hazard to expensive equipment. A famous example from the North Sea is the uncontrolled blowout that occurred at the West Vanguard platform the sixth of October 1985. During a drilling pause for pipe connection, gas from a shallow overpressured zone flowed with great force up through the wellbore. Attempts to control the blowout did not succeed, and the platform had to be abandoned under the roaring sound from the blowout. One man was killed, and the material damage was enormous (NOU(1986:16), 1986).

Based on the previous, it is no surprise that research on pressure control and pressure prediction is of great interest to the industry. However it is also important for other reasons. Knowledge of pore pressure can help in estimating the effectiveness of hydrocarbon seals, finding migration pathways, basin geometry and provide input for basin modeling Dutta (2002b).

The dominant methods for evaluating pore pressures come from measurements at the wellbore. Repeat formation tester tools (RFT's) offer a direct measurement of the pore pressure in permeable formations. In impermeable formations such as thick shales, the pore pressure may be estimated based on well logging methods and from drilling parameters such as penetration rate and mud weights. However, such measurements are highly uncertain.

Although well data can be used to predict pore pressures at some distance from a well, it is of interest to use other methods for evaluating the pore pressure. After all, well data only provide measurements along the well path. An alternative method comes from basin modeling, which can provide information on how the pore pressure has developed over geological time. However, the results from basin modeling are critically dependant on the input parameters (Borge, 2000). Methods based on seismic data are attractive because the seismic velocities depend on pore pressure. Thus, seismic data, in theory, provide a measurement of the pore pressure. The use of seismic data to estimate pore pressures is the main topic of this thesis.

## 2 Basic concepts

High pore pressures have been observed at drilling sites all over the world, both on- and offshore. The frequently encountered overpressures in the Gulf of Mexico have been particularly well studied and observed, since this is an important area of hydrocarbon production, but the phenomenon have been observed in many other places, including the North Sea, the Caspian Sea, Pakistan and the Middle East (Fertl, 1976). The nature and origin of pore pressures are manifold and complex. The demands for better understanding and pre-drill prediction of pore pressure are substantial. The industry spends considerable sums on research, and the efforts have paid off.

In order to investigate the nature of abnormal pore pressures some practical definitions have been made. The overburden pressure is defined as the combined weight of sediments and fluid overlying a formation. Mathematically, the overburden pressure can be defined as

$$S(z) = \int_{z_0}^z \rho(z) g dz, \quad (2)$$

where

$$\rho(z) = \phi(z)\rho_f(z) + (1 - \phi(z))\rho_m(z). \quad (3)$$

In equation (3),  $\phi$  is the porosity, while  $\rho_f$  and  $\rho_m$  are the fluid and rock matrix densities, respectively. If the density is known, the overburden pressure can be measured.

The effective pressure is defined as

$$p_e = S - np, \quad (4)$$

where  $p$  is the pore fluid pressure, and  $n$  is called the Biot coefficient. For static compression of the rock frame, the Biot coefficient is defined as (Fjær et al., 1989)

$$n = 1 - \frac{K_{fr}}{K_s}, \quad (5)$$

where  $K_{fr}$  is the bulk modulus of the rock frame and  $K_s$  is the bulk modulus of the mineral that the rock is composed of. For soft materials,  $n = 1$ .

It is also convenient to define the pressure gradient  $G$ , which strictly speaking is not really a gradient, but an engineering term. The pressure gradient is simply defined as the ratio of pressure to burial depth. Pressure gradients can describe both overburden, fluid and effective pressures. As an example, in the Gulf of Mexico, the overburden gradient is found to be very close to 1 psi/ft, while normal pressure conditions (i.e. hydrostatic pressure) correspond to a fluid pressure gradient of about 0.465 psi/ft (Dutta, 1987).

From the definitions above it is clear that a high pore pressure will give a correspondingly low effective pressure. The degree of overpressure may in extreme cases be such that the effective pressure equals zero, and in some rare cases even is less than zero. Table 1 summarizes degrees of pressures encountered based on experience from the Gulf of Mexico, as given in Dutta (1987).

**Table 1:** Geopressure characterization according to Dutta (1987).

Fluid pressure gradient (Psi/ft)	Geopressure characterization
$0.465 < G < 0.65$	soft or mild
$0.65 < G < 0.85$	intermediate or moderate
$G > 0.85$	hard

According to Fertl (1976), all occurrences of overpressure in the subsurface are associated with a permeability barrier, that simultaneously acts as a pressure barrier. This barrier

prevents fluid to flow along a pressure gradient. The nature of such a seal can differ greatly at different localities. Low permeability shales have often been observed to act as pressure barriers, but also faults can form such barriers.

The processes in which high pressures develop in the vicinity of the pressure barriers are complex. Smith (1971) describe how high pressures can develop in areas where there have been a rapid deposition of sediments, allowing seals to form before excess fluid has escaped from deeper layers. The increasing weight of the overburden will tend to decrease the porosity, and hence the pore space. However, if the formation is sealed, the fluid has nowhere to escape and starts to carry some of the weight of the overburden. The result is that the fluid pressure is increased. This process is often termed “undercompaction” or “compaction disequilibrium”, and is one of the major causes of abnormally high pore pressures (Dutta, 2002b).

Tectonic activity may also cause high pressures. Physical deformation of geological formations may for instance change the volume in which the sealed-off pore fluid exist, thus changing the pressure. Salt diapirism is an example of physical deformation of the subsurface. Areas where salt tectonism is frequent are often associated with high pore pressures (e.g., Gulf of Mexico).

High pressures may also develop as a result of chemical processes in the rock or pore fluid. These processes can be triggered at a certain temperature. For instance, it is an accepted view that high pressures may develop as a result of clay dehydration. At a certain temperature, water which is chemically bonded in the clay may dissolve and become part of the pore fluid. Free water molecules occupy more space than water molecules bonded in the clay, and as a result the pore pressure increases. Another chemical/temperature controlled pressure generating mechanism is quartz cementation, although the latter is debated.

Often, abnormally high pressures are not due to a single mechanism alone, but a combination of two or more mechanisms.

### **3 Seismic pore pressure prediction**

The concept of pore pressure prediction from acoustic data was explored already in the 1960's. Pennebaker (1968) was among the first to describe a method for predicting pore pressures from sonic log data. Eaton (1972) presented a mathematical expression which related sonic traveltimes to pore pressure. Reynolds (1970) described how velocities derived from seismic data could be used for pore pressure. All methods take advantage of the fact that sonic velocities depend on the effective pressure, and hence the pore

pressure.

The relation between effective pressure and velocity depend heavily on the texture and mineral composition of the rock. For instance, for unconsolidated sandstones, the P-wave velocity vary significantly with effective pressure (Domenico, 1977). The mechanism thought to be important here is the strengthening of grain contacts with increasing effective pressure. When applying external load to unconsolidated sand, the contacts between the individual grains become stronger. Thus the stiffness of the sand is increased. This leads to an increased P-wave velocity (Mindlin and Deresiewicz, 1953). On the other hand, velocities in consolidated rocks may also vary significantly with pressure. This is not due to strengthening of grain contacts, but rather to microscopic cracks in the rock. When applying external pressure, these cracks tend to close, thus creating contacts at the crack surfaces. As a result, the P-wave velocity increases. However, for consolidated rocks with little cracks, the velocities may not vary very much with pressure. In fact it can be shown (Dvorkin et al., 1991) that a granular rock with cemented grain contacts, have no pressure dependence at all.

The cause of geopressuring may be significant for discriminating between normal and high pore pressure based on seismic velocities. In the previous section, undercompaction was mentioned as one of the most important geological processes for buildup of abnormally high pore pressures. A consequence of undercompaction is that the porosity of the sediments is preserved. This means that undercompacted sediments are more porous than compacted sediments. The porosity is one of the key factors determining the velocity of a rock. Both theoretical considerations and experiments show that seismic velocities in general decrease with increasing porosity. Thus, undercompacted sediments tend to have lower velocities than compacted sediments. In cases where the cause of geopressuring is due to other geological processes, the porosity does not have to be abnormally high. However, the mechanisms mentioned above (contact stiffness and microcracks) may still influence the velocity.

## 4 Motivation for the thesis

Pore pressure estimation from seismic data is a multidisciplinary subject that require intimate knowledge of seismic data processing as well as an understanding of rock physics. The key parameters for seismic pore pressure prediction are the P-wave and S-wave velocities ( $V_p$  and  $V_s$ ). All pore pressure prediction work rely on a direct or indirect relationship between pore pressure and  $V_p$ ,  $V_s$ , or both. Therefore, a crucial part of pore pressure estimation from seismic data is to obtain accurate velocity information. This has been the focus for much of the published literature on this subject.

We may separate velocity analysis techniques into traveltime-based methods and amplitude-

based methods. Methods based on seismic traveltime take advantage of the fact that the time it takes for a seismic wave to pass through a medium is determined by the velocity of the medium. Modern techniques involving velocity analysis on 3D prestack migrated seismic data and traveltime tomography are capable of producing high-resolution velocity fields suitable for pore pressure prediction.

Amplitude-based methods take advantage of the fact that the strength of the reflection amplitudes depend on the velocity contrasts. The advantage of using seismic amplitudes for velocity determination is that we obtain the interval velocities near the seismic reflector. This is in contrast to the velocities obtained with conventional velocity analysis, which must be converted to interval velocities before the pore pressure is estimated (Dutta, 2002b). In addition, velocities derived from seismic amplitudes have higher temporal resolution than velocities derived from traveltimes. Both prestack seismic data and stacked seismic data can be used for velocity determination from amplitudes. State-of-the-art techniques like, for instance, prestack amplitude inversion can give velocities with high temporal resolution, suitable for pore pressure prediction.

While both traveltime- and amplitude-based methods have been used for pore pressure estimation, there has been little focus on combining information from traveltime and amplitudes. Uncertainties are inherent in seismically derived velocities. Hence, it may be impossible to draw conclusions based on one set of velocity data. Adding a second set of independent measurements can increase the confidence. In the first three papers of this thesis, it is shown how seismic pore pressure estimation can benefit from using seismic amplitudes as well as traveltime. The processing technique used for this purpose are conventional velocity analysis and analysis of peak amplitudes extracted from seismic data.

In order to obtain an estimate of the pore pressure from seismic velocities, one must know how the velocities are influenced by pore pressure. As discussed in the previous section, there are several mechanisms that determine the dependency of seismic velocities on pore pressure, and both lithology and cause of geopressuring is important. Thus, for pore pressure prediction, it is necessary to have good knowledge of the local geology.

Repeated (time-lapse) seismic data offer a unique possibility to obtain knowledge of how the local lithology respond to different pore pressures. Knowledge of how the pore pressure has changed over time, combined with analysis of time-lapse seismic data gives insight in how velocities are affected by pore pressure on a seismic scale. Time-lapse seismic data are used in four out of the five papers presented in this thesis. The first two time-lapse papers show how the sensitivity of seismic velocities to pressure can be determined from repeated seismic data. This knowledge can be used to estimate the pore pressure in undrilled prospects in the area. The last two time-lapse papers are more general processing papers, where the focus is on how we can estimate velocity changes in a time-lapse seismic data set.



In an exploration setting, we rarely have the possibility to use time-lapse seismic data in order to find the relation between pressure and velocities. One of the papers in the thesis focuses on how we can obtain a rock physics model for pore pressure estimation in this case. By using well data, we obtain a model that can be used to determine the pore pressure both conventional velocity analysis and amplitude analysis.

As mentioned in the introductory part, there are two basic seismic attributes that contain information on the seismic velocity; traveltimes and seismic amplitude. Velocities obtained from seismic traveltimes have low temporal resolution, typically 2-4 Hz according to (Dutta, 2002b). The reason for this is that a reflected seismic wave must pass through the rocks overlying the reflecting interface before it is recorded at the subsurface. Naturally, the propagation velocity is not constant in these overburden rocks. As the geology varies, so does the velocity of the seismic wavefront. Thus, the recorded traveltimes for a particular seismic event only give a measure of the *average* propagation velocity of the seismic wave. This velocity is often referred to as the stacking velocity, because it is used to produce the best image in a seismic stack. However, it is not a velocity in the true physical sense. It does not give the propagation velocity of the seismic wavefront in any of the particular geological layers (rock velocity) that the wave went through.

In order to deduce the rock velocity, one usually thinks of the earth as divided into discrete layers. If the rock velocity in the  $N$  upper layers is known, and if the stacking velocity at the reflection time of layer  $N + 1$  is known, one can obtain the rock velocity of layer  $N + 1$  from these quantities (Dix' equation). This way one can obtain rock velocities in a top-down procedure, starting with a stacking velocity field and the rock velocity of the uppermost layer.

## 5 Organisation of the thesis

The thesis consists of 8 chapters, including this introductory part. The main part of the thesis is organized into five independent papers. The papers are given as individual chapters, and are organized sequentially, starting at chapter 3. The first paper (chapter 3) is entitled "Pore pressure detection sensitivities tested with time-lapse seismic data". It was submitted to Geophysics in June 2003, and was accepted for publication in December 2004. In this paper we use time-lapse seismic data from the Gullfaks Field in the North Sea to estimate velocity changes in a hydrocarbon reservoir as a result of a pore pressure increase.

The second paper (chapter 4) is entitled "Pore pressure prediction at Haltenbanken". The topic of this paper is pore pressure prediction across sealing faults using velocity analysis and amplitude analysis. We use a dataset from Haltenbanken in the Norwegian Sea to demonstrate the method.

The third paper (chapter 5) is entitled “Pore pressure prediction - what can we learn from 4D?” This paper was published in Recorder, the journal of the Canadian Society of Exploration Geophysicists (CSEG). The primary author of this paper is Professor Martin Landrø, Dept. of petroleum engineering and applied geophysics, Norwegian university of science and technology. In this paper an amplitude-based approach of pore pressure prediction across faults is presented.

The fourth paper (chapter 6) is entitled “A spectral ratio method for time-lapse seismic monitoring on the Gullfaks Field”. In this paper we use a special technique of convolution-deconvolution in the f-k domain to estimate time-lapse changes in the reflectivity at interfaces. We use an example from the Gullfaks Field to demonstrate the method.

The fifth paper (chapter 7) is entitled “Discrimination of phase and amplitude attributes in time-lapse seismic streamer data”.. This paper was submitted to Geophysics in June 2003, and is currently in a review process. The primary author of this paper is dr. Jesper Spetzler, who is currently working as a Post. Doc. Researcher at the Technical University of Delft, Netherlands. In this paper, we demonstrate a method for detecting changes in a time-lapse seismic dataset.

For completeness I have added a modeling chapter aimed to explain some of the basic physics of seismic pore pressure prediction using seismic amplitude analysis with offset (chapter 2), and a closing chapter (chapter 8).



## Chapter 2

# Seismic amplitudes in pore pressure prediction

As mentioned in the introductory part, there are two basic seismic attributes that contain information on the seismic velocity; traveltime and seismic amplitude. Velocities obtained from seismic traveltime have low temporal resolution and do not measure the true propagation velocity of the seismic wave. Seismic amplitudes, on the other hand, depend on the reflection coefficient of a contrast in the subsurface, which is directly related to the propagation velocity of the seismic wave. However seismic amplitude analysis is also less robust than velocity analysis based on traveltime. In this chapter, we study how pore pressure affect seismic amplitudes.

The value of seismic amplitudes for pore pressure prediction can be motivated by the limitations of conventional traveltime based velocity analysis. The traveltime  $t_0$  at normal incidence and the traveltime  $t$  at some offset  $x$ , and can be related to seismic velocity through

$$t^2 = t_0^2 + \frac{x^2}{V^2}. \quad (1)$$

Equation (1) is often referred to as the normal moveout (NMO) equation. The velocity  $V$  is the average velocity between the surface and the depth of the seismic reflector. The residual moveout is given by  $\Delta t = t - t_0$  and is known from the seismic. In velocity analysis, one chooses the velocity that gives the best estimate for  $\Delta t$ . However, the velocity in equation (1) is not suitable for pore pressure prediction. For this purpose we need the true propagation velocity of the seismic wave. One can obtain an estimate for the true propagation velocity by assuming that the earth is divided in discrete layers with constant velocity. If the propagation velocity in layer  $i$  is given by  $v_i$ , and the internal traveltime is

given by  $t_i$ , then the rms velocity down to the base of layer  $N$  can be written as

$$V_{\text{rms}} = \frac{\sum_{i=1}^N v_i^2 t_i}{\sum_{i=1}^N t_i}. \quad (2)$$

Equation (2) is the well known Dix' equation. The  $V_{\text{rms}}$  typically differs from the velocity  $V$  in equation (1) by only a few percent. Hence, by assuming  $V = V_{\text{rms}}$ , one can obtain estimates for the interval velocities  $v_i$  by using equation (2) recursively.

Equation (1) is valid only for a horizontally layered isotropic earth and straight raypaths. Velocity analysis software uses complex mathematical tools to compensate for dip and curvature in the subsurface, and for raypath bending. It is also possible to correct for velocity anisotropy. However, these corrections require that we know the velocity field in advance. This can be solved by using velocities from equation (1) as input, and then repick velocities in order to repeat the process until a satisfactory result is obtained. Velocity anisotropy can be estimated e.g., from VSP data. This way one can obtain a robust velocity field. However, the velocities obtained in this manner have a low temporal resolution. It is not feasible to simply increase the number of layers  $N$  in equation (2) in order to increase the resolution. As is shown in Chapter 3 of this thesis, the layers must be of a certain thickness in order to get reliable interval velocities. The temporal resolution of interval velocities from conventional velocity analysis is typically 2-4 Hz, according to Dutta (2002b). This normally corresponds to intervals thicker than 200 m.

The relative success of velocity analysis for pore pressure prediction can be explained by the nature of abnormally high pore pressures in shale. When overpressure is generated by disequilibrium compaction, as explained in Chapter 1, the thickness of the overpressured zone may extend over several hundreds of meters, more than enough to detect by conventional velocity analysis, provided that the overpressure is accompanied by a sufficient reduction in velocity. However, it is widely recognized that overpressures can exist in isolated zones, too thin to detect by conventional velocity analysis. For instance, severe overpressures can be found in shallow gas pockets only tens of meters thick. Another interesting example is overpressure generated by fluid injection in hydrocarbon reservoirs. In these cases, seismic amplitude analysis can serve as a tool for pore pressure prediction.

We separate between prestack and poststack seismic amplitude analysis. In poststack amplitude analysis we assume normal incidence seismic waves. This is well suited for estimation of the acoustic impedance. Prestack amplitude analysis uses the variation of amplitude with offset (AVO) to obtain elastic parameters. The resolution of elastic parameters derived from seismic amplitude analysis is limited by the seismic bandwidth. Thus, it is possible to obtain velocities at a much finer scale than with conventional velocity analysis. However, seismic amplitude analysis is also less robust than conventional velocity analysis. The signature of a recorded seismic event is affected by everything that the wave has passed through on its way from source to receiver.

# 1 Theory

The concept of seismic amplitude analysis is based on the fact that seismic amplitudes carry detailed information on subsurface rock properties. True rock velocities can, in principle, be deduced from seismic amplitudes.

In the idealized case of a plane wave incident on a horizontal interface separated by two homogeneous media, the PP reflection coefficient is given by Zoeppritz' equations (see e.g. Aki and P, 1980). An approximation for the PP reflection coefficient can be written (Smith and Gidlow, 1987):

$$R_{PP}(\theta) = \frac{1}{2} \left( \frac{\Delta V_p}{V_p} + \frac{\Delta \rho}{\rho} \right) - 2 \frac{V_s^2}{V_p^2} \left( \frac{\Delta \rho}{\rho} + 2 \frac{\Delta V_s}{V_s} \right) \sin^2 \theta + \frac{\Delta V_p}{2V_p} \tan^2 \theta, \quad (3)$$

where  $\theta$  is the incidence angle, and  $\Delta V_p/V_p$ ,  $\Delta V_s/V_s$ , and  $\Delta \rho/\rho$  are the contrasts in P-wave velocity, S-wave velocity and density across the interface.

Equation (3) can be written as:

$$R_{PP} = R_0 + G \sin^2 \theta, \quad (4)$$

where

$$\begin{aligned} R_0 &= \frac{1}{2} \left( \frac{\Delta \alpha}{\alpha} + \frac{\Delta \rho}{\rho} \right) \\ G &= -2 \frac{\beta^2}{\alpha^2} \left( \frac{\Delta \rho}{\rho} + 2 \frac{\Delta \beta}{\beta} \right) + \frac{1}{2} \frac{\Delta \alpha}{\alpha} \frac{\tan^2 \theta}{\sin^2 \theta} \end{aligned} \quad (5)$$

Equation (4) is often called the “two term AVO equation” and is attractive because it is linear in  $\sin^2 \theta$ . Equation (4) is the starting point for conventional AVO analysis. From the parameters  $R_0$  and  $G$ , called the AVO intercept and gradient, it is possible to deduce elastic parameters.

It is not straightforward to estimate  $R_0$  and  $G$  from seismic prestack data. An obvious limitation is noise in the seismic data, which inherently will introduce uncertainties. However, let us for the moment assume that we can get reliable estimates for  $R_0$  and  $G$ . The question of how these quantities are affected by pore pressure still remains.

There are many factors that determine the elastic parameters of a rock. Most important are the properties of the rock frame, or skeleton, such as mineralogy and porosity. These properties do not depend on the external conditions of the rock. However, the external conditions also contribute significantly to the elastic parameters. For instance, pore pressure affects the P- and S-wave velocity, while fluid saturation affects the P- wave velocity and the density. In order to predict pore pressure from seismic amplitude data, it is useful

to know how different external conditions affect the seismic reflectivity. Furthermore, there are properties of a rock that are not taken into account in equation (3), but which still may affect the reflectivity. Anisotropy and anelasticity are examples of such properties. In order to see how we can separate pore pressure from fluid saturation, and how anisotropy and anelasticity affect the reflectivity, we have performed seismic modeling with a series of models.

## 2 AVO modeling

As a reference model, we assume a one-dimensional two-layer model with a cap rock (shale) overlying a reservoir (sandstone). Initially, the reservoir is 100% oil saturated. Both the cap rock and the reservoir are normally (hydrostatic) pressured. Furthermore, we assume that the rocks of the reference model are isotropic and homogeneous. The elastic parameters are given as Model 1 in Table 1.

Seismic modeling is done using a coarse finite-difference scheme (Holberg, 1987). This enables us with great flexibility to model different cases. In the modeling, we only record the P-waves in order to simulate a marine seismic experiment. The maximum incidence angle considered is approximately 30 degrees, which is about the maximum angle for which the approximation in equation (3) is valid.

An NMO-corrected synthetic seismogram for the reference model is shown in Figure 1. From this seismogram, we extract the peak amplitudes along the reflector. The extracted amplitudes are scaled by a constant factor, such that the scaled amplitude at zero offset equals the theoretical reflection coefficient at zero offset. This way, the scaled amplitudes for all offsets are assumed to represent the true reflection coefficient. From the scaled amplitudes, we can calculate values for  $R_0$  and  $G$  in equation (4). Figure 2 shows a plot of the scaled amplitudes (reflection coefficient) versus  $\sin^2 \theta$ . Linear regression on the scaled amplitudes give  $R_0 = 0.029$  and  $G = -0.21$ . This is close to the theoretical values estimated from equations (5), which is  $R_0 = 0.029$  and  $G = -0.24$ . The small discrepancy for  $G$  can probably be explained by the fact that equation (4) only is an approximation to the true reflection coefficient.

In order to simulate variations in rock properties, we introduce perturbations to the reference model. Seismic modeling is carried out with the perturbed model, and values for  $R_0$  and  $G$  are estimated. We consider in all 14 different cases, including the reference model. First, we study the effect of pore pressure alone on seismic amplitudes. Next, we include the effect of variations in fluid saturation, anisotropy and attenuation.

**Table 1:** Two-layer models used in synthetic modeling

	Cap rock					Reservoir				
	$V_p$ (m/s)	$V_s$ (m/s)	$\rho$ (kg/m <sup>3</sup> )	$\epsilon$	$\delta$	$Q$	$V_p$ (m/s)	$V_s$ (m/s)	$\rho$ (kg/m <sup>3</sup> )	$\epsilon$ $\delta$ $Q$
Model 1	2500	1200	2550				2600	1500	2600	
Model 2	2500	1200	2550				2543	1467	2600	
Model 3	2500	1200	2550				2288	1320	2600	
Model 4	2500	1200	2550				2288	1256	2600	
Model 5	2250	1080	2550				2288	1320	2600	
Model 6	2500	1200	2550				2708	1458	2650	
Model 7	2500	1200	2550				2404	1537	2475	
Model 8	2500	1200	2550	0.1	0		2600	1500	2600	
Model 9	2500	1200	2550	0.5	0.1		2600	1500	2600	
Model 10	2500	1200	2550	0.5	0.1		2288	1320	2600	
Model 11	2500	1200	2550			300	2600	1500	2600	50
Model 12	2500	1200	2550			300	2600	1500	2600	5
Model 13	2500	1200	2550			10	2600	1500	2600	5
Model 14	2500	1200	2550			10	2288	1320	2600	5



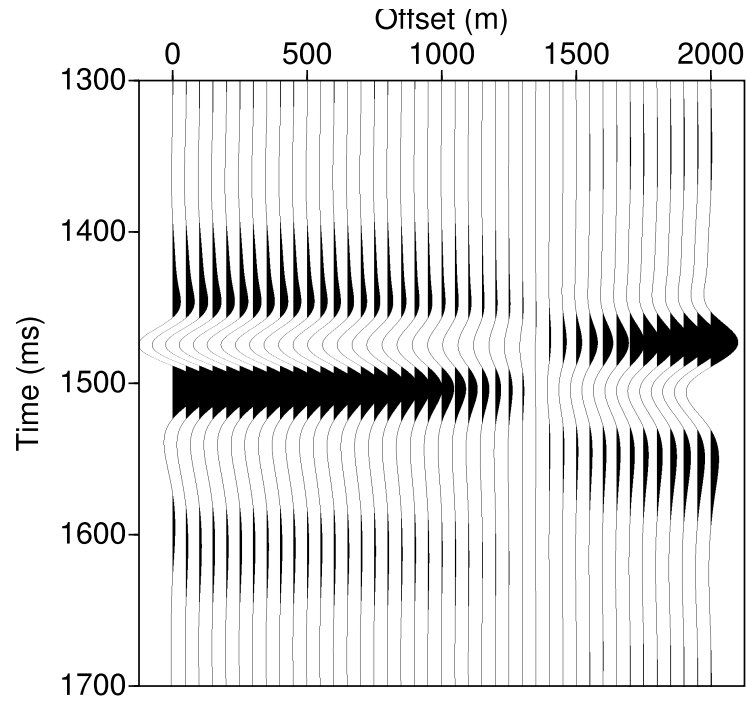


**Figure 1:** Seismogram showing NMO-corrected prestack seismic data computed from the reference model.

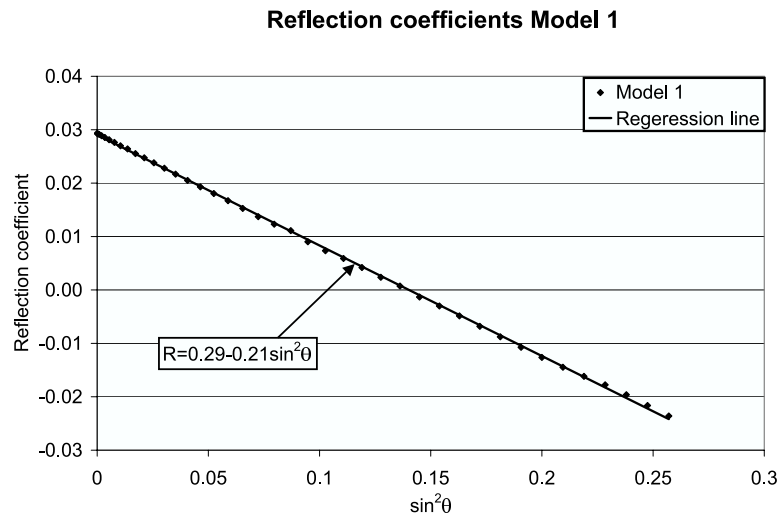


**Figure 2:** Estimated reflection coefficients from the synthetic seismic shown in Figure 1. The AVO parameters  $R_0$  and  $G$  are computed from linear regression on the data.

## 2.1 Pore pressure

Based on ultrasonic measurements on core plugs, Eberhart-Phillips et al. (1989) presented expressions relating effective pressure to seismic velocities for sandstones. Although these expressions by no means are valid for all types of sandstone, we will assume that the reservoir sandstone (layer 2) in our model obey these expressions.

Figure 3 shows the relative change in P-wave velocity as function of effective pressure, calculated from the expressions given by Eberhart-Phillips et al. (1989). The curve is normalized to 40 MPa, which we will assume corresponds to normal (hydrostatic) pressure conditions.

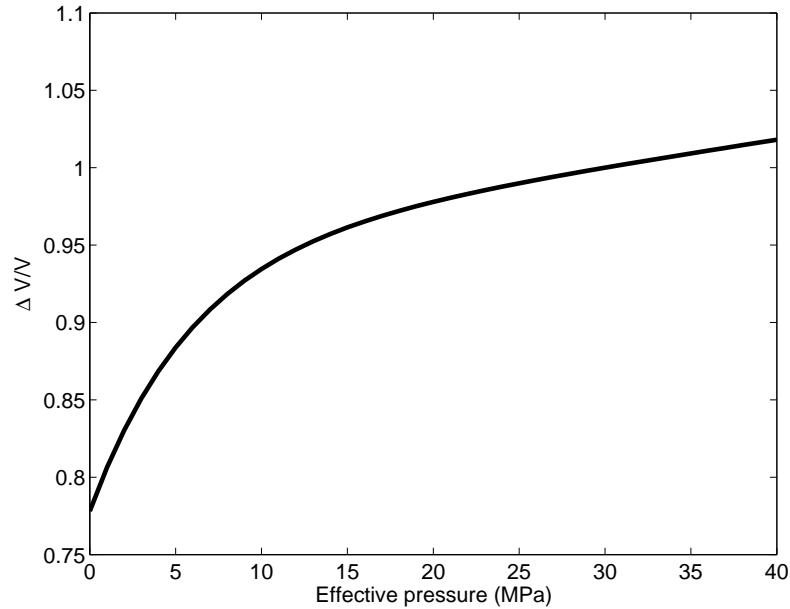


**Figure 3:** Relative change in P-wave velocity vs. effective pressure. The curve is computed from expressions given in Eberhart-Phillips et al. (1989) with the assumption that the P-wave velocity at 40 MPa effective pressure is 2600 m/s.

As a first perturbation to the reference model, we assume that the pore pressure in the reservoir sandstone is 10 MPa above normal. This corresponds to a reduction in P-wave velocity of 2.2%, according to figure 3. We will assume that the relative reduction in S-wave velocity as a result of 10 MPa overpressure is identical to the reduction in P-wave velocity, i.e., 2.2%. This assumption is used extensively throughout this thesis, and it is therefore interesting to see what kind of error we can expect. The density is assumed to be insensitive to pore pressure changes, and is therefore kept constant in this model. The

elastic parameters for this model are given as Model 2 in table 1.

Next, we increase the overpressure to 25 MPa above normal. This gives a reduction in P-wave velocity of 12 % according to figure 3. The  $V_p/V_s$  ratio is still assumed to be constant with pressure, and the density is unchanged. The elastic parameters for this case are given as Model 3 in Table 1.

(Eberhart-Phillips et al., 1989) also gave expressions relating S-wave velocity to effective pressure. Figure 4 shows the  $V_p/V_s$  ratio vs effective pressure calculated from the expressions for P- and S-wave velocity. We have set the  $V_p/V_s$  ratio at 40 MPa to 1.73, corresponding to our reference model (Model 1). We construct a new model (Model 4) with 25 MPa overpressure, and where the  $V_p/V_s$  ratio varies according to figure 4.

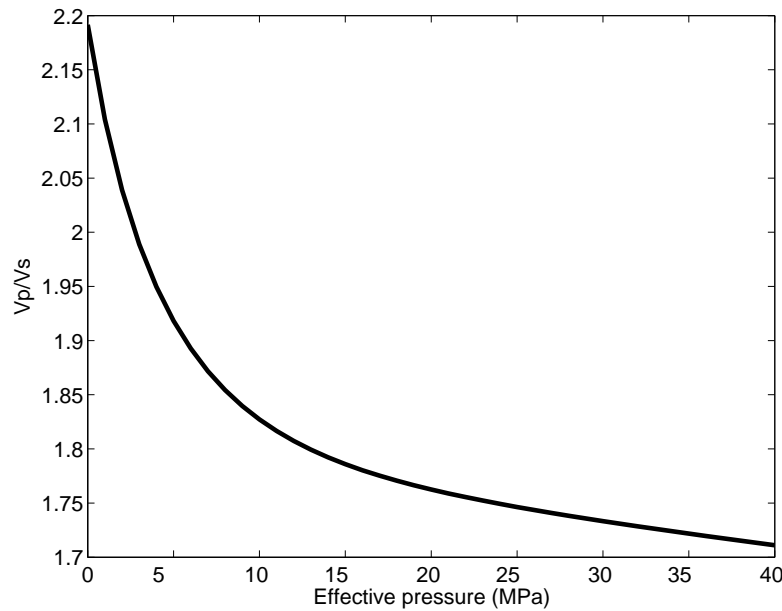


**Figure 4:**  $V_p/V_s$  ratio vs. effective pressure. The curve is computed from expressions given in Eberhart-Phillips et al. (1989) with the assumption that the  $V_p/V_s$  ratio at 40 MPa is 1.73

Finally, we consider the possibility of an overpressured cap rock as well as an overpressured reservoir. Figure 5 show the relative change in P-wave velocity as function of effective pressure used for the cap rock. This figure is representative for ultrasonic measurements on a shale sample by Jonston (1987). However, it is not thought to describe a general behaviour of velocities with pressure in shale. Again, we assume an overpressure of 25 MPa and a constant  $V_p/V_s$  ratio with pressure. The elastic parameters are given as Model 5 in table 1.

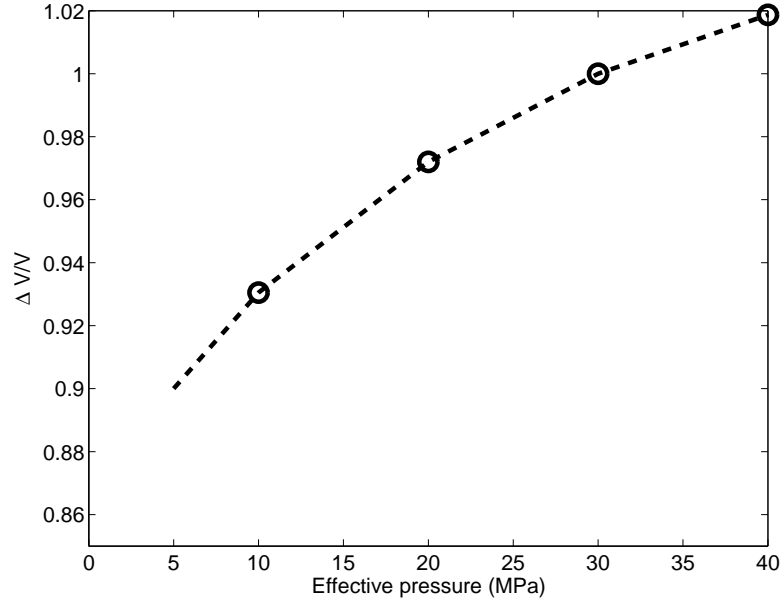


**Figure 5:** Relative change in P-wave velocity vs. effective pressure used for cap rock. The circles represent points measured by Jonston (1987), while the dotted line is a freehand “regression line”.

**Table 2:** Fluid properties used for fluid substitution

	Bulk modulus (GPa)	Density /kg/m <sup>3</sup>
Oil	1.5	800
Water	2.3	1000
Gas	0.25	300

## 2.2 Fluid saturation

The Biot-Gassmann equations (see e.g. Mavko et al., 1998) are commonly used to predict changes in elastic parameters as a result of change in fluid content. We use these equations to construct models where the oil in the reference model is replaced by either oil or gas. It is mainly the P-wave velocity and the density that are sensitive to the type of pore fluid. The S-wave velocity is less affected. We only consider fluid substitution in the reservoir sandstone. The porosity is set to 20%. The fluid parameters necessary to perform fluid substitution with the Biot-Gassmann equations are bulk moduli and densities of oil, water and gas. The parameters we have used are given in Table 2.

First, we consider the case where the oil has been replaced by water. For simplicity, we let the water saturation after fluid substitution be 100%. The elastic parameters for the water-saturated model are given as Model 6 in Table 1.

Next, we consider the case where the oil has been replaced by gas. Here, we assume that the gas saturation after fluid substitution is 100%. The elastic parameters for the gas-saturated model are given as Model 7 in table 1

## 2.3 Anisotropy

While we often idealize the earth as being isotropic, it is almost never the case. Anisotropy means that the propagation velocity of the seismic wavefront depend on the direction of propagation. We consider only weak anisotropy in a transversely isotropic medium. In this case, the degree of anisotropy can be described by Thomsen's parameters  $\epsilon$ ,  $\delta$  and  $\gamma$  (Thomsen, 1985). Since we do not record S-waves, we let the parameter  $\gamma = 0$ . This will not affect the results.

We restrict ourselves to the case of an anisotropic cap rock. Carcione et al. (1998) presented anisotropy parameters for Kimmeridge Shale in the North Sea. From this we estimate reasonable ranges for the anisotropy parameters to be approximately  $0.1 < \epsilon < 0.5$  and  $-0.1 < \delta < 0.1$ . We consider three cases with anisotropic cap rock.

First, we let the anisotropy be fairly moderate with  $\epsilon = 0.1$  and  $\delta = 0$ . The P-wave and S-wave velocity and the density is kept as in the reference model. This is given as Model 8 in Table 1.

Next, we let  $\epsilon = 0.5$  and  $\delta = 0.1$ . This corresponds to a relatively significant anisotropy in the cap rock. This is given as Model 9 in Table 1.

Finally, we consider the case where the reservoir is overpressured 25 MPa above normal and with  $\epsilon = 0.5$  and  $\delta = 0.1$ . This is given as Model 10 Table 1.

## 2.4 Attenuation

As a seismic wave propagates through the earth, some of its energy is transferred to heat. This phenomenon is known as seismic attenuation. Some of the mechanisms contributing to attenuation are described by H et al. (1979). The amount of attenuation is often

described by the quality factor  $Q$ , which is defined as

$$Q = \frac{2\pi}{\frac{\Delta E}{E}}, \quad (6)$$

where  $\Delta E/E$  is the fraction of energy lost per cycle. The quality factor varies for different lithologies, and it has been reported (Carcione et al., 1998) that contrasts in quality factors may affect the seismic reflectivity.

In the seismic modeling, we consider four different cases of attenuation. We use quality factors ranging from 5 (high attenuation) to 300 (low attenuation). This is approximately the range used by L and R (1994) for synthetic modeling.

First, we consider a case with low attenuation, but with a contrast in quality factor between the cap rock ( $Q = 300$ ) and the reservoir sandstone ( $Q = 50$ ). The parameters, including quality factors for this model are given as Model 11 in Table 1.

Next, we increase the contrast by letting the attenuation in the reservoir be higher ( $Q = 5$ ). This is given as Model 12 in Table 1.

Next, we also let the attenuation in the cap rock be high ( $Q = 10$  while we still let  $Q = 5$  in the reservoir. Thus, we decrease the contrast in attenuation. This is given as Model 13 in Table 1.

Finally, we keep the quality factors as in model 13, but increase the pore pressure by 25 MPa in the reservoir. This is given as Model 14 in Table 1.

### 3 Results

In Table 3 we have summarized values for  $R_0$  and  $G$  found for each of the models, along with the change in  $R_0$  and  $G$  compared with the reference model (Model 1). Plots similar to Figures 1 and 2 are given in appendix A.

We may attempt to see what separates pore pressure from the other rock properties by constructing plots of  $\Delta R_0$  versus  $\Delta G$ . For instance, it can be seen that if the pore pressure in the reservoir increases while the pore pressure in the cap rock is kept constant,  $\Delta R_0 < 0$  while  $\Delta G > 0$ . Furthermore, it seems like  $|\Delta R_0|$  is of the same order of magnitude as  $|\Delta G|$ , although for the case of varying  $Vp/Vs$  ratio with pressure, the change in AVO gradient is somewhat larger. For the case of overpressure cap rock as well as overpressured overburden, both  $|\Delta R_0|$  and  $|\Delta G|$  are small, indicating that pore pressure will be difficult to detect from seismic amplitudes in this case.

**Table 3:** AVO parameters from synthetic modeling

	$R_0$	$G$	$\Delta R_0$	$\Delta G$
Model 1	0.029	-0.21		
Model 2	0.018	-0.19	-0.011	0.01
Model 3	-0.035	-0.14	-0.064	0.07
Model 4	-0.035	-0.09	-0.064	0.012
Model 5	0.018	-0.19	-0.011	0.02
Model 6	0.059	-0.16	0.03	0.05
Model 7	-0.035	-0.26	-0.064	-0.05
Model 8	0.029	-0.22	0.0	-0.01
Model 9	0.029	-0.29	0.0	-0.08
Model 10	-0.034	-0.18	-0.063	0.03
Model 11	0.029	-0.21	0.0	0.0
Model 12	0.029	-0.27	0.0	-0.06
Model 13	0.027	-0.084	-0.006	0.13
Model 14	-0.034	-0.04	-0.063	0.17

Fluid substitution seems to differ from pore pressure in the AVO parameters  $R_0$  and  $G$ . For substitution of oil with water, we find  $\Delta R_0 > 0$  and  $\Delta G > 0$ . For substitution of oil with gas, we find  $\Delta R_0 < 0$  and  $\Delta G < 0$ . Thus, a way to separate pore pressure effects from fluid effects can be to determine in which quadrant  $\Delta R_0$  and  $\Delta G$  plots. Although we have modeled for only two cases of fluid substitution, we are fairly confident of the effect of pore fluid on seismic amplitudes. For instance, substitution of 100% oil with, say, 60% water and 40% oil, will have the same qualitative effect on the elastic parameters, and hence on  $\Delta R_0$  and  $\Delta G$  as substitution of 100% oil with 100% water. Figure 6 gives a schematic overview of the effects of fluid saturation and pore pressure on seismic amplitudes.

For anisotropy and attenuation it is not straightforward to predict in which quadrants  $\Delta R_0$  and  $\Delta G$  plot. Although we notice a slight decrease in  $\Delta G$  as a result of increasing the anisotropy parameter  $\epsilon$  (Models 8-9), we have not modeled enough cases with variation of the anisotropy parameters and quality factors conclude that anisotropy and attenuation have distinct AVO signatures. However, it is interesting to see what kind of errors we make if we do not take these properties into account.

As is evident from the results of modeling with models 8-14, anisotropy and attenuation may lead to significantly different values for the AVO parameters than in cases where these effects are not present. This, in turn, may lead to wrong estimates of the elastic parameters. The AVO intercept,  $R_0$  is not considerably altered, because we have scaled the zero offset amplitude to the zero offset reflection coefficient. However, there are

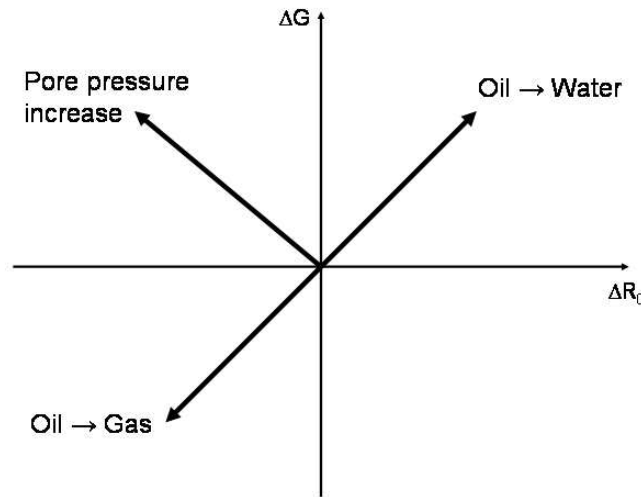


**Figure 6:** Schematic plot of the effect of pore pressure and fluid substitution on  $R_0$  and  $G$ . The arrows indicate how the different reservoir conditions affect the AVO signal. Note that this is only valid for the top reservoir interface.

significant differences in the AVO gradient  $G$ .

Comparing the AVO intercept and gradient of the Models 8-14 with the reference model is interesting to see what anisotropy and attenuation does to the seismic reflectivity. However, for pore pressure prediction, it is more relevant to compare a normally pressured model to an overpressured model with the same anisotropy or attenuation parameters. The difference in AVO gradient and intercept between Models 9 (normal pressure, anisotropic) and 10 (overpressure, anisotropic) gives  $\Delta R_0 = -0.063$  and  $\Delta G = 0.11$ . The value for  $\Delta G$  is different from the value obtained with no anisotropy present (0.07), but is qualitatively in agreement with Figure 6. A similar comparison of Models 13 (normal pressure, attenuation) and 14 (overpressure, attenuation) give  $\Delta R_0 = -0.061$  and  $\Delta G = 0.08$ , again in agreement with Figure 6. Thus, predicting changes in pore pressure may be possible in cases with significant anisotropy and attenuation. However, it is important that we compare seismic data from formations with similar anisotropy and/or attenuation parameters.



## 4 Discussion and conclusions

Through synthetic modeling we have seen that pore pressure may affect the seismic reflectivity, but that also fluid saturation, anisotropy and attenuation are important. We have not by far covered all possible cases. However, we do see a general pattern which makes it possible to separate between pore pressure and pore fluid effects (Figure 6).

In the case where both the cap rock and the reservoir was overpressured, the change in reflectivity from the reference model was small. This is expected, since the reflectivity depends on the contrast in elastic parameters. When we increase the pressure in both the cap rock and the reservoir, the change in contrast is smaller than if we change the pressure in just one layer. However, this does not necessarily mean that it is impossible to detect abnormal pressures if both the cap rock and the reservoir is overpressured. The change in contrast across the reflecting interface is governed by the pressure-velocity relationships in the cap rock and the reservoir. I

Anisotropy and attenuation do affect the AVO parameters  $R_0$  and  $G$ , and hence elastic parameters extracted from them. However, changes in  $R_0$  and  $G$  due to pore pressure are not significantly affected. For instance, comparing two models with attenuation gave approximately the same pressure effect on  $R_0$  and  $G$  as comparing two models without attenuation.

The knowledge of how the AVO parameters change with pressure and saturation is very useful from seismic reservoir monitoring (time lapse seismic). In time lapse seismic experiments, we are interested in changes in elastic parameters over time. In this case, the baseline survey serves as a reference, and it is possible to estimate changes in the AVO parameters  $R_0$  and  $G$ . In this case, we are comparing seismic data from the same location, we can be confident that the lithology does not change between the two surveys. Hence, time lapse changes in the seismic data are likely to be due to a change in external conditions like fluid saturation and pore pressure.

In an exploration setting, however, it is not obvious how we can use the knowledge of how AVO parameters change with saturation and pressure. How do we compute a change in the parameters  $R_0$  and  $G$  if we have only one seismic dataset? One possible solution is to compare seismic amplitude data across fault planes. If the lithologies at both sides of the fault are comparable, we may get reasonable estimates for  $\Delta R_0$  and  $\Delta G$  across the fault plane. Thus, we may use seismic amplitudes to predict pore pressure across faults. However, since we normally have limited control of the lithology in an exploration case, the uncertainties will inherently be larger than in a time lapse setting.

## A Modeling results

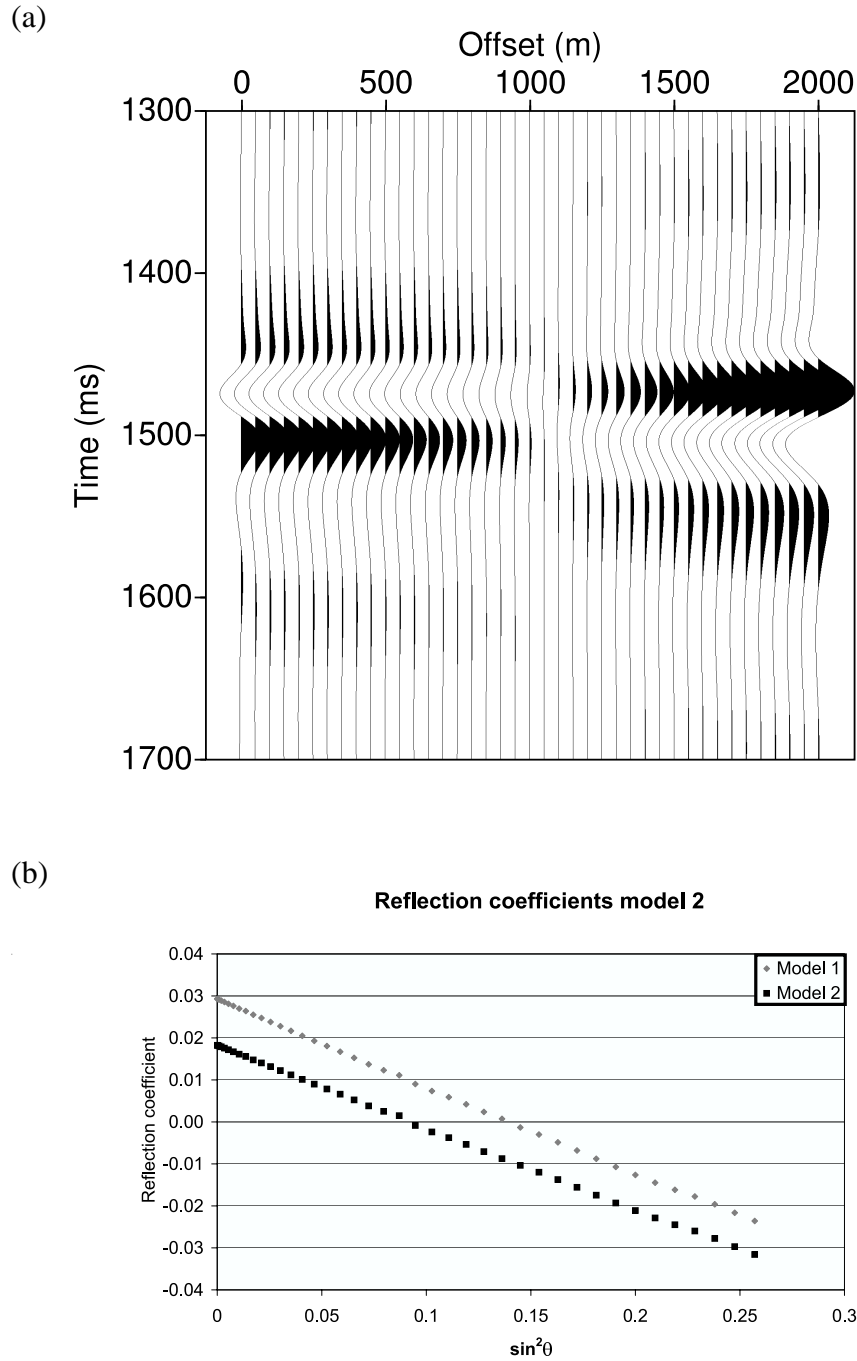


**Figure 7:** (a) Seismogram showing NMO-corrected prestack seismic data computed from Model 2. (b) Estimated reflection coefficients from the synthetic seismic shown above (black squares), and estimated reflection coefficients for Model 1 (gray diamonds)

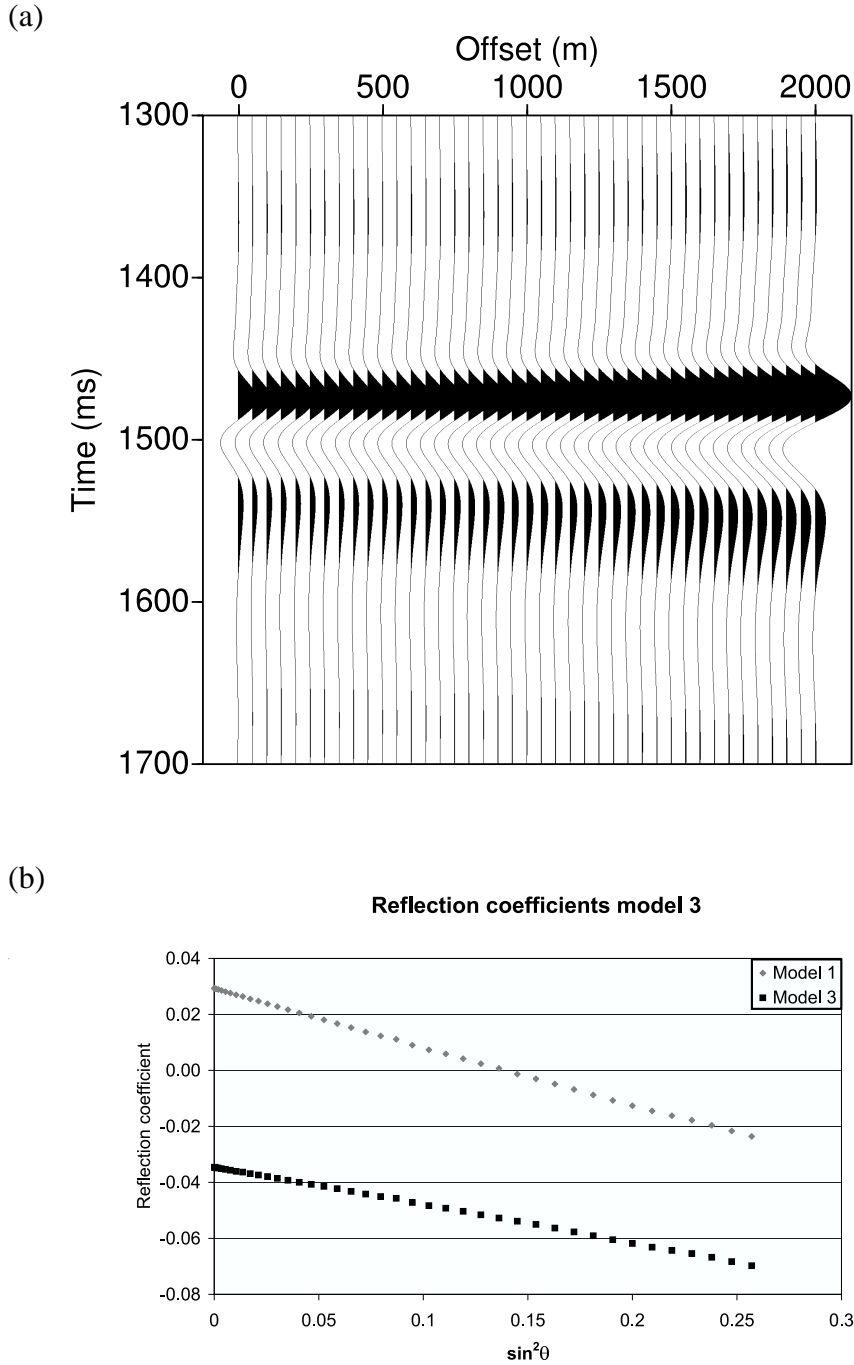


**Figure 8:** (a) Seismogram showing NMO-corrected prestack seismic data computed from Model 3. (b) Estimated reflection coefficients from the synthetic seismic shown above (black squares), and estimated reflection coefficients for Model 1 (gray diamonds)

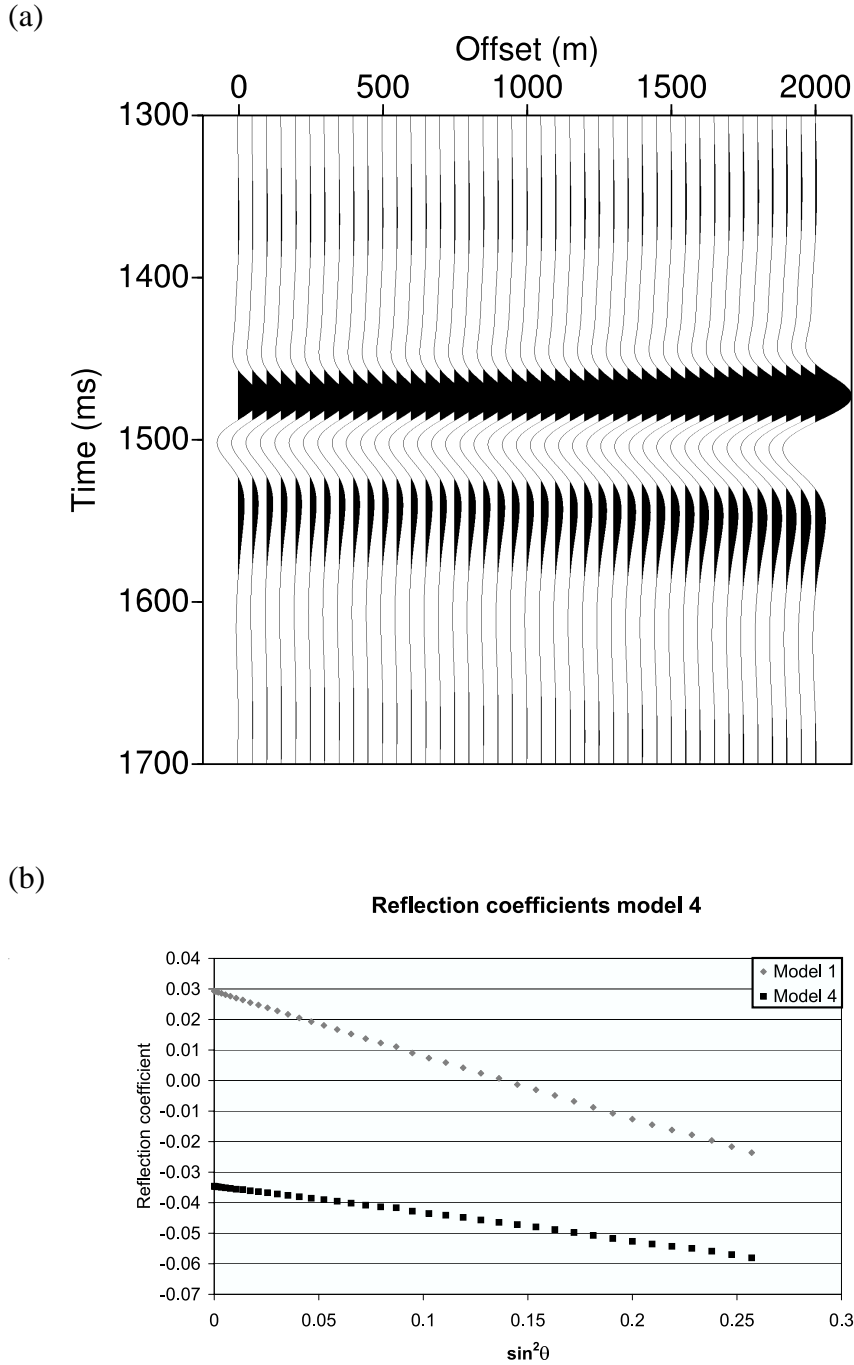


**Figure 9:** (a) Seismogram showing NMO-corrected prestack seismic data computed from Model 4. (b) Estimated reflection coefficients from the synthetic seismic shown above (black squares), and estimated reflection coefficients for Model 1 (gray diamonds)

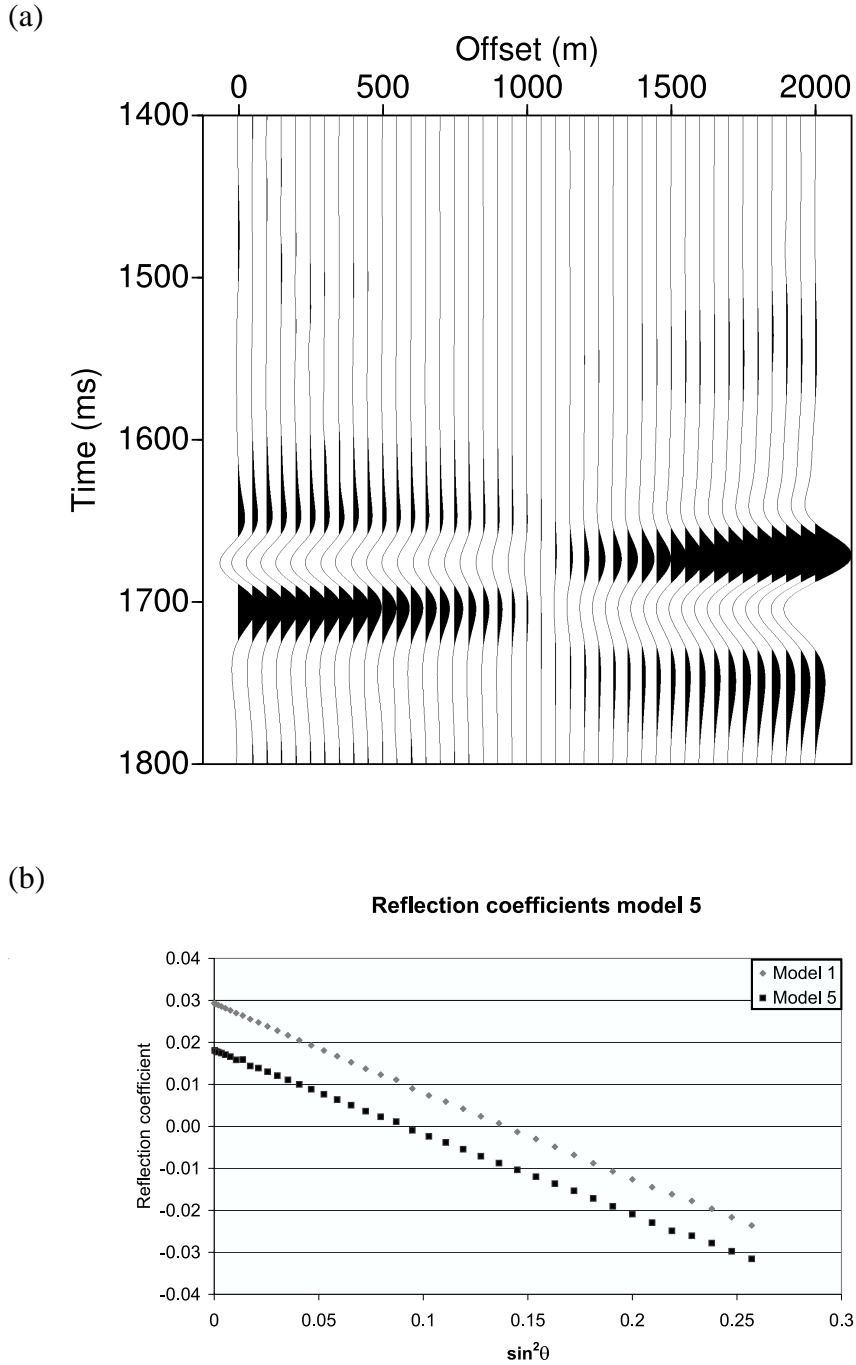


**Figure 10:** (a) Seismogram showing NMO-corrected prestack seismic data computed from Model 5. (b) Estimated reflection coefficients from the synthetic seismic shown above (black squares), and estimated reflection coefficients for Model 1 (gray diamonds)

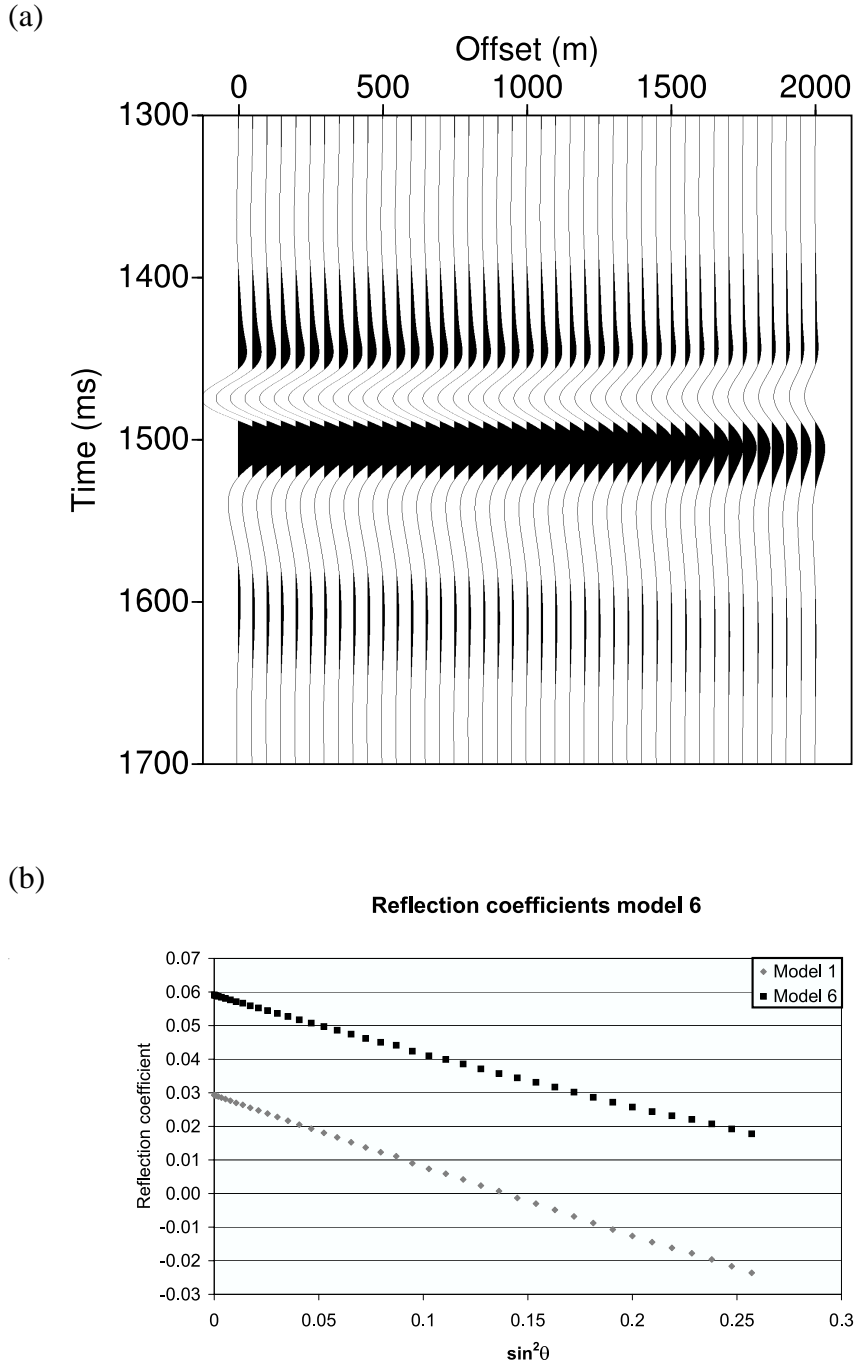


**Figure 11:** (a) Seismogram showing NMO-corrected prestack seismic data computed from Model 6. (b) Estimated reflection coefficients from the synthetic seismic shown above (black squares), and estimated reflection coefficients for Model 1 (gray diamonds)

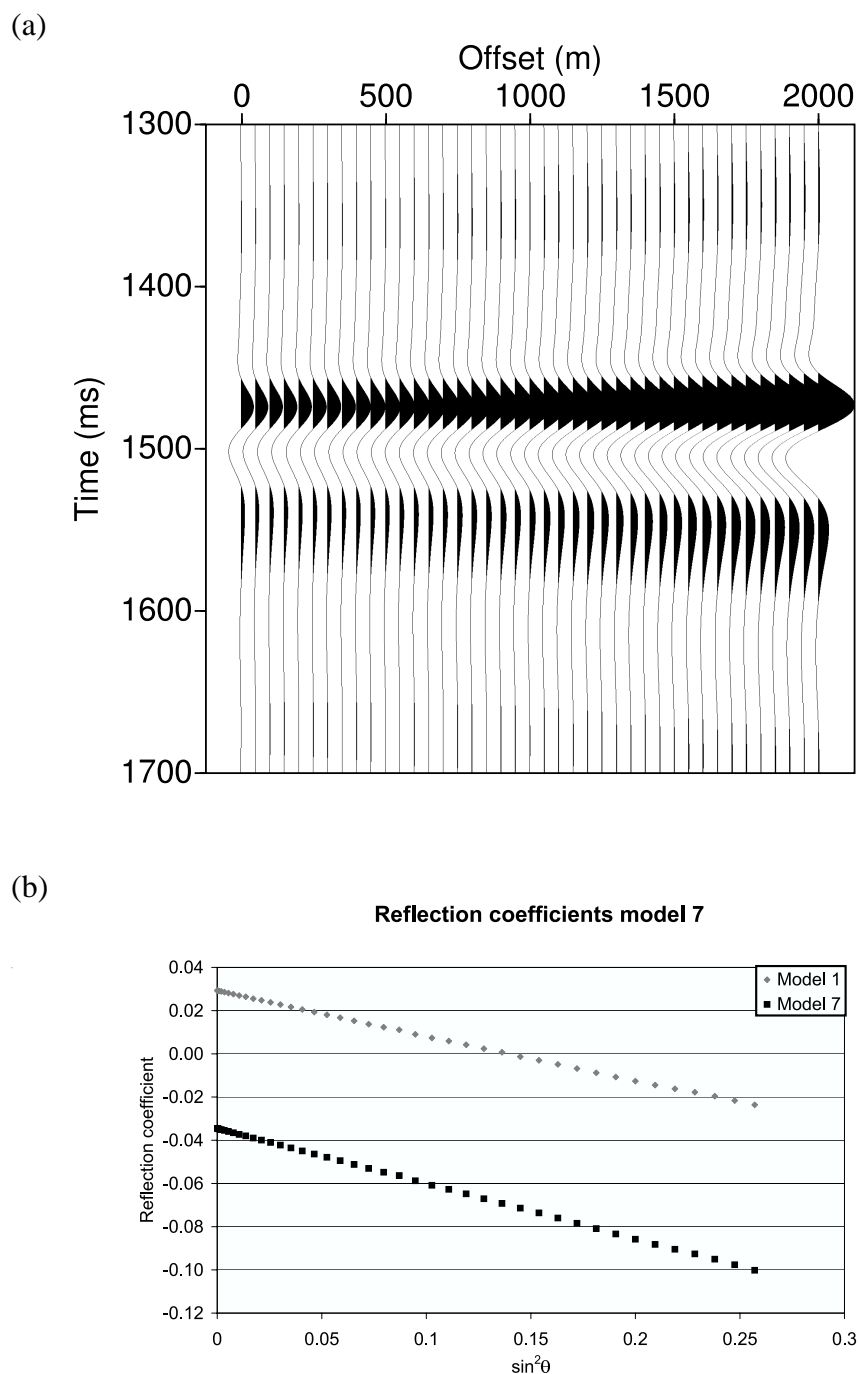


**Figure 12:** (a) Seismogram showing NMO-corrected prestack seismic data computed from Model 7. (b) Estimated reflection coefficients from the synthetic seismic shown above (black squares), and estimated reflection coefficients for Model 1 (gray diamonds)

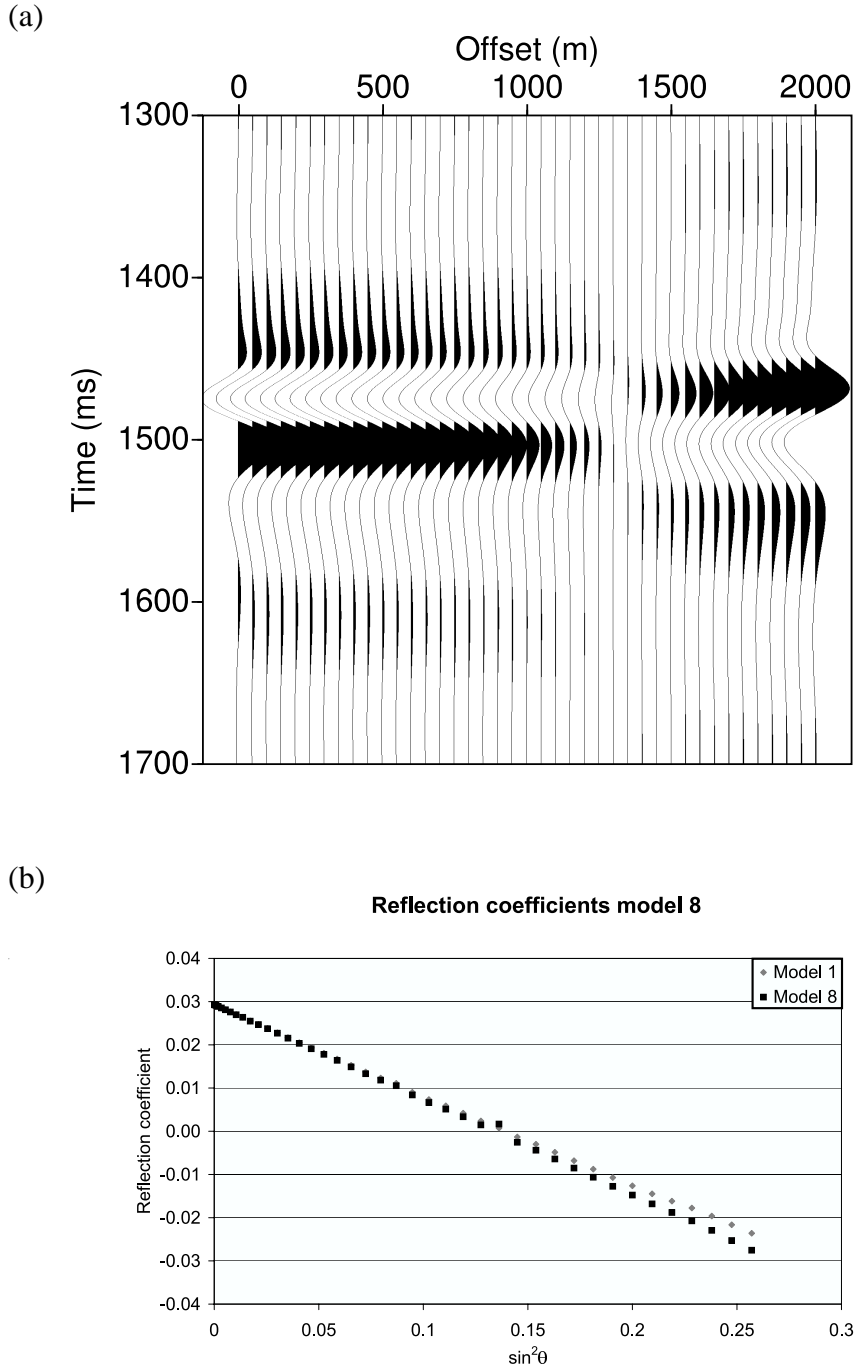


**Figure 13:** (a) Seismogram showing NMO-corrected prestack seismic data computed from Model 8. (b) Estimated reflection coefficients from the synthetic seismic shown above (black squares), and estimated reflection coefficients for Model 1 (gray diamonds)



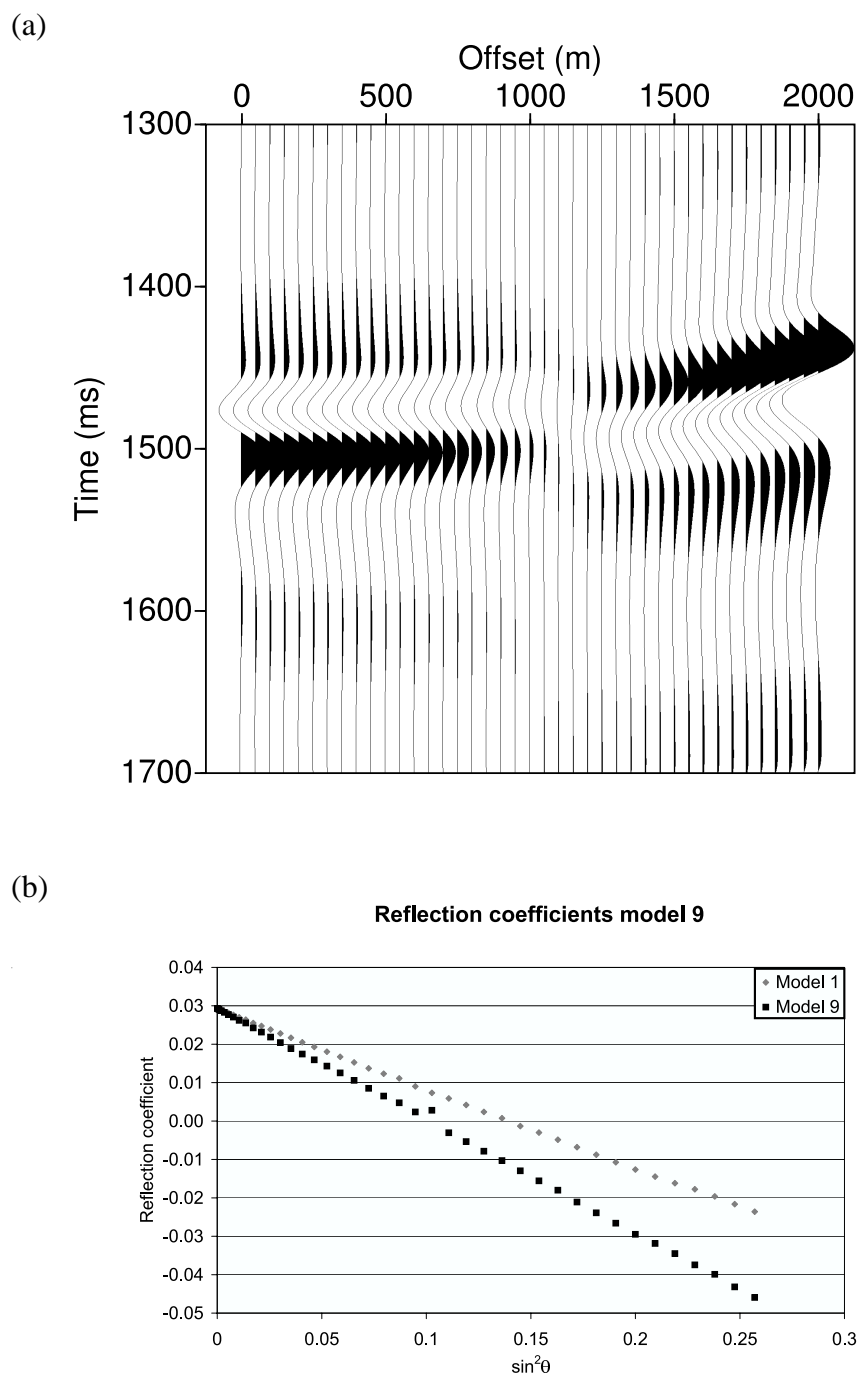


**Figure 14:** (a) Seismogram showing NMO-corrected prestack seismic data computed from Model 9. (b) Estimated reflection coefficients from the synthetic seismic shown above (black squares), and estimated reflection coefficients for Model 1 (gray diamonds)

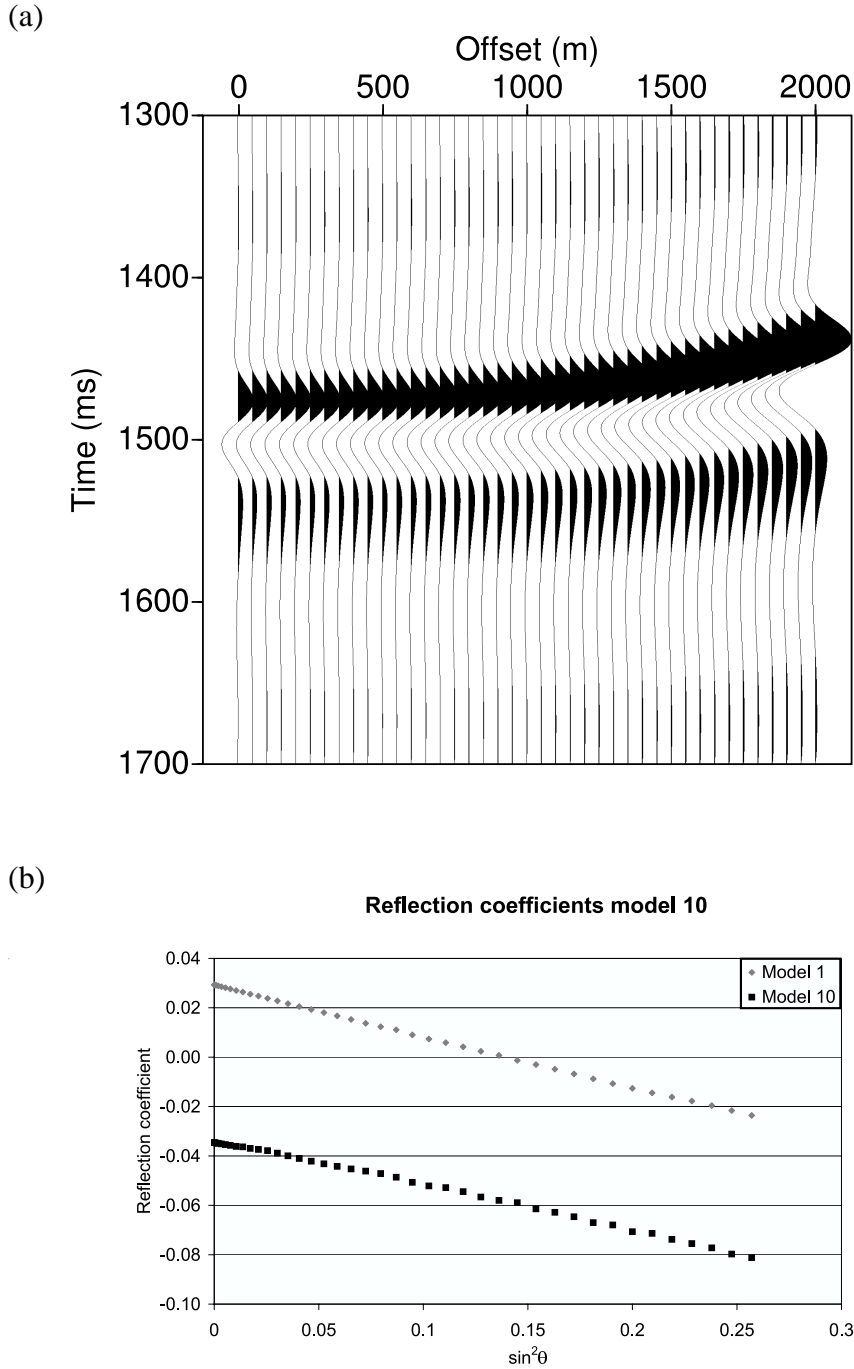
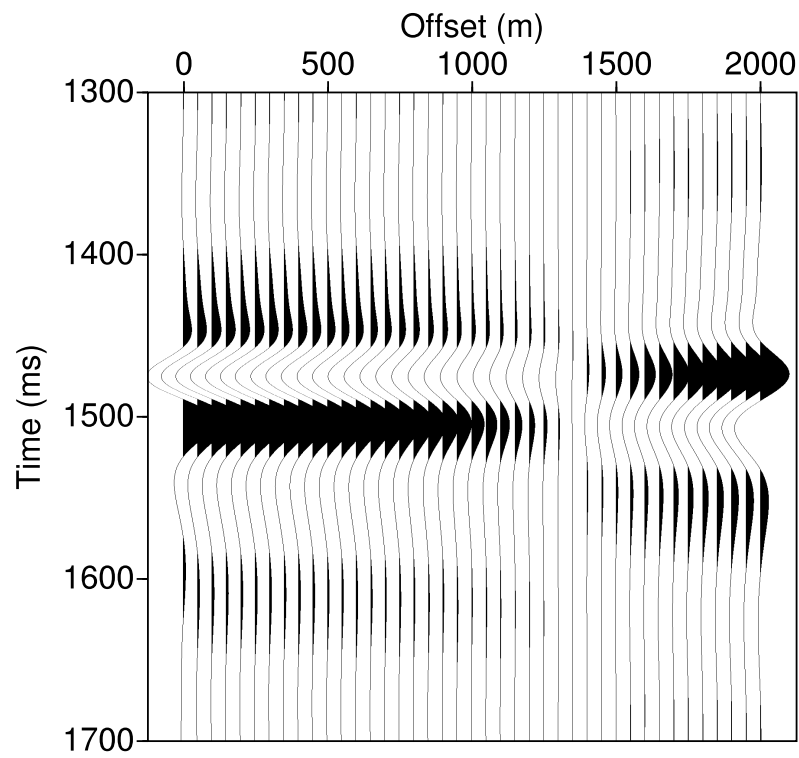


**Figure 15:** (a) Seismogram showing NMO-corrected prestack seismic data computed from Model 10. (b) Estimated reflection coefficients from the synthetic seismic shown above (black squares), and estimated reflection coefficients for Model 1 (gray diamonds)

(a)



(b)

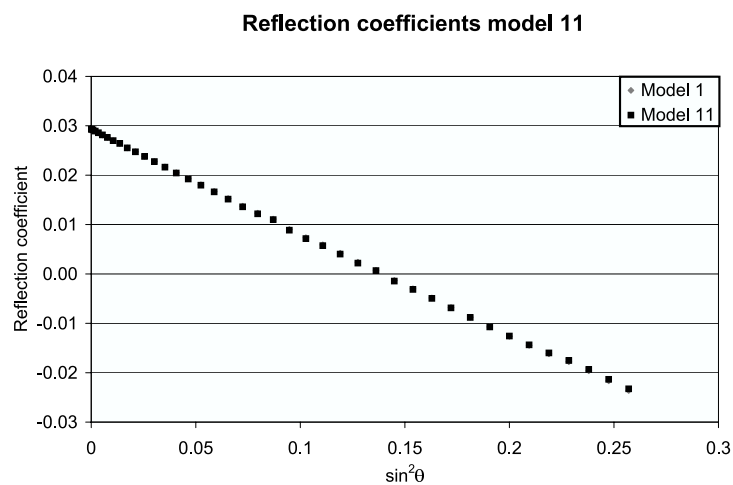


**Figure 16:** (a) Seismogram showing NMO-corrected prestack seismic data computed from Model 11. (b) Estimated reflection coefficients from the synthetic seismic shown above (black squares), and estimated reflection coefficients for Model 1 (gray diamonds)

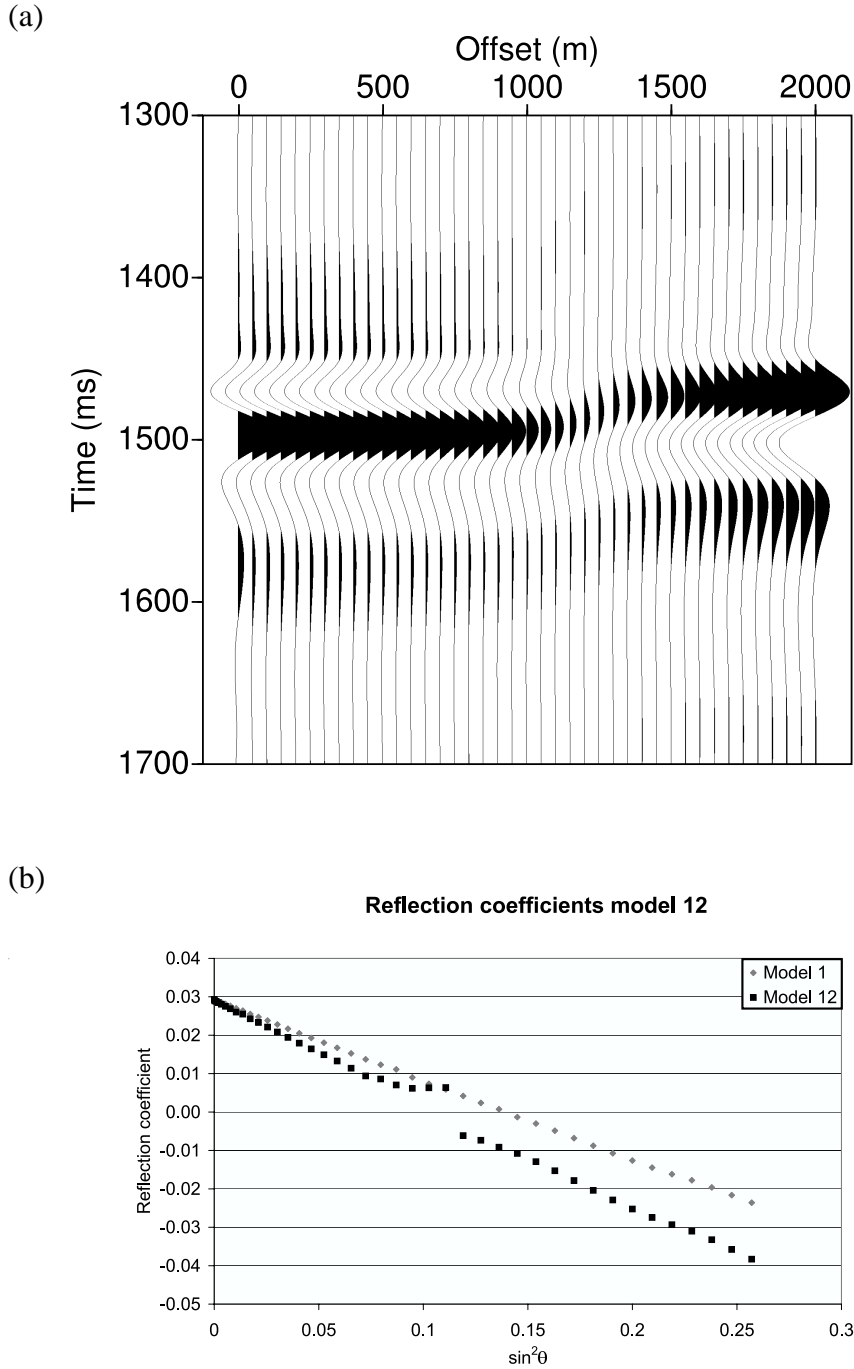


**Figure 17:** (a) Seismogram showing NMO-corrected prestack seismic data computed from Model 12. (b) Estimated reflection coefficients from the synthetic seismic shown above (black squares), and estimated reflection coefficients for Model 1 (gray diamonds)

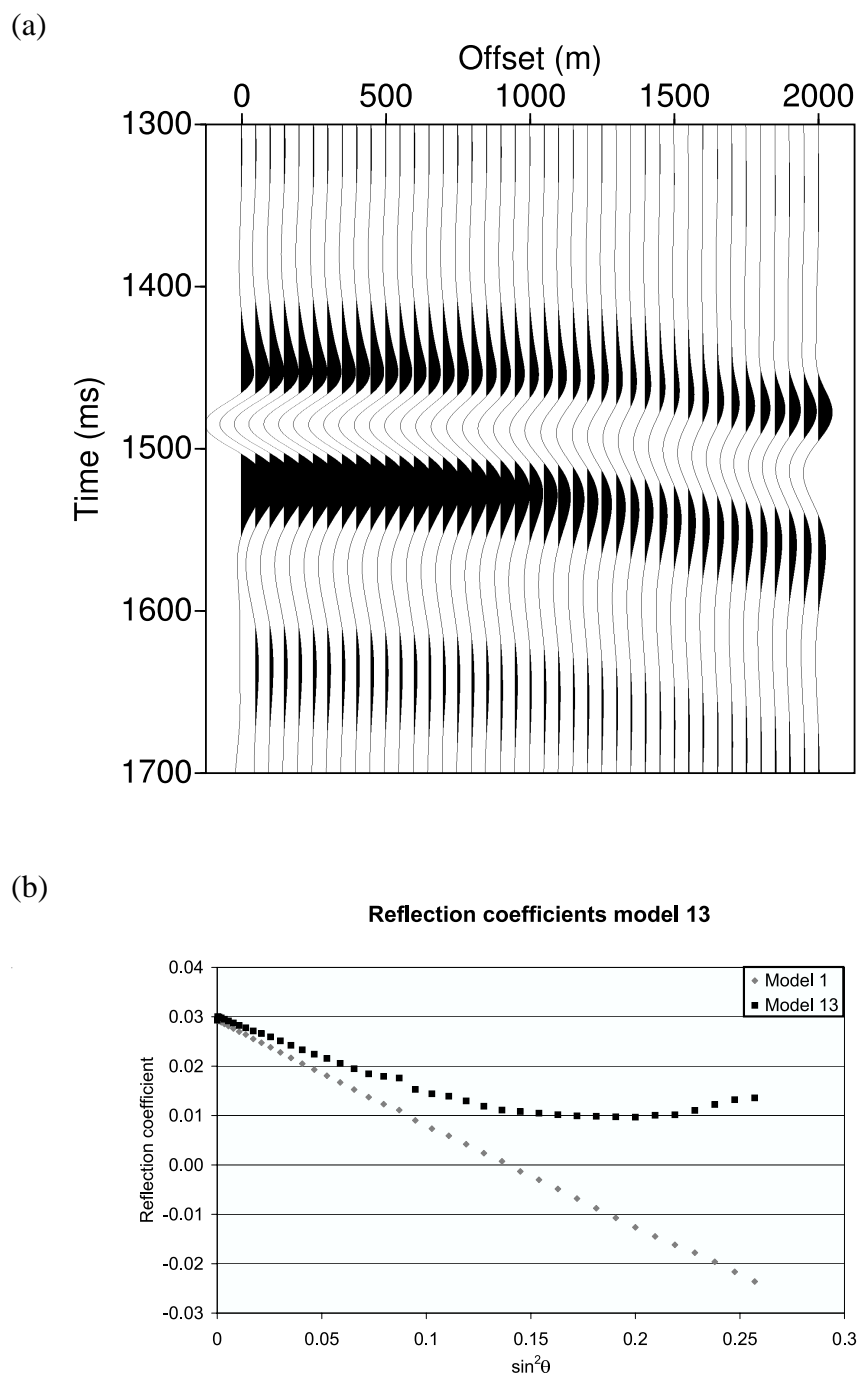


**Figure 18:** (a) Seismogram showing NMO-corrected prestack seismic data computed from Model 4. (b) Estimated reflection coefficients from the synthetic seismic shown above (black squares), and estimated reflection coefficients for Model 1 (gray diamonds)

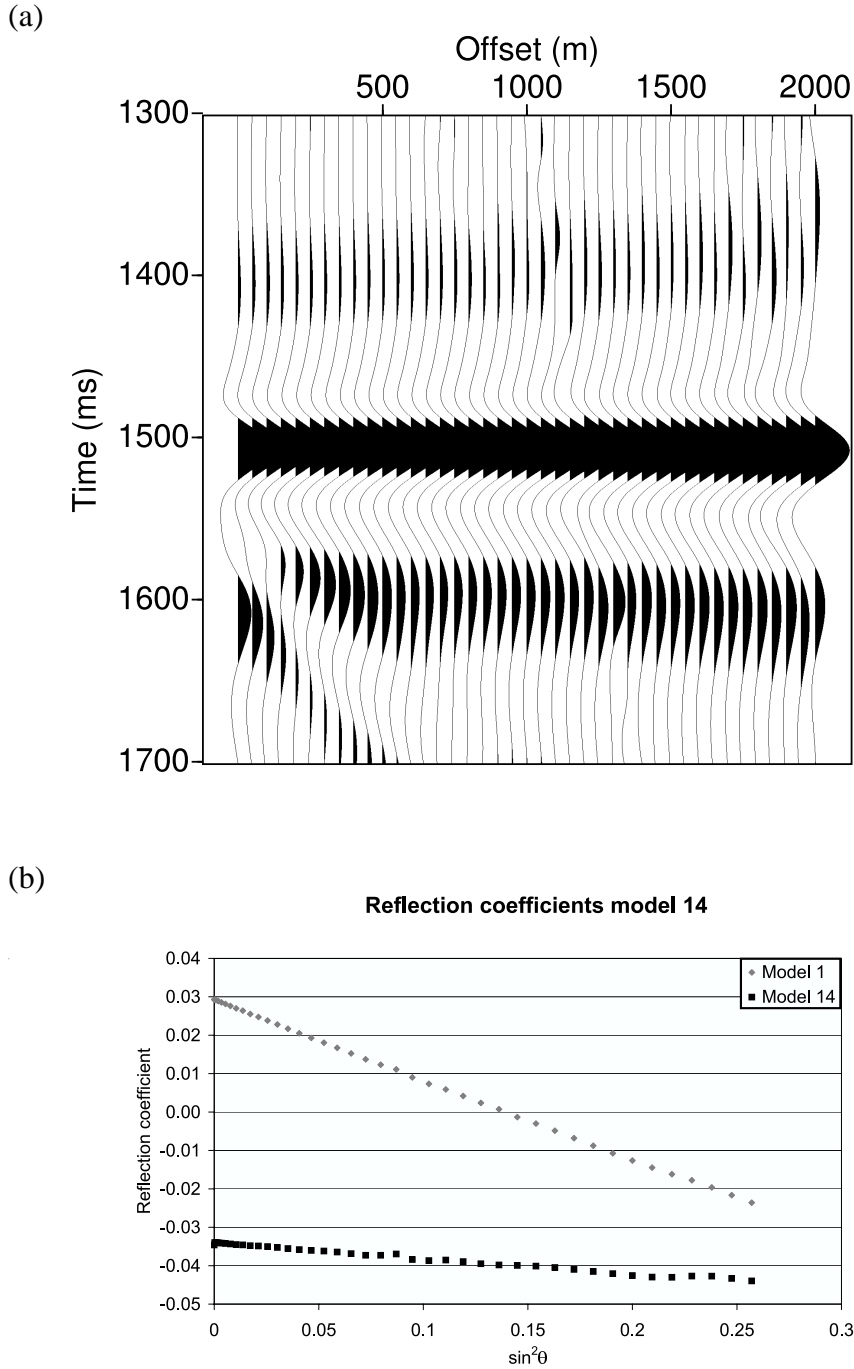


**Figure 19:** (a) Seismogram showing NMO-corrected prestack seismic data computed from Model 14. (b) Estimated reflection coefficients from the synthetic seismic shown above (black squares), and estimated reflection coefficients for Model 1 (gray diamonds)



## Chapter 3

# Pore pressure sensitivities tested with time-lapse seismic data

Øyvind Kvam and Martin Landrø

*Department of petroleum engineering and applied geophysics  
Norwegian University of Science and Technology  
N-7491 Trondheim, Norway*

**ABSTRACT:** In an exploration context, pore pressure prediction from seismic data relies on the fact that seismic velocities depend on pore pressure. Conventional velocity analysis is a tool that may form the basis for obtaining interval velocities for this purpose. However, velocity analysis is inaccurate, and in this paper we focus on the possibilities and limitations of using velocity analysis for pore pressure prediction. A time-lapse seismic dataset from a segment that has undergone a pore pressure increase of 5-7 MPa between the two surveys is analyzed for velocity changes using detailed velocity analysis. A synthetic time lapse survey is used to test the sensitivity of the velocity analysis with respect to noise. The analysis shows that the pore pressure increase can not be detected by conventional velocity analysis because the uncertainty is much greater than the expected velocity change for a reservoir of the given thickness and burial depth. Finally, by applying AVO analysis to the same data, we demonstrate that seismic amplitude analysis may yield more precise information about velocity changes than velocity analysis.



# 1 Introduction

It is known that seismic velocities depend on pore pressure. This fact has been used for pre-drill pore pressure estimation for a long time. Pennebaker (1968) was among the first to describe a method based on seismic velocities to predict pore pressure. In this work, the author suggests that velocities derived from seismic can be used as an indicator of abnormally high pressures. If the velocities differ from the normal velocity trend in the area, this may be an indicator of abnormal subsurface pressures. The normal velocity trend can be derived from, e.g., well logs from the area, or well information combined with seismic. Eaton (1972) presents another method to quantify the pore fluid pressure from seismic velocities (travel times). The Eaton equation relates sonic travel times to pore pressure, overburden stress and normal pressure conditions. This approach has been used successfully to predict pore pressures worldwide.

It is important to obtain as accurate information as possible about the subsurface rock velocities for pore pressure prediction purposes. Several authors have described methods to derive velocities from seismic, suitable for pore pressure prediction. Early techniques (e.g. Reynolds, 1970) use unprocessed CMP-gathers to construct semblance panels on which velocity analysis is performed. Since that, velocity analysis methods have been refined, and the most up-to-date techniques are designed to compensate for dip and lateral variations in the subsurface. In a recent paper, Dutta (2002b) gives an excellent review of pressure prediction using velocities derived from seismic data.

Although velocity analysis methods for pore pressure prediction have become very advanced in recent years, the quality of the derived velocities is limited by the quality of the seismic data. This paper focuses on the possibilities and limitations of using seismic velocity analysis to obtain information about pore pressure. We examine a time lapse seismic data set from a reservoir compartment at the Gullfaks Field in the North Sea that has undergone a significant pore pressure increase due to water injection. Repeated seismic data acquisition is presently the closest we can get to a full-scale controlled seismic experiment, and offer a unique possibility to test the seismic response to changes in reservoir conditions such as pressure, saturation, and temperature. Thus, time lapse seismic data are not only valuable for reservoir monitoring. They can also serve as a test ground for seismic exploration methods. If a method aims to diagnose reservoir properties in an exploration context it is good practice to check its response to known changing reservoir conditions as exist for many time lapse data examples.

Figure 1 shows measured pore pressures in the Cook formation from the production start in 1988. Note that the pore pressure started to increase rapidly in December 1995, about the same time as water injection was initiated. In 1996, the pore pressure was 5-7 MPa greater than the virgin pressure measured at production start. Time lapse seismic data from 1985 and 1996 have been analyzed with respect to velocity changes using detailed velocity analysis. This was also discussed previously by Kvam and Landrø (2001).

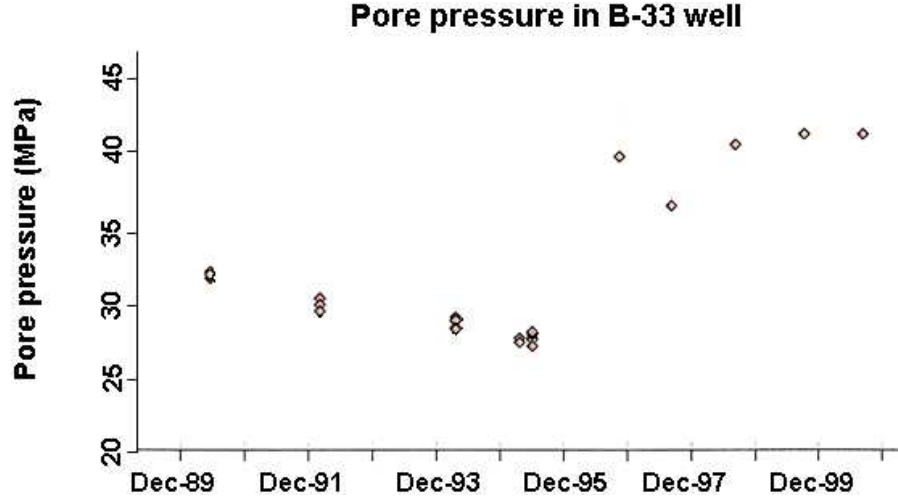


**Figure 1:** Pore pressures measured in the Cook segment. The data are taken from the B-33 well at Gullfaks.

The Gullfaks 4D seismic study (Landrø et al., 1999) showed that fluid effects were visible both on a single seismic dataset, and as amplitude changes observed on seismic difference data (obtained by subtracting the two datasets). The structural mapping of the Gullfaks Field is discussed by Fossen and Hesthammer (1998). Structurally, the field can be separated into three contrasting compartments: a western domino system with fault block geometry, a deeply eroded horst complex, and a transitional accommodation zone (graben system). The reservoir sands are of early and middle Jurassic age, representing shallow marine to fluvial deposits. Approximately 80 % of the recoverable reserves are in the Brent Group, 14 % in the Statfjord and Lunde formations, and the remaining 6 % in the Cook Formation. The time lapse seismic data used in the present work are taken from a segment within the Cook Formation. The data will be used to test whether a pore pressure increase of 5-7 MPa is detectable by conventional velocity analysis. Furthermore, synthetic seismic modeling is used for sensitivity analysis. Finally, amplitude variations with offset are evaluated as an additional tool for pore pressure prediction.

## 2 Theory

Most pressure-velocity relationships are described in terms of effective pressure rather than pore pressure. For practical purposes, the effective pressure  $P_{\text{eff}}$  can be expressed as (Christensen and Wang, 1985)

$$P_{\text{eff}} = P_{\text{overb}} - \eta P_{\text{pore}}, \quad (1)$$

where  $P_{\text{overb}}$  is the overburden pressure and  $P_{\text{pore}}$  is the pore fluid pressure.  $\eta$  is the Biot coefficient, which is related to the bulk moduli of the rock frame,  $K_{\text{fr}}$ , and the solid

material,  $K_s$ , through

$$\eta = 1 - \frac{K_{fr}}{K_s}. \quad (2)$$

For soft rocks,  $\eta \approx 1$ . The effective pressure is a more meaningful parameter than the pore pressure, since it is directly related to the bulk and shear moduli of the rock, and hence also to the seismic (P- and S-wave) velocities.

There are no models or theories that can describe the exact dependence of seismic velocities on effective pressure. Such a theory would contain a large number of adjustable parameters, and would probably be too complex to derive from first principles. Grain pack models like the Walton model (Walton, 1987) are idealized models that typically describe the pressure dependence in a random pack of identical spheres. Adjustable parameters are the Poisson's ratio of the grain material, Young's modulus of the grain material, porosity of the grain pack and a coordination number, representing the number of contact points per grain. The coordination number is, in principle, itself pressure dependent, but is treated as a constant in the Walton theory. The grain pack models can be used to describe granular materials, e.g., unconsolidated sands. However they do not take into account cementation and microcracks, which also influence the pressure dependence of the rock. Therefore, experimental relationships from ultrasonic measurements on cores are often used, the pitfall here being the representativeness of the core (upscaling, core damage etc.), as discussed by Nes et al. (2000).

Numerous experiments (e.g. Eberhart-Phillips et al., 1989) show that both P- and S-wave velocities depend strongly on effective pressure. The main trend for sandstones is that velocities increase with increasing effective pressure, and that the increase is more pronounced for lower effective pressures. Experiments also show that the  $V_p/V_s$  ratio is relatively insensitive to the effective pressure (Huffmann and Castagna, 2001). The exception is when the effective pressures are low, typically below 1 MPa. In this range, a more pronounced dependency of the  $V_p/V_s$  ratio on  $P_{eff}$  is observed. For the majority of published experiments, the  $V_p/V_s$  ratio decreases with increasing  $P_{eff}$ .

Figure 2 shows average measured P-wave velocities versus effective pressure from 29 ultrasonic dry core measurements from the Gullfaks Field. The error bars represent the standard deviations of the measurements. The velocities are scaled by the measured velocity at 5 MPa effective pressure. The data points indicate that a reduction in effective pressure from 5 MPa to 2 MPa will give a velocity reduction of 5% - 11%. Well measurements from the Cook segment on Gullfaks show initial pore pressures about 32 MPa, increasing to about 37-39 MPa after water injection. The initial effective pressure is assumed to be about 6 MPa. Assuming that the effective pressure has dropped to 1 MPa after water injection, figure 2 can give us an idea of the velocity reduction due to the pore pressure increase. It is difficult to give an exact range for the velocity reduction as a result of a decrease in effective pressure from 6 MPa to 1 MPa, as there are no data for these pressure points. However, it is reasonable to assume that the velocity reduction is in the range of 10%-20%. The experiments indicate that the S-wave velocities show a similar

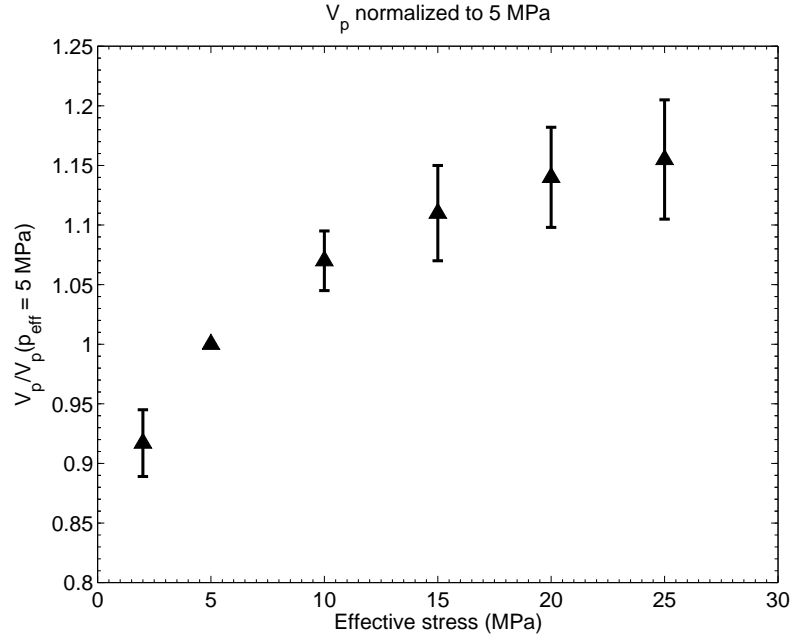


**Figure 2:** P-wave velocity change versus effective pressure, normalized to 5 MPa. The triangles are average values from ultrasonic measurements on 29 dry core plugs from Gullfaks. The error bars correspond to the standard deviation for the measurements.

behaviour with pressure (see Landrø et al., 1999, Figure 3). Therefore, in this study, we will treat the  $V_p/V_s$  ratio as constant with respect to pressure.

The impact of a velocity change on the seismic data, of course, depends on several factors. First, the burial depth and thickness of the reservoir zone must be in reasonable proportion to each other in order for a velocity change to be detectable. The stacking velocity is an average velocity. Thus, a thin reservoir at large burial depth will obviously affect the stacking velocities less than a thick, shallow reservoir. Second, the quality of the data and our ability to interpret horizons are important.

The importance of burial depth and thickness can be illustrated with a simple example. The stacking velocity, which is obtained from velocity analysis, is approximately the same as the rms (root mean square) velocity. Assume a two-layer model, where the upper layer represents the overburden, and the lower layer represents the reservoir. Correspondingly, we denote the interval velocity and internal two-way vertical traveltime as  $v_o$  and  $t_o$ , respectively, for the upper layer, and  $v_r$  and  $t_r$  for the lower layer. The rms velocity is then given as (Dix's formula)

$$V_{\text{rms},1}^2 = \frac{v_o^2 t_o + v_r^2 t_r}{t_o + t_r}. \quad (3)$$

If we perturb the velocity of the lower layer with  $\Delta v_r$ , the internal traveltime in this layer will change. The new rms velocity is then

$$V_{\text{rms},2}^2 = \frac{v_o^2 t_o + (v_r + \Delta v_r)^2 (t_r + \Delta t_r)}{t_o + (t_r + \Delta t_r)}, \quad (4)$$

where  $\Delta t_r$  is the change in traveltime in layer 2.

From these formulas, we calculate the change in rms velocity to the lowest order to be

$$\Delta V_{\text{rms}} = \sqrt{V_{\text{rms},2}^2} - \sqrt{V_{\text{rms},1}^2} \approx \frac{\Delta v_r}{2} \frac{t_r}{t_o + t_r} \left( \frac{v_r}{V_{\text{rms},1}} + \frac{V_{\text{rms},1}}{v_r} \right), \quad (5)$$

where we have assumed that  $\Delta v_r/v_r \ll 1$ ,  $\Delta t_r/t_r \ll 1$ , and  $\Delta v_r/v_r \approx -\Delta t_r/t_r$ . The factor  $t_r/(t_o + t_r)$  in equation (5) can be interpreted as reservoir thickness divided by burial depth. This shows, as expected, that the change in rms velocity is small when the overburden is thick compared to the reservoir. The factor  $v_r/V_{\text{rms},1} + V_{\text{rms},1}/v_r$  can be regarded as a scaling factor. Note that when the burial depth approaches zero (no overburden),  $\Delta V_{\text{rms}} \rightarrow \Delta v_r$ , since  $t_o \rightarrow 0$  and  $V_{\text{rms},1} \rightarrow v_r$ . Also, when the reservoir thickness approaches zero,  $\Delta V_{\text{rms}} \rightarrow 0$ .

In order to estimate the expected change in rms velocity at Gullfaks, we use the values  $V_{\text{rms},1} = 2030$  m/s,  $t_o = 2100$  ms,  $v_r = 2630$  m/s,  $t_r = 60$  ms, and  $\Delta v_r = 500$  m/s. The values for  $V_{\text{rms},1}$  and  $t_o$  are taken from the seismic data, while the values for  $v_r$  and  $t_r$  are taken from a well log. The value for  $\Delta v_r$  is obtained assuming a 20% velocity decrease as discussed above. With these values, equation (5) gives a decrease in rms velocity of  $\Delta V_{\text{rms}} \approx 15$  m/s.

In an exploration setting, the objective is to estimate differences in interval velocities ( $\Delta v_r$ ), e.g., across faults, or compared to a normal compaction trend. In order to investigate the uncertainty in  $\Delta v_r$  due to burial depth and thickness, we rewrite formula (5) as

$$\Delta v_r = 2\Delta V_{\text{rms}} \frac{t_o + t_r}{t_r} \left( \frac{v_r}{V_{\text{rms},1}} + \frac{V_{\text{rms},1}}{v_r} \right)^{-1}. \quad (6)$$

Following the method of Landrø (2002) we estimate the uncertainty in  $\Delta v_r$  to be

$$\begin{aligned} \delta(\Delta v_r) = \sqrt{2} \left( \frac{v_r}{V_{\text{rms},1}} + \frac{V_{\text{rms},1}}{v_r} \right)^{-\frac{1}{2}} \\ \times \sqrt{\left[ \frac{t_o + t_r}{t_r} \delta(\Delta V_{\text{rms}}) \right]^2 + \left[ \frac{\Delta V_{\text{rms}}}{t_r} \delta(t_o) \right]^2 + \left[ \frac{t_o}{t_r^2} \Delta V_{\text{rms}} \delta(t_r) \right]^2}. \end{aligned} \quad (7)$$

Here,  $\delta(\Delta V_{\text{rms}})$  is the uncertainty in the difference in rms velocity, while  $\delta(t_o)$  and  $\delta(t_r)$  are the uncertainties in traveltimes through the overburden and reservoir, respectively. The first term under the square root in equation (7) will usually dominate, since  $\delta(t_o)/t_r$

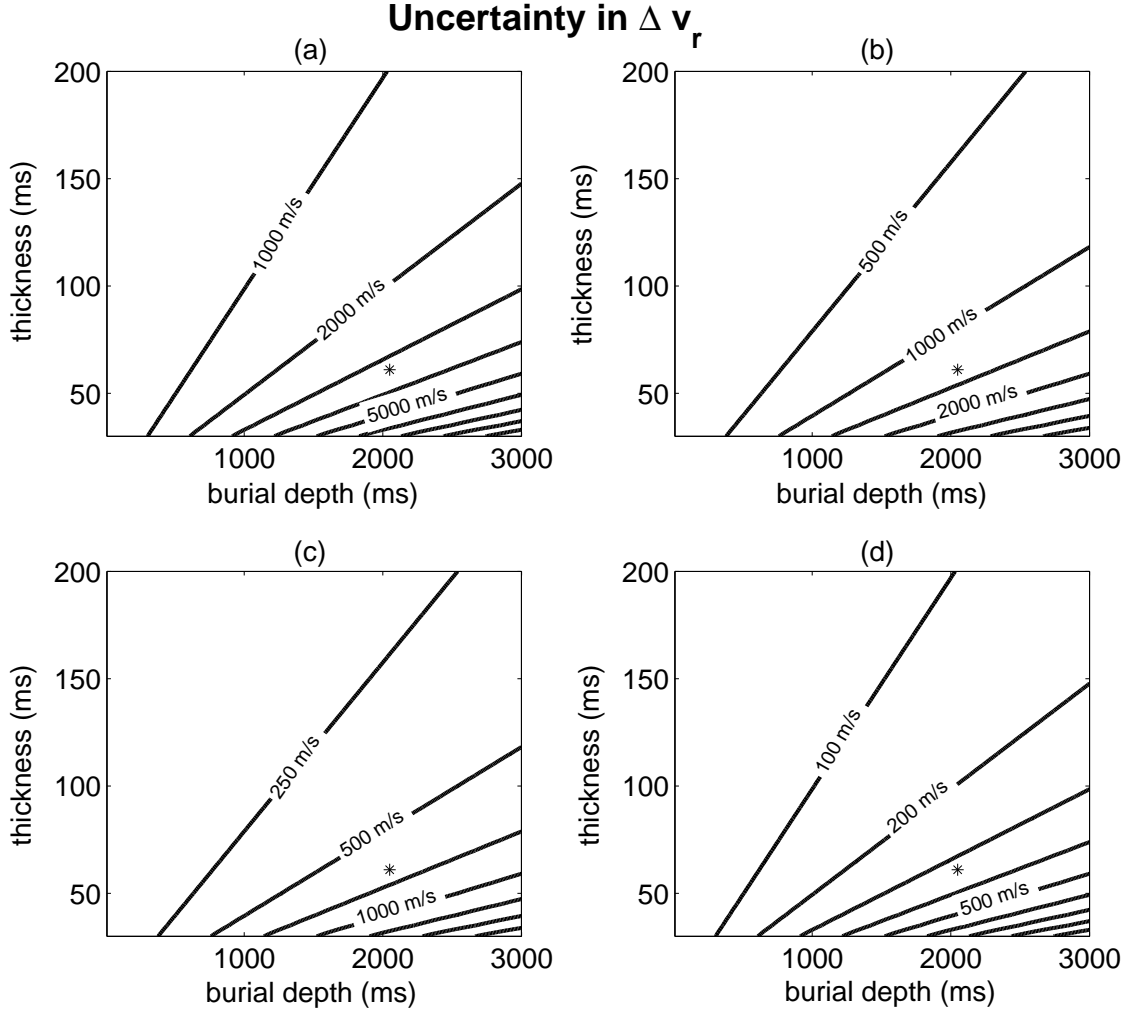


**Figure 3:** Contour plots of the uncertainty in  $\Delta v_r$  versus burial depth and thickness for four different levels of  $\Delta V_{\text{rms}}$ . (a)  $\Delta V_{\text{rms}} = 100$  m/s. (b)  $\Delta V_{\text{rms}} = 40$  m/s. (c)  $\Delta V_{\text{rms}} = 20$  m/s. (d)  $\Delta V_{\text{rms}} = 10$  m/s. The asterisk (\*) indicates the reservoir depth and thickness for the Cook Formation at Gullfaks. Thickness and burial depth are here measured in ms and not in meters.

and  $\delta(t_r)/t_r$  are usually much less than 1. Thus, a good approximation for the uncertainty in interval velocity change is

$$\delta(\Delta v_r) = \sqrt{2} \left( \frac{v_r}{V_{\text{rms},1}} + \frac{V_{\text{rms},1}}{v_r} \right)^{-\frac{1}{2}} \frac{t_o + t_r}{t_r} \delta(\Delta V_{\text{rms}}). \quad (8)$$

Figures 3a-3d show contour plots of  $\delta(\Delta v_r)$  for four different levels of  $\delta(\Delta V_{\text{rms}})$  versus burial depth and thickness. Using the numerical example above, we see that in order to detect a 20% decrease in interval velocity, the uncertainty in rms velocity must be less than 20 m/s.

Since velocity differences in thin segments are difficult to point out by conventional velocity analysis, we consider an independent approach to the problem. A well known method for estimating subsurface rock properties is analysis of seismic amplitude variation with offset (AVO analysis). Seismic amplitudes carry information of subsurface velocities, and can therefore aid in detecting abnormal pore pressures.

Seismic amplitudes do not depend on reservoir thickness, as long as the reservoir is thicker than the tuning threshold. However, since the S/N ratio decreases with depth, amplitude analysis also gets more uncertain as the depth increases. In addition, amplitude analysis requires true amplitude processing, which is difficult. Other limiting factors are near-surface inhomogeneities and incorrect offset-to-angle conversions. Ideally one or more wells should be used for calibration and processing of amplitude data, however this information is not readily available for exploration problems. Therefore, in an exploration setting with little prior knowledge of the target area, amplitudes should be used together with velocity analysis, and not as a stand-alone tool.

We consider a two-layer model, a cap rock (layer 1) above a reservoir (layer 2). We denote the P-wave velocity and S-wave velocity in layer 1  $\alpha_1$  and  $\beta_1$ , respectively. Similarly we write  $\alpha_2$  and  $\beta_2$  for layer 2. Using the Smith and Gidlow approximation for the PP reflection coefficient, Landrø (2001) found that the change in reflectivity due to a pore pressure change in layer 2 can be written

$$\begin{aligned} \Delta R_{PP}^P(\theta) = & \frac{1}{2} \frac{\Delta\alpha^P}{\alpha} - \frac{4\beta^2}{\alpha^2} \frac{\Delta\beta^P}{\beta} \sin^2 \theta + \frac{\Delta\alpha^P}{\alpha} \tan^2(\theta) - \frac{1}{4} \left( \frac{\Delta\alpha\Delta\alpha^P}{\alpha^2} + \frac{\Delta\alpha^{P2}}{\alpha^2} \right) \\ & - \frac{2\beta^2}{\alpha^2} \left( \frac{\Delta\beta\Delta\beta^P}{\beta^2} + \frac{\Delta\beta^{P2}}{\beta^2} + \frac{\Delta\rho\Delta\beta^P}{\rho\beta} - \frac{\Delta\rho\Delta\alpha^P}{\rho\alpha} - 2\frac{\Delta\beta\Delta\alpha^P}{\alpha\beta} - 2\frac{\Delta\beta^P\Delta\alpha^P}{\alpha\beta} \right) \sin^2 \theta \\ & - \frac{1}{4} \left( \frac{\Delta\alpha\Delta\alpha^P}{\alpha^2} + \frac{\Delta\alpha^{P2}}{\alpha^2} \right) \tan^2 \theta \end{aligned} \quad (9)$$

where  $\alpha = 1/2(\alpha_1 + \alpha_2)$  and  $\beta = 1/2(\beta_1 + \beta_2)$ , while  $\Delta\alpha^P/\alpha$  and  $\Delta\beta^P/\beta$  denote the relative change in P- and S-wave velocity in layer 2 due to a pore pressure change. This formula is valid to the second order in  $\Delta\alpha^P/\alpha$  and  $\Delta\beta^P/\beta$ . If we make the assumption of unchanged  $V_p/V_s$  then equation (9) gives

$$\begin{aligned} \Delta R_{PP}^P(\theta) = & \frac{1}{2} \frac{\Delta\alpha^P}{\alpha} \left[ 1 - \frac{1}{2} \left( \frac{\Delta\alpha}{\alpha} + \frac{\Delta\alpha^P}{\alpha} \right) \right] \\ & + \frac{1}{2} \frac{\Delta\alpha^P}{\alpha} \left[ -\frac{8\beta^2}{\alpha^2} + \frac{4\beta^2}{\alpha^2} \left( \frac{\Delta\beta}{\beta} + \frac{\Delta\alpha^P}{\alpha} \right) + \left( 1 - \frac{1}{2} \left( \frac{\Delta\alpha}{\alpha} + \frac{\Delta\alpha^P}{\alpha} \right) \right) \frac{\tan^2 \theta}{\sin^2 \theta} \right] \sin^2 \theta \end{aligned} \quad (10)$$

or

$$\Delta R_{PP}^P(\theta) = \Delta R_0 + \Delta G \sin^2(\theta). \quad (11)$$

In the latter expression we have used the notation of the standard two term AVO equation

$$R_{PP} = R_0 + G \sin^2(\theta), \quad (12)$$

where  $R_0$  is the AVO intercept, and  $G$  is the AVO gradient. Equation (10) shows that for an increase in pore pressure, a plot of  $\Delta G_0$  versus  $\Delta R_0$  is a point in the quadrant of the  $(\Delta R_0, \Delta G)$ -plane defined by  $\Delta R_0 < 0$  and  $\Delta G < 0$  for realistic values of  $\beta/\alpha$ . As a numerical example, consider the two-layer model given by  $\alpha_1 = 2000$ ,  $\beta_1 = 1000$ ,  $\rho_1 = 2500$  for the cap rock, and  $\alpha_2 = 2500$ ,  $\beta_2 = 1300$ ,  $\rho_2 = 2600$  for the reservoir rock. Assume a pore pressure increase in the reservoir rock causing a drop of 10% in both P-wave and S-wave velocity, such that  $\alpha'_2 = 2250$ , and  $\beta'_2 = 1170$ . From the properties of the cap rock and the reservoir rock, we compute  $\Delta\alpha/\alpha = 0.222$ ,  $\Delta\beta/\beta = 0.261$ ,  $\Delta\alpha^p/\alpha = -0.111$ , and  $\beta/\alpha = 0.511$ . Inserting the numbers into equation (10) gives

$$\Delta R_0 = \frac{1}{2} \cdot (-0.111) \left[ 1 - \frac{1}{2}(0.222 - 0.111) \right] = -0.052, \quad (13)$$

and

$$\Delta G = \frac{1}{2} \cdot (-0.111) \left[ (-8) \cdot 0.511^2 + 4 \cdot (0.261 - 0.111) + \left( 1 - \frac{1}{2}(0.222 - 0.111) \right) \right] = 0.055. \quad (14)$$

In equation (14) we have assumed that  $\sin \theta \approx \tan \theta$ .

If we have established values for  $\Delta R_0$  and  $\Delta G$ , we can estimate the change in interval velocity in layer 2 due to pore pressure changes from equation (10).

### 3 Seismic modeling of an overpressured zone

The purpose of the synthetic modeling is to test the sensitivity of velocity analysis and amplitude analysis to velocity changes in the reservoir zone. Based on stacked data from a representative in-line from the Gullfaks Field, a 2D geological model of a cross section was made. The model consists of 11 layers, and P-wave velocities were determined from velocity analysis of the real seismic data, as well as from well log information. The S-wave velocities were estimated from a linear  $V_p$ - $V_s$  relationship (Castagna et al., 1985). Densities were taken from well logs. The initial P-wave velocity model is shown in Figure 4. This model was used in an elastic finite-difference modeling scheme. The reservoir zone is indicated with arrows in Figure 4.

Two synthetic 2D surveys were generated from the geological model. The first survey (Survey 1) was generated with reservoir velocities corresponding to the initial reservoir state. The second survey (Survey 2) had velocities corresponding to the overpressured reservoir state. In order to simulate a velocity decrease consistent with a pore pressure increase of 5-7 MPa, both the P- and the S-wave velocities were reduced by 20%, in accordance with Figure 2. The density was kept unchanged for the two surveys (see Landrø et al., 1999, Figure 3)



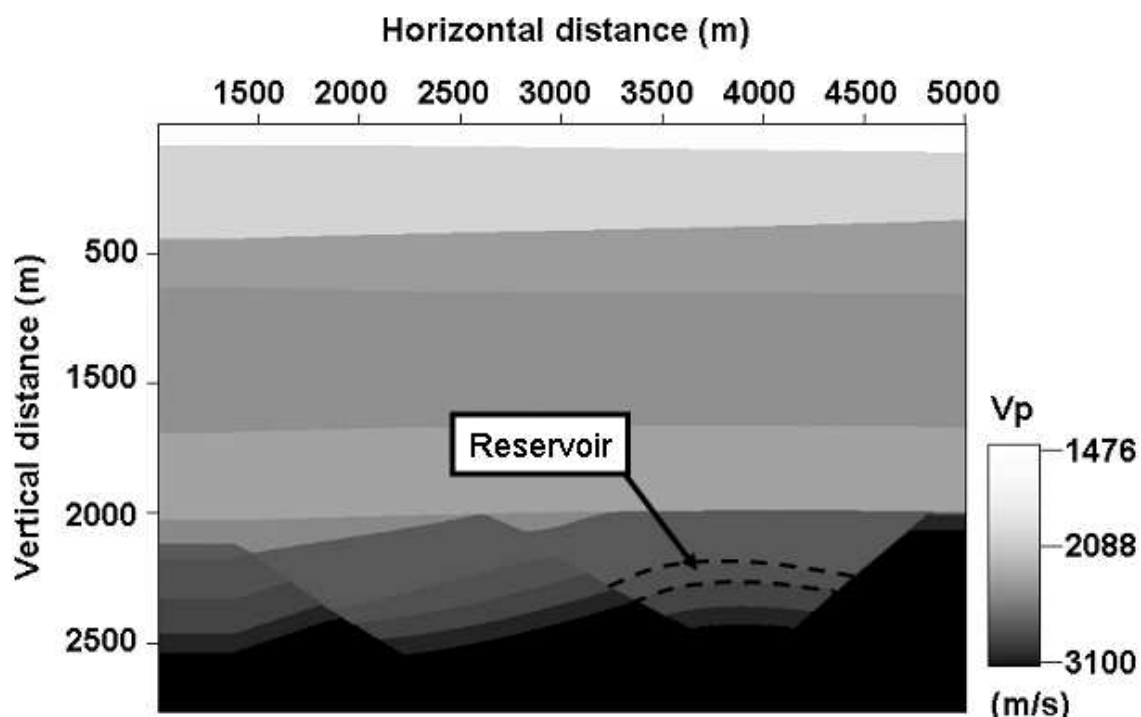


**Figure 4:** The 2D geological model used for synthetic modeling. The reservoir is indicated with an arrow.

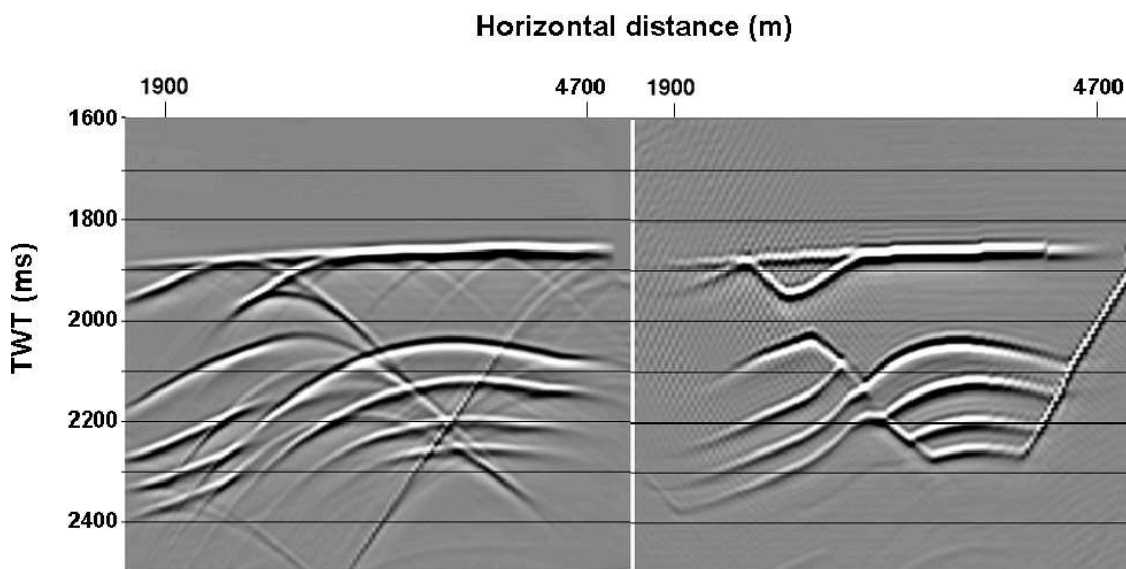


**Figure 5:** Comparison of unmigrated (left) and prestack time migrated (right) sections of the synthetic data, after stack.

**Table 1:** Model parameters used in synthetic experiment (Survey 1)

Layer no.	$V_p$ (m/s)	$V_s$ (m/s)	Density (kg/m <sup>3</sup> )
1 (water)	1476	0	1000
2	1758	800	1800
3	2132	800	1900
4	2216	900	2000
5	2088	850	2100
6	2271	910	2118
7	2580	1180	2300
8 (reservoir)	2630	1340	2350
9	2710	1280	2200
10	2900	1400	2400
11	3100	1500	2500

A 2D elastic finite-difference scheme was used to generate synthetic seismic data from the model in Figure 4. The modeling was based on a coarse grid scheme (Holberg, 1987), with a grid cell size of  $4 \times 4$  meters, and a Ricker wavelet with a maximum frequency of 60 Hz was used as source. The parameters for the baseline survey are given in Table 1.

Before the analysis, the synthetic seismic data were taken through the following processing steps: 1) Normal moveout correction, 2) Dip moveout correction, 3) Prestack time migration in the f-k domain, and 4) Inverse normal moveout correction. The known baseline velocity function was used for all steps, both for Survey 1 and for Survey 2. The purpose of this was to obtain a better lateral resolution and remove interfering wavefields. In addition, the amplitudes were restored. Thus, the prestack time migrated data were more suited for both velocity analysis and amplitude analysis than the raw data. Figure 5 shows a comparison between unmigrated and migrated stacked seismic sections. Figure 6 shows a comparison of two prestack migrated CMP gathers from the same CMP position, but with different reservoir velocities.

### 3.1 Velocity analysis

Velocity analysis was performed on each CMP gather of the migrated data. Figure 7 shows a comparison of semblance plots from the same CMP for the baseline and monitor surveys. By visual inspection, we observe a slight velocity decrease below 2100 ms. In order to test the sensitivity of the analysis with respect to random noise, four different levels of signal-to-noise ratios (S/N) were analyzed,  $S/N = \infty$ , 10, 1 and 0.5. For each inspected CMP location, the velocity picks for the monitor survey (Survey 2) were sub-

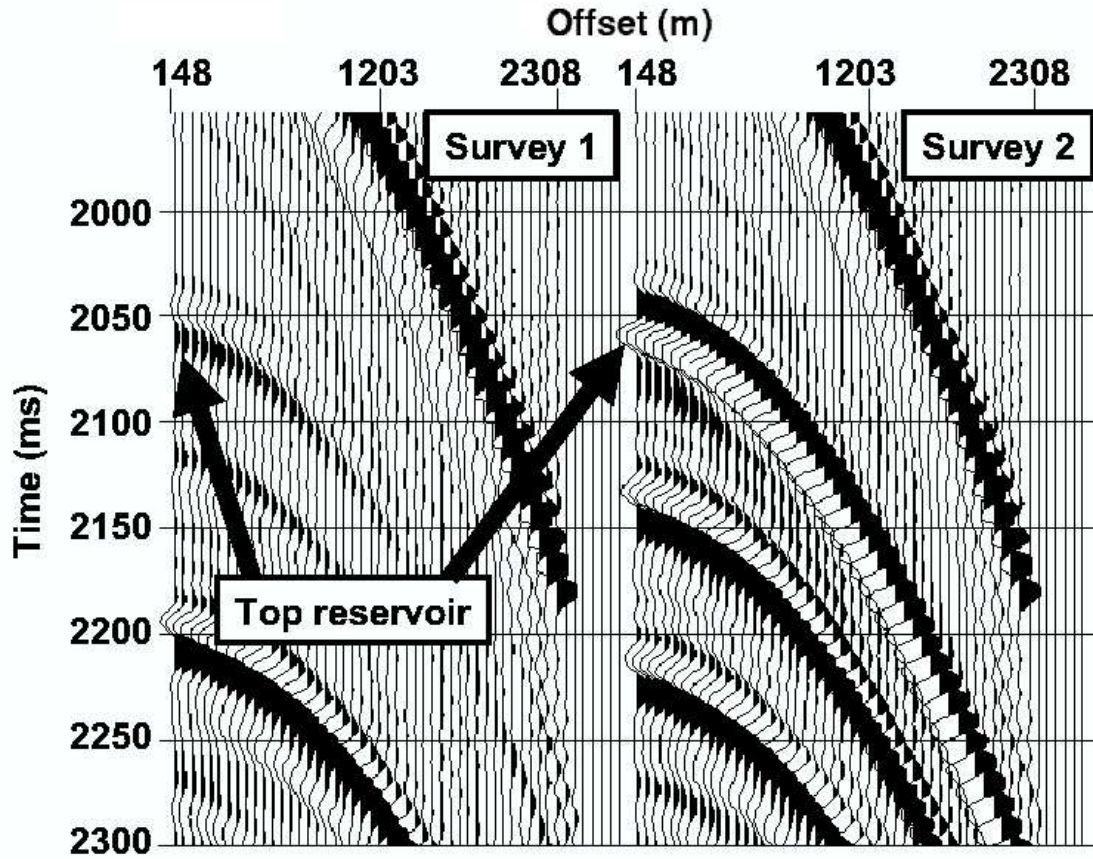


**Figure 6:** Comparison of synthetic prestack time migrated CMP gathers from the same CMP position. Left: baseline survey (Survey 1). Right: P- and S-wave velocities are reduced by 20% in the reservoir (Survey 2). The migration was performed using the same (baseline) velocity function for both gathers.

tracted from the corresponding velocity picks for Survey 1. This way, we got a value for the change in stacking velocity,  $\Delta V$ , at spatially similar points, thus accounting for spatial variations in the geology.

Figures 8a-8d shows the difference in stacking velocity belonging to the reservoir section from a comparison of Survey 1 and monitor Survey 2 for  $S/N = 10$ . The histograms show a rms velocity decrease of approximately 9 m/s, with an error of approximately  $\pm 8$  m/s at the base reservoir reflector. This is found to be consistent, within uncertainty bounds, with an expected rms velocity change of 15 m/s. The scattering effects in the data are probably caused by the presence of dip and inaccuracies in the velocity picking. Figures 9a-9d shows the corresponding result for  $S/N = 0.5$ . In this case, we observe that it is hard to detect velocity changes within the standard deviation. Table 2 summarizes the observed velocity differences for comparison of Survey 2 and Survey 1. The synthetic experiments indicate that for a  $S/N$  ratio less than 0.5, it will be difficult to detect velocity

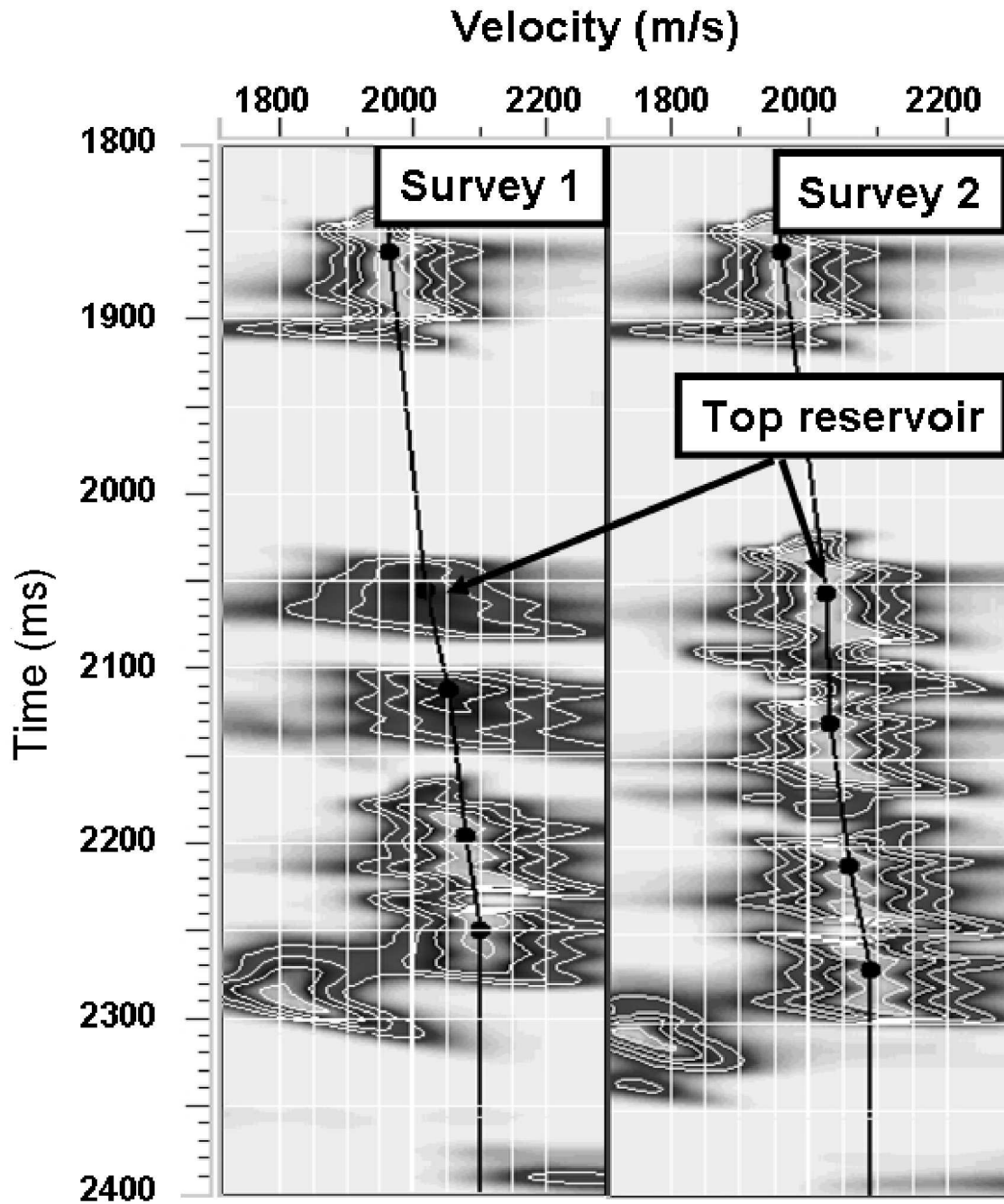


**Figure 7:** Comparison of semblance panels of synthetic data for the same CMP. Left: reference survey (Survey 1), Right: monitor survey (Survey 2) with reservoir velocity lowered by 20%.

**Table 2:** Estimated reduction in stacking velocity for synthetic Survey 2. Synthetic Survey 1 is the reference. The numbers are given as an average over all CMP's  $\pm$  one standard deviation.

Horizon	$\Delta V$ (m/s) no noise	$\Delta V$ (m/s) $S/N = 10$	$\Delta V$ (m/s) $S/N = 1$	$\Delta V$ (m/s) $S/N = 0.5$	$\Delta V$ (m/s) equation (6)
Top res.	$4.5 \pm 9.8$	$4.3 \pm 8.3$	$1.0 \pm 12.8$	$7.1 \pm 14.8$	0.0
Base res.	$-9.2 \pm 8.3$	$-12.4 \pm 10.2$	$-13.9 \pm 11.9$	$-12.8 \pm 18.8$	-15.0
Base res.+100 m	$-11.9 \pm 7.1$	$-16.0 \pm 5.9$	$-19.5 \pm 9.6$	$-14.0 \pm 14.1$	N/A
Base res.+180 m	$-9.1 \pm 10.7$	$-9.1 \pm 8.9$	$-16.6 \pm 10.9$	$-16.7 \pm 20.5$	N/A

changes of 20% using conventional velocity analysis, for the given reservoir geometry, thickness, and depth.

### 3.2 AVO analysis

The synthetic CMP gathers in Figure 6 show a clear difference in amplitude at the top reservoir reflector. A detailed AVO analysis was done on the synthetic data in order to test the sensitivity of seismic amplitudes to a pore pressure increase. We used the same S/N ratios for the AVO analysis as for the velocity analysis. A time window of approximately 40 ms was selected around the top reservoir event, and peak amplitudes were extracted. Offset-to-angle conversion was performed assuming a constant horizontal slowness.

A scaling factor of 238 was found to reproduce the zero-offset reflection coefficient quite well for both surveys. Figure 10 shows the means of the scaled amplitudes for  $S/N = \infty$  compared with the reflection coefficient computed from Zoeppritz' equation for the PP-reflection coefficient. Note that there is a discrepancy at about  $15^\circ - 20^\circ$  incidence angle, which is due to an interfering wavefield. Except for the global scaling factor of 238, no calibration of the amplitudes was necessary.

In accordance with equation 12, we estimated values for  $R_0$  and  $G$ . The values for the different surveys were then subtracted to give values for  $\Delta R_0$  and  $\Delta G$ . As for the velocity analysis, we have subtracted values for spatially equivalent points. Figures 11a-11b shows results for  $S/N=10$  and  $S/N=0.5$ . The values obtained for  $\Delta R_0$  are close to the theoretical values corresponding to a velocity decrease of 20% for Survey 2. For  $\Delta G$ , there is a bias toward too low values, possibly due to dip in the reflector.

We observe that there is only a small scatter in the  $\Delta R_0$  values, while there is a large scatter for  $\Delta G$ . This may partly be explained by problems with interfering wavefields, to which  $\Delta G$  probably is most sensitive. In addition, since the top reservoir reflector has a

$\Delta V$ , synthetic data,  $S/N=10$

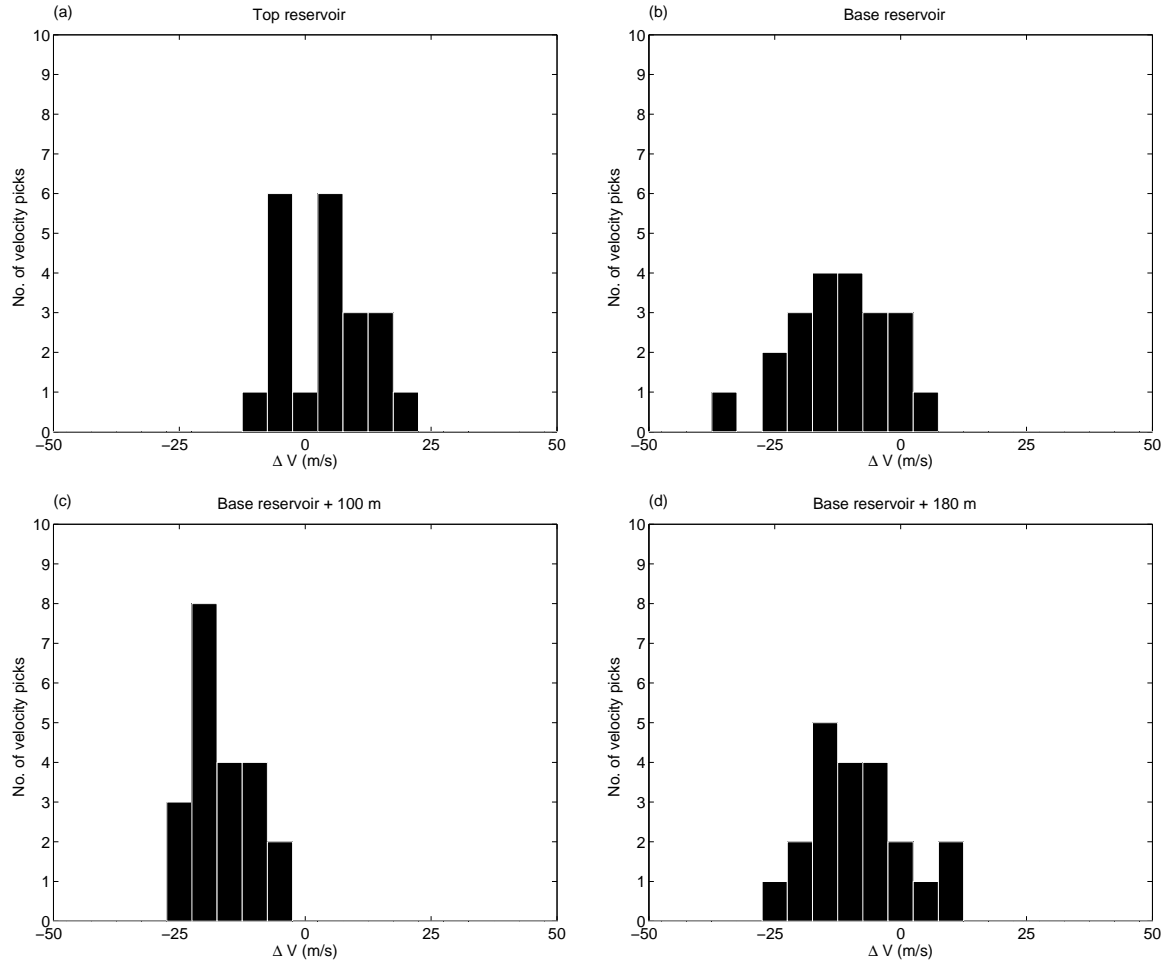


**Figure 8:** Histograms showing the observed change in stacking velocity between Survey 2 and Survey 1 for  $S/N = 10$ . (a) top reservoir interface. (b) base reservoir interface. (c) 100 m below base reservoir. (d) 180 m below the reservoir.

curvature, focusing effects of the migration may be an issue. Finally, the scatter in  $\Delta R_0$  and  $\Delta G$  does not increase much as the  $S/N$  ratio decreases from 10 to 0.5. This is in contrast to the velocity analysis, where this resulted in approximately a doubling of the uncertainty of the rms velocity (Table 2).

## 4 Velocity analysis on real data

The real time-lapse seismic data consists of two 3D marine datasets from surveys carried out in 1985 and in 1996. 5 in-lines (labeled 2741, 2751, 2761, 2771, and 2781) were

$\Delta V$ , synthetic data,  $S/N=0.5$

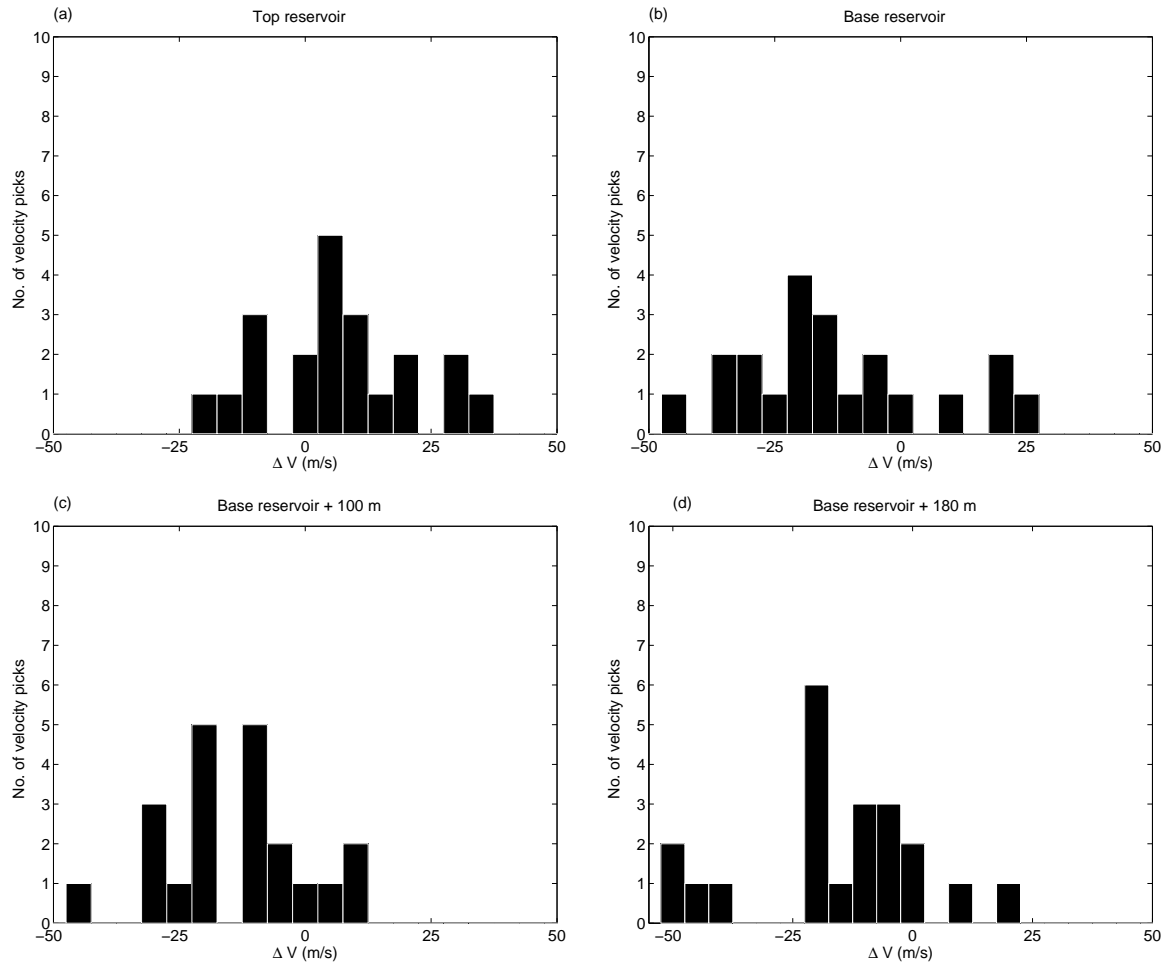


**Figure 9:** Histograms showing the observed change in stacking velocity between Survey 2 and Survey 1 for  $S/N = 0.5$ . (a) top reservoir interface. (b) base reservoir interface. (c) 100 m below base reservoir. (d) 180 m below the reservoir.

selected. The cross-line distance between these in-lines was 125 meters. For each in-line, 30 CMP gathers with a CMP spacing of 25 m. were analyzed. Figure 12 shows a map of the selected area. Prior to analysis, the data had gone through a company processing procedure involving the same processing steps as were used for the synthetic data. That is, NMO, DMO, prestack time migration, and inverse NMO, using the best estimate of the velocity field.

Conventional velocity analysis was performed on these CMP gathers. Two semblance plots for the same CMP location in 1985 and 1996 are shown in Figure 13. The top reservoir reflector is easy to interpret in both the 1985 data and the 1996 data. However, the base reservoir interface is hard to interpret on the real data. Velocities below the reservoir thus had to be picked on deeper reflectors. To illustrate this point, CMP gathers

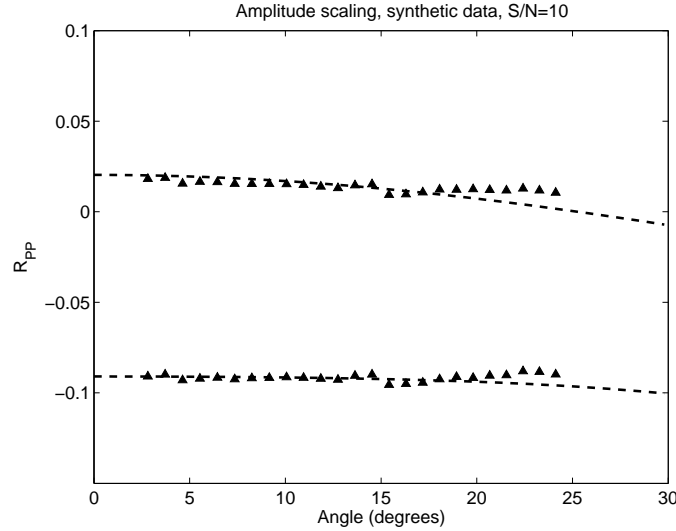


**Figure 10:** Scaled peak amplitudes for top reservoir interface compared with theoretical reflectivities from Zoeppritz' equations. Upper: Survey 1, bottom: Survey 2

from the same location are shown in Figure 14. Note that there are differences in the time lapse seismic data also above the top reservoir. This is probably related to production changes in a more shallow reservoir.

As for the synthetic case, velocity differences for corresponding CMP locations were acquired. Figures 4a and 4b show these picks for the top reservoir interface, and below the base reservoir, respectively. We observe that the uncertainty in the estimated velocity differences is on the order of 40 m/s, which is far above the expected rms velocity change of 15 m/s. This means that the real data example shows that it is not possible to detect a 5-7 MPa pore pressure increase by conventional time-lapse velocity analysis.

## 5 AVO analysis on real data

A prominent feature of the seismic data from this segment is a significant change in amplitude at the top reservoir interface (see Figure 14). Since this amplitude change is observed in most CMP gathers in the time-lapse data, it is believed to be caused by a change in the rock properties in the reservoir, or just above the reservoir. In order to see if the amplitude change is consistent with a pore pressure increase in the reservoir, a detailed AVO analysis was done.



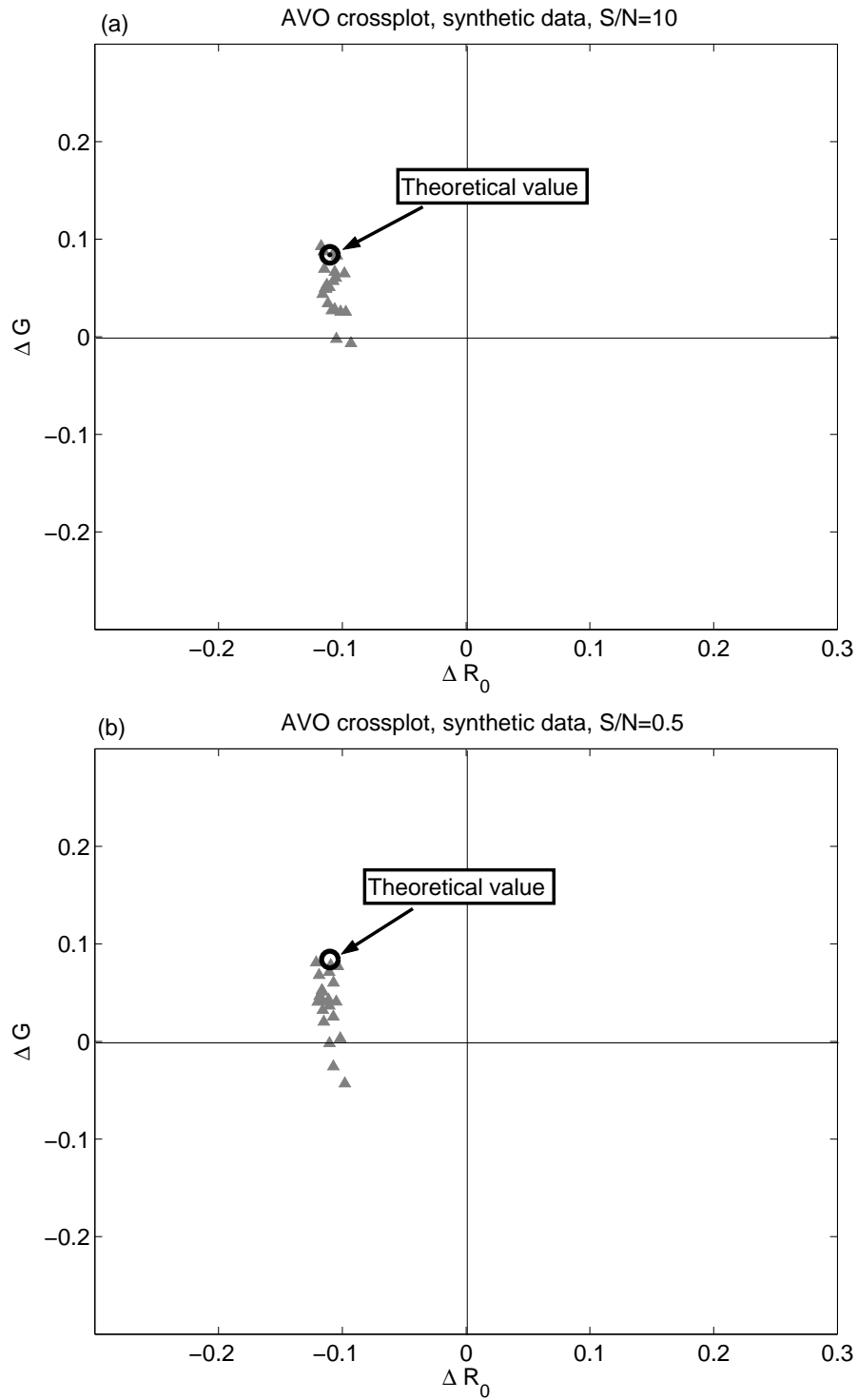


**Figure 11:** Plot of  $\Delta G$  vs.  $\Delta R_0$  for synthetic data. (a) S/N=10, and (b) S/N=0.5. The black circle indicates the theoretical value, computed from equation (10).

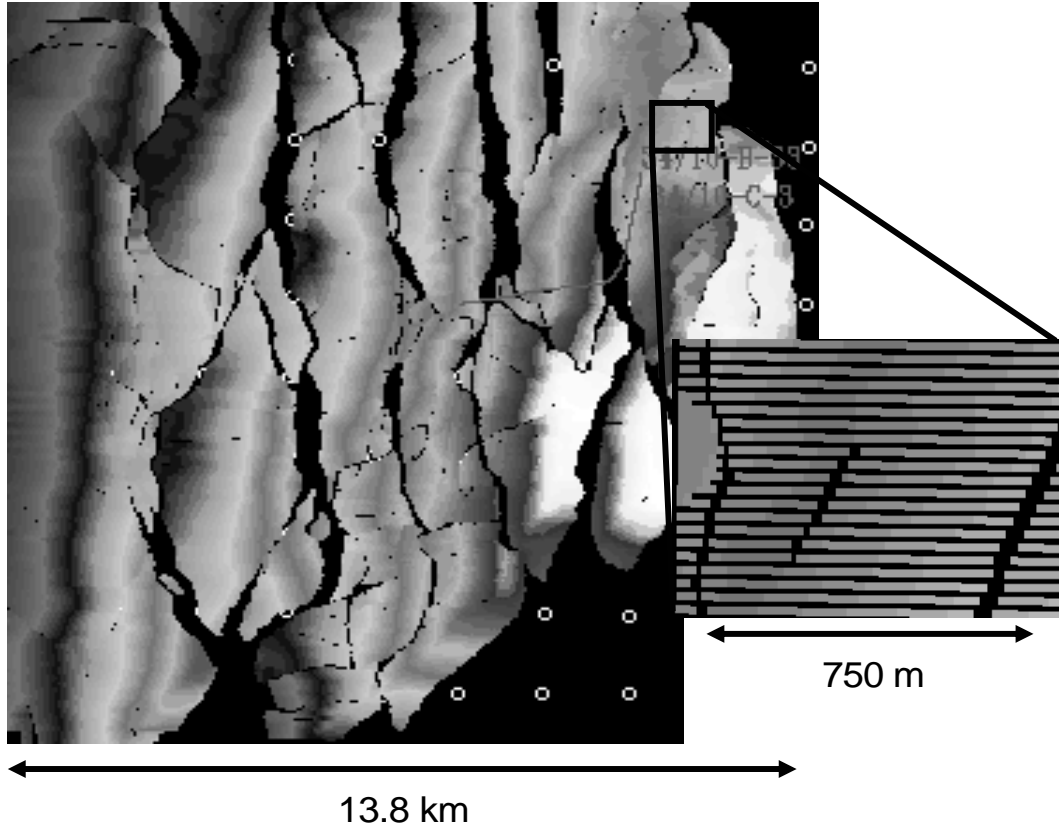


**Figure 12:** Map of the Top Cook interface on Gullfaks. The analyzed data are from the highlighted area.

As for the synthetic data, a time window of approximately 40 ms width was selected around the top reservoir event for each CMP, and peak amplitudes were extracted. As before, offset-to-angle conversion was performed assuming constant horizontal slowness. Next, the amplitudes were calibrated to reflection coefficients. This was done in the following way; based on velocity and density logs from the C-3 well at Gullfaks, we made a two-layer model for the top Cook interface, representing pre-production conditions (Table 3). The well did not include S-wave velocities. However, measurements at Gullfaks indicate a  $V_p/V_s$ -ratio of about 1.8 at this depth. From the model, reflection coefficients were calculated using Zoeppritz' equations. The amplitudes were scaled by a linear scaling factor of the form  $a(1 + b\theta)$  where  $\theta$  is the angle of incidence. We found that  $a = 1/30$  and  $b = -0.015$  gave a reasonable fit to the modeled reflectivity, as shown in Figure 16.

It should be mentioned that this scaling procedure is not accurate. Calibration to an overlying reflector gave very different values for the scaling parameters  $a$  and  $b$ . This ambiguity adds uncertainty to the quantification of the AVO parameters  $\Delta R_0$  and  $\Delta G$ . However, for a given reflector, there is no need to apply different scaling factors for the two data sets (1985 and 1996). This can be seen by investigating the AVO signal at a

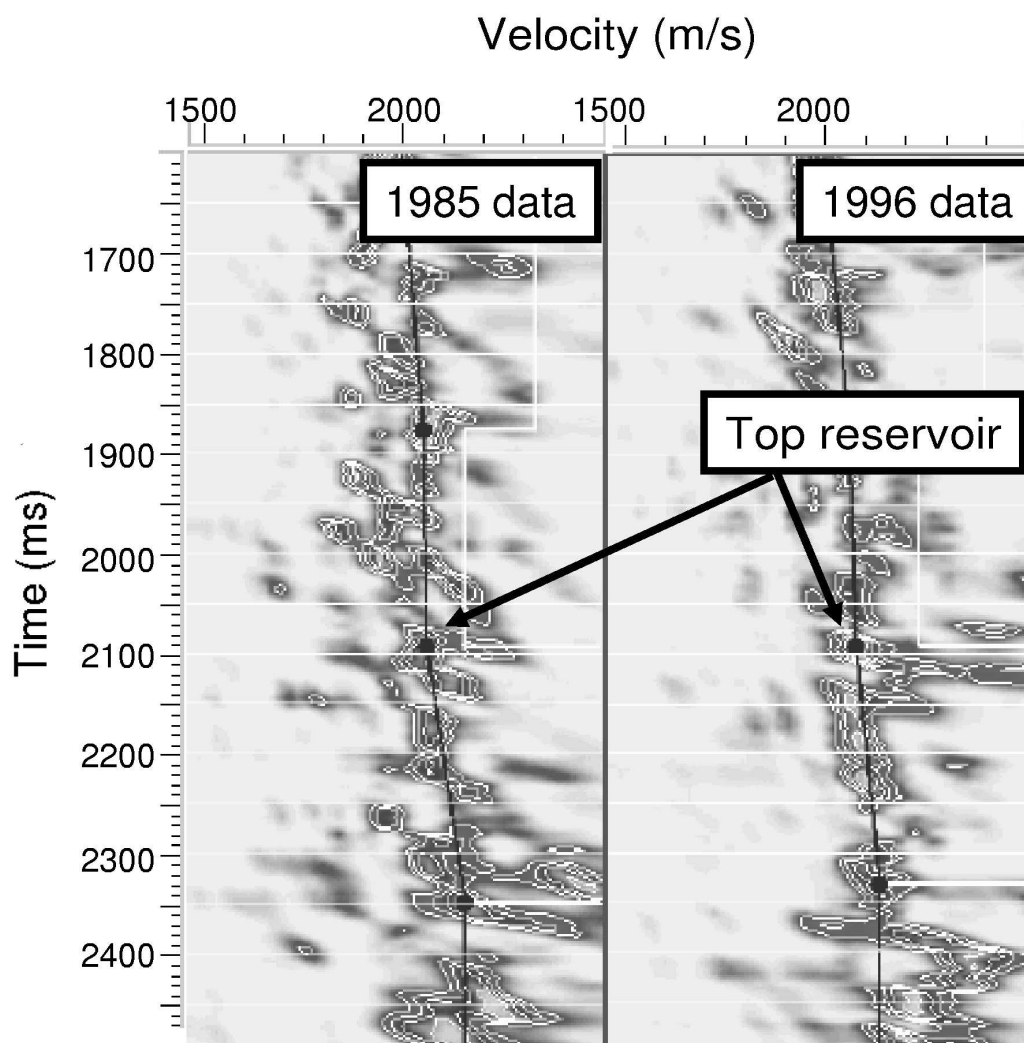


**Figure 13:** Comparison of semblance panels of real data for the same CMP. Left: reference survey, Right: monitor survey.

**Table 3:** Two-layer model for top Cook interface used in calibration of amplitudes.

	$V_p$ (m/s)	$V_s$ (m/s)	Density ( $\text{kg/m}^3$ )
Layer 1	2580	1430	2350
Layer 2	2630	1460	2150

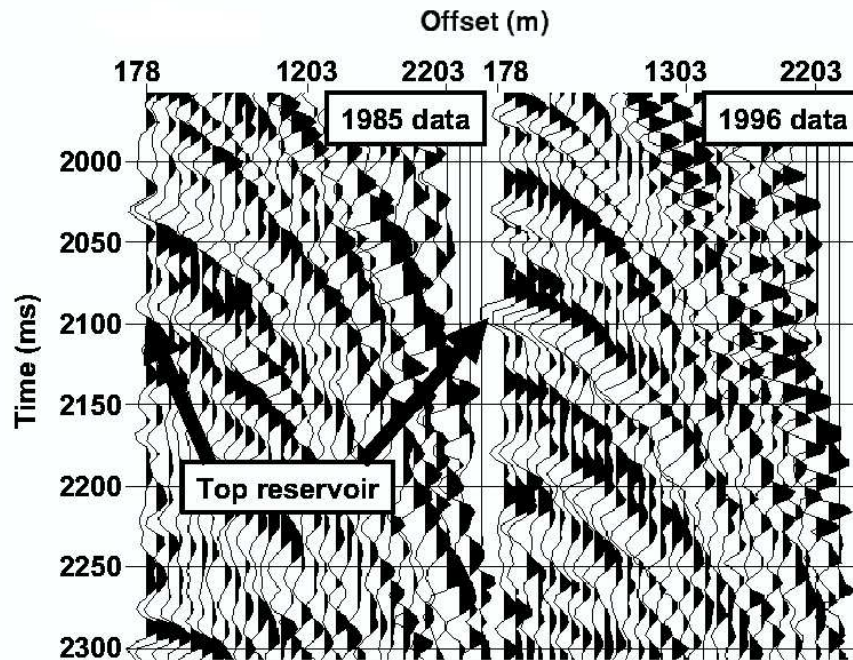


**Figure 14:** Comparison of prestack CMP gathers from the same CMP (real data). Note the amplitude difference at about 2100 ms. This reflector corresponds to the top Cook interface. The differences above the top Cook interface are probably production imprints from the shallower Brent reservoir.

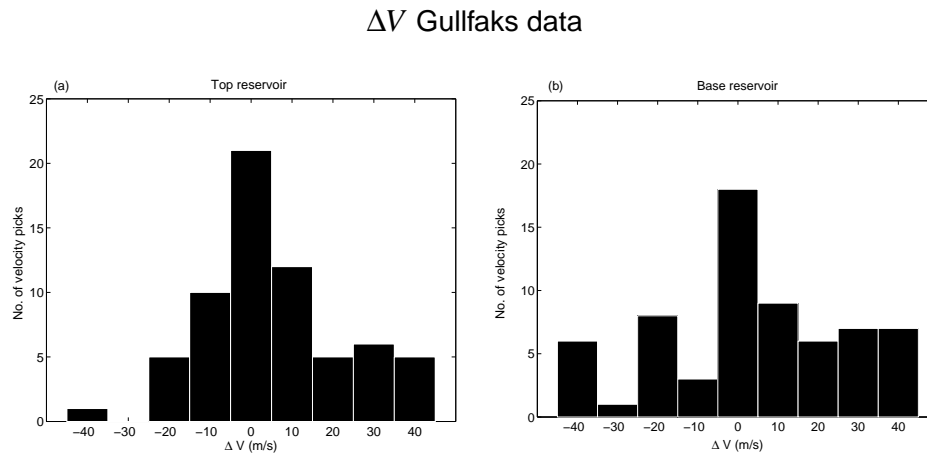


**Figure 15:** Histograms showing the observed change in stacking velocity between the 1985 data and the 1986 data. (a) top reservoir interface. (b) base reservoir interface.

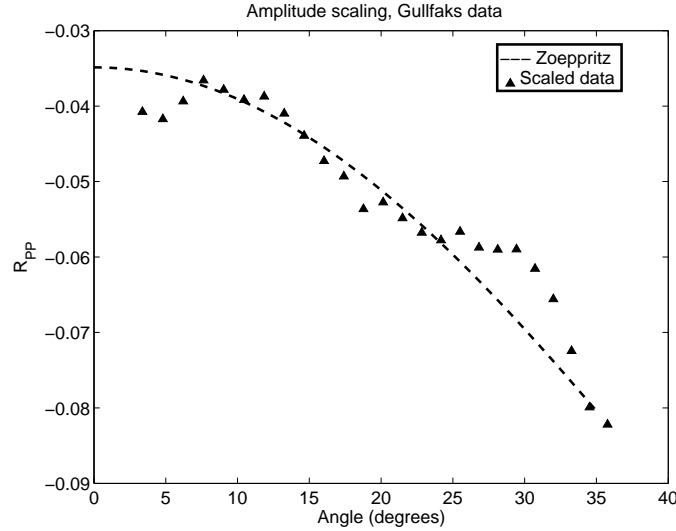


**Figure 16:** Illustration of scaling procedure used to calibrate the real data. The dotted line is the PP reflection coefficient for Top Cook, computed from velocity and density data from the C-3 well at Gullfaks. The amplitudes were scaled by a linear relation of the form  $a(1 + b\theta)$ , where  $\theta$  is the angle of incidence. The scaled amplitudes are shown as triangles.

position away from the changing reservoir. Figures 17a and 17b show a prestack gather from an inline approximately 2 km to the north of the study area, taken from the 1985 data (a) and the 1996 data (b). We have highlighted two reflectors, one in the overburden at about 1500 ms, and one close to reservoir depth at about 2000 ms. No time-lapse changes are expected in this area. By extracting peak amplitudes from these reflectors for 10 adjacent gathers and taking the average, we ended up with the result shown in Figure 18.

It can be seen from Figure 18 that the amplitudes for the 1985 data are largely comparable to the amplitudes for the 1996 data. There are some discrepancies between approximately 600 m to 1400 m offset. However, this trend was not observed in the study area, and is likely to be a local effect caused by e.g., cable feather. Thus, by using the same scaling for the Top Cook interface for both data sets, we can have confidence in the qualitative behaviour of  $\Delta R_0$  and  $\Delta G$ .

Based on equation (12), intercept and gradient values for each CMP were computed for both the 1985 data and the 1996 data. From this, estimates of  $\Delta R_0$  and  $\Delta G$  were computed. Figure 19 shows a crossplot of the estimated  $\Delta G$  values versus the estimated  $\Delta R_0$  values. For a uniform change of the velocity, one would expect the data points to be scattered around a single point as in Figure 11. However, in Figure 19, the data seem to

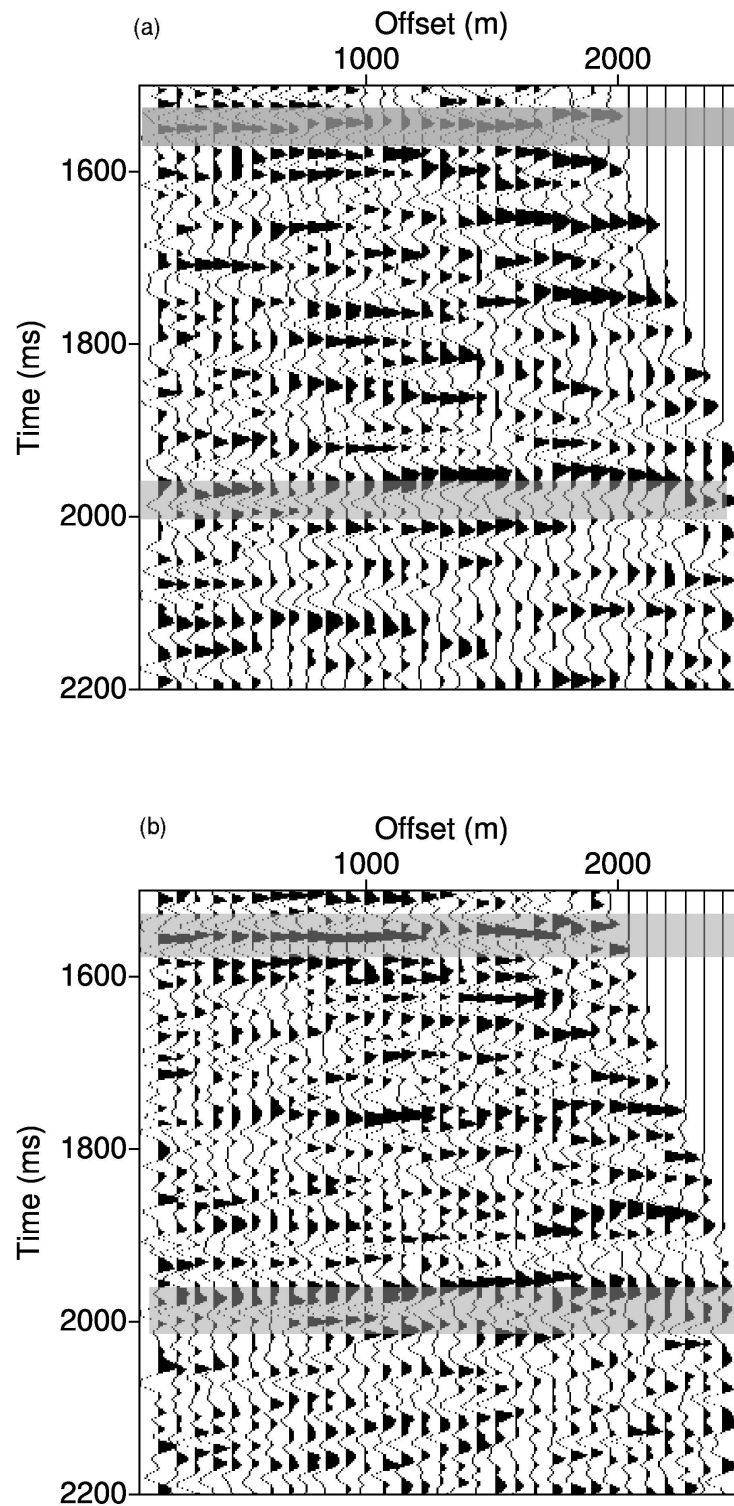


**Figure 17:** NMO-corrected prestack gather from an inline 2 km north of the study area. (a): 1985 data, and (b): 1996 data. The highlighted reflectors were used to compare the two data sets.

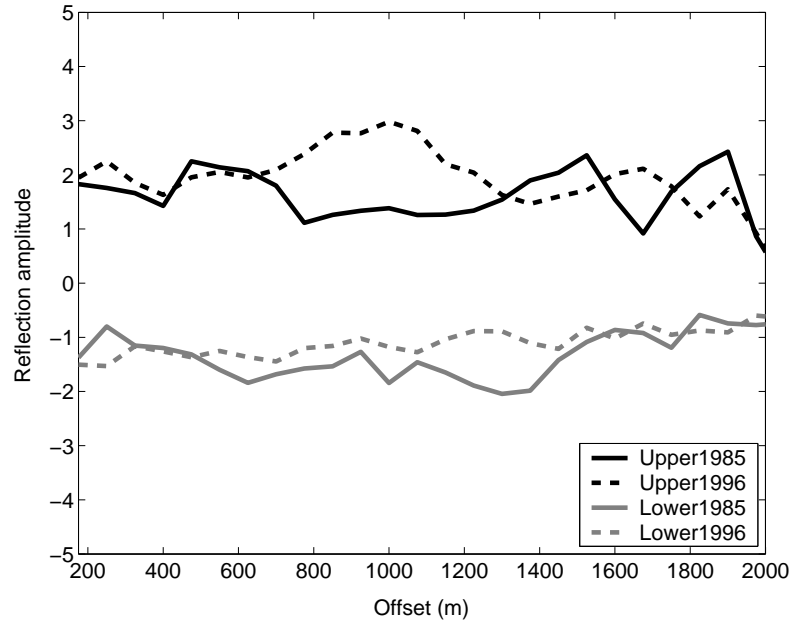


**Figure 18:** Reflection amplitudes from the highlighted reflectors in Figure 17. The curves were computed by taking the average amplitude for 10 adjacent gathers. In the legend, Upper 1985 refers to the amplitude of the shallower reflector in the 1985 vintage, and so on.

have a negative correlation. This is a common feature of noise in the data, indicating that the S/N ratio is lower for the real data than for the synthetic case with noise added.

In addition to different noise levels, we speculate that the observed difference in AVO behaviour between synthetic and real data may be due to a difference in the nature of noise present. While the noise in the synthetic data is white noise, randomly added to each individual trace, the noise in the real data may be both of random and systematic nature. Examples of effects causing systematic noise are interfering wavefields and near-surface inhomogeneities.

Despite the high level of noise in the real data, we can draw some conclusions. For  $\Delta R_0$ , negative values dominate, while for  $\Delta G$  there are both positive and negative values, with a slight bias toward positive values. This is in agreement with a pore pressure increase, which should plot in the fourth quadrant of Figure 19, as discussed before. However, there is a significant scatter in  $\Delta G$ . Thus, in this case we can not conclude that pressure has changed based on the AVO gradient. On the other hand, the values for  $\Delta R_0$  are confined between  $-0.059$  and  $-0.011$  (standard deviation) with a mean of approximately  $-0.035$ . This gives a velocity decrease of 7%. Thus, the amplitude analysis do not support the view that velocities have decreased with as much as 10%-20%. Compare with the solid line in Figure 19 which is computed from equation (10).

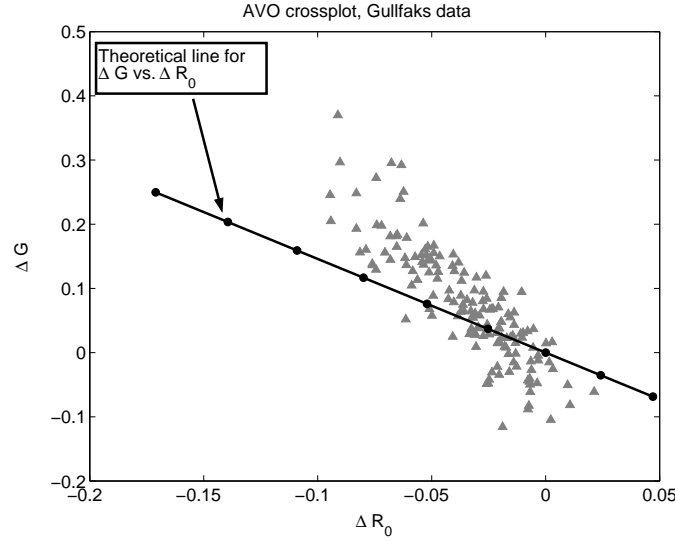


**Figure 19:** Crossplot of  $\Delta G$  versus  $\Delta R_0$ . The line corresponds to theoretical values for different values of  $\Delta\alpha^P/\alpha$  ranging from -0.3 (left) to 0.1 (right), in steps of 0.05, marked by circles.

The mechanisms assumed to have impact on the time-lapse seismic data in this case are fluid saturation changes (27% of the estimated oil reserves had been produced from this segment at the time when the second survey was acquired) and pore pressure changes. According to Landrø (2001) the change in AVO intercept and gradient due to pure saturation changes can be written

$$\begin{aligned}\Delta R_0 &= \left( \frac{1}{2} \frac{\Delta\alpha^F}{\alpha} + \frac{\Delta\rho^F}{\rho} \right), \\ \Delta G &= \frac{1}{2} \left( \frac{\Delta\alpha^F}{\alpha} \right),\end{aligned}\tag{15}$$

to the lowest order. Here, the superscript  $F$  denote changes in seismic parameters due to saturation (fluid) changes in the reservoir. An increase in water saturation will increase both the density and P-wave velocity in the reservoir. Thus, for pure saturation changes, both  $\Delta R_0$  and  $\Delta G$  will be positive. A fluid correction would require subtraction of appropriate values for  $\Delta R_0$  and  $\Delta G$ , and therefore tend to rotate the data points in Figure 20 further down and to the left. This may explain why we obtain only an 7% velocity decrease from  $\Delta R_0$ .



## 6 Discussion

The pressure increase that was observed in the well could not be seen by velocity analysis of the seismic data. There are numerous reasons why velocity analysis does not work in this study. A consideration of the synthetic data results indicates that data quality is an important issue. As the signal-to-noise ratio decreases uncertainties increase. The increase in uncertainty from  $S/N = 1$  to  $S/N = 0.5$  is much more pronounced than the corresponding increase between  $S/N = 10$  and  $S/N = 1$ . This suggests that the relationship between uncertainties and  $S/N$  ratios is strongly nonlinear.

Failure to recognize reflectors at the base of the reservoir forced us to pick velocities at greater depths. As a result, a possible velocity change is harder to detect since the stacking velocity, which is an average velocity, is expected to be less affected at depths far below the reservoir where the time-lapse changes have taken place. However, there is no clear indication in the synthetic data that this should be the case here. The observed change in stacking velocity is approximately the same 100-180 m below the base of the reservoir as it is at the base.

The fact that the reservoir zone is thin (only 80 meters) makes a velocity change hard to detect. Even in noise-free synthetic data the observed change in stacking velocity is small. From equation (5) we find that a change of 20% in interval velocity in a reservoir of this thickness and burial depth will give a change in rms velocity of about 15 m/s. This is in good agreement with the synthetic study, where the reservoir is perturbed with a change in interval velocity of 20 %, while the observed change in stacking velocity is found to be  $9.2(\pm 8.3)$  m/s for noise-free data. Since the uncertainty in  $\Delta V_{\text{rms}}$  is of the order of 40 m/s for the real data, we can not expect to see such a small velocity change here.

AVO analysis has the advantage that it does not depend on the thickness of the altered zone, as long as the thickness is above the tuning threshold. The requirement for detecting of changes is that the reflectivity be altered sufficiently. However, getting accurate velocity information from the AVO signal is a challenge. For instance, limited well control increases the uncertainty away from the borehole. In addition, effects like anisotropy and attenuation may affect the AVO signal, and hence introduce errors if we do not compensate for them.

In the analysis, we have assumed that the properties of the cap rock overlying the reservoir do not change with time. This assumption is not valid if the cap rock is influenced by production effects. Since the cap rock is relatively impermeable, it is not likely that the pore fluid content here has changed much. In addition, the observed pore pressure increase in the reservoir must mean that the cap rock is sealing with respect to pressure. However, the pressure front may partly penetrate the cap rock, creating a gradual change

in pressure at the top reservoir interface, rather than an abrupt change. Hence, water injection in the reservoir may have influenced the fluid pressure in the cap rock as well, resulting in a change in the elastic parameters of the rock overlying the reservoir. Such an effect may explain the discrepancy between the observed change in AVO signature at the top reservoir interface and the predicted change.

The results from the amplitude analysis on synthetic and real data indicate that the difference in zero offset reflection coefficient,  $\Delta R_0$  is a more reliable measure than the difference in AVO gradient  $\Delta G$ . Hence, our analysis suggest that stacked amplitude would yield the most stable results. However, it is good practice to check the amplitude variation with offset, as any significant difference in AVO gradient will increase the confidence in the results.

In this study we have used a simple method of time-lapse seismic amplitude analysis. By picking the peak amplitude at the top reservoir interface for both the baseline and monitor surveys, we estimate the change in the AVO parameters  $R_0$  and  $G$ . This method does not take into account the fact that the recorded wavefield from a reflecting interface often is composed of a series of events (tuning). In the synthetic study this was not an issue, since the model consisted of homogeneous layers with a thickness greater than the seismic wavelength. However, for the real case, both the cap rock and the reservoir rock are probably layered at a finer scale than the seismic wavelength. One way to resolve this problem, is to perform a full waveform inversion on the seismic data. For the current data set, a full waveform inversion on stacked amplitudes could probably have given more reliable results.

In an exploration case, the more important problem is predicting pore pressures rather than detecting pore pressure changes. In that case, we have very little knowledge of the subsurface in advance. For exploration problems, AVO analysis could serve as a supplement to other methods (e.g., velocity analysis) for pore pressure prediction purposes, rather than as a stand-alone tool.

## 7 Conclusions

Synthetic modeling and results from analyzing real time lapse seismic data show that velocity analysis is not accurate enough to detect a 5-7 MPa pore pressure increase in an 80 m thick reservoir rock at 2000 meters depth. Theoretical considerations show that the accuracy of time lapse velocity analysis decreases abruptly with increasing burial depth, and decreasing reservoir thickness.

For the real data, we are forced to pick velocities at events below the base reservoir. This

means that we include segments that have not been subject to any time lapse changes. However this seems to be of less importance than the data quality and reservoir thickness.

Amplitude analysis reveals changes that are consistent with a decrease in interval velocity in the reservoir zone. The estimated AVO parameter  $\Delta R_0$  was found to be consistent with a velocity decrease of approximately 7% in the reservoir. The results for the change in AVO gradient,  $\Delta G_0$  are inconclusive, meaning that in this case,  $R_0$  gives the most reliable information. There are uncertainties related to the scaling procedure and fluid changes in the reservoir. Therefore, although there is a high level of confidence that the reservoir velocity has decreased, the estimated decrease of 7% is uncertain.

Although the accuracy of velocity analysis quickly degrade with depth (Figure 3), it may yield valuable information about velocity anomalies at shallow depths. Abnormal pore pressures are often located in thick shale units in the overburden. In such cases, velocity analysis is a favourable method for pore pressure prediction. For limited shallow zones associated with high reflectivity, e.g., shallow gas, amplitude analysis may serve as a supplement to velocity analysis.

In thinner and deeper zones, amplitudes seem to indicate velocity anomalies better than velocity analysis. This can be useful for detecting lateral variations in pore pressure, e.g., across faults. However, since pressure anomalies often extend vertically and laterally well beyond hydrocarbon reservoirs, they still may be detectable by velocity analysis. Thus, for seismic exploration, this study indicates that amplitudes could be useful in combination with velocity analysis in order to detect pressure anomalies in limited zones. However, it is a requirement that differences in pore pressure are accompanied by sufficient differences in velocity. In this example, it was possible to detect velocity changes based on amplitude analysis since the pressure change at Gullfaks have resulted in a significant change in velocity (10%-20%).

## 8 Acknowledgements

Statoil ASA and their Gullfaks partners, Norsk Hydro AS and Petoro AS, are acknowledged for permission to present the data. The associate editor, Rodney Calvert, and two anonymous reviewers are acknowledged for helpful suggestions.

# Chapter 4

## Pore pressure estimation from seismic data on Haltenbanken

Øyvind Kvam and Martin Landrø

*Department of Petroleum Engineering and Applied Geophysics  
Norwegian University of Science and Technology  
N-7491 Trondheim, Norway*

**ABSTRACT:** We have used regional porosity trends and empirical relationships between effective pressure and seismic velocities to derive a model for seismic pore pressure prediction at Haltenbanken in the Norwegian Sea. The model predicts significant velocity variations between the normally pressured reservoir rocks at the Lavrans Field and the highly overpressured reservoir rocks at Kristin. Conventional velocity analysis and seismic amplitude analysis are used to resolve the pore pressure differences between Lavrans and Kristin.

### 1 Introduction

Abnormally high subsurface pore pressures have been encountered in most parts of the world. Offshore Norway, overpressures are common in Jurassic reservoir sandstones both in the northern North Sea and the Norwegian Sea. At Haltenbanken, offshore Mid-Norway, pore pressures as high as twice the hydrostatic pressure have been reported in Late Jurassic sandstones at the Kristin Field.

It is known that seismic velocities are sensitive to pore pressure. This can be used to

predict overpressures from seismic data prior to drilling. The concept of seismic pore pressure prediction date back to Pennebaker (1968). The field has received much interest, as the oil industry have started to explore areas where abnormal pore pressures are frequently encountered (deepwater, deeper drilling targets). Much of the published work focus on deriving accurate seismic velocity information for pore pressure prediction. Conventional velocity analysis (Reynolds, 1970) is still a much used tool for pore pressure prediction purposes. However, more modern techniques, like velocity tomography (Sayers et al., 2002) and seismic amplitude analysis (Carcione et al., 2003) are becoming usual. For a review of velocity analysis techniques used for pore pressure prediction, see Dutta (2002b).

In this study, we use velocity analysis and seismic amplitude analysis to predict pore pressures along a 2D seismic line from Haltenbanken. First, we develop a rock physics model for the relation between seismic velocities and pore pressure. The model is based on grain contact theory (Mindlin and Deresiewicz, 1953), and is calibrated to well data. Regional porosity trends are used to correct for porosity variations, which may significantly affect seismic velocities, and hence the pore pressure prediction. Next, velocity information is extracted from the seismic data using conventional velocity analysis and seismic amplitude analysis. We focus mainly on data from the Lavrans Field and the Kristin Field. Finally, by comparing the results of the seismic analysis to the predictions of the model, we estimate the pore pressure at the Kristin Field, assuming that the pressure at Lavrans is known. The methodology described here is well suited for pore pressure prediction across sealing fault planes, where the pressure at one side of the fault is known.

## 2 Study area

Haltenbanken is located offshore mid-Norway. Discoveries have been made on structural highs, including the Åsgard Field, the Kristin Field, The Lavrans Field, and several small satellite fields. Currently, Åsgard is the only producing field, while Kristin is under development. A map of the hydrocarbon resources at Haltenbanken is shown in Figure 1. The position of the 2D seismic line used in this study is also shown.

Reservoir sandstones are found in the Early Jurassic Tilje Formation, and in the Middle Jurassic Ile and Garn Formations, representing deltaic to shallow marine deposits (see f.i. Hermanrud et al., 1998). The reservoir depth is approximately 4.4-4.8 km. The pore pressure within the reservoir units vary greatly. At Lavrans, the pore pressures are only slightly higher than hydrostatic ( $\approx 50$  MPa), while at Kristin there has been measured pressures up to 90 MPa, which is nearly twice as high as the hydrostatic pressure. At 4.7 km depth, this gives a pore pressure gradient of 19 kPa/m (0.84 Psi/ft), which is a moderate to hard overpressure according to the geopressure characterization of Dutta

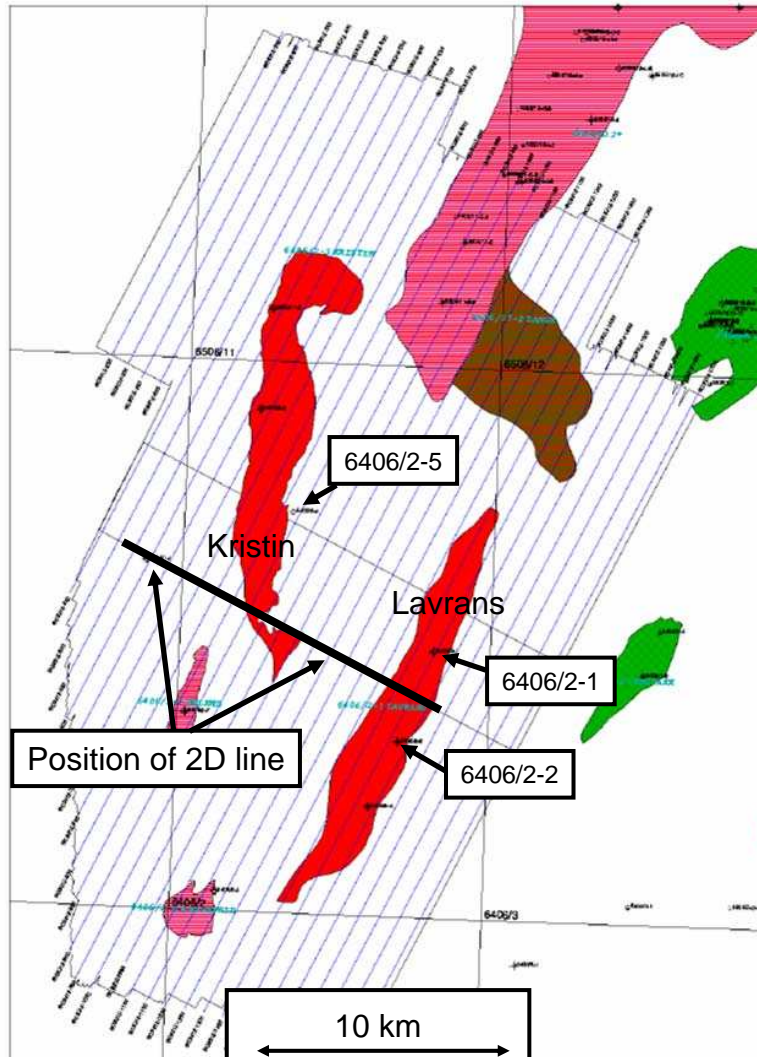


**Figure 1:** Map of Haltenbanken. The position of the 2D seismic line used in this study is marked with a black line.

(1987). In this paper, we will use the Kristin and Lavrans Fields as study areas, since they are separated into two very different pressure regimes. The reservoir rocks at both locations are assumed to have the same depositional origin, and are therefore well suited for this study.

### 3 A model for pore pressure prediction at Haltenbanken

In this section, we discuss the relationship between seismic velocities and pore pressure at Haltenbanken, and a model for pore pressure prediction in the area is developed. However, first, we define some useful quantities.

#### 3.1 Effective pressure

We will express any dependency of pore pressure through the effective pressure, or more precisely, the vertical component of the effective stress, which is defined as (see f.i. Christensen and Wang, 1985)

$$p_e = S - np. \quad (1)$$

Here  $S$  is the external load and  $p$  is the pore pressure. The factor  $n$  is known as the Biot coefficient. The Biot coefficient can be defined through

$$n = 1 - \frac{K_{fr}}{K_s}, \quad (2)$$

where  $K_{fr}$  is the bulk modulus of the rock frame and  $K_s$  is the bulk modulus of the solid material. For soft rocks,  $n \approx 1$ . In this case, the effective pressure is equal to the differential pressure  $p_d = S - p$ . For harder rocks,  $n$  is less than 1. However, since the frame bulk modulus  $K_{fr}$  itself is pressure dependent, we must expect  $n$  to be pressure dependent. In this study, we will assume that  $n = 1$ , so that  $p_e = p_d$ .

It is possible to obtain an estimate of the differential pressure for a stratigraphic column with normal pore fluid pressure from equation (1). The overburden stress can be computed by integrating the bulk density  $\rho(z)$ . Thus, the differential pressure at depth  $d$  can be computed as

$$p_d(d) = g \int_0^d \rho_b(z) dz - g\rho_w d, \quad (3)$$

where  $g$  is the gravitational constant and  $\rho_w$  is the density of water. Figure 2 shows the differential pressure vs depth calculated from a density log at Lavrans. We note that at 4400 m, which is the approximate burial depth for the top of the reservoir at Lavrans, the differential pressure is about 46 MPa.

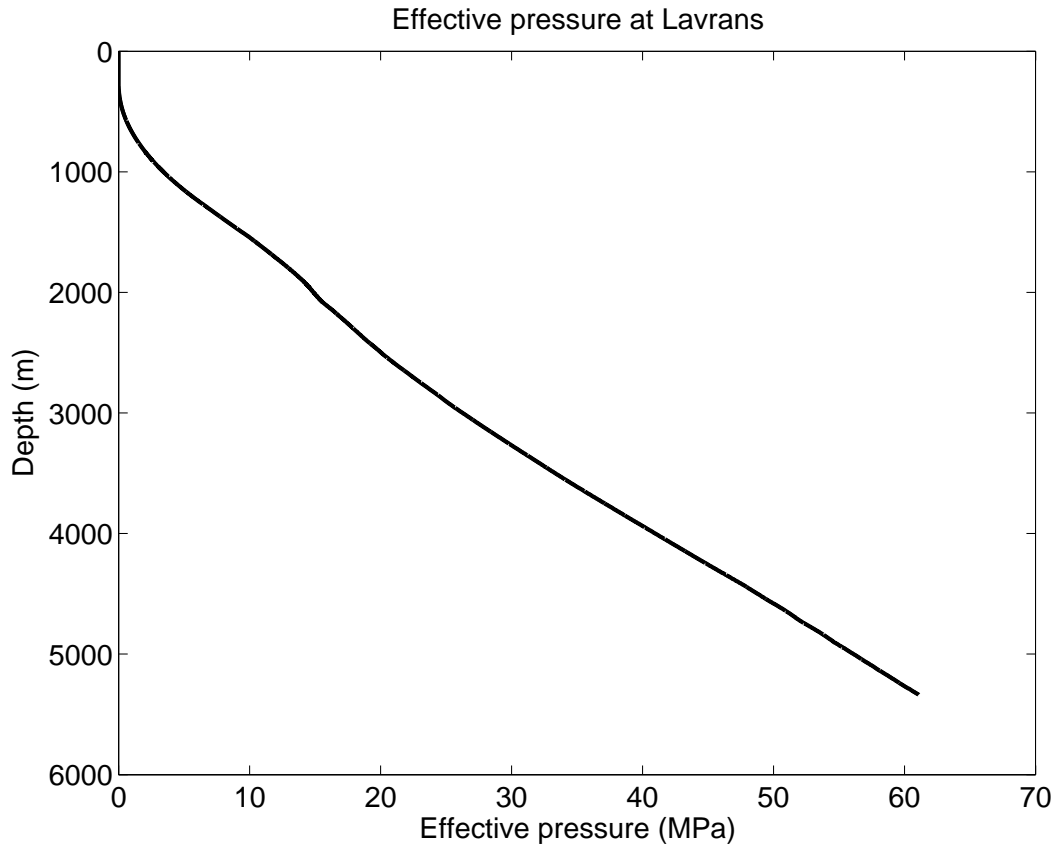


**Figure 2:** Effective pressure computed from density log at Lavrans.

The burial depth for the reservoir at Kristin is approximately 4700 m along the seismic line used in this study. The extra thickness of the overburden at Kristin consists mainly of Cretaceous shales. Assuming an average density of  $2500 \text{ kg/m}^3$  of these shales gives a differential vertical pressure of 51 MPa at Kristin. Note that the pressures are computed with the assumption that the pore pressures both at Kristin and Lavrans are hydrostatic, which is not the case.

### 3.2 Known methods for pore pressure prediction

The aim of this study is to separate different pressure regimes from seismically derived velocity data at Haltenbanken. In order to do this, we must establish a relationship between velocities and pore pressure. Thus, we need a link between rock properties and seismic properties. Rock physics is the tool that provides such a link. Many authors have published work on pore pressure prediction from seismic velocity data.



Known mechanisms of abnormal pressure generation in the subsurface are discussed by Fertl (1976). One of the most common mechanisms is undercompaction due to rapid sedimentation (compaction disequilibrium). This is often the case for thick shale units where the sedimentation rate has been high. Due to the low permeability of shales, pore fluid is prevented from being squeezed out of the formation. The pore fluid is forced to carry some of the weight of the overburden, resulting in abnormally high pore pressures and high porosities.

In the case of disequilibrium compaction, it is the high porosities that cause the relationship between seismic velocities and pore pressure. Various velocity-porosity relationships exist in the literature. Commonly used relationships are the Wyllie equation, Nur's critical porosity model, and the Hill average (see e.g. Mavko et al., 1998). In addition, experimental relationships exist (Han et al., 1986). They all have in common that high porosities lead to low seismic velocities. Consequently, abnormally high pore pressures can be detected from seismic data. The Eaton approach (Eaton, 1972) is a widely used method for pore pressure prediction that is based on this assumption. Dutta (2002a) also assumes a correlation between porosity and pore pressure. In general, such methods require calibration to a local compaction trend. These methods are widely accepted and have proven successful. Thus, if the high pressures observed at Haltenbanken are due to disequilibrium compaction, we can use established methods for predicting the pore pressure from seismic data.

An extensive study by Hermanrud et al. (1998b) addressed the cause of abnormally high pore pressures in the reservoir rocks at Haltenbanken. They found that the porosities in reservoir sandstones were generally higher in overpressured zones than in normally pressured zones. However, they found no evident relationship between porosity and pore pressure in the intra-reservoir shales. This means that disequilibrium compaction is probably not the main reason for overpressuring at Haltenbanken.

If the overpressure at Haltenbanken is not driven by compaction, what possibilities do we have for pore pressure prediction from seismic data? First, we must realize that the assumption that high pore pressures are accompanied by high porosities does not apply. As discussed above, the relation between seismic velocities and pore pressure is often thought to reflect a relation between porosity and pore pressure. For the intra-reservoir shales at Haltenbanken no such relation exists. However, Hermanrud et al. (1998b) found consistently lower velocities in the high pressure areas for both sandstones and shales. This indicates a *direct* relationship between velocities and pore pressure. Unfortunately, there exists little documentation on velocity and stress in shales in the literature. For sandstones, there has been a considerable amount of published work. Measurements on unconsolidated sands (Domenico, 1977) and consolidated low-porosity sandstones (Khaksar et al., 1999) reveal that the velocities change significantly with pressure, while the porosity hardly changes at all. Thus, we can try to establish a direct relation between velocity and pressure for Haltenbanken.

Equations that express the P- and S- wave velocities of a sandstone as a function of the effective stress were presented by Eberhart-Phillips et al. (1989). These were based on ultrasonic measurements of a large number of sandstone core samples. However, there are some caveats in using these equations for pore pressure prediction at Haltenbanken. First, the equations are strictly only valid for the core plugs examined. We have no warranty that the reservoir sandstones at Haltenbanken obey the same pressure-velocity relationship. Second, measurements on core plugs do not necessarily represent the in situ rock. The process of coring may damage the rock sample and alter the elastic properties of the rock, as discussed by Nes et al. (2000). Third, there are significant volumes of shale interbedded with the reservoir rocks at Haltenbanken, and although we could use the equations for the reservoir sandstones, we do not have similar expressions for shales.

Since none of the established methods seem suitable for pore pressure predictions at Haltenbanken, we choose an approach where we use well data from known overpressured formations in the area to estimate a pressure-velocity relationship.

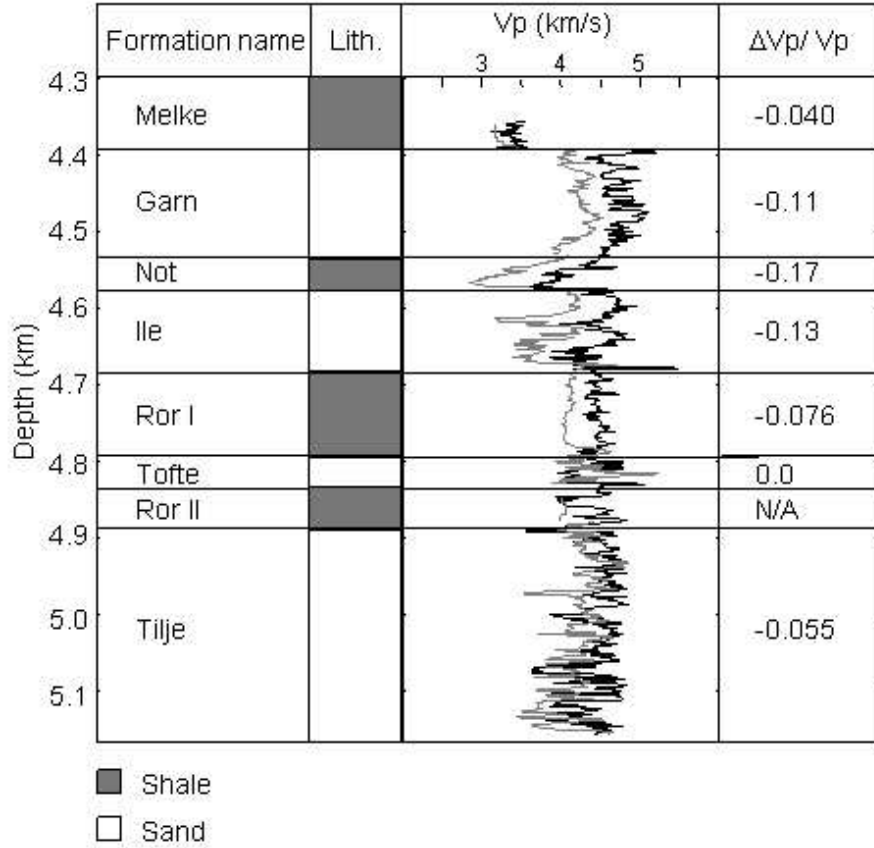
### 3.3 Pressure dependent velocities at Haltenbanken

Figure 3 shows a plot of two sonic logs, along with the stratigraphy of the reservoir rocks at Haltenbanken. Well 6406/2-1 is located at the Lavrans Field, approximately 2 km north of the 2D seismic line used in this study. The pore pressure in the reservoir section shown in Figure 3 is close to hydrostatic in this well. Well 6406/2-3 is located on the Kristin Field, approximately 4 km north of the 2D line. In this well, the pore pressure is abnormally high. The pore pressure gradient in this well is about 18 kPa/m, which is almost twice as high as hydrostatic pressure. The log from Kristin has been stretched to match the stratigraphy of Lavrans. Note that there is a strong correlation, but that the sonic log from the Lavrans Field show consistently higher velocities than those from the Kristin Field.

Is the difference in pore velocity related to the difference in pore pressure? In order to answer that, we must first look at other possible causes for velocity variations at Haltenbanken.

One of the most important factors determining the velocity of a rock is the porosity. Since burial history can affect the porosity significantly (diagenesis, compaction), it is possible that the high velocities observed in the sonic log from Lavrans are due to porosity variations. Ultrasonic core measurements (Han et al., 1986; Vernik, 1997) suggest a strong linear correlation between velocity, porosity and clay content in shales and sandstones. For the reservoir sandstones at Haltenbanken, we estimate the porosity,  $\phi$ , from the density log,  $\rho$  as

$$\phi = \frac{\rho_s - \rho}{\rho_s - \rho_f}, \quad (4)$$



**Figure 3:** Velocity logs from normally pressured (black line) and highly overpressured (grey line) well.

where  $\rho_s$  and  $\rho_f$  are the densities of the grain material and the pore fluid, respectively. We assume that  $\rho_s=2650 \text{ kg/m}^3$  (quartz) and  $\rho_f=1000 \text{ kg/m}^3$  (water). Figure 4 shows a plot of sonic velocity vs. estimated porosity for the Ile formation. The data are taken from well 6406/2-1. Note that there is a strong linear correlation between the porosity and the velocities. The cluster of low velocities for low porosities in Figure 4 are from the upper part of the Ile formation, and are likely to be shale points. Figure 5 show similar plots for the Garn, Tofte, and Tilje sandstone formations from well 6406/2-1. The weaker correlation in the Tilje Formation can probably be explained by large variations in clay content, as suggested by gamma log readings. A linear fit to the sandstone points in Figure 4 gives

$$\Delta V_p = V_p(\phi_2) - V_p(\phi_1) = -4469\Delta\phi, \quad (5)$$

for the P-wave velocity  $V_p$ . Here,  $V_p$  is in units of m/s. We use equation (5) to correct for

porosity variations in sandstones.

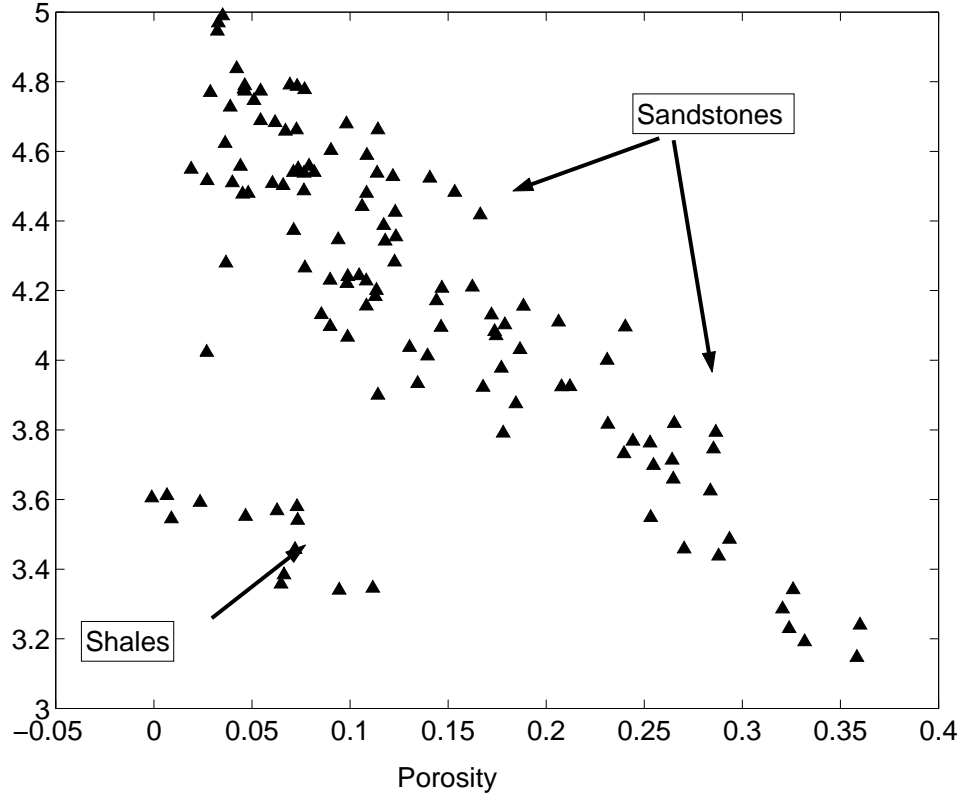


**Figure 4:** Crossplot of velocity vs. porosity in Ile Fm.

For the shale formations, we do not observe a strong correlation between estimated porosity and velocity. This might be due to heterogeneities in the shale formations. Figure 6 shows a plot of velocity vs. estimated porosity from the Lower Ror Formation (Ror II) from wells 6406/2-1 and 6406/2-2. A linear fit to these data gives

$$\Delta V_p = -2469 \Delta \phi. \quad (6)$$

We use equation (6) to correct for porosity variations in shales.

In addition to porosity, differences in pore fluid content also may cause differences in velocity. However, we will assume that the fluid content in the reservoir sandstones at Kristin and Lavrans is similar, such that this does not affect the sonic velocities at Haltenbanken.

Figure 7 shows estimated porosity and sonic logs for the two wells shown in Figure 3. The sonic log from well 6406/2-1 has been corrected for velocity differences using equations (5)-(6). We still observe a difference in velocity between Kristin and Lavrans.

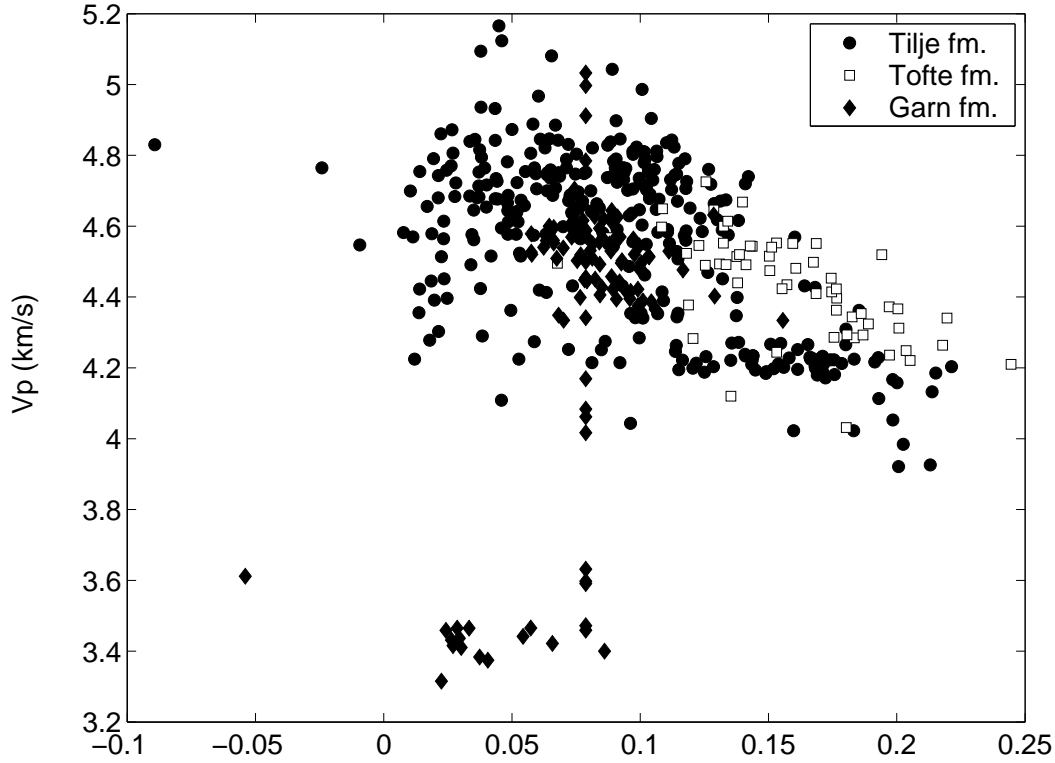


**Figure 5:** Crossplot of velocity vs. porosity in Garn, Tofte and Tilje Fms.

Figure 7 is a good indication of pressure dependent velocities at Haltenbanken. This view is supported by Hermanrud et al. Thus, we conclude that pore pressure have a significant impact on the velocities in the reservoir rocks at Haltenbanken.

### 3.4 Porosity trends on Haltenbanken

As we have seen above, porosity variations must be taken into consideration when establishing a relationship between velocity and pore pressure. We do this by examining regional porosity trends, taken from a large number of wells at Haltenbanken. Figure 8 shows measured core porosities vs. depth in the Garn Formation from Hermanrud et al. Although there are only a few measurements for high-pressure wells (pore pressure  $\geq 20$  MPa above hydrostatic pressure), we observe a linear trend of decreasing porosity with depth for both normal- to medium-pressure wells and high-pressure wells. Thus, we assume

$$\phi = A + Bd, \quad (7)$$

where  $A$  and  $B$  are constants, and  $d$  is the depth.

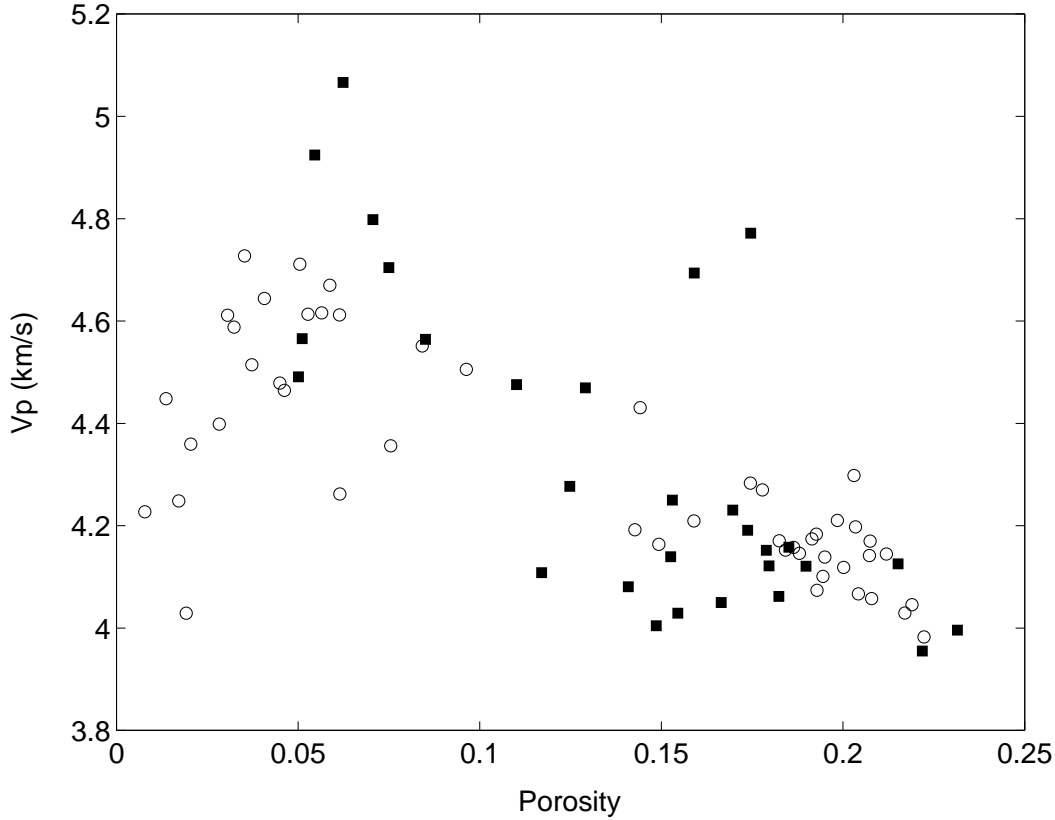


**Figure 6:** Crossplot of velocity vs. porosity in lower Ror Fm.

We use the data points in Figure 8 to estimate values for  $A$  and  $B$ . For normally pressured reservoir sandstones, we find (fractional porosities)

$$\phi = -8.9 \cdot 10^{-5}d + 0.49, \quad (8)$$

while for overpressured reservoir sandstones we estimate

$$\phi = -8.9 \cdot 10^{-5}d + 0.53. \quad (9)$$

Here  $d$  is the depth in meters. For shales, Hermanrud et al. found little variation in the porosity with depth and pore pressure. Hence, we only correct for regional porosity trends in sandstones.

### 3.5 Modified Herz-Mindlin theory for pore pressure prediction

The Herz-Mindlin theory gives the dry (unsaturated) bulk modulus ( $K_{\text{dry}}$ ) and the shear modulus ( $G$ ) of a random pack of spherical grains as a function of effective pressure

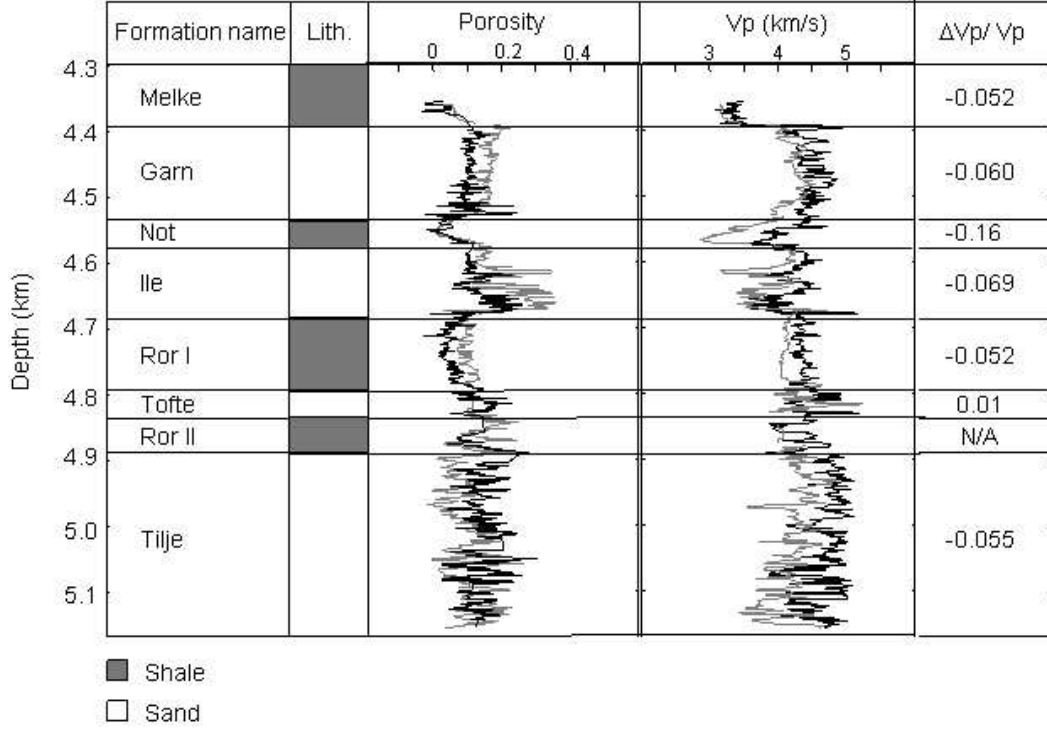


**Figure 7:** Same as figure 3, but the sonic log from the normally pressured well is corrected for porosity differences.

through (see e.g. (Mavko et al., 1998))

$$\begin{aligned}
 K_{\text{dry}} &= A_1 p_e^{\frac{1}{3}}, \quad A_1 = \left[ \frac{C^2(1-\phi)^2 G_s^2}{18\pi^2(1-\nu)^2} \right]^{\frac{1}{3}}, \\
 G &= A_2 p_e^{\frac{1}{3}}, \quad A_2 = \frac{5-4\nu}{5(2-\nu)} \left[ \frac{3C^2(1-\phi)^2 G_s^2}{2\pi^2(1-\nu)^2} \right]^{\frac{1}{3}}.
 \end{aligned} \tag{10}$$

Here,  $C$  is the average number of contacts per grain,  $G_s$  is the shear modulus of the grain material, and  $\nu$  is the Poisson's ratio of the grain material. From this, we get for the P-wave and S-wave velocities

$$\begin{aligned}
 V_{p,\text{dry}} &= \sqrt{\frac{K_{\text{dry}} + \frac{4}{3}G}{\rho}} \propto p_e^{\frac{1}{6}}, \\
 V_s &= \sqrt{\frac{G}{\rho}} \propto p_e^{\frac{1}{6}}.
 \end{aligned} \tag{11}$$

That is, the velocity in a dry random pack of spheres is proportional to  $p_e^{1/6}$ . It is reasonable to think of a sandstone as a pack of randomly positioned grains.

Experiments on unconsolidated sands and glass beads (Domenico, 1977) agree well the

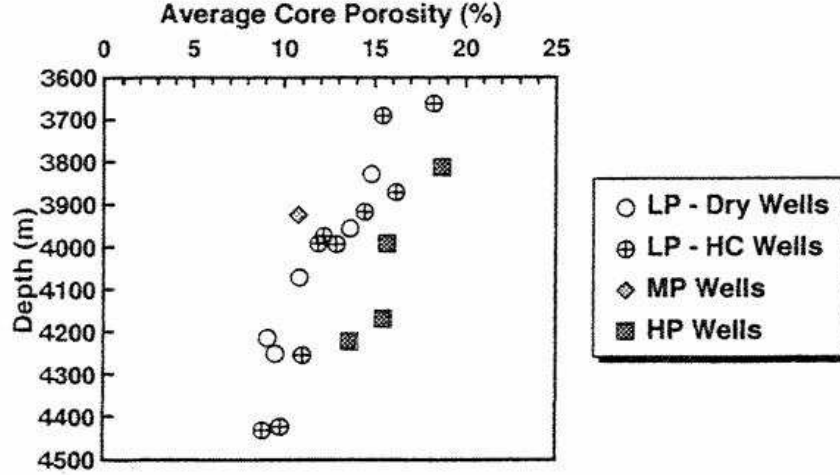


**Figure 8:** Measured core porosities in the Garn Formation at Haltenbanken from Hermanrud et al. (1998). Normal to medium pressured wells are represented by circles, high pressured wells are represented by squares.

Herz-Mindlin theory. However, for consolidated sandstones the sensitivity to pressure changes is smaller than predicted by equations (10). It can be shown (Dvorkin et al., 1991) that the stiffness of a cemented grain contact does not change with pressure at all.

In order to compensate for variations in pressure-velocity relationships, but still keep the simple formalism of the Herz-Mindlin theory, we modify equations (10) slightly. This can be done by substituting the exponent  $1/3$  with a lithology-dependent exponent  $\kappa$ . Thus, equations (10) become

$$\begin{aligned} K_{\text{dry}} &= A_1 p_e^\kappa \\ G &= A_2 p_e^\kappa. \end{aligned} \quad (12)$$

An expression for the saturated P-wave velocity ( $V_p$ ) can be obtained from Gassmann's equation (Mavko et al., 1998) which state that

$$\rho V_{p,\text{sat}}^2 = K_p + K_{\text{dry}} + \frac{4}{3}G, \quad K_p = \frac{(1 - \frac{K_{\text{dry}}}{K_s})^2}{\frac{\phi}{K_f} + \frac{(1-\phi)}{K_s} - \frac{K_{\text{dry}}}{K_s^2}}. \quad (13)$$



In equation (13),  $K_f$  is the bulk modulus of the pore fluid and  $K_s$  is the bulk modulus of the rock material. To the lowest order in  $K_{\text{dry}}$ ,  $K_p$  can be written as

$$K_p \approx \frac{1}{\frac{\phi}{K_f} + \frac{(1-\phi)}{K_s}} - A_3 K_{\text{dry}} \quad , \quad A_3 = \frac{1}{K_s} \frac{\frac{2\phi}{K_f} + \frac{1-2\phi}{K_s}}{\left(\frac{\phi}{K_f} + \frac{(1-\phi)}{K_s}\right)^2}. \quad (14)$$

The approximation is illustrated in Figure 9, which shows plots of  $K_p$  vs  $K_{\text{dry}}/K_s$  for different porosities.

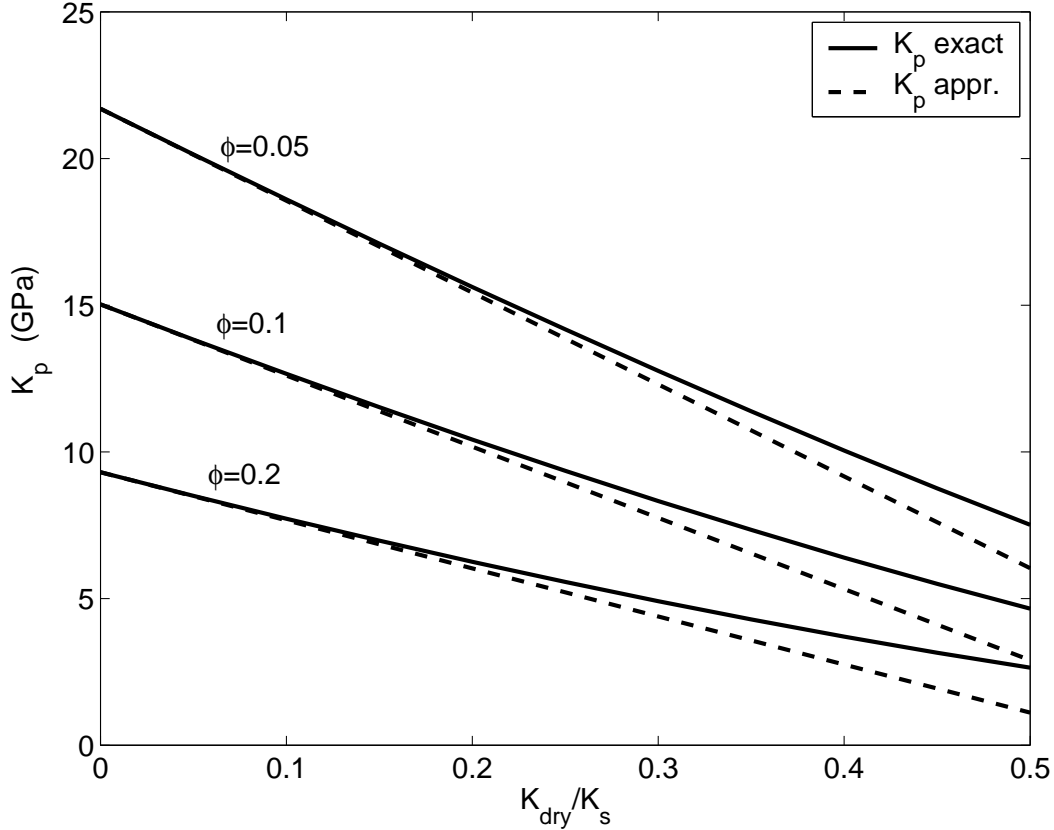


**Figure 9:** Approximation for  $K_p$ . The bulk modulus of the fluid is set to 2.3 GPa (water) and the bulk modulus of the solid material is set to 37 GPa (quartz).

Note that the first term in equation (14) is identical to the Reuss lower bound,  $K_R$ , for the bulk modulus. This is the bulk modulus for a suspension of particles in a fluid. We now insert equations (12) and (14) into equation (13). This gives

$$\rho V_{p,\text{sat}}^2 \approx K_R + A p_e^\kappa, \quad (15)$$

where  $A = A_1 + A_2 + A_3$ . Equation (15) can be interpreted as follows; when  $p_e = 0$ , there is no contact between the grains. Hence, the medium is a suspension, and  $V_p$  is determined by the Reuss lower bound. As  $p_e$  increases, the grain contacts become stronger, and the velocity increases.

If the porosity and the properties of the pore fluid and the solid material are known,  $K_R$  can be estimated from equation (14). For the reservoir rocks at Haltenbanken, we used  $K_f = 2.3$  GPa (water), and the porosity was estimated from density log data using equation (4). The solid bulk modulus,  $K_s$  was estimated from log data in the following way; from equations (5) and (6), velocities for zero porosity were determined. The density of the solid was assumed to be  $\rho_s = 2650$  kg/m<sup>3</sup> (quartz).  $K_s$  was then determined from  $K_s = \rho_s V^2(\phi = 0) \approx 39$  GPa for sandstones, and  $K_s \approx 25$  GPa for shales. Next, porosities for each formation was estimated from the density log. Equation (14) was used to find values for  $K_R$ . As an example, the value for  $K_R$  for the Melke formation was estimated from well 6406/2-1 to be 9 GPa.

If we know  $V_p$  for two different values of  $p_e$ , say  $p_1$  and  $p_2$ ,  $\kappa$  can be estimated, since we have from equation (15)

$$\frac{\frac{V_p(p_1)}{V_p(0)} - 1}{\frac{V_p(p_2)}{V_p(0)} - 1} = \left(\frac{p_1}{p_2}\right)^\kappa, \quad (16)$$

which leads to

$$\kappa = \ln \left( \frac{\frac{V_p(p_1)}{V_p(0)} - 1}{\frac{V_p(p_2)}{V_p(0)} - 1} \right) \left[ \ln \left( \frac{p_1}{p_2} \right) \right]^{-1}. \quad (17)$$

$V_p(0)$  is the velocity for zero differential pressure, which is obtained from  $pV_p^2(0) = K_R$ . In equations (16)-(17) we have assumed that the density is constant. However, we use well logs from different locations to find values for  $\kappa$ . Thus, we introduce a small error if the density is not the same in the wells.

Once we have obtained a value for  $\kappa$ , it is easy to obtain a value for  $A$ , since, from equation (15)

$$A = \frac{1}{p_e^\kappa} (\rho V_{p,\text{sat}}^2 - K_R) \quad (18)$$

We will use equations (17) and (18) to obtain values for  $\kappa$  and  $A$  in both shales and sandstones. It is not intuitive to think of shale as a granular medium. However, experimental work indicate that velocities in shales depend on pore pressure in the same way as sandstones do. I.e., velocities increase with increasing effective pressure (Jones and Wang, 1981; Jonston, 1987). Compared to velocities in sandstones, velocities in shale do not tend to taper off so fast for high effective pressures, however the effect is observed (Hornby et al., 1994). As for sandstones, the relationship is very lithology-dependent.

Table 1 summarizes values for  $\kappa$  and  $A$  calculated for the stratigraphic units in the reservoir rocks at Haltenbanken. The left column gives values obtained from comparing wells 6406/2-1 and 6406/2-3, and the right column gives values obtained from comparing wells 6406/2-2 and 6406/2-3. There are considerable variations in  $\kappa$  and  $A$  between the stratigraphic units. In addition, the values computed from different wells do in general not

**Table 1:** Parameters for velocity estimation

Formation	Well 6406/2-1		Well 6406/2-2	
	$\kappa$	$A$	$\kappa$	$A$
Melke	0.22	0.32	0.23	0.27
Garn	0.12	4.9	0.02	22.1
Not	0.55	0.001	0.28	0.071
Ile	0.14	2.6	0.05	11.3
Ror I	0.11	3.6	0.13	4.4
Tofte	0.06	10.3	0.11	4.9
Ror II	N/A	N/A	N/A	N/A
Tilje	0.25	0.39	0.20	8.3

coincide. Note, however, that most values of  $\kappa$  are significantly smaller than  $1/3$ , which is predicted by the Herz-Mindlin theory.

The pressure-velocity relationships resulting from the values of  $\kappa$  and  $A$  in Table 1 are not directly usable for pore pressure prediction. The temporal resolution of conventional velocity analysis is too coarse to estimate interval velocities for each stratigraphic unit. Thus, we need an expression that relate the interval velocity ( $V_p$ ) of the entire stratigraphic column to effective pressure. This is achieved by estimating values for  $\kappa$  and  $A$ , treating the reservoir as one unit. Since we have used two normally pressured wells, and one overpressured well to find  $\kappa$  and  $A$ , we get two relationships between velocity and differential pressure. Figure 10 shows the average of these, normalized to 50 MPa, which is the approximate differential pressure at Kristin.

In addition to a velocity model for the entire reservoir to be used with velocity analysis, we need a model for amplitude analysis. We are going to investigate a sand-shale interface (Top garn). Figures 11 and 12 shows the average relationships for  $\Delta V_p/V_p$  and  $\Delta V_s/V_s$ , respectively, for sandstones (solid line) and shales (dotted line).

The pore pressure can now be estimated as follows. Assume that we have derived the interval velocity  $V_1$  from a reservoir of known effective pressure (Lavrans), and the interval velocity  $V_2$  a reservoir of unknown effective pressure (Kristin). Furthermore, suppose that we have corrected  $V_1$  and  $V_2$  for regional porosity variations. The relative difference in velocity is

$$\frac{\Delta V}{V} = \frac{V_2 - V_1}{V_1}. \quad (19)$$

The effective pressure in the unknown area can now be estimated by finding the value of  $p_e$  in Figure 10 which correspond to the value of  $\Delta V/V$ . The pore pressure can then be found by using equation (1).

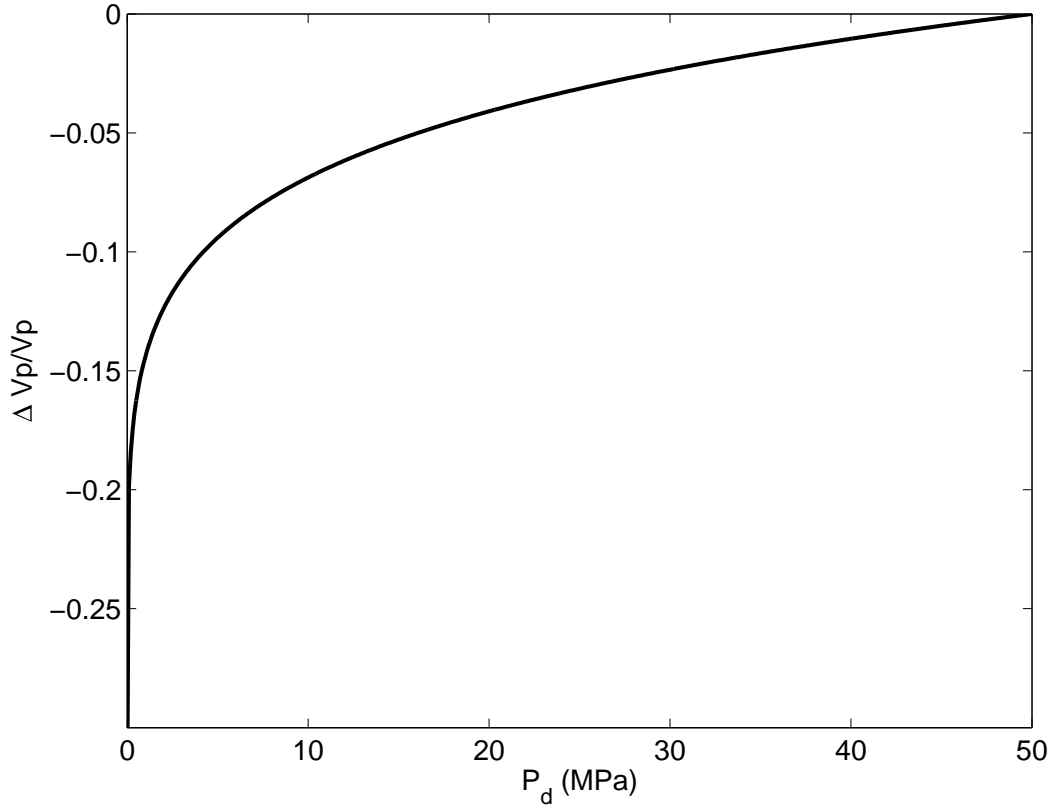


**Figure 10:** Relative change in P-wave velocity for entire reservoir

## 4 Seismic data analysis at Haltenbanken

In this section, we show the results of the seismic data analysis. A section of the 2D seismic line is shown in Figure 13, with the position of the Kristin and Lavrans Fields indicated. First, we apply conventional velocity analysis to estimate the interval velocities at Kristin and Lavrans. Next, we apply seismic amplitude analysis to the Top Garn interface in order to examine the reflectivities at the two fields. A comparison of the results to the rock physics model derived above gives estimates of the pore pressure.

### 4.1 Velocity analysis

Semblance velocity analysis based on the NMO equation assumes a flat-layered earth. Since the Lavrans Field is structurally complex, this does not necessarily give the true velocities. In order to correct for dipping structures, we performed velocity analysis after DMO and prestack migration on common offset gathers (see Yilmaz, 2001, page

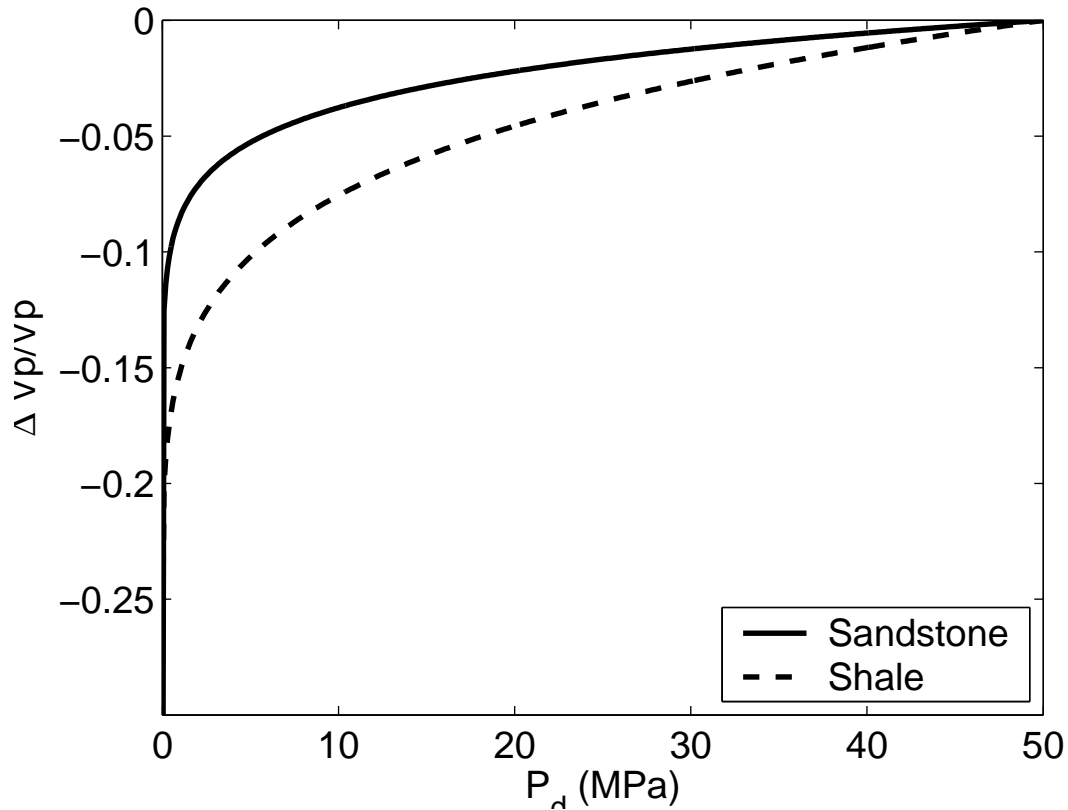


**Figure 11:** Relative change in P-wave velocity vs. effective pressure for sandstones (solid line) and shales (dotted line) at Haltenbanken.

88). A detailed velocity analysis was performed over the Lavrans and Kristin Fields. 50 prestack time migrated CMP locations were inspected for both Fields. Figure 14 shows an NMO-corrected CMP-gather from the Lavrans. The Top Garn reflector can be seen at approximately 3770 ms. The seismic data are relatively noisy at this depth, this may lead to ambiguities in the velocity analysis, if not addressed properly.

In order to reduce the uncertainty and to obtain a robust velocity field we defined a set of criterions for a valid velocity pick;

1. Each velocity pick must be on a semblance peak. Corresponding semblance peaks must be visible for at least 10 adjacent CMP's.
2. Each velocity pick must be made on a time corresponding to a seismic event in the stacked section.
3. The difference between the maximum and the minimum picked velocity for a given event should not exceed 400 m/s.

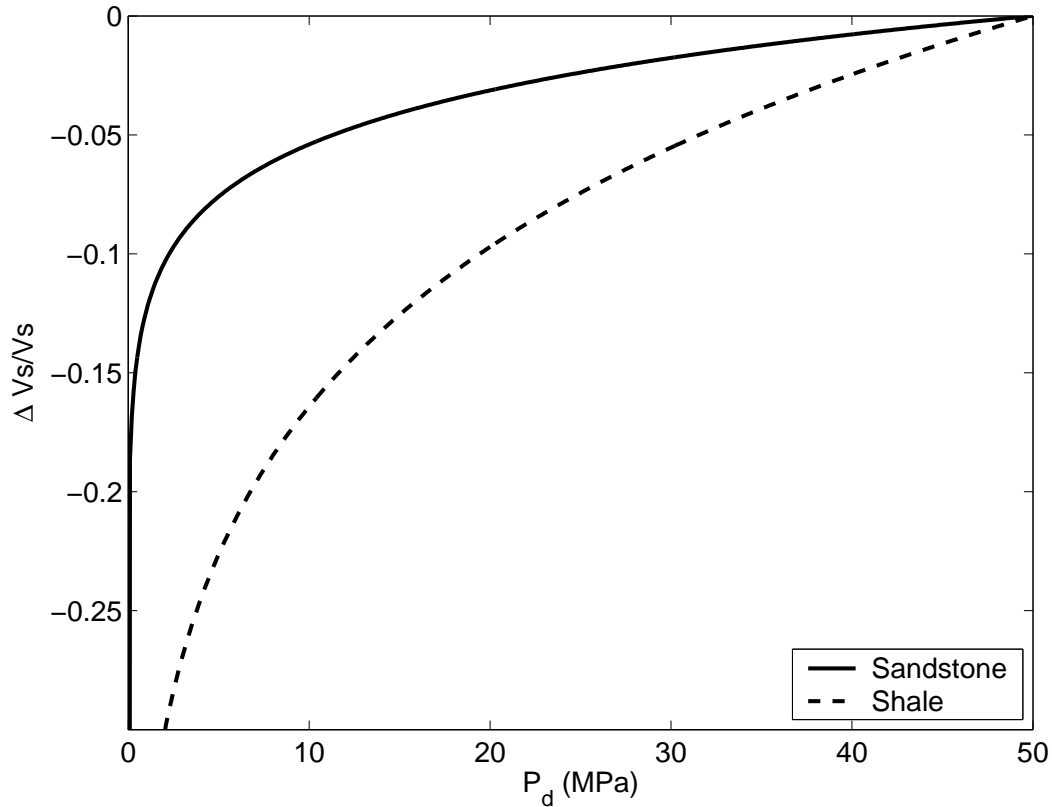


**Figure 12:** Relative change in S-wave velocity vs. effective pressure for sandstones (solid line) and shales (dotted line) at Haltenbanken.

Figure 15 shows a stacked seismic section along with the times for velocity picks at Lavrans. The upper event is approximately 400 ms above the reservoir, the middle event is close to the top reservoir event (within 100 ms), while the lower event is approximately 600 ms below the reservoir. A corresponding seismogram for the Kristin Field is shown in Figure 16. Figures 8a-8c show histograms of the velocity picks For Lavrans, while Figures 9a-9c show corresponding histograms for Kristin. Mean values and standard deviations for the velocity picks are given in Table 2.

**Table 2:** Mean velocities (stacking) from velocity analysis

Horizon no	$V_{st}$ Lavrans (m/s)	$V_{st}$ Kristin (m/s)
1	$2375 \pm 51$	$2333 \pm 39$
2	$2542 \pm 47$	$2498 \pm 28$
3	$2882 \pm 59$	$2716 \pm 50$

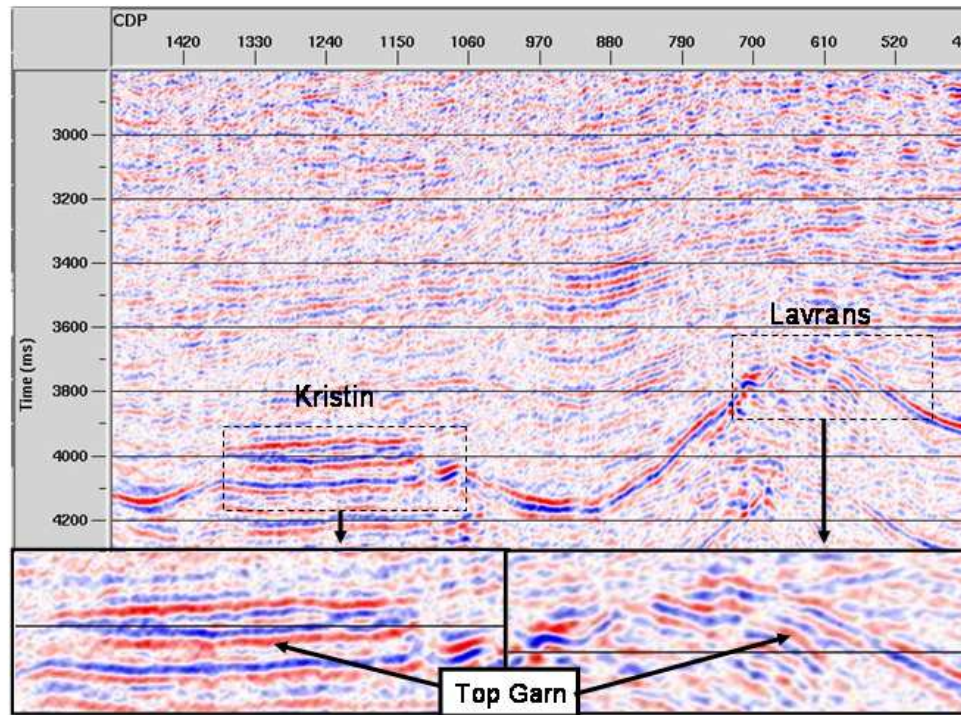


**Figure 13:** Migrated stack of the seismic line used in the study. The areas of interest are enlarged at the bottom of the figure. The location of the Top Garn reflector is indicated with arrows.

Using Dix' equation, we compute the interval velocity above the reservoir and within the reservoir for Lavrans and Kristin. The results are given in Table 3. From velocity analysis, we observe a mean interval velocity within the reservoir at Lavrans of 4392 m/s, however, the uncertainty is very high (415 m/s, standard deviation). The sonic log gives an interval velocity of 4219 m/s, which is within the uncertainty range derived from velocity analysis. At Kristin the average interval velocity within the reservoir is estimated to be 4188 ( $\pm 450$ ) m/s.

**Table 3:** Mean velocities (interval) from velocity analysis

Layer	$V_{st}$ Lavrans (m/s)	$V_{st}$ Kristin (m/s)
above reservoir	$3476 \pm 480$	$3427 \pm 332$
within reservoir	$4392 \pm 415$	$4188 \pm 450$

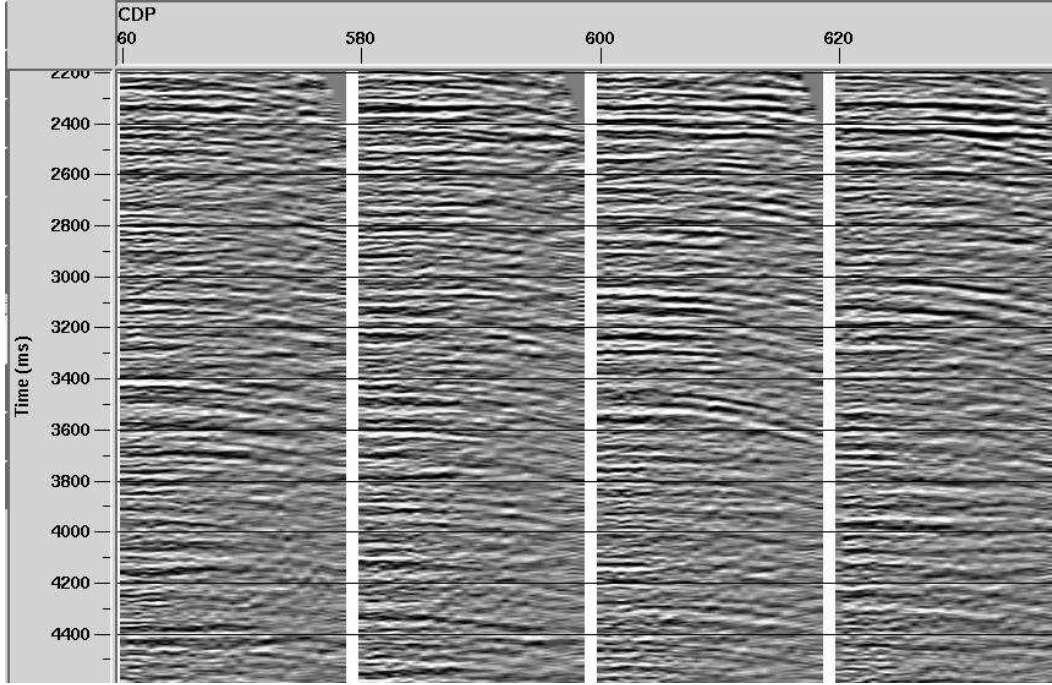


**Figure 14:** Prestack time migrated CMP gathers from the Lavrans Field. The Top Garn reflector is visible at approximately 3770 ms.

Because the level of uncertainty is very high in the derived interval velocities, we observe no significant difference in reservoir interval velocity between Lavrans and Kristin. However, sonic log data from well 6406/2-2 at Lavrans give an average reservoir interval velocity of 4219 m/s, which is only 173 m/s lower than the interval velocity derived from the seismic data. This increases the confidence in the estimated interval velocities.

If the observed difference in interval velocity between Lavrans and Kristin is real, we can estimate the pore pressure at Kristin. First, we correct for expected porosity differences due to difference in burial depth, as discussed before. The difference in burial reservoir depth between Lavrans and Kristin is approximately 300 m along the inspected seismic line, and the pore pressure at Lavrans is known to be normal. If the pore pressure at Kristin is normal, equation (8) gives the expected difference in porosity as

$$\Delta\phi = \phi_2 - \phi_1 = -0.027, \quad (20)$$

where  $\phi_2$  is the porosity in the reservoir sandstones at Kristin, and  $\phi_1$  is the porosity in the reservoir sandstones at Lavrans. However, if Kristin is highly overpressured, we must use equation (9) for the porosity here. This gives

$$\Delta\phi = \phi_2 - \phi_1 = 0.026. \quad (21)$$

The difference in velocity in reservoir sandstones due to porosity differences is computed from equation (5)

$$\Delta V = 121 \text{ m/s}, \quad (22)$$



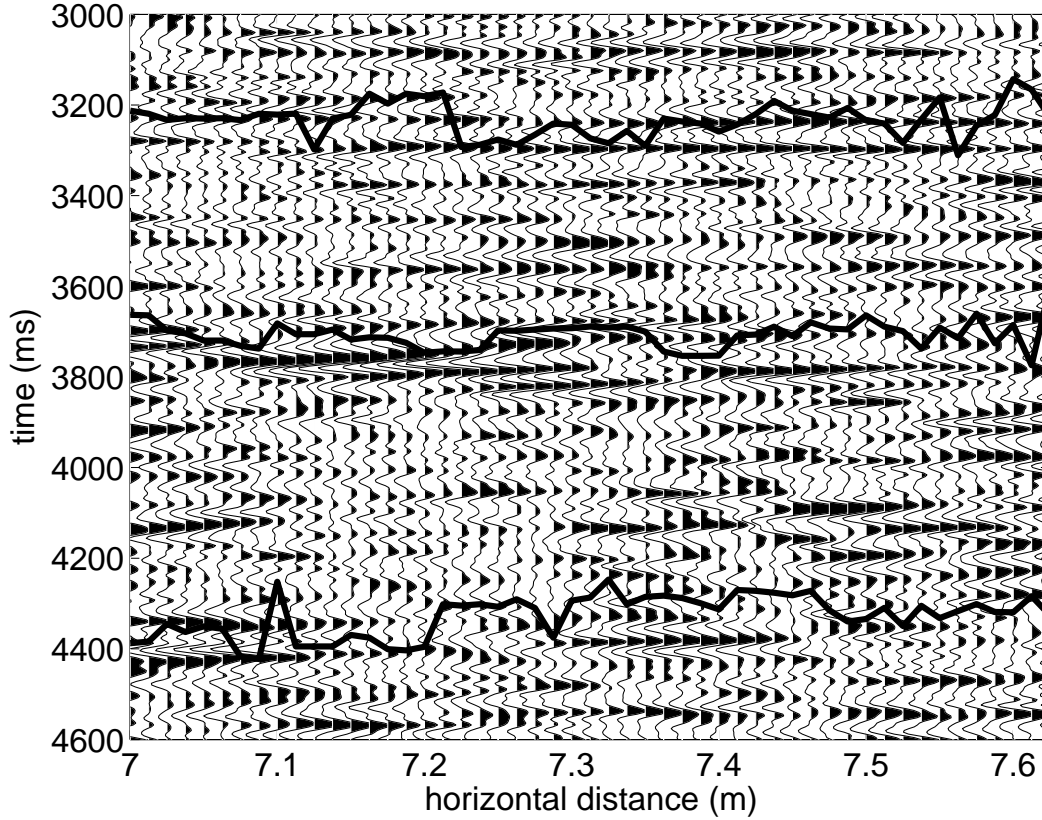


**Figure 15:** Zoomed in view of the stack at Lavrans. Top Garn is seen at approximately 3770 ms to the left, dipping upwards to about 3700 ms to the right. The black lines represents the times of velocity picking.

for the case where the pore pressure at Kristin is normal to moderate, and

$$\Delta V = -116 \text{ m/s}, \quad (23)$$

for the case where the pore pressure at Kristin is high.

The fractional volume of sandstones in the reservoir is estimated from the well logs to be about 0.4. Thus, we estimate the velocity difference due to porosity variations for the total reservoir volume to be

$$\Delta V = 0.4\Delta V_{\text{sst}} + 0.6\Delta V_{\text{shale}} = 48 \text{ m/s}, \quad (24)$$

if we use equation (22) (normal to moderate pressure), and

$$\Delta V = -46 \text{ m/s}, \quad (25)$$

if we use equation (23) (high pressure). Assuming that the pore pressure at Kristin is normal to moderate we use equation (24) to adjust the velocity at Lavrans for porosity

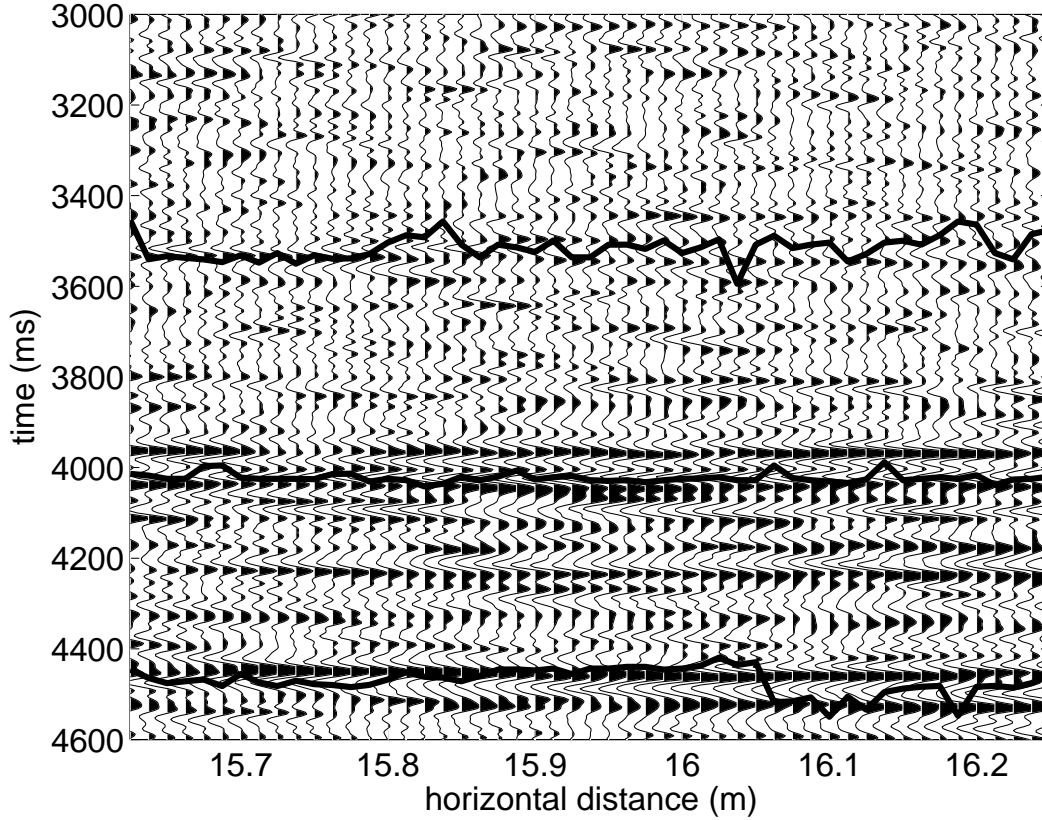


**Figure 16:** Zoomed in view of the stack at Kristin. Top Garn is seen at approximately 4050 ms. The black lines represents the times of velocity picking.

differences. This gives a velocity difference of  $4188 - (4392 + 48) \text{ m/s} = -252 \text{ m/s}$ , or  $\Delta V/V = -0.057$ . This gives an effective pressure at Kristin of approximately 14 MPa (Figure 10), corresponding to an overpressure of approximately 36 MPa. This is not consistent with the assumption of normal to moderate pore pressure at Kristin.

On the other hand, if we assume that the pore pressure at Kristin is high, we must use equation (25) to correct for porosity variations. In this case, we get a velocity difference of -158 m/s, giving a relative difference in velocity of  $\Delta V/V = 0.036$ . This gives an effective pressure of approximately 22 MPa, corresponding to an overpressure of 28 MPa, which is still in the high pressure range. Thus the velocity analysis indicate that Kristin is highly overpressured, with an estimated pore pressure of 28 MPa above hydrostatic pressure. However, the uncertainties are large.

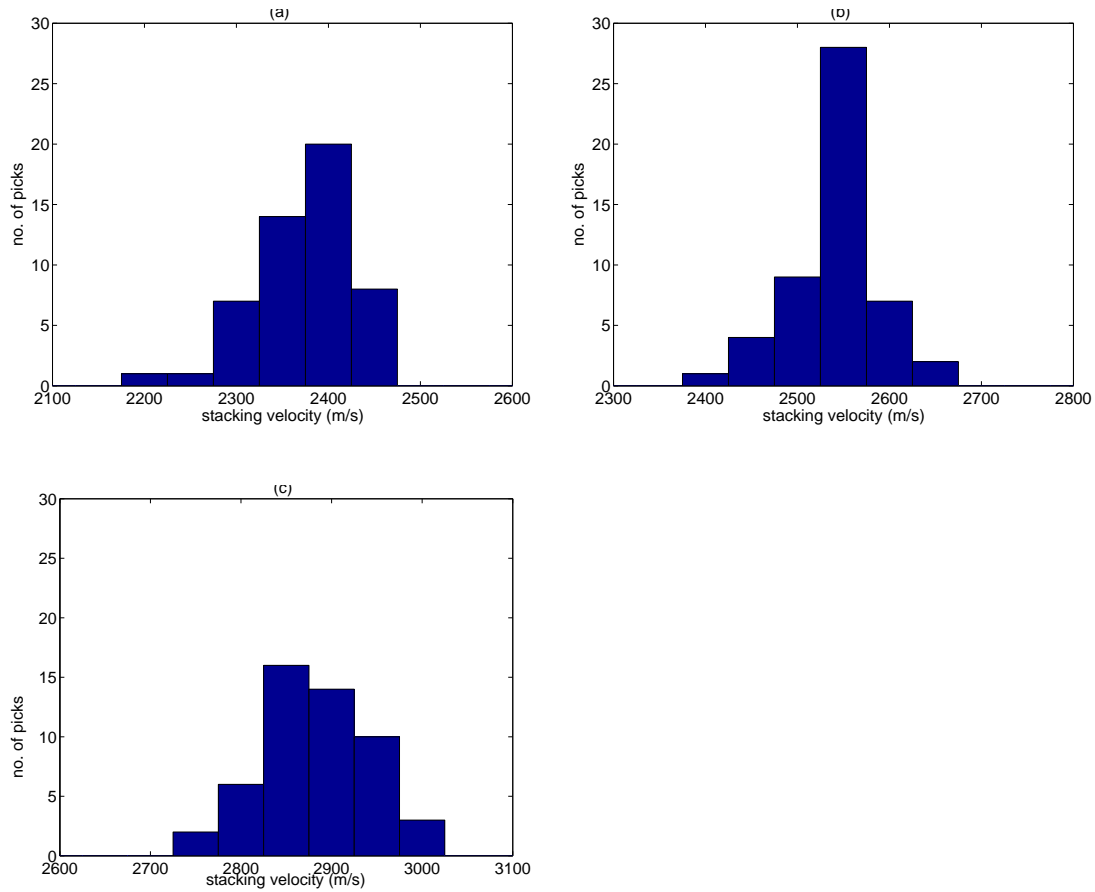


**Figure 17:** Histogram of the velocity picks at Lavrans, corresponding to the upper line in Figure 15

## 4.2 Amplitude analysis

### Theory

The top of the reservoir sandstones at Haltenbanken is marked by the Top Garn interface which is visible both on Kristin and Lavrans (see Figure 13). The sonic logs in Figure 3 show a significant jump in P-wave velocity at about 4250 m, associated with the Top Garn interface. The analysis in the previous sections indicate that the velocities of both the Melke Formation and the Garn Formation are sensitive to pore pressure. In order to see how the reflectivity of the Top Garn interface changes with pore pressure, we may perform some simple calculations based on standard AVO equations.

Assume a two-layer model where the P-wave velocity, S-wave velocity and density in the upper layer (shale) are given by  $\alpha_1$ ,  $\beta_1$ , and  $\rho_1$ , respectively. Similarly, we denote the

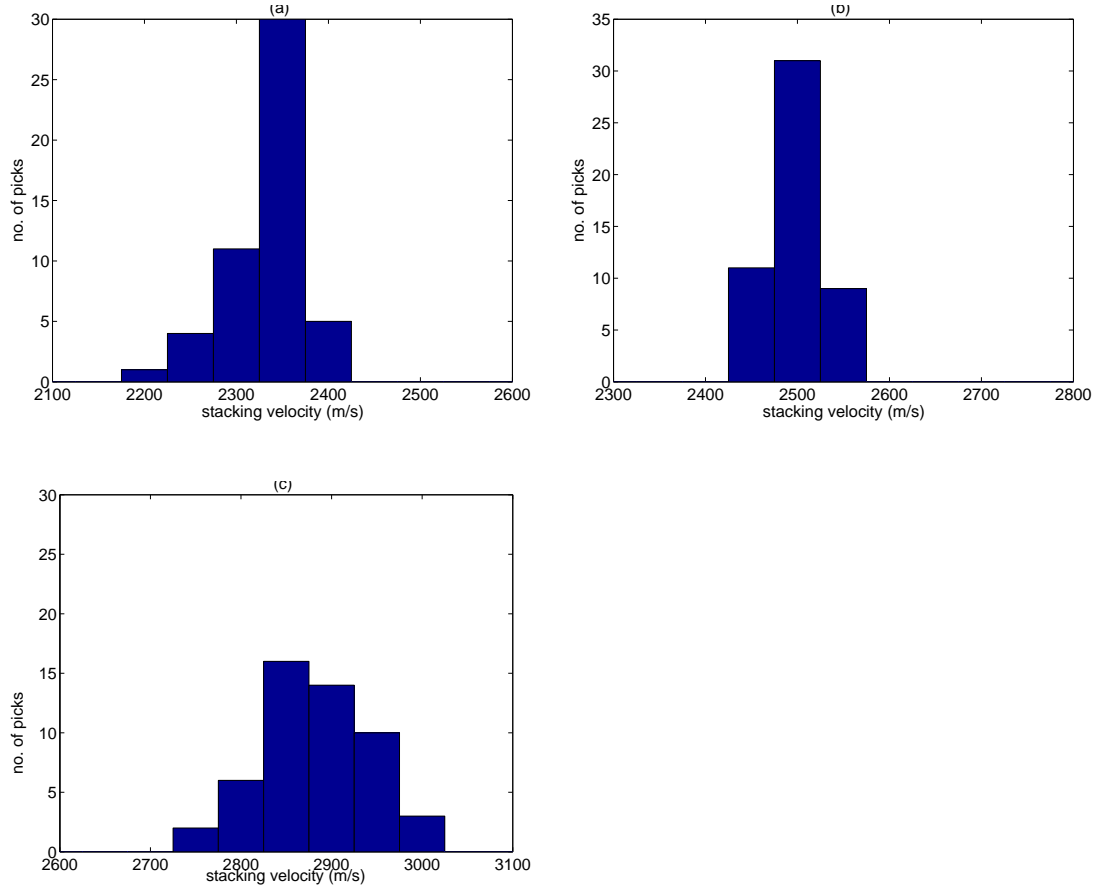


**Figure 18:** Histogram of the velocity picks at Lavrans, corresponding to the upper line in Figure 15

P-wave velocity, S-wave velocity and density for the lower layer (sandstone) by  $\alpha_2$ ,  $\beta_2$ , and  $\rho_2$ . The Smith and Gidlow approximation for PP-reflectivity is given as

$$R_{PP} = \frac{1}{2} \left( \frac{\Delta\alpha}{\alpha} + \frac{\Delta\rho}{\rho} \right) - 2 \frac{\beta^2}{\alpha^2} \left( \frac{\Delta\rho}{\rho} + 2 \frac{\Delta\beta}{\beta} \right) \sin^2 \theta + \frac{\Delta\alpha}{2\alpha} \tan^2 \theta, \quad (26)$$

where  $\Delta\alpha = \alpha_2 - \alpha_1$ ,  $\alpha = 1/2(\alpha_1 + \alpha_2)$ , and so on.  $\theta$  is the angle of incidence. Equation (26) can be written as

$$R_{PP} = R_0 + G \sin^2 \theta, \quad (27)$$

where

$$\begin{aligned} R_0 &= \frac{1}{2} \left( \frac{\Delta\alpha}{\alpha} + \frac{\Delta\rho}{\rho} \right) \\ G &= -2 \frac{\beta^2}{\alpha^2} \left( \frac{\Delta\rho}{\rho} + 2 \frac{\Delta\beta}{\beta} \right) + \frac{\Delta\alpha}{2\alpha} \frac{\tan^2 \theta}{\sin^2 \theta}. \end{aligned} \quad (28)$$

$R_0$  and  $G$  are commonly referred to as the AVO intercept and gradient, respectively.

Now assume that the velocities and density changes in both layers, such that  $\alpha_1 \rightarrow \alpha'_1 = \alpha_1 + \Delta\alpha_1$ ,  $\alpha_2 \rightarrow \alpha'_2 = \alpha_2 + \Delta\alpha_2$  etc. This is representative for a change in position along the interface from the Lavrans Field to the Kristin Field. The change in reflectivity as a result of velocity and density changes in both layer 1 and layer 2 can be written

$$\begin{aligned}\Delta R_0 &= \frac{1}{2} \left[ \left( \frac{\Delta\alpha'}{\alpha'} - \frac{\Delta\alpha}{\alpha} \right) + \left( \frac{\Delta\rho'}{\rho'} - \frac{\Delta\rho}{\rho} \right) \right] \\ \Delta G &= -2 \frac{\beta^2}{\alpha^2} \left[ \left( \frac{\Delta\rho'}{\rho'} - \frac{\Delta\rho}{\rho} \right) + 2 \left( \frac{\Delta\beta'}{\beta'} - \frac{\Delta\beta}{\beta} \right) \right] \\ &\quad + \frac{1}{2} \left( \frac{\Delta\alpha'}{\alpha'} - \frac{\Delta\alpha}{\alpha} \right) \frac{\tan^2 \theta}{\sin^2 \theta}.\end{aligned}\tag{29}$$

Here, we have assumed that  $\beta'^2/\alpha'^2 \approx \beta^2/\alpha^2$ .

From equation (29) we may make some observations of the qualitative behaviour of  $R_0$  and  $G$ . For instance, it is clear that if the P-wave contrast at Kristin ( $\Delta\alpha'/\alpha'$ ) is larger than the P-wave contrast at Lavrans ( $\Delta\alpha/\alpha$ ), this will give a positive contribution to  $\Delta R_0$ . Our calculations above indicate that this is the case, since the P-wave velocity for shales seems to be more sensitive to pore pressure than the P-wave velocity for sandstones (Figure 11). However, an increase in P-wave velocity contrast may be countered by a decrease in density contrast.

In order to see how  $\Delta R_0$  changes with pore pressure, we insert numbers for the Melke and Garn Formations into equation (29). Table 4 shows estimated P-wave velocities and densities from well 6406/2-1 at Lavrans. The velocities in the Garn Formation and

**Table 4:** Estimated p-wave velocities and densities for the Melke and Garn Formations from well 6406/2-1

Formations	$V_p$ (m/s)	Density (kg/m <sup>3</sup> )
Melke	3391	2567
Garn	4726	2473

Melke Formation at Kristin for different pressures are calculated using the relationship shown in Figure 11. Note, however, that in order to get a consistent estimate for the velocity at Kristin, we need to make a porosity correction, according to equation (5) for the Garn Formation. The porosity difference is calculated using equations (8) for normal to moderate pressure at Kristin and (9) for high pressure, with  $\Delta d = 300$  m.

In a similar manner, we calculate the density in the Garn Formation at Kristin. In the case of normal to moderate pore pressure at Kristin we use equation (8), and estimate

the density to be  $2518 \text{ kg/m}^3$ . In the case of high pressure at Kristin we use equation (9) and estimate the density to be  $2427 \text{ kg/m}^3$ . We have assumed water as the pore fluid ( $\rho_w=1000 \text{ kg/m}^3$ ) and quartz as the solid material ( $\rho_s=2650 \text{ kg/m}^3$ ).

In the case of normal to moderate pore pressure at Kristin, we get the curve shown in Figure 4.2a for the relationship between  $\Delta R_0$  and differential pressure at Kristin. the corresponding relationship for high pore pressure is shown in Figure 4.2b. Note that in both cases  $\Delta R_0$  increase as the pressure at Kristin increases.

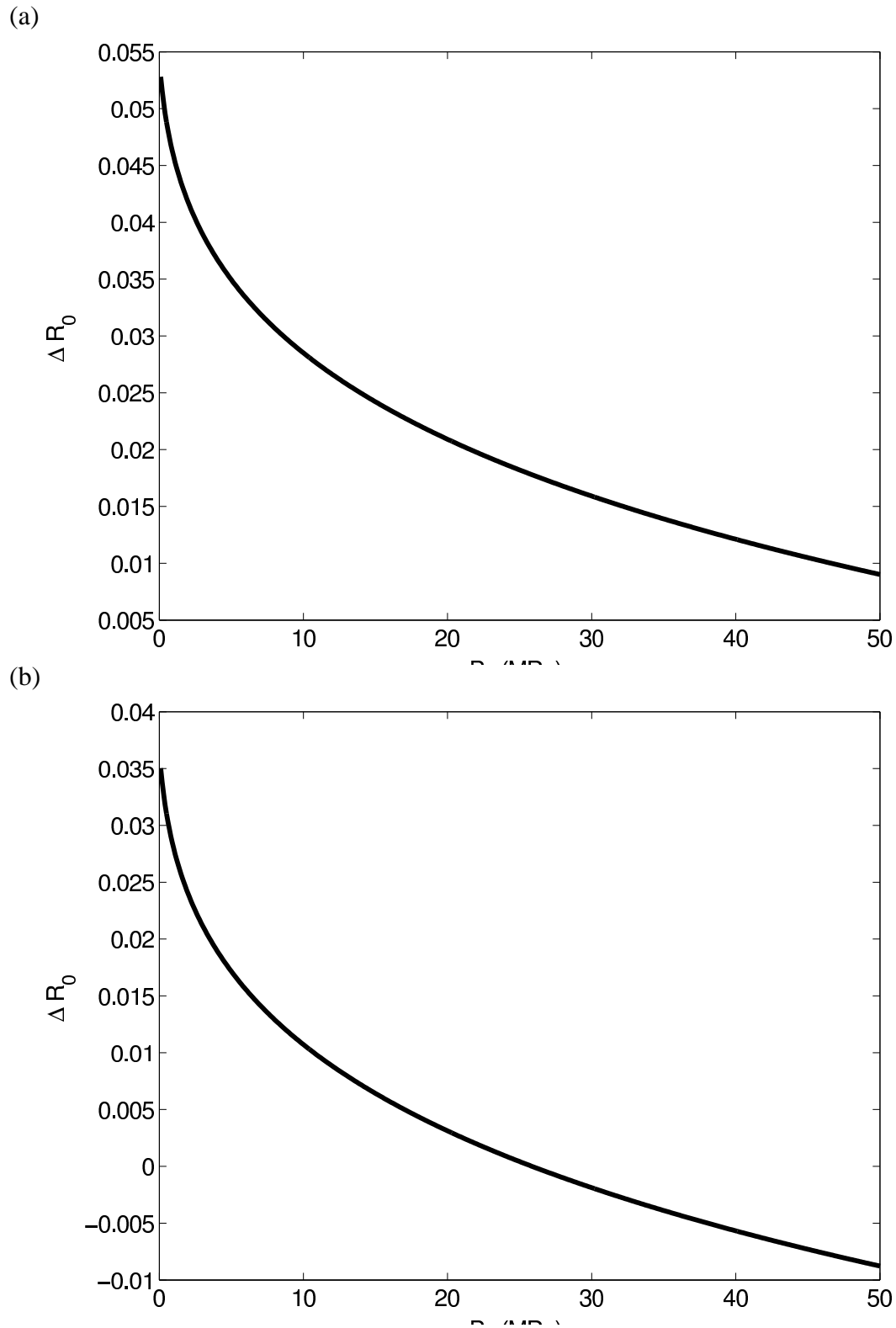
Since we do not have any estimates of the S-wave velocity, we can not perform a similar analysis for  $\Delta G$ . However, Figure 12 indicate that the S-wave velocity in shales is much more sensitive to changes in pore pressure than the S-wave velocity in sandstones. Hence, if Kristin is highly overpressured, we may expect that the S-wave velocity contrast at the Top Garn interface is larger here than at Lavrans. From equation (29) this gives a negative contribution to  $\Delta G$ . In the calculations above the difference in density between Kristin and Lavrans was found to be small. It is therefore likely that the S-wave velocity term in equation (29) will dominate, and that  $\Delta G < 0$  for high pore pressures at Kristin.

## Data analysis

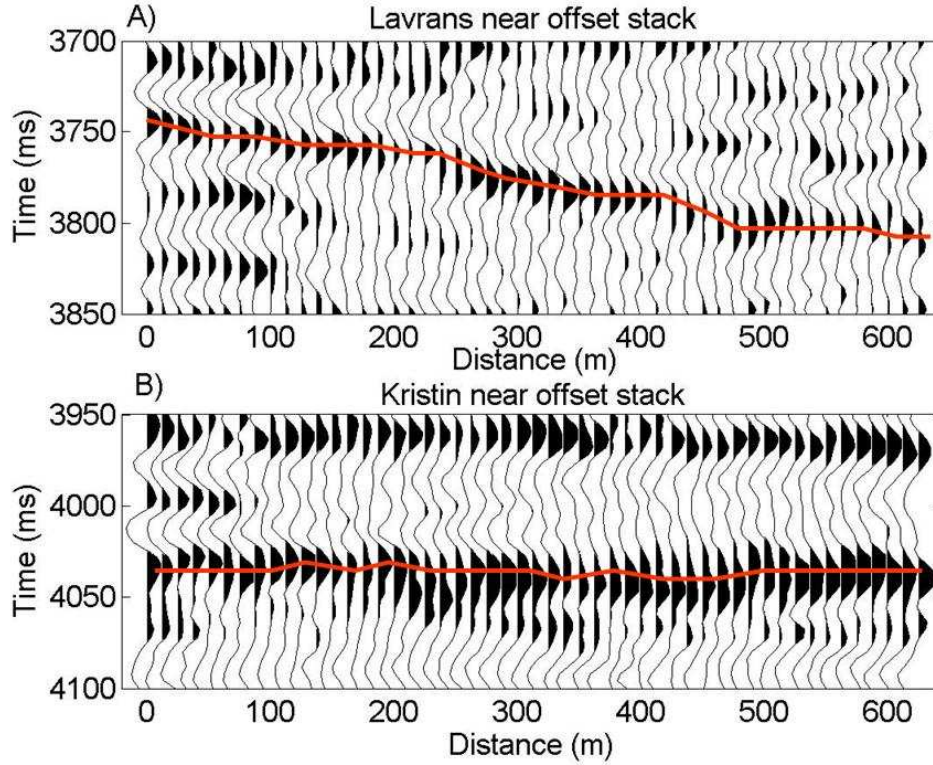
Amplitude analysis was performed for the same CMP range that was subject to the velocity analysis. The top Garn reflector is indicated with arrows in Figure 13. We computed partial stacks for three different angle ranges,  $0^\circ - 10^\circ$ ,  $10^\circ - 20^\circ$ , and  $20^\circ - 30^\circ$ . The peak amplitude for the Top Garn reflector was extracted for each of the partial stacks. Figures 20a and 20b shows the near offset stacks from Lavrans and Kristin. Note that the signal from the Top Garn reflector is stronger At Kristin. Figure 21 show the mean amplitudes at Lavrans and Kristin, scaled by a constant factor which was chosen such that the near-offset amplitudes from Lavrans fitted the modeled reflection coefficient (solid line). The averaged and scaled mid-offset amplitudes at Lavrans are significantly weaker than the modeled reflection coefficient. At Kristin, however, the mid-offset amplitude is stronger than the near-offset amplitude.

Figure 22 show five adjacent NMO-corrected prestack migrated gathers from the Lavrans Field (left) and the Kristin Field (right). The Top Garn reflector is indicated on the Figure. Figure 23 show scaled reflection amplitude versus offset for these CMP's. Despite a high degree of fluctuations in the data, there is a notable trend that the amplitude at far offsets is higher at Kristin (triangles) than at Lavrans (circles). At near offsets there is no apparent difference.

Because of problems with scaling of the far-offset data, we chose to use only the near-offset range for estimation of pressure differences. Using the scaled near-offset am-



**Figure 19:** Plots of  $\Delta R_0$  vs. differential pressure for different pressure regimes at Kristin. (a): normal to moderate pore pressure. (b): high pore pressure.



**Figure 20:** Near offset stacks from Lavrans and Kristin.

plitudes in figure 21, we estimate that the difference in zero-offset reflectivity between Lavrans and Kristin,  $\Delta R_0$  is approximately  $0.05 \pm 0.03$  for the Top Garn interface. This is an indication of overpressure at Kristin which was found to give  $\Delta R_0 > 0$ . However, it is not immediately clear which of the Figures 4.2 that is relevant for the situation at Kristin. For instance, in Figure 4.2a a value of  $\Delta R_0 = 0.5$  gives a differential pressure at Kristin of about 0 MPa, corresponding to an overpressure of about 50 MPa. However, this figure was computed with the assumption that the pore pressure at Kristin is normal to moderate ( $\lesssim 20$  MPa). This is clearly a contradiction. In Figure 4.2b, the highest value of  $\Delta R_0$  is about 0.035. This is within the uncertainty range that were estimated for  $\Delta R_0$ . Thus, the estimated value for  $\Delta R_0$  indicate that the reservoir rocks at Kristin are highly overpressured.

The data analysis indicate a value of  $\Delta G$  which is greater than zero. However, the theoretical considerations above indicate that for high pore pressures at Kristin,  $\partial \Delta G < 0$ . This may be due to poor data quality. The Lavrans Field is structurally complex, meaning that true amplitude processing may be difficult. If the observations are correct, there may be an error in the model, or it may be an indication of an effect that we did not compensate for, e.g., differences in clay content.



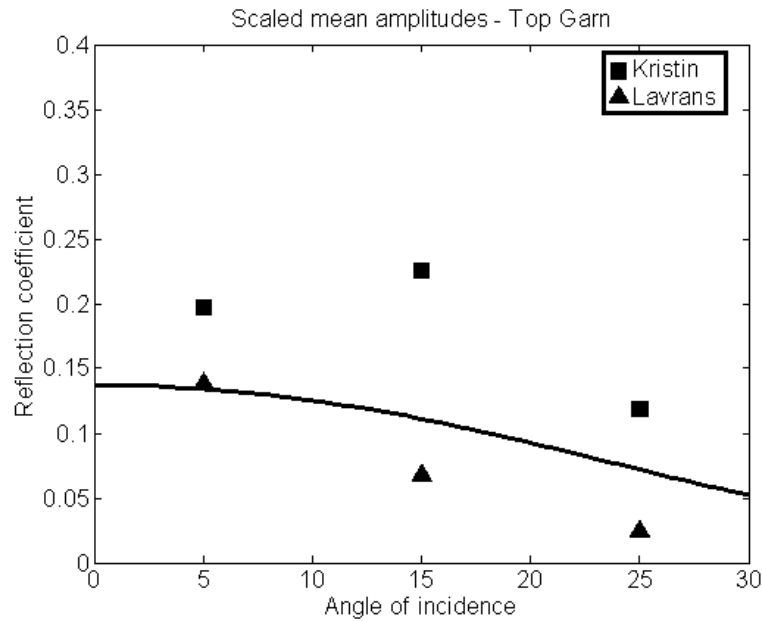


**Figure 21:** Scaled amplitudes from near- mid- and far-offset stacks from Lavrans (triangles) and Kristin (squares). The solid line represents the PP-reflectivity at Lavrans computed from Zoeppritz' equations.

## 5 Discussion

The derived relationships for velocity versus differential pressure are based on log data from three wells. These wells are not necessarily representative for the reservoir rocks at Haltenbanken. However, there is good correlation between well logs from different locations, as seen in Figure 3. This increases the confidence in the representativeness of the log data. Still, there are variations in the velocity-pressure relationships obtained from different wells (Table 1). A larger number of wells is probably needed to get a reliable well calibration for the pressure-velocity relationship. In addition, the argument for using a functional form inspired by grain contact theory is questionable. While the Herz-Mindlin theory has a clear physical basis, this is not the case when we substitute the exponential value of  $1/6$  with an arbitrary exponent  $\kappa$ .

While the methodology described here attempts to compensate for lateral variations in porosity, we have not addressed variations in clay content. The assumption of laterally constant clay content means that (5)-(6) can be ignored. However, it is unlikely that this

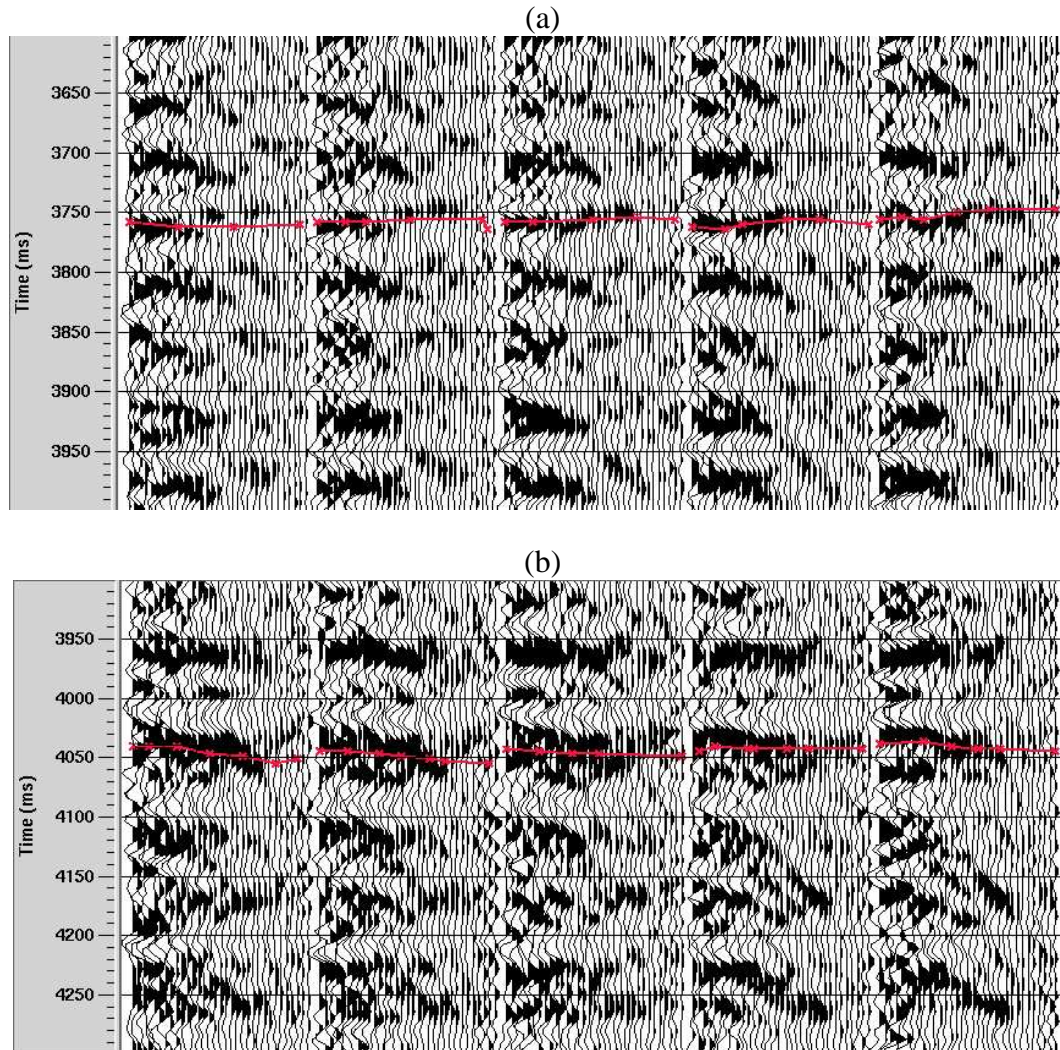


**Figure 22:** Prestack Gathers from Lavrans (a) and Kristin (b). The top Garn interface is marked.

is the case. It is therefore important to have an understanding of the sensitivity of seismic velocities to clay content. For sandstones, (Han et al., 1986) estimated that an increase in the fractional volume of clay of 0.1 gives a decrease in p-wave velocity of approximately 200 m/s. Velocities are also known to vary with clay content in shales (Vernik, 1997). Thus, lateral variations in clay content may have significant impact on velocities.

In the analysis, we have assumed that the fluid content at the two locations is the same. As for the clay content this assumption is not necessarily true. Since the velocity of a rock is influenced by the fluid content, this means that we may have made a mistake here. However, the importance of fluid content is closely related to the porosity of the rock. Since the porosity in the reservoir section is relatively low ( $< 15\%$ ), the error we make by ignoring fluid content is probably not too severe.

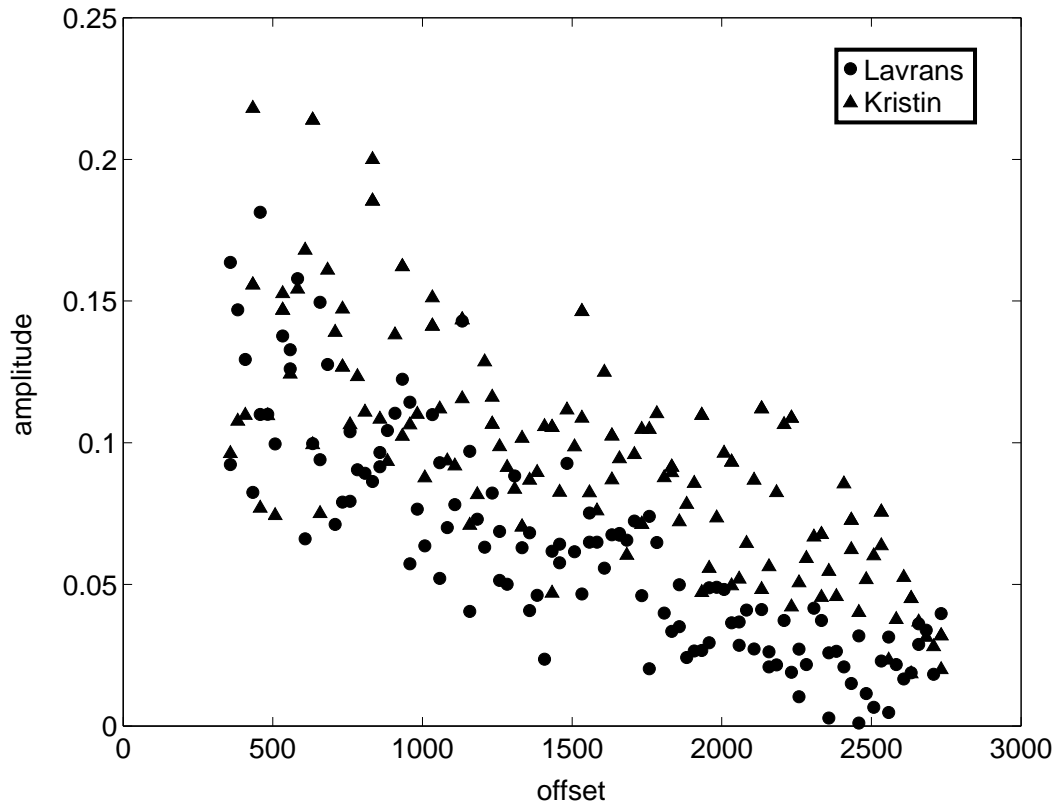


**Figure 23:** Extracted peak amplitudes from top Garn interface.

The reservoir sandstones at Haltenbanken are at a burial depth of more than 4 km. At this depth, the quality of the seismic data is relatively poor. As a result, there are significant uncertainties in the results. Poor resolution in the seismic forced us to pick velocities at different time intervals at Lavrans and Kristin. Furthermore, the results from the velocity analysis show no significant difference in interval velocity between Kristin and Lavrans. The uncertainty in the interval velocity is of the order of 450 m/s (standard deviations), which is larger than the expected velocity difference due to overpressure at Kristin. Thus, the calculated overpressure at Kristin (28 MPa), which is based on average velocities, is uncertain. Sonic log data increase the confidence in the average values, but still the uncertainties are large.

There are also large uncertainties in the amplitude analysis. The far offset response is not in agreement with overpressure at Kristin, according to our model. This may be indicative of some effect that we did not compensate for. However, it may very well be due to poor seismic data quality, especially at Lavrans, which is structurally complex.

## **6 Conclusions**

We have presented a rock physics model that can be used to predict pore pressure differences across faults. The model incorporates compensation for porosity variations with depth, using regional porosity-depth trends.

Conventional seismic velocity analysis was applied to a 2D seismic line covering the Lavrans and Kristin Fields. The interval velocity was found to be 204 m/s lower at Kristin than at Lavrans. This is in agreement with an overpressure of 28 MPa at Kristin.

Seismic amplitude analysis at the Top Garn interface indicate that the P-wave velocity contrast is larger at the Kristin Field than at the Lavrans Field. This result is confirmed by sonic logs, and is an indication of high pore at Kristin. However, we could only make qualitative inferments about the pore pressure from amplitude analysis. The seismic data quality was not good enough to get a reliable estimate for the pore pressure.

## **Acknowledgments**

Statoil ASA and their license partners are acknowledged for permission to use and present the data. We thank Eirik Vik, Gunn Mari Grimsmo Teige and Sigurd Hansen at Statoil for discussions and for providing useful information about the Haltenbanken Field.



# Chapter 5

## Pore pressure estimation - what can we learn from 4D?

Martin Landrø and Øyvind Kvam

*Department of petroleum engineering and applied geophysics  
Norwegian University of Science and Technology  
N-7491 Trondheim, Norway*

**ABSTRACT:** Most methods for pressure prediction from seismic are based on detection of low velocity anomalies. The significant growth of time-lapse seismic surveys gives us a possibility to check the robustness and limitations of these classical prediction methods, and might also lead to new methods for pressure prediction that can be used in exploration. Using a simple geo-mechanical model (Hertz-Mindlin) it is shown that the AVO-response of a pressure anomaly is opposite of for instance a fluid anomaly. It is suggested that these simple AVO-observations could be combined with more conventional methods, in order to reduce the uncertainty in pressure prediction from seismic. Main limitations are the validity of the geo-mechanical model, the assumption of constant lithology between the normal and anomalous segments and the validity of the Gassmann model. A 4D-example from a 30% porosity sandstone reservoir shows that a 5-7 MPa pore pressure increase leads to an amplitude change at the top reservoir interface that is explained by approximately 20% decrease in P-wave velocity.

The observed pull-down effect (time lapse travel-time shift) measured over the whole reservoir thickness is of the order of only 4-6 ms, indicating a gradual change in velocity below the top reservoir event, decreasing with depth. Time-lapse velocity analysis is not precise enough to pick up this gradual velocity change between the two surveys. 4D data from segments undergoing a pore pressure decrease of 2-4 MPa does not show amplitude or travel-time shifts above the background noise level. Thus one might say that

4D observations indicate that over-pressured rocks should be easier to detect by seismic methods than rocks with anomalous low pore pressure.

## 1 Introduction

Interpretation of time-lapse seismic data depends on knowledge of the relation between the seismic parameters and typical reservoir parameters we want to map, as for instance pore pressure changes and fluid saturation changes. The established link for bridging the gap between the two types of parameters is rock physics. For saturation effects, the Gassmann equations form a reasonable working platform, enabling us to make quantitative estimates for how much each of the seismic parameters changes with for instance water saturation. However, for pore pressure changes, we claim that the corresponding platform is weaker: we have to rely on ultrasonic core measurements in order to establish a link between pore pressure changes and corresponding changes in seismic parameters. One major weakness of the core measurements is that the core sample is damaged during the coring process (Nes et al., 2000). Artificial cracks are probably formed during the anisotropic stress unloading process. Even if the core sample is reloaded to simulate in situ stress conditions for the ultrasonic core measurements, it is not very likely to assume that the original crack state of the sample is re-established again. Furthermore, we have to deal with the upscaling problem for our core measurements: Is the ultrasonic measurements made at the small core sample representative at seismic scale?

## 2 The Hertz-Mindlin model: an attempt to relate velocity to pressure

Various contact models have been proposed to estimate effective moduli of a rock. Some of these models are presented by Mavko et al. (1998) in their rock physics handbook. The Hertz-Mindlin model (Mindlin and Deresiewicz, 1953) can be used to describe the properties of precompacted granular rocks. The effective bulk modulus of a dry random identical sphere packing is given by

$$K_{\text{eff}} = \sqrt[3]{\frac{C^2(1-\phi)\mu^2}{18\pi^2(1-\nu)^2}P} \quad (1)$$

and the effective shear modulus is given by

$$\mu_{\text{eff}} = \frac{5-4\nu}{5(2-\nu)} \sqrt[3]{\frac{3C^2(1-\phi)\mu^2}{2\pi^2(1-\nu)^2}P} \quad (2)$$

where  $\nu$  and  $\mu$  are the Poisson's ratio and shear modulus of the solid grains, respectively,  $\phi$  is the porosity,  $C$  is the average number of contacts per grain and  $P$  is the effective or net pressure.

The relation between net stress and reservoir pore pressure can be defined as (see for instance Christensen and Wang, 1985):

$$P = P_{\text{ext}} - \eta P_{\text{pore}} \quad (3)$$

where  $P$  is effective pressure,  $P_{\text{ext}}$  is external pressure,  $P_{\text{pore}}$  is pore pressure, and  $\eta$  is the coefficient of internal deformation, a usually unknown parameter, often assumed to be close to one. However, if  $\eta$  differs from one, this will lead to stretching of the velocity versus pressure curves, and hence a corresponding increase in the uncertainty associated with the estimated pressure and saturation changes. The fact that we actually do not know the internal deformation coefficient  $\eta$ , is a limiting factor for quantitative use of rock physics measurements for pore pressure estimation. In a rock physics experiment, we measure the net or effective pressure ( $P$ ), while in a reservoir, we measure the pore pressure ( $P_{\text{pore}}$ ).

The P ( $V_p$ ) and S ( $V_s$ ) wave velocities are now given as

$$V_p = \sqrt{\frac{K_{\text{eff}} + \frac{4}{3}\mu_{\text{eff}}}{\rho}}, \quad (4)$$

$$V_s = \sqrt{\frac{\mu_{\text{eff}}}{\rho}}. \quad (5)$$

The density is

$$\rho = \phi \rho_f + (1 - \phi) \rho_{\text{ma}}, \quad (6)$$

where  $\rho$  and  $\rho_{\text{ma}}$  are the fluid and matrix densities, respectively. If we assume that the density of the quartz sand is not changing much during pressure changes, we see from equations (1)-(6) that the relative change in P-wave velocity versus net pressure change is given as

$$\frac{\Delta V_p}{V_p} = \left( \frac{P}{P_0} \right)^{\frac{1}{6}} - 1, \quad (7)$$

where  $P_0$  denotes the effective pressure at the initial pressure conditions. Similarly we obtain for the relative S-wave velocity change

$$\frac{\Delta V_s}{V_s} = \left( \frac{P}{P_0} \right)^{\frac{1}{6}} - 1, \quad (8)$$

which means that according to the Hertz-Mindlin model the relative change in P and S-wave velocity should be equal. Ultrasonic core measurements done at core samples from some of the North Sea sand reservoirs indeed show that the relative changes in P-



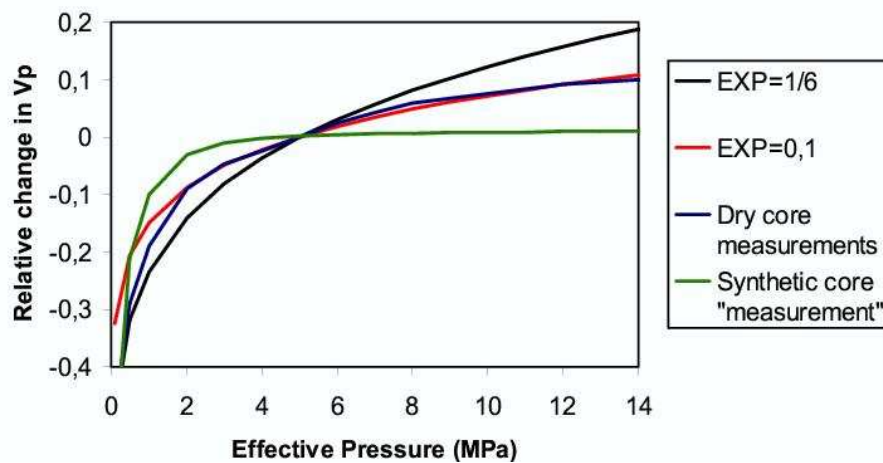


**Figure 1:** Schematic figure showing relative change in P-wave velocity as a function of net pressure for the Hertz-Mindlin model ( $\text{exp}=1/6$ ), modified Hertz-Mindlin model ( $\text{exp}=1/6$ ), dry core measurements and synthetic core measurement. Here we have assumed that the initial net pressure is 5 MPa. The synthetic core measurement curve does not represent real measurements, but has been drawn on the basis of the published work by Nes et. al., 2000.

and S-wave velocities are fairly similar. However, comparison with dry core measurements often show that the exponent in equations (7) and (8) should be chosen closer to  $1/10$  rather than  $1/6$ . Recent experiments done by Nes et al performed on artificial sandstone indicate that this exponent is less than  $1/10$ . Figure 1 is an attempt to illustrate the uncertainty in determining velocity versus pressure curves. In this figure the results of Nes et al is sketched on the basis of their publication, and does not represent the real measurements.

The key message from this section is that there are large uncertainties associated with the establishment of the velocity versus pressure curves. These uncertainties are multi-causal: up-scaling issues related to ultrasonic core measurements (are the rock physics measurements representative at seismic frequencies?), the coring process itself (as discussed by Nes et al), the unknown internal deformation coefficient (equation (3)), variability in core sample quality and so on. Therefore, alternative ways of estimating the velocity versus pressure curve is highly desirable, and in the present paper I will show some attempts to use the reservoir itself as a laboratory for obtaining such additional information.

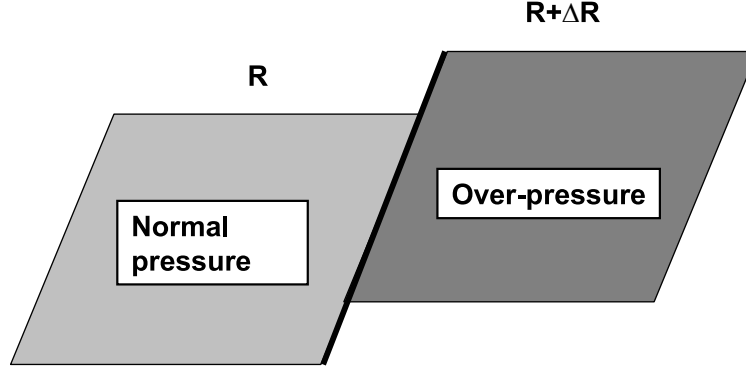


**Figure 2:** Schematic illustration of two segments separated by a fault acting as a pressure barrier between normal and over-pressured rocks. Assuming that the thickness and lithology is the same for the two segments, the change in reflectivity ( $\Delta R$ ) is assumed to be caused by the pressure difference.

### 3 Simple equations for overpressure detection based on Hertz-Mindlin theory

In the previous section it was shown that the relative changes in P and S wave velocities were the same for pressure changes. This observation can be used to derive simple equations relating the change in reflectivity due to changes in pore pressure. Figure 2 illustrates a situation of a fault acting as a pressure barrier between two segments. A simplified expression for the PP reflection coefficient versus incidence angle can be written (Smith and Gidlow, 1987):

$$R_{PP}(\theta) = \left( \frac{\Delta V_p}{V_p} + \frac{\Delta \rho}{\rho} \right) - 2 \frac{V_s^2}{V_p^2} \left( \frac{\Delta \rho}{\rho} + 2 \frac{\Delta V_s}{V_s} \right) \sin^2 \theta + \frac{\Delta V_p}{2V_p} \tan^2 \theta, \quad (9)$$

where  $\rho$  is the density and  $\theta$  is the incidence angle, and  $\Delta V_p$  etc represents the change in P-wave velocity across the interface. For crystalline rocks, it is often assumed that the porosity and hence, the density changes caused by pressure changes are small, and thus we will assume zero changes in density across the sealing fault. The change in reflectivity across the fault barrier (Figure 2) is therefore given as

$$\Delta R_{PP}^P(\theta) = \frac{1}{2} \frac{\Delta V_p^P}{V_p} - 4 \frac{V_s^2}{V_p^2} \frac{\Delta V_s^P}{V_s} \sin^2 \theta + \frac{\Delta V_p^P}{2V_p} \sin^2 \theta, \quad (10)$$

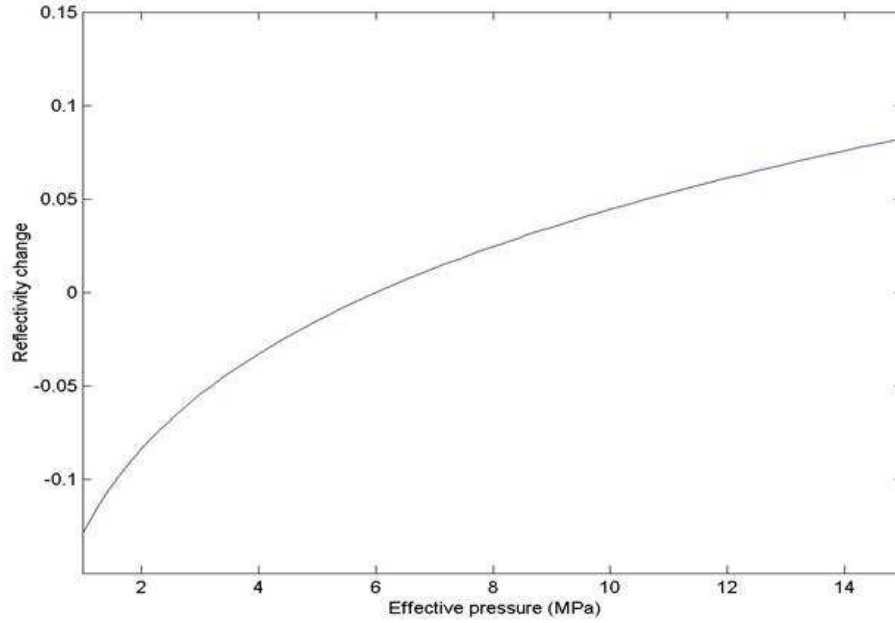


**Figure 3:** Change in zero offset reflectivity versus effective pressure using the Hertz-Mindlin model. The initial (or reference) effective pressure has been set to 6 MPa in the current example. Notice that a pore pressure increase correspond to a decrease in the effective pressure.

where  $\Delta V_p^P$  and  $\Delta V_s^P$  denote change in P-wave and S-wave velocity caused by pressure changes, respectively. Using equations (7) and (8), assuming an average  $V_p$  to  $V_s$  ratio of 2 (for shallow depths this ratio can be significantly higher), and further assume that  $\sin^2 \theta \sim \tan^2 \theta$  we obtain

$$\Delta R_{PP}^P(\theta) = \frac{1}{2} \frac{\Delta V_p^P}{V_p} \cos^2 \theta. \quad (11)$$

Finally, by inserting equation (7), a direct relation between reflectivity change and effective pressure is obtained:

$$\Delta R_{PP}^P(\theta) = \frac{1}{2} \left[ \left( \frac{P}{P_0} \right)^{\frac{1}{6}} - 1 \right] \cos^2 \theta. \quad (12)$$

This means that the change in reflectivity between the normal pressured segment and the over-pressured segment has a weak AVO-behavior (slight changes with offset), given that the  $V_p$  to  $V_s$  ratio is around 2. In addition to conventional velocity estimation for over-pressure prediction, the simple formula given above can be used in a semi-quantitative way to identify potential abnormal pressure segments. Notice that for a pore pressure increase, the effective pressure,  $P$ , is decreasing, resulting in a negative change in reflectivity (equation (12)), as illustrated in Figure 3.

## 4 Fluid effects

In an exploration setting, one major challenge is to distinguish between pressure and lithology changes between the two segments shown in Figure 2. However, if we assume that the lithology is the same for the two segments, and assume that the segment to the left is water-filled and the segment to the right contains hydrocarbons, the change in reflectivity can be written as (see Landrø, 2001):

$$\Delta R_{PP}^F(\theta) = \frac{1}{2} \left( \frac{\Delta V_p^F}{V_p} + \frac{\Delta \rho}{\rho} \right) + \frac{\Delta V_p^F}{2V_p} \tan^2 \theta. \quad (13)$$

For many sand reservoir rocks, the density change is less than the velocity change, so a (very rough) approximation for the reflectivity change caused by fluid change is

$$\Delta R_{PP}^F(\theta) = \frac{1}{2} \frac{\Delta V_p^F}{V_p} \frac{1}{\cos^2 \theta}. \quad (14)$$

This means that a fluid effect and a pressure effect has opposite AVO-effects, a light increase for fluid changes, and a slight decrease for pressure changes, as shown in Figure 4. In Figure 4, the zero offset reflection coefficients have been chosen to be equal (or normalized to each other). The main limitation of this method is of course that we assume that the seismic parameters do not change significantly between the two segments sketched in Figure 2. A real data example, taken from a 4D case study is shown in Figure 5, where we can observe a slight amplitude decrease with offset after a pressure increase within the Cook Formation. Furthermore, we observe a slight amplitude increase (best visible on the near and mid offset stack, not so convincing from mid to far) with offset for the fluid marker at the 1985 data. In an exploration case, the uncertainty associated with a similar interpretation technique based on Figure 4 is much higher.

## 5 PS-converted data

A simplified version of the PS reflection coefficient is given as (Aki and P, 1980)

$$R_{PS}(\theta) = \frac{1}{2} \sin \theta \left[ \left(1 + 2 \frac{V_s}{V_p}\right) \frac{\Delta \rho}{\rho} + 4 \frac{V_s}{V_p} \Delta V_s V_s \right] \quad (15)$$

Following the same procedure as in the previous sections we find that for a pressure change, the corresponding PS reflectivity changes by (assuming a VP to VS ratio of 2)

$$\Delta R_{PS}^P(\theta) = \frac{\Delta V_s^P}{V_s} \sin \theta. \quad (16)$$

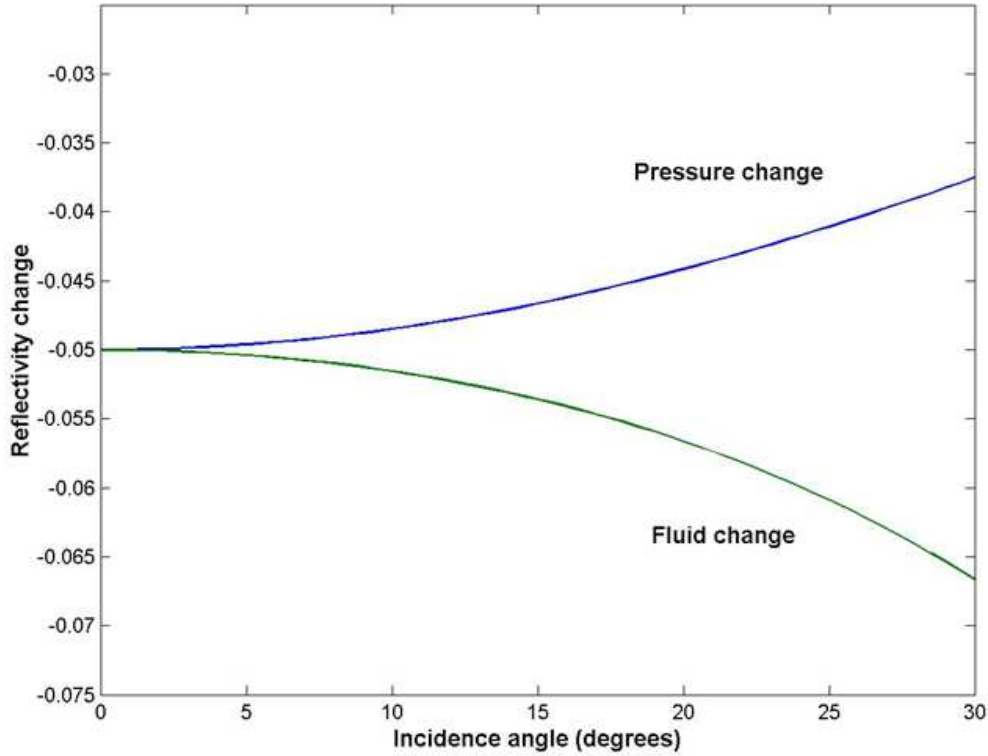


**Figure 4:** Reflectivity change versus incidence angle for two segments with identical lithology undergoing pressure changes and fluid changes, assuming that the density changes are small. In both cases, we expect a weak AVO-effect, but in opposite directions. The zero offset reflectivity has been chosen to be equal for the pressure and fluid case (in practice, the near offset amplitudes might be normalized to each other).

For fluid changes we find correspondingly

$$\Delta R_{\text{PS}}^{\text{F}}(\theta) = \frac{\Delta V_s^{\text{F}}}{V_s} \sin \theta. \quad (17)$$

This means that the PS-reflectivity changes have (to the lowest order) the same AVO-behaviour. The sign of the parameter contrasts depends on whether we are considering a pressure increase, a water to hydrocarbon fluid change or vice-versa.

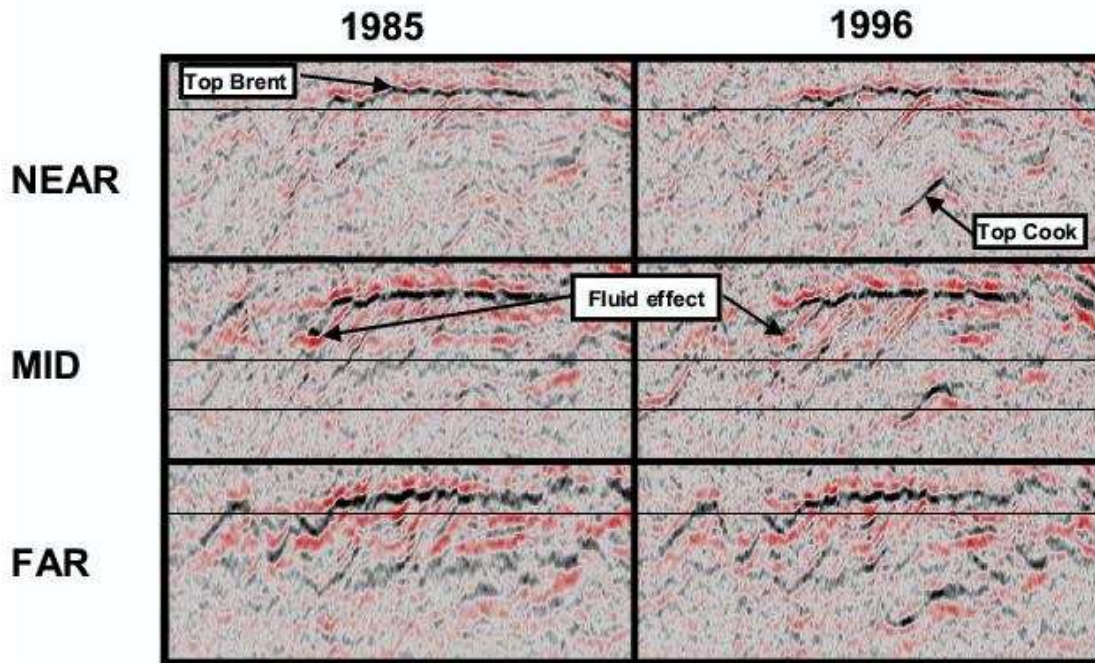


**Figure 5:** Near, mid and far offset stacks (top to bottom) from 1985 (left) and (1996) right. Notice the significant amplitude increase from 1985 to 1996 for the near offset data at top Cook. (Within this formation a significant pore pressure has been measured). Furthermore, notice a slight decrease in amplitude with offset for the 1996 data set. The fluid signal, associated with the original oil-water contact level (marked on the mid offset sections) shows the opposite trend: An amplitude increase with offset (observed on the 1985 data), and a significant decrease in amplitude for all offsets for the 1996 data, caused by water flushing. These field observations are supported by the simplified theoretical curves shown in Figure 4.

## 6 A 4D example: Velocity changes caused by a pore pressure increase

Figure 6 shows a time-lapse seismic profile from a segment where the reservoir pressure has increased by approximately 6-8 MPa between the seismic surveys. A significant amplitude change is observed at the top reservoir interface. A detailed discussion of this case can be found in Landrø (2001). There are significant variations in the size of this amplitude increase. A simple 1D modeling study based on well logs indicate that a P-wave velocity drop of at least 20% is necessary to explain the observed amplitude increase. This is illustrated in Figure 7. The reservoir thickness is approximately 80 m within the over-pressured segment. If a 20% velocity reduction is imposed for the whole reservoir thickness, a corresponding time-shift (or time-delay) of 20-30 ms should be

observed on the time-lapse seismic data. This is however not the case, and therefore a gradual velocity change has been suggested in Figure 7. This gradual velocity change is to some extent supported by the increase in the gamma-log versus depth within the reservoir section (Figure 7). Although this time-lapse experiment is not a proof that the velocity should drop significantly for a pore pressure increase, it gives support to all the four curves displayed in Figure 1. As the number of time-lapse seismic surveys is increasing we think we will see more and more examples of this kind, where seismic velocities can be coupled to observed pressure changes within the reservoir. In most case examples there are limitations caused by reservoir heterogeneity, fluid and temperature changes taking place at the same time etc.

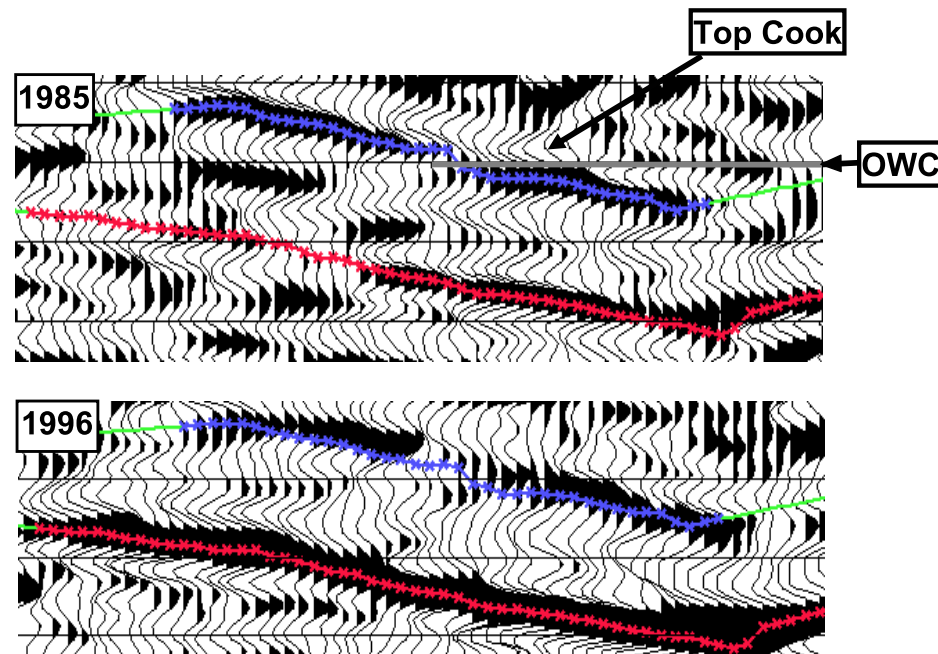


**Figure 6:** A seismic profile from the over-pressured Cook-segment. Notice the strong amplitude increase at the top Cook interface from 1985 to 1996. Furthermore notice a relatively small pull-down effect for the near base Cook interface (marked with a blue line at the two profiles). Printed with permission from EAGE.

## 7 What about seismic effects caused by pore pressure decrease?

In the Gullfaks 4D seismic study (Landrø et al., 1999) several examples of pore pressure increases were found. The opposite effect, a pore pressure decrease, was not found, however. Even in areas within the water-zone where the measured pore pressure decrease



**Comparison between synthetic seismogram based on acoustic impedance from well C-3 and real time lapse seismic (black= 85; red = 96)**

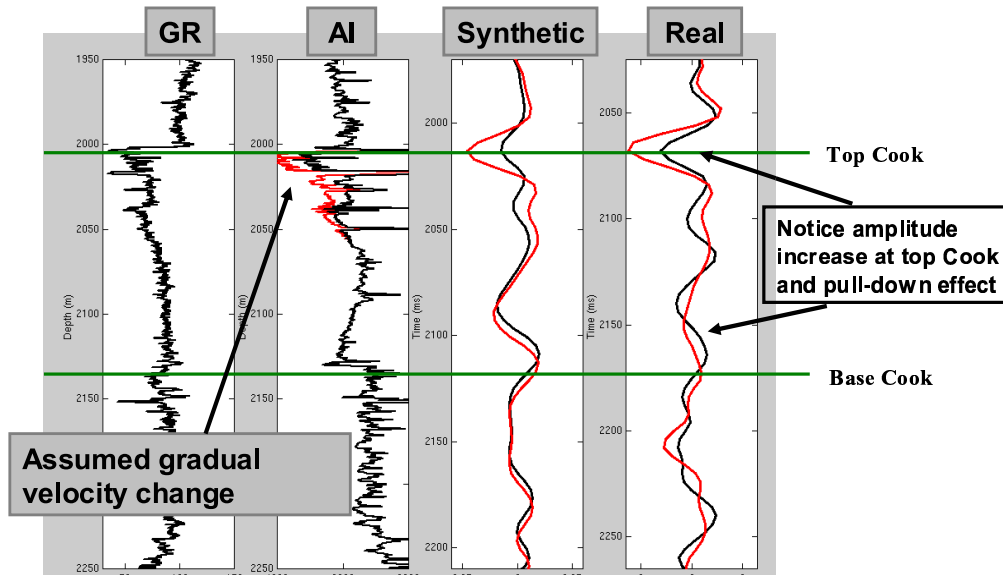


**Figure 7:** Gammalog, acoustic impedance, synthetic seismogram and real seismic (from left to right) for well C3. Black line refers to measurements from 1985, while the red line shows assumed changes in acoustic impedance and corresponding effect upon the synthetic seismogram, while the red curve to the right shows the seismic trace from 1996. Here we have assumed a gradual change in velocity below the top Cook interface. Printed with permission from EAGE.

was of the order of 2-4 MPa, no clear anomalies were observable on the 4D seismic data. The repeatability level of the Gullfaks 4D data was rather low, of the order of 50-70 % in RMS difference between baseline and monitor surveys. Last year, a dedicated experiment was done at Gullfaks, in order to further test the possibilities of detecting a pore pressure decrease (Landrø et al., 2002). A 12-level VSP tool was installed in one well, while a neighboring injector well was shut down in order to generate a pore pressure drop. The measured pore pressure decrease was 2.5 MPa. Although the analysis of the results of this test is not finalized yet, it seems clear that the effect on the 4D VSP data is rather small. One might therefore say that this “controlled” experiment, together with the 4D observations on this field, gives us a strong indication that pore pressure decreases are far less observable on 4D seismic data, compared to pore pressure increases.



## 7.1 Conventional velocity analysis, is it accurate enough to detect a pressure increase of 6 MPa at 2000 m reservoir depth?

The example presented above can also be used to cast some insight into the sensitivity problem of using conventional velocity analysis for overpressure prediction. A thorough velocity analysis has been performed by Øyvind Kvam (PhD student). He analyzed 40 CMP-gathers before and after the pressure increase, and found that the uncertainty in the velocity picking was larger than the estimated velocity change based on the velocity analysis. This is shown in Figure 8. There are several possible explanations for this, the major is probably the gradual velocity change mentioned in the previous section. The thickness and the depth of the over-pressured unit are crucial factors strongly impacting our ability to use velocity analysis as a tool for pressure prediction. The sensitivity for detecting abnormal velocity changes decreases rapidly with depth, while the uncertainty in velocity estimation increases rapidly with depth. This is illustrated in Figure 9. It is important to underline that the velocities displayed in figures 8-9 are RMS-velocities and not interval velocities as discussed in the previous sections.

### Real data, results

- 40 picks made for each event
- Linear regression (least squares)

$$\frac{\Delta V_{rms}}{V_{rms}} = -0.00027 \pm 0.07$$

Uncertainty is approximately 7% at 2000 m depth

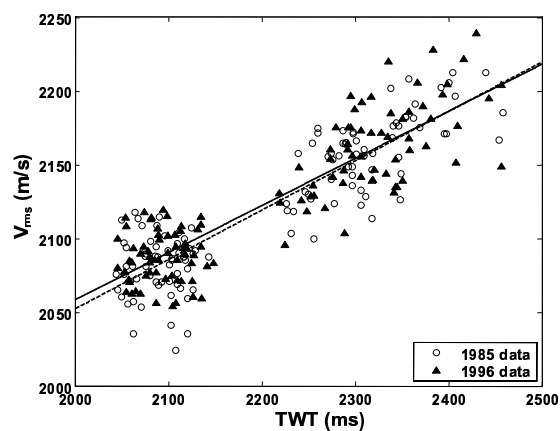


**Figure 8:** Velocity analysis results from 40 time-lapse CMP-gathers from a reservoir segment where the pore pressure has increased by approximately 6-7 MPa due to water injection.

## Is it possible to estimate zone for reliable pore pressure prediction?

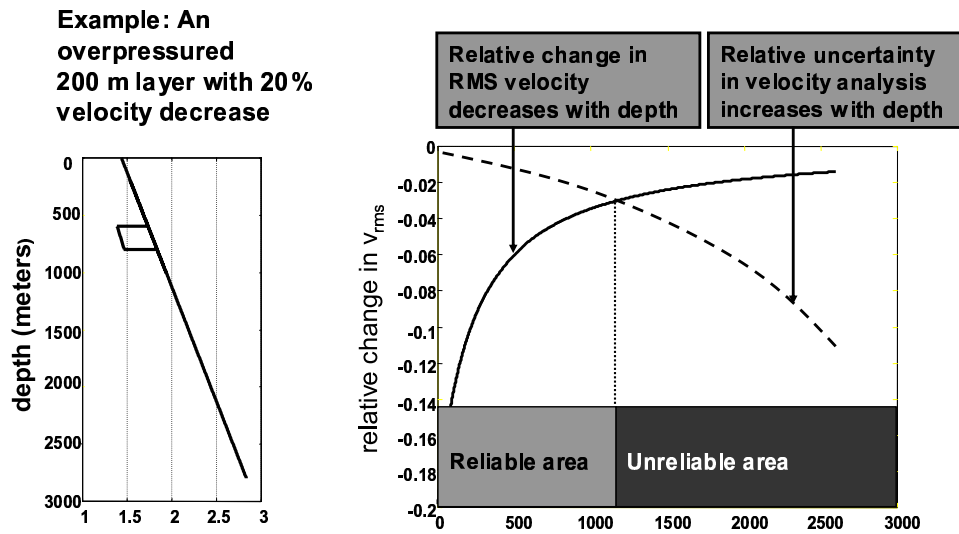


**Figure 9:** Schematic illustration showing that the reliability of pressure detection via seismic velocity decreases rapidly with burial depth.

## 8 Discussion

New simple AVO-formulas show that the AVO-difference between a normal segment and an anomalous segment (over-pressured or hydrocarbon-filled), is opposite for a pressure effect compared to a fluid effect. These AVO-formulas are based on the Hertz-Mindlin theory, which predicts that the relative change in P-wave velocity is equal to the relative change in S-wave velocity when the rock pressure is changing. For some sandstone reservoirs, ultrasonic core measurements support this assumption (from Figure 3 in Landrø et al. (1999), we observe that the relative change in P- and S-wave velocities are around 4% for a 4 MPa decrease in net pressure, and approximately 10% for a 4 MPa increase in net pressure). It should be stressed that this assumption is based only upon the Hertz-Mindlin model and some rather sparse core measurements. Therefore, these simplified AVO-formulas should be used with care for other rock types. Another limitation is of course that it is assumed that the lithology between the two segments (see

Figure 2) is constant. A relatively small change in lithology between the two segments might of course mislead the AVO-interpretation technique suggested in this paper. Therefore, it is important that the suggested method is regarded as complementary to the more established pressure prediction methods, based on velocity analysis.

Time-lapse velocity analysis applied on a “controlled” over-pressured segment demonstrates clearly two critical factors: thickness and depth of the over-pressured layer. The uncertainty associated with our pressure predictions increases rapidly with depth, and decreases rapidly with the layer thickness.

## 9 Conclusion

Recent 4D seismic case studies show that pressure effects are visible and detectable as 4D amplitude differences. There are also strong indications that pore pressure increases are easier to detect than pore pressure decreases. This observation is in agreement with most ultrasonic core measurements. Based on the Hertz-Mindlin theory it can be shown that a pressure anomaly has the opposite AVO-behavior (decrease) of a fluid anomaly (increase). This simple observation can be used as a complementary interpretation technique for identification of over-pressured segments. 4D seismic has also shown that seismic amplitudes are robust, often more robust than travel-time differences. Correspondingly, we should put more emphasis on the use of amplitudes (and AVO) also for pressure prediction in an exploration setting.

## Acknowledgment

Statoil and the Gullfaks licence partner, Norsk Hydro and Petoro are acknowledged for permitting this paper to be presented. Martin Landrø acknowledges financial support from the EC project ENK6-CT-2000-00108, ATLASS. Alexey Stovas is acknowledged for comments to the manuscript.

## Chapter 6

# A spectral ratio approach to time-lapse seismic monitoring on the Gullfaks Field

Øyvind Kvam<sup>1</sup>, Jesper Spetzler<sup>2</sup> and Martin Landrø<sup>1</sup>

<sup>1</sup> *Department of Petroleum Engineering and Applied Geophysics  
Norwegian University of Science and Technology  
N-7491 Trondheim, Norway*

<sup>2</sup> *Department of Geotechnology  
Technical University of Delft  
PO. Box 5028, NL-2600 GA Delft, The Netherlands*

**ABSTRACT:** We present a spectral ratio method for monitoring of time-lapse seismic data. The relative change in reflection coefficient at an interface and the change in two-way traveltimes is computed by convolution-deconvolution of prestack time-lapse seismic data. The outcome is used as input for time-lapse AVO analysis in order to find time-lapse changes in elastic parameters. Application of the method to synthetic seismic data and real seismic data from the Gullfaks Field show that the results agree well with the results achieved by AVO analysis from peak amplitudes. However, due to the nonlinear nature of ratio data, the uncertainties are larger. We propose that this method can serve as a fast, but less accurate, alternative to conventional time-lapse AVO methods.

# 1 Introduction

Time-lapse seismic data offer the possibility to monitor physical changes in the subsurface over time. Repeated acquisition of seismic data has become a standard tool in the petroleum industry, and is used e.g., to find saturation and pressure changes in reservoirs, as input to reservoir simulation models, and to plan new wells. Successful case histories, like the Gullfaks 4D study (Landrø et al., 1999), the Duri steamflood project (Jenkins et al., 1997a), have demonstrated the potential of seismic reservoir monitoring.

Changes in the physical conditions of the subsurface over time may manifest themselves as amplitude and traveltime changes in time-lapse seismic data. The most important properties are the ones that are affected by hydrocarbon production, namely pore pressure, fluid saturation and reservoir temperature (Jack, 1998). Analysis of the behaviour of seismic reflection amplitude with offset (AVO analysis) is a commonly used technique to resolve physical changes from time-lapse seismic data. Landrø (2001) uses AVO analysis to separate between pore pressure and saturation changes in a time-lapse seismic dataset.

It is important to realize that differences in a time-lapse seismic dataset is not necessarily caused by changes in the physical properties of the subsurface. Due to e.g., changing weather conditions, tidal variations, and developments in acquisition technology, it is not possible to repeat a seismic experiment 100%. Careful planning of the acquisition is the key factor for a successful time-lapse seismic experiment. However it is possible, to some extent, to correct for undesirable non-repeatability effects in time-lapse seismic data post-acquisition. Rickett and Lumley (2001) presented a cross-equalization flow to correct for non-repeatability effects in time-lapse seismic data.

In this study, we apply a spectral ratio-technique to estimate time-lapse changes at reflecting interfaces. By calibrating reflection amplitudes to a shallow reflector, we suppress artificial time-lapse changes due to differences in source wavelet between different surveys. Thus, we apply a post-acquisition approach to reduce undesirable noise due to differences in source wavelets and changes in the overburden. This is relevant for comparing datasets where different air guns have been used to create the source signal. The method is tested on both synthetic and real time-lapse seismic data.

The real data are taken from a segment of the Gullfaks Field in the North Sea. At Gullfaks, oil reserves are found in middle to late Jurassic sandstones at approximately 1950-2300 meters depth. 80% of the original reserves are located in the Brent Group, while the remaining reserves are found in the Statfjord and Cook formations. The time-lapse data consist of a subset of two 3D seismic surveys acquired in 1985 (baseline survey) and 1996 (monitor survey). 5 inlines was chosen from a area covering  $500 \times 750$  meters. This segment was chosen because there is a very clear time-lapse signal here. Figure 1 shows a comparison of stacked sections from the baseline survey (top) and the monitor

survey (bottom). Note the difference in stack amplitude at the Top Cook reflector. This is probably caused by an increase in the pore pressure of 5-7 MPa in the Cook Formation as a result of water injection.

The outcome from the spectral ratio-processing is the relative change in reflection amplitude at a seismic target reflector and the change in traveltime between the two surveys. These data are compared to the results of AVO analysis from peak amplitudes and cross-correlation data.

## 2 Theory

The spectral ratio-technique used here is described in detail by Spetzler and Kvam (2003). For completeness we will summarize it here. The methodology is easy to comprehend if we think in terms of convolution. The simplest convolutional model states that the seismic trace,  $f(t)$ , is a convolution of a source wavelet  $s(t)$  with a reflectivity series  $r(t)$ ,

$$f(t) = s(t) * r(t), \quad (1)$$

where the asterisk (\*) denotes convolution. Figure 2 shows a 1D acoustic model, a zero-offset reflectivity series, and the resulting zero-offset synthetic trace. We now select a time window around the deepest reflection in the synthetic trace (about 1520 ms), and produce a new trace  $\hat{f}(t)$ , which is equal to  $f(t)$  within the time window, and zero elsewhere. Let  $R_A$  be the reflection coefficient of the deepest spike in the reflectivity series, and let  $t_A$  be the corresponding time. It is clear that  $\hat{f}(t)$  is reproduced with a convolution between the source wavelet and this spike,

$$\hat{f}(t) = s(t) * R_A \delta(t - t_A) = R_A \int_{-\infty}^{\infty} s(\tau) \delta((t - t_A) - \tau) d\tau = R_A s(t - t_A). \quad (2)$$

In Figure 2,  $R_A = 0.15$  and  $t_A = 1520$  ms.

The Fourier transform of  $R_A \delta(t - t_A)$  is given by  $R_A e^{i\omega t_A}$ . Thus, according to the convolution theorem, the convolution in equation (2) can be written in the frequency domain as

$$\hat{F}(\omega) = S(\omega) R_A e^{i\omega t_A}, \quad (3)$$

where  $S(\omega)$  is the Fourier transform of the source wavelet.

Now, assume that the convolution illustrated in Figure 2 is repeated with a different source wavelet,  $s'(t)$ . Further, we assume that the reflectivity series is perturbed both in value and along the time axis. Specifically,  $R_A \rightarrow R_B$ , and  $t_A \rightarrow t_B$ . The steps described in equations (1)- (3) now give

$$\hat{F}'(\omega) = S'(\omega) R_B e^{i\omega t_B}. \quad (4)$$

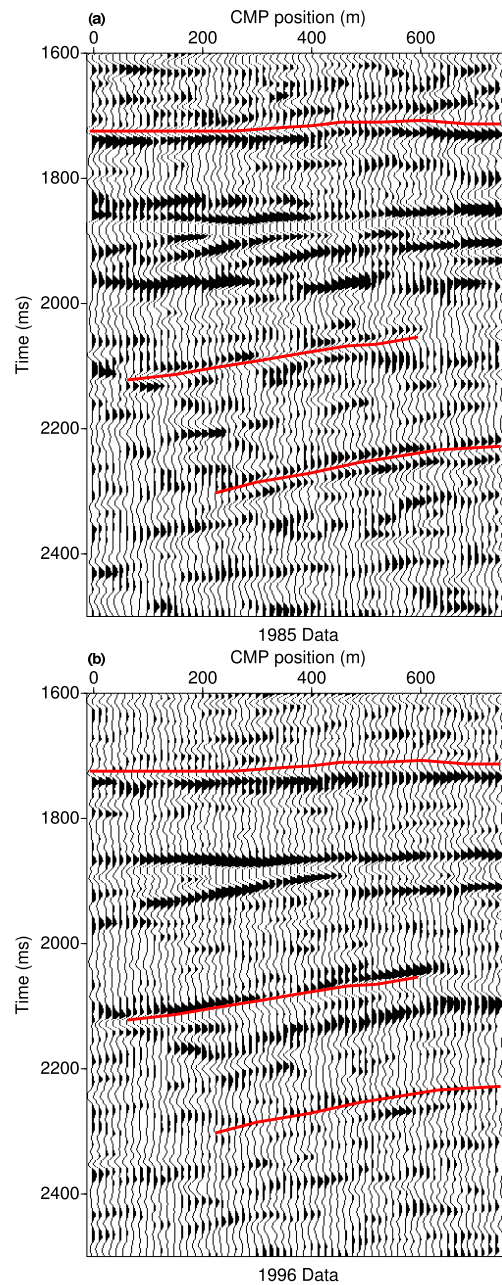


**Figure 1:** Comparison of stacked data from inline 2761. (a) baseline survey, and (b) monitor survey. The upper interpreted horizon is used for source wavelet substitution, the middle horizon is the Top Cook, and the lower is the Top Statfjord.

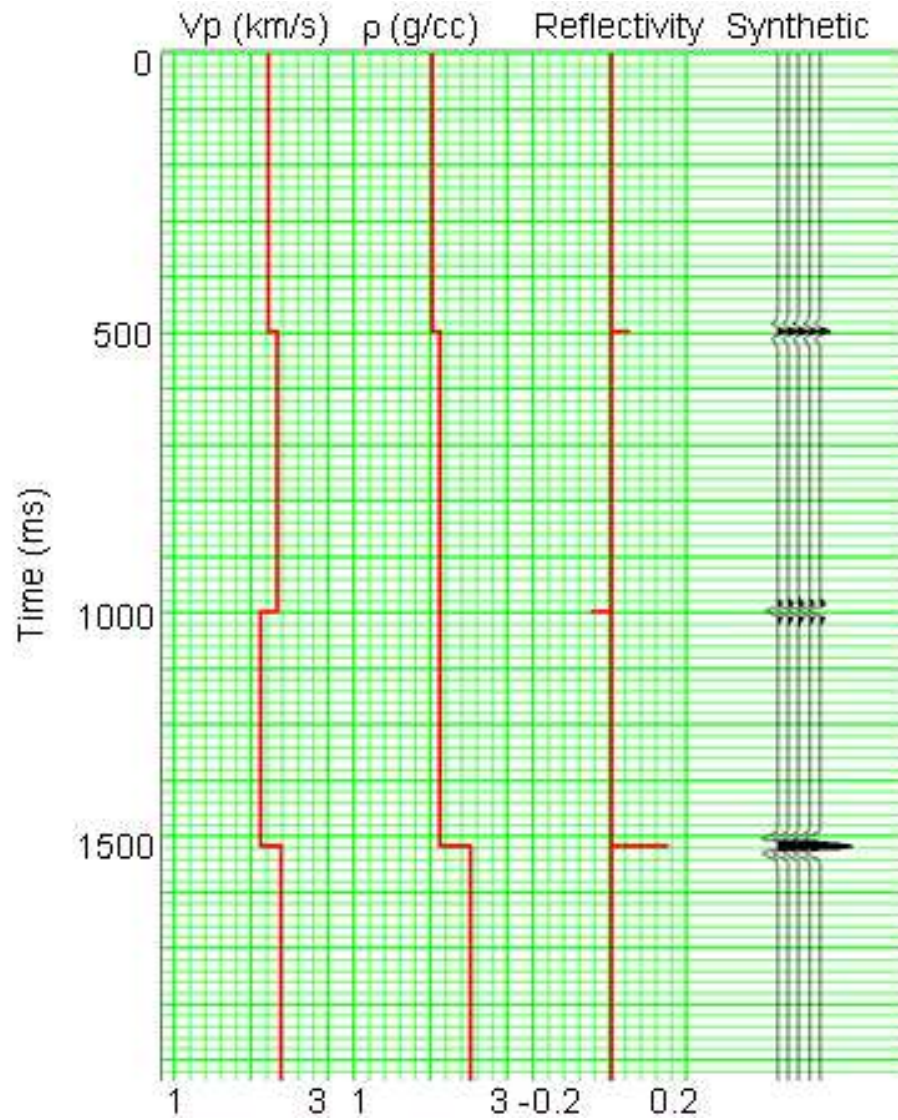


**Figure 2:** P-wave model (left), density model, reflectivity series, and synthetic trace (right). The synthetic trace is computed by convolving the input wavelet with the reflectivity series. The input wavelet is a Ricker wavelet with central frequency of 30 Hz.



The new situation is described in Figure 3 with  $R_B = 0.05$  and  $t_B = 1500$  ms. We now perform the operation  $S'(\omega)\hat{F}/S(\omega)\hat{F}'$  which can be regarded as a convolution-deconvolution operation in the frequency domain. The result is

$$\frac{S'(\omega)\hat{F}}{S(\omega)\hat{F}'} = \frac{S'\omega S(\omega)R_A e^{i\omega t_A}}{S\omega S'(\omega)r_B e^{i\omega t_B}} = \frac{R_A}{R_B} e^{i\omega \delta t}, \quad (5)$$

where  $\delta t = t_A - t_B$  is the difference in traveltime. By taking the complex norm of equation (5) we obtain the absolute value of the ratio of reflection coefficients,  $|R_A/R_B|$ , and by taking the complex angle, we obtain the traveltime shift multiplied by the frequency  $-\omega \delta t$ . In order to obtain the sign of  $R_A/R_B$ , the polarity of the reflected signal from the target reflector must be examined. If the polarity is reversed in the monitor data,  $R_A/R_B$  is negative.

In a time-lapse setting, the procedure described above is equivalent to measuring the relative change in reflection coefficient (absolute value) at an interface and the change in traveltime. In the example shown in Figures 2-3, we should obtain  $|R_A/R_B| = 0.15/0.05 = 3$ , and  $\delta t = 1520 - 1500 = 20$  ms. Figure 4 shows the result of applying the operation in equation (5) to the synthetic traces.

## Effect of fine layering

Equation (5) states that the norm of the complex number  $S'(\omega)\hat{F}/S(\omega)\hat{F}'$  is independent of frequency, and that the complex angle is a linear function of frequency. However, this is an idealization. Consider the situation in Figure 5, where the target reflector now is surrounded by finely layered media. The resulting reflected wave now has a much more complex shape, and the primary reflection corresponding to the target reflector is partly distorted due to tuning effects. Again, we introduce a time-lapse change in the model, causing the reflectivity and the traveltime for the target reflector to change. This is illustrated in Figure 6.

Applying the spectral ratio method to the new traces now gives a different result than the traces with no fine-layering applied. Figure 7a shows a plot of the complex norm of the left hand side of equation (5) as a function of frequency. Note that the fine layering introduces significant fluctuations with frequency. Thus, equation (5) is no longer valid. However, we can partly restore the ratio of reflectivity by averaging over a frequency band for which the S/N ratio is good. In the example above we have used Ricker wavelets for the baseline and monitor traces with central frequencies of 30 Hz and 20 Hz, respectively. Averaging over a frequency band ranging from 10 to 40 Hz gives  $R_A/R_B = 2.3$ . The peak amplitudes give a ratio of 2.2.

We do not obtain a satisfactory result for the time shift for the fine layered modeling.

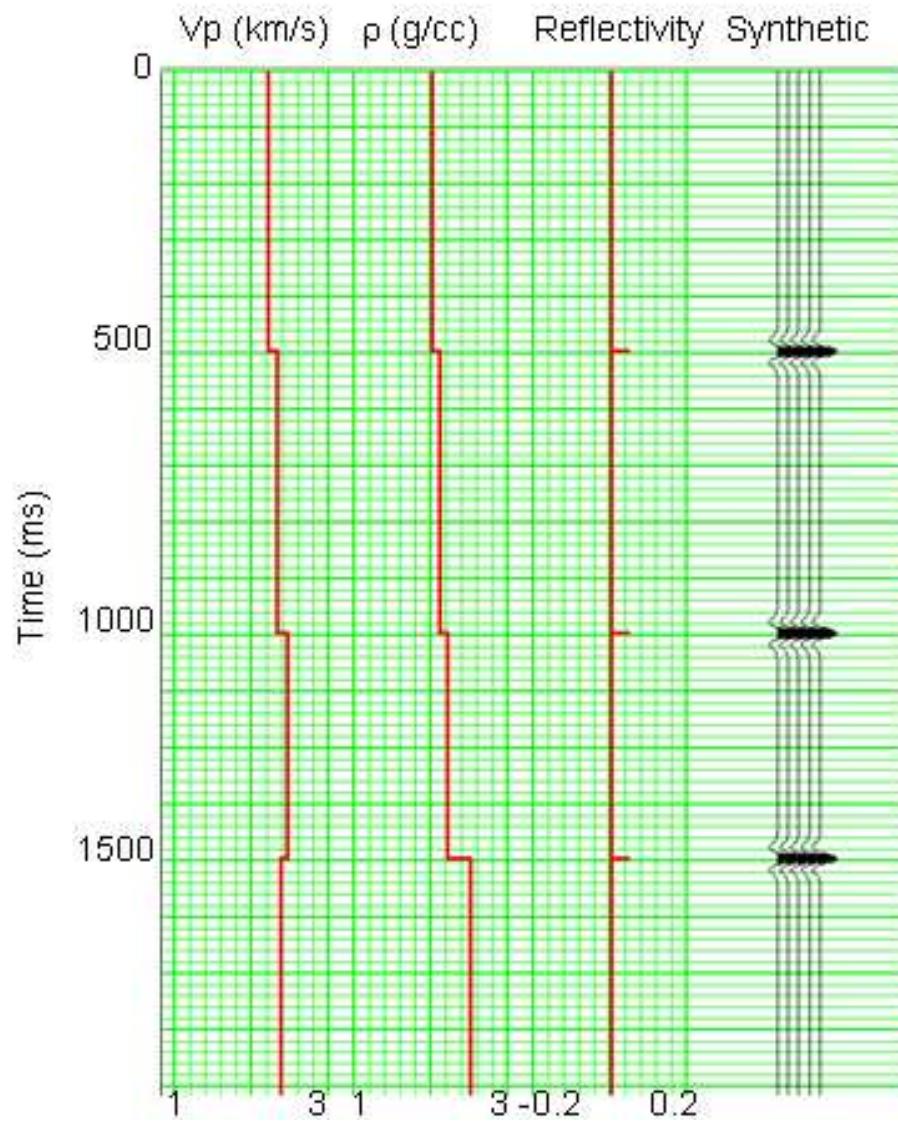


**Figure 3:** Same as Figure 2, except that the lowest reflector is shifted upwards with 20 ms, and the reflectivity is changed from 0.15 to 0.05. The input wavelet is a Ricker wavelet with central frequency of 20 Hz.

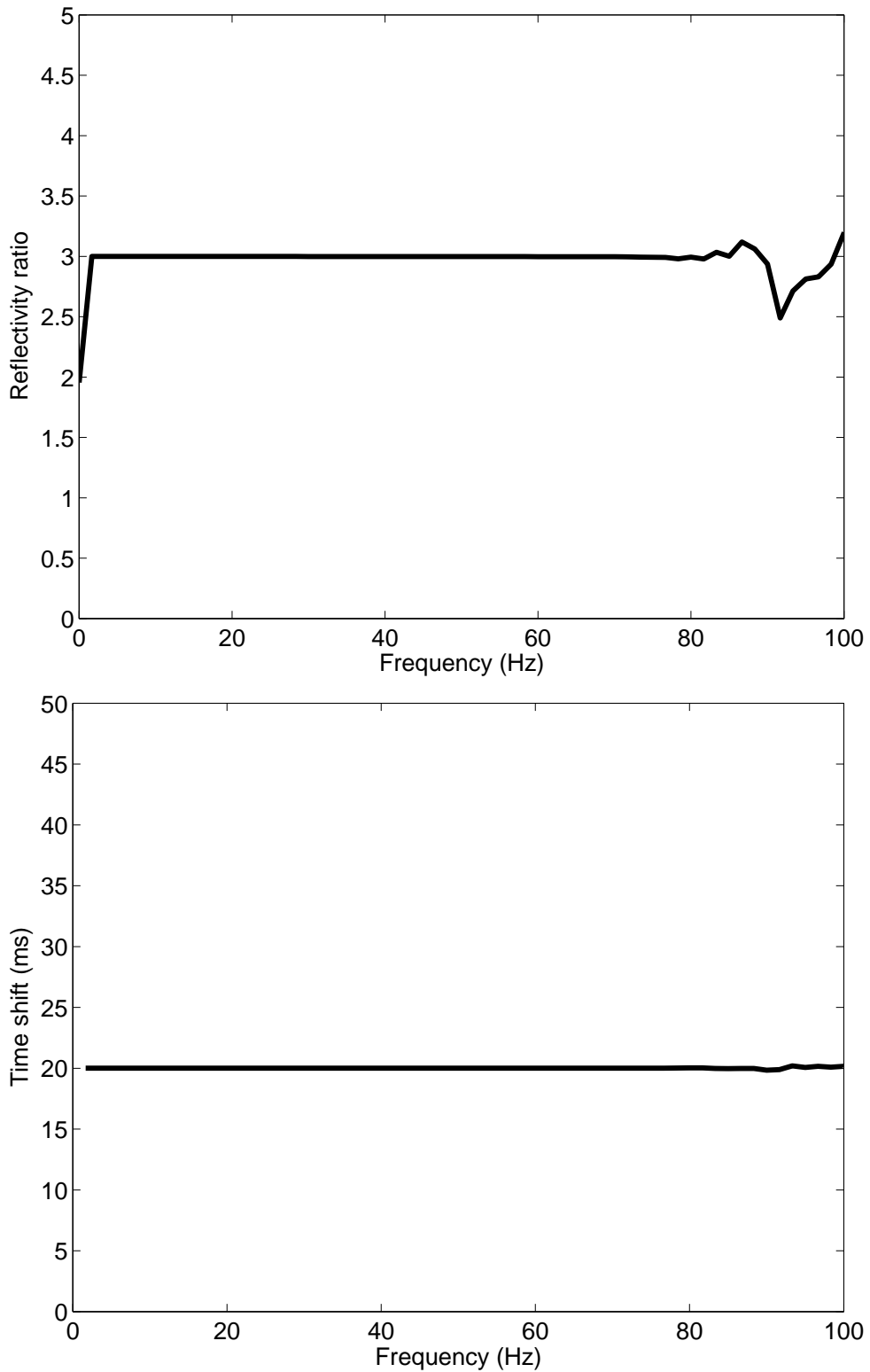


**Figure 4:** Ratios of reflectivity (top) and time shifts (bottom) for the lowest reflector in Figures 2 and 3, computed with equation (5). Note that the values are constant with frequency over the bandwidth of the wavelet (20 Hz Ricker wavelet).

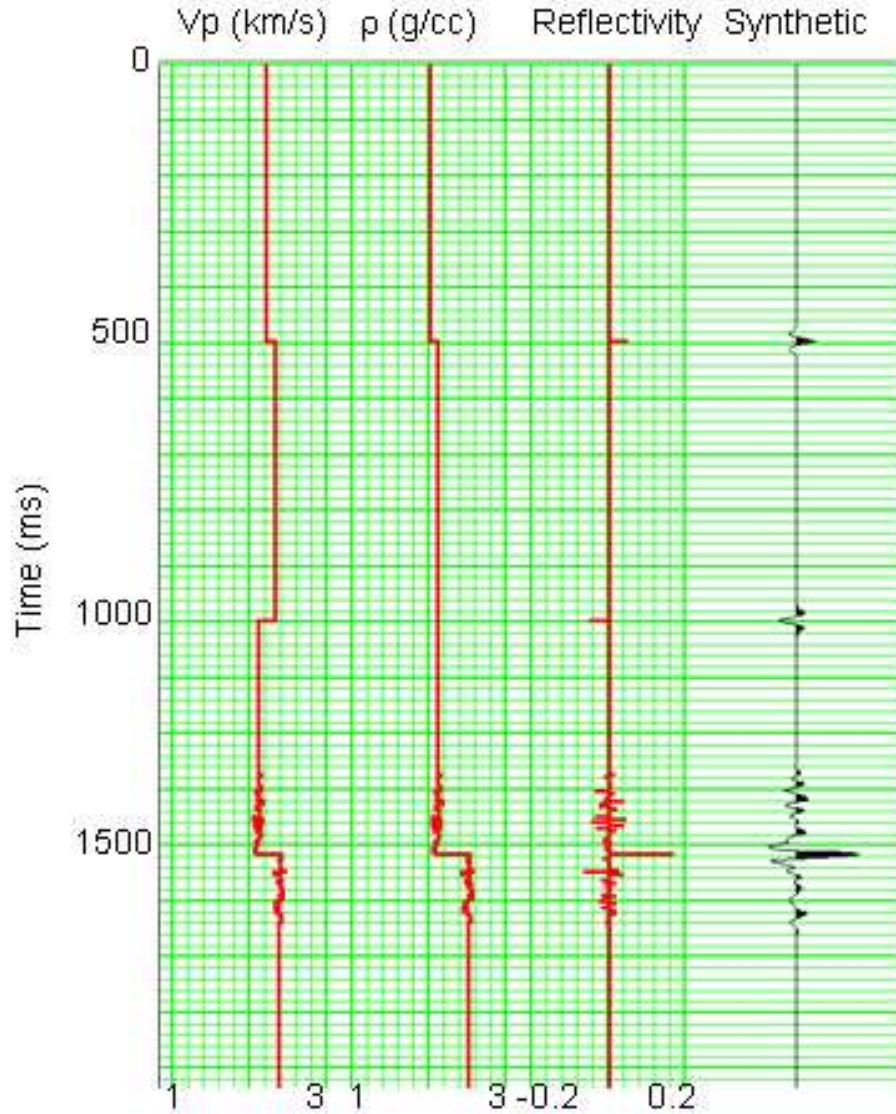


**Figure 5:** Same as Figure 2, except that we have added fine layers around the deepest reflector.

Figure 7b (solid line) shows a plot of the complex angle vs frequency for the left hand side of equation (5), divided by  $2\pi$ . According to equation (5), this is a straight line with slope  $\Delta t$  and intercept 0 (dotted line). Instead, we observe that the fine layering has introduced a constant phase shift. Computing the time shift by dividing by the frequency in this case gives an erroneous result. However, a least squares fit in the frequency range between 10 Hz and 40 Hz gives a slope of  $\Delta t = 22$  ms. In comparison, the peak amplitudes of the target reflector for the baseline and monitor traces are separated 20 ms apart.

We have not discussed complicating factors such as attenuation, geometrical spreading and transmission loss. However, we argue (Spetzler and Kvam, 2003) that these will be

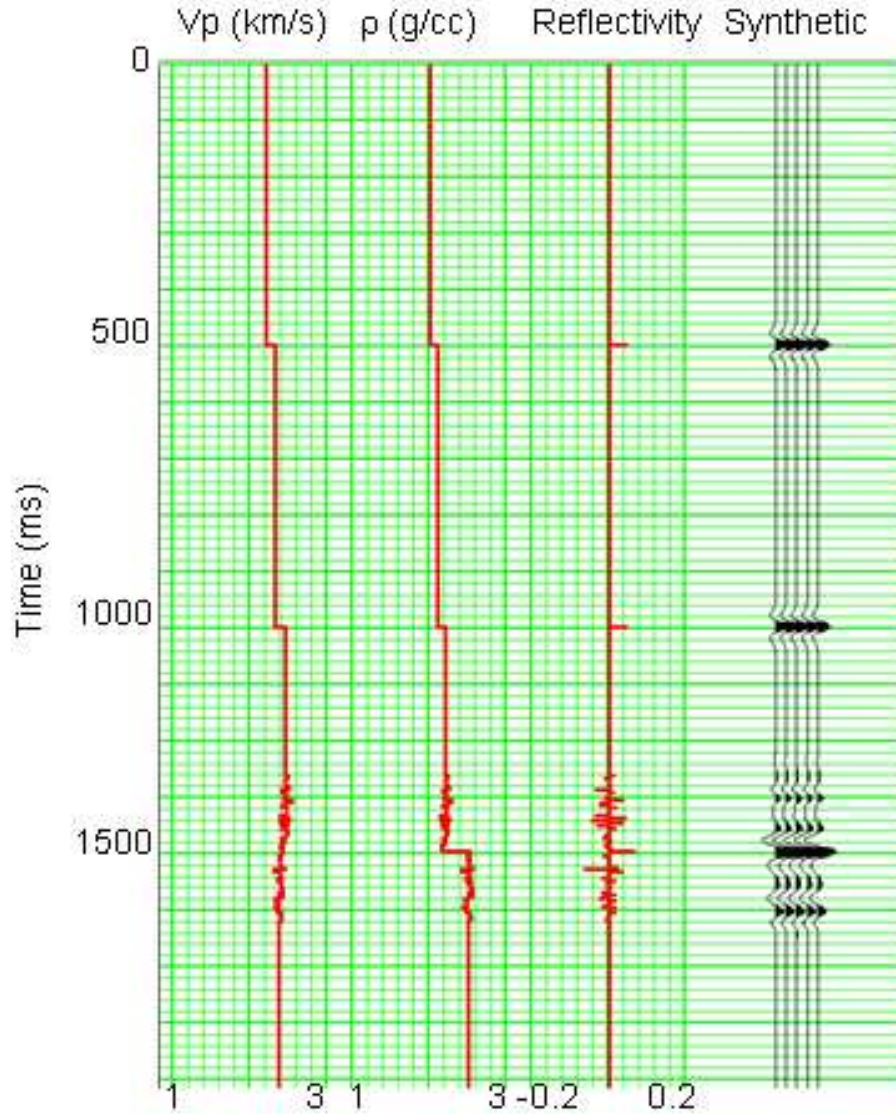


**Figure 6:** Same as Figure 3, except that we have added fine layers around the deepest reflector.

approximately equal for the two surveys, so that the effect of this will be negligible in equation (5). Further, by using wave theory instead of convolution, we show that the expression in equation (5) also is valid for nonzero offsets.

The operation in equation (5) requires that we know the source wavelet for the two cases. Usually this is not the case, so we propose (Spetzler and Kvam, 2003) to substitute the expression for the source wavelet with the reflected signal from a shallow reflector for which no time-lapse changes are expected. This introduces additional uncertainties, since it is possible that the reflected signal used for this substitution is contaminated with tuning effects or interfering wavefields.



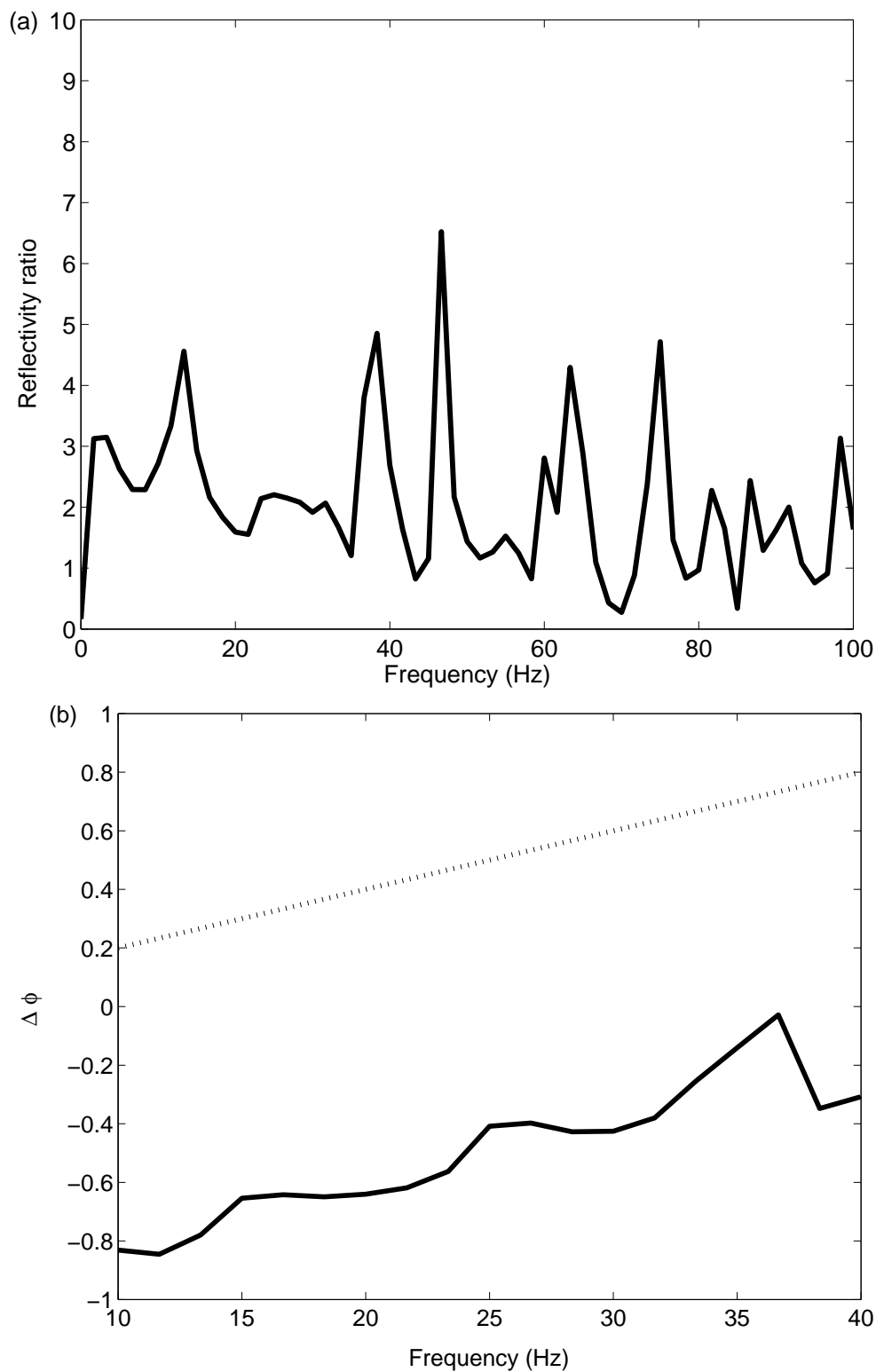


**Figure 7:** Ratios of reflectivity (a) and phase difference (b) for the lowest reflector in Figures 5 and 6, computed with equation (5).

## 2.1 From amplitude ratios to seismic parameters

Once the reflectivity ratio and time shift data are obtained, the challenge is to interpret them in terms of changes in the P-wave velocity ( $V_p$ ) and S-wave velocity ( $V_s$ ) and density ( $\rho$ ). While it is relatively easy to interpret time shift data in terms of changes in  $V_p$ , the reflectivity ratios need a closer examination. A popular way to extract information on  $V_p$ ,  $V_s$ , and  $\rho$  from AVO data is to use linear theory. Consider a two-layer model where  $V_p$ ,  $V_s$ , and  $\rho$  in the upper layer are given by  $\alpha_1$ ,  $\beta_1$ , and  $\rho_1$ , respectively. Similarly, the elastic properties of the lower layer are described by  $\alpha_2$ ,  $\beta_2$ , and  $\rho_2$ . The Smith and Gidlow approximation for the PP-reflection coefficient is given by

$$R_{PP} = \frac{1}{2} \left( \frac{\Delta\alpha}{\alpha} + \frac{\Delta\rho}{\rho} \right) - 2 \frac{\beta^2}{\alpha^2} \left( \frac{\Delta\rho}{\rho} + 2 \frac{\Delta\beta}{\beta} \right) \sin^2 \theta + \frac{\Delta\alpha}{2\alpha} \tan^2 \theta \quad (6)$$

where  $\Delta\alpha = \alpha_2 - \alpha_1$ ,  $\alpha = 1/2(\alpha_1 + \alpha_2)$ , and so on. equation (6) is linear in the contrast parameters  $\Delta\alpha/\alpha$ ,  $\Delta\beta/\beta$ , and  $\Delta\rho/\rho$ , and is therefore well suited for AVO analysis. However, we measure the ratio of reflection coefficients, which is highly nonlinear. Consider the case when  $r'$  is very small. In this case, even a small change in the contrast parameters will give a large change in the ratio  $R_A/R_B$ . In fact, it is very likely that  $R_B = 0$  at a certain offset, giving a singularity in  $R_A/R_B$ .

By assuming initial values for  $R_A/R_B$  and an initial elastic model at the time of the baseline survey, we attempted to extract information on the change in  $V_p$ ,  $V_s$ , and  $\rho$  directly using a linear inversion algorithm (Kvam and Spetzler, 2003). However, the results for synthetic data was not convincing because the inversion was unstable with regard to small perturbations in the input model. We therefore adopt a different approach.

We will assume that we have an estimate of the reflection coefficient  $R_A$ , at a target interface for the baseline survey. This can be obtained by scaling the amplitudes for the baseline survey so that they fit a modeled reflectivity e.g., from a well log. The reflectivity for the same interface at the time of the monitor survey,  $R_B$  is then given by

$$R_B = R_A \frac{R_B}{R_A} = \frac{R_A}{r}, \quad (7)$$

where  $r$  is the measured ratio of reflection coefficients.

Equation (6) can be rewritten in terms of the standard two-term AVO equation

$$R_{PP} = R_0 + G \sin^2 \theta, \quad (8)$$

where  $R_0 = \Delta\alpha/\alpha + \Delta\rho/\rho$  and  $G = \Delta\alpha/2\alpha \cos^2 \theta - 2\beta^2/\alpha^2 (\Delta\rho/\rho + 2\Delta\beta/\beta)$ . By assuming a change in the elastic properties of layer 2, such that  $\alpha_2 \rightarrow \alpha_2 + \Delta\alpha_2$ ,  $\beta_2 \rightarrow \beta_2 + \Delta\beta_2$ , and  $\rho_2 \rightarrow \rho_2 + \Delta\rho_2$ , it can be shown that the change in  $R_0$  and  $G$  can be written as (Landrø,

2001)

$$\begin{aligned}\Delta R_0 &= \frac{\Delta\alpha_2}{\alpha} + \frac{\Delta\rho_2}{\rho} \\ \Delta G &= -2\frac{\beta^2}{\alpha^2} \left( \frac{\Delta\rho_2}{\rho} + 2\frac{\Delta\beta_2}{\beta} \right)\end{aligned}\tag{9}$$

to the lowest order. In order to compute changes in the elastic parameters from equations (9), we must assume relationships between  $\Delta\alpha/\alpha$ ,  $\Delta\beta/\beta$ , and  $\Delta\rho/\rho$ . This can be obtained from theory of rock physics, or direct measurements from the study area. For instance, for a pore pressure increase, it is reasonable to assume that the density does not change, while  $\Delta\beta_2/\beta \approx \Delta\alpha_2/\alpha$ . (Landrø, 2001). .

### 3 Results

The spectral ratio-technique described above was used to extract amplitude and phase data for both synthetic and real data. The results are compared to the results of using more standard techniques.

#### 3.1 Synthetic study

A 2D elastic model was produced based on stacked synthetic data from the Gullfaks Field. The P-wave velocity model is shown in Figure 8, with the target zone indicated. In order to simulate a time-lapse experiment, we performed two synthetic surveys with different  $V_p$  and  $V_s$  in the target zone. The synthetic data was produced using a coarse finite-difference scheme (Holberg, 1987). Both datasets were computed using the same wavelet. The following processing procedure was applied to the data: 1) NMO using the known velocity field, 2) Zero-offset time migration on common offset gathers, 3) inverse NMO using the known velocity field.

Figure 9 shows a migrated stack of the reservoir section from the monitor survey. The top and base reservoir events are clearly visible in the stacked data. Figures 10a and 10b show a comparison of two prestack gathers from the baseline survey (a) and the monitor survey (b), zoomed in on the top reservoir event. Note that for the baseline survey, there is a polarity shift in the amplitude the top reservoir event. Because of the interfering wavefield, it is hard to tell at which offset the polarity shifts.

In order to test the validity of the spectral ratio method for this dataset, we consider the stacked traces in Figures 11a (baseline data) and 11b (monitor data). Figure 12 (solid



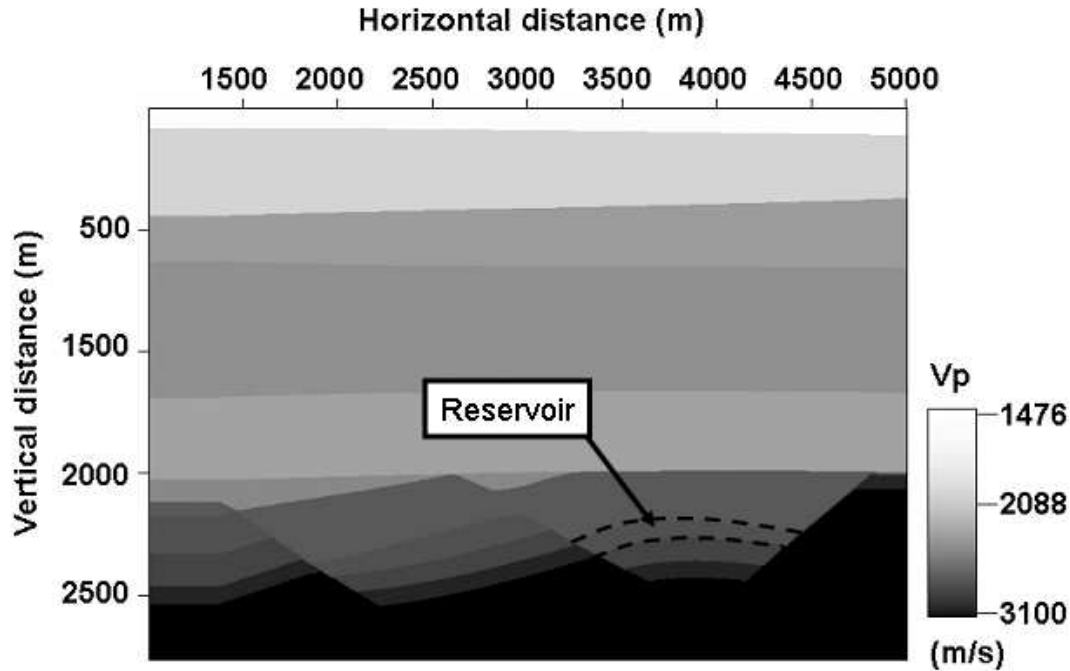


**Figure 8:** P-wave model used for synthetic modelling. The reservoir is indicated on the figure.

line) shows the reflectivity ratio computed with the spectral ratio method for one of the traces. Again, we observe that the ratio is not a constant with frequency, in contradiction to equation (5). However, in this case, we do not expect severe problems with tuning. The reservoir and the surrounding layers are isotropic and homogeneous, and are well defined in the synthetic data (Figure 9). The fluctuation with frequency is probably related to the geometry in the model, and inaccuracies in the prestack time migration.

In Figure 12, the observed ratios are smaller than the theoretical value (dotted line) which is obtained by computing zero offset reflection coefficients from the baseline and monitor model and taking the ratio. Averaging over a frequency band of 15-40 Hz gives a ratio of reflectivity of . Table 1 summarizes the observed reflectivity ratios and time shifts for the top and base reservoir reflectors, averaged over the 10 traces. Note that the results obtained by peak amplitude analysis do not differ considerably from the results of the spectral ratio method. Thus, for this synthetic dataset, the spectral ratio method gives satisfactory results.

For prestack AVO analysis, the top reservoir and bottom reservoir reflectors were isolated, and reflectivity ratios and time shifts were calculated using the spectral ratio method explained above. In addition, we extracted the peak amplitudes for both reflectors for comparison. In order to minimize problems with interfering wavefields, f-k filtering was applied to the data. Figure 13 shows the reflectivity ratio versus incidence angle for one CMP of the Top reservoir reflector. Note that there is reasonable correspondence

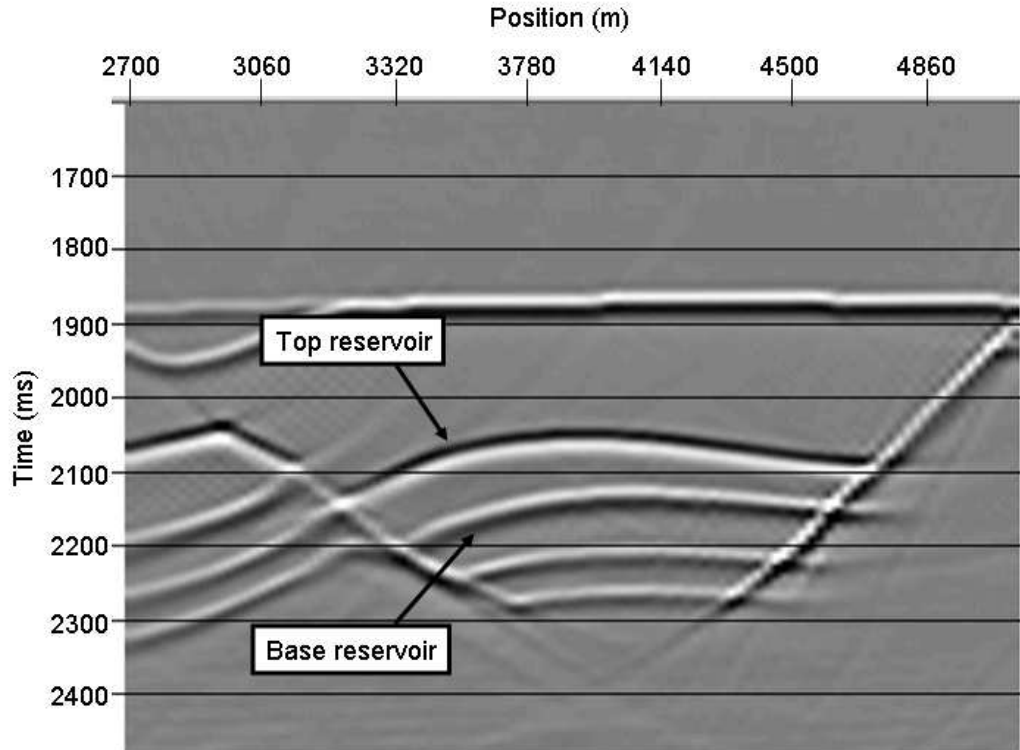


**Figure 9:** Migrated stack of synthetic monitor data, zoomed in on reservoir section. The top and base reservoir reflectors are indicated with arrows.

**Table 1:** Reflectivity ratios and time shifts from analysis of 10 stacked traces for synthetic time-lapse data.

	$R_A/R_B$ , top res.	Time shift, top res. (ms)	$R_A/R_B$ , base res.	Time shift, base res. (ms)
Spectral ratio	$0.20 \pm 0.04$	$0 \pm 4$	$0.16 \pm 0.04$	$17 \pm 5$
Peak ampl.	$0.15 \pm 0.03$	$0 \pm 1$	$0.13 \pm 0.02$	$16 \pm 1$
Expected	0.22	0	0.19	15

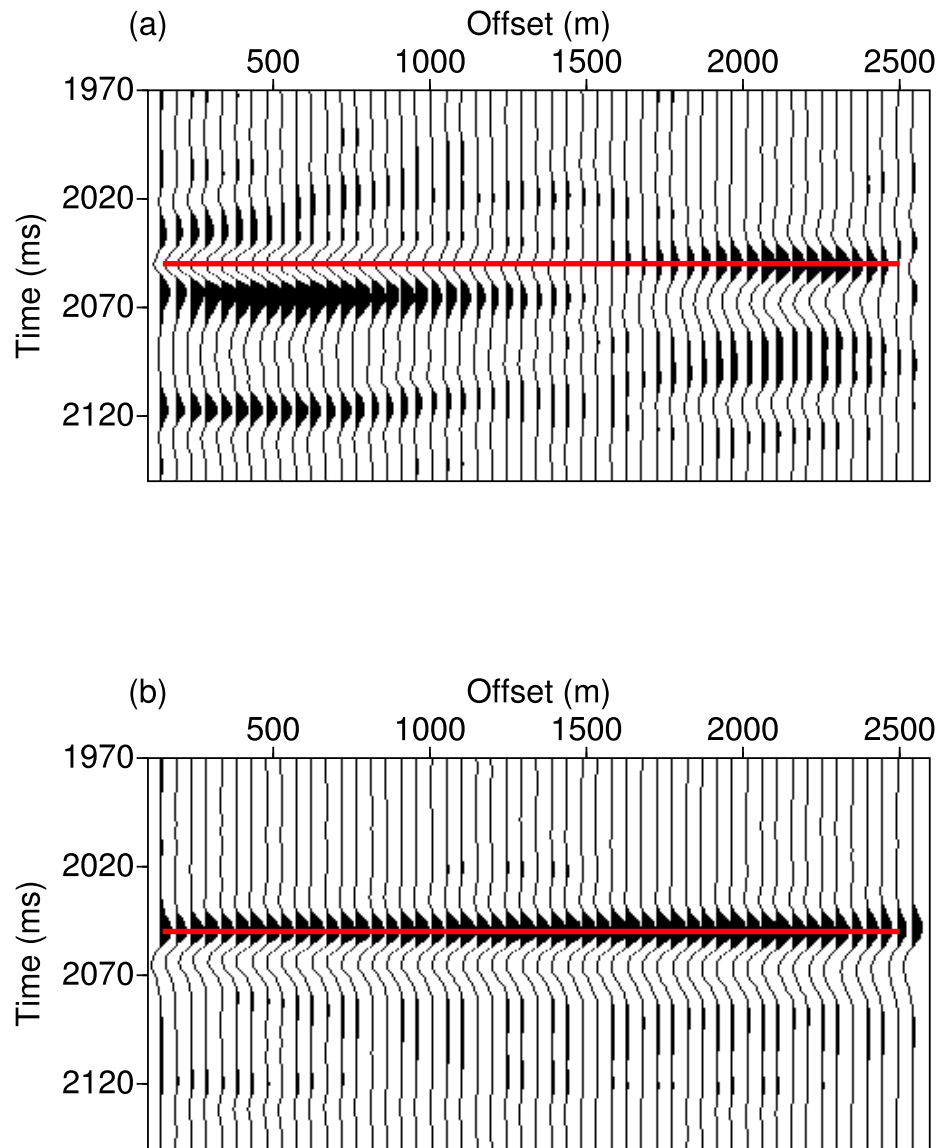


**Figure 10:** Comparison of prestack migrated synthetic gathers from the baseline (a) and monitor (b) synthetic surveys. The solid line marks the top reservoir interface. The baseline gather is upscaled compared to the monitor gather. Note the polarity shift in (a).

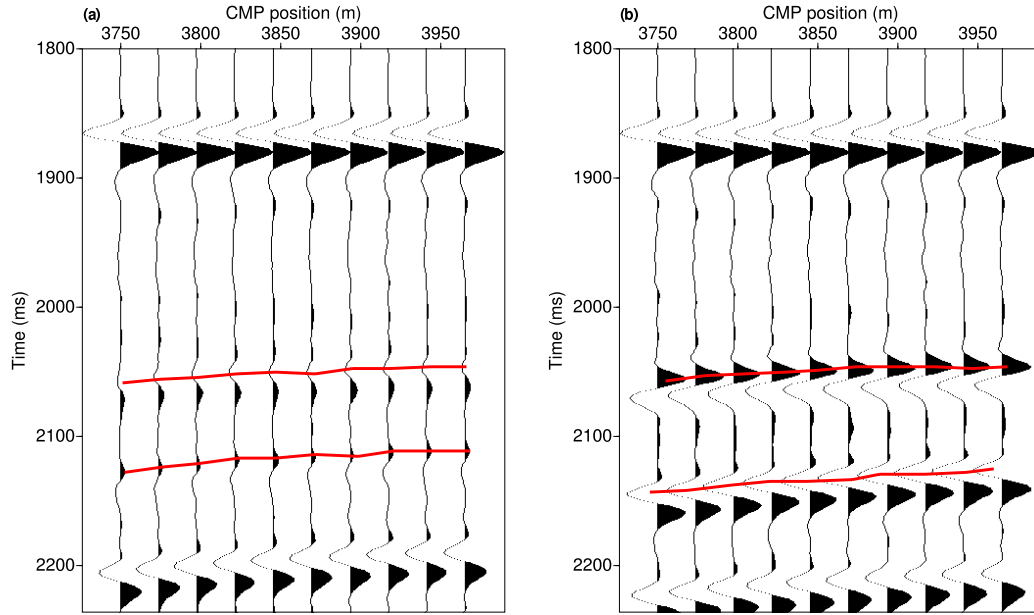
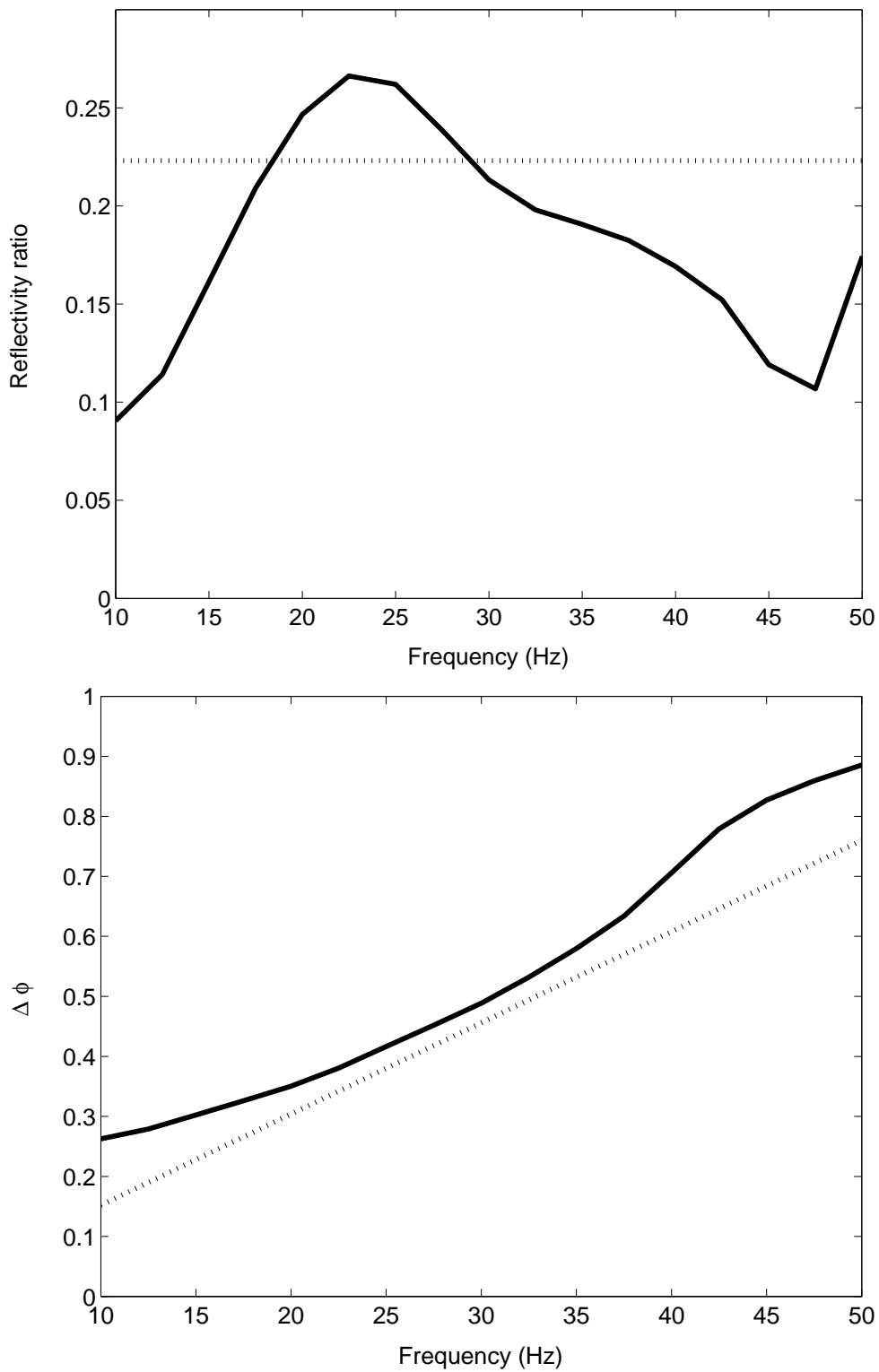


**Figure 11:** Stacked traces from baseline synthetic survey (a) and monitor synthetic survey (b) used to test spectral ratio method. The top and base reservoir events are indicated on the figure.

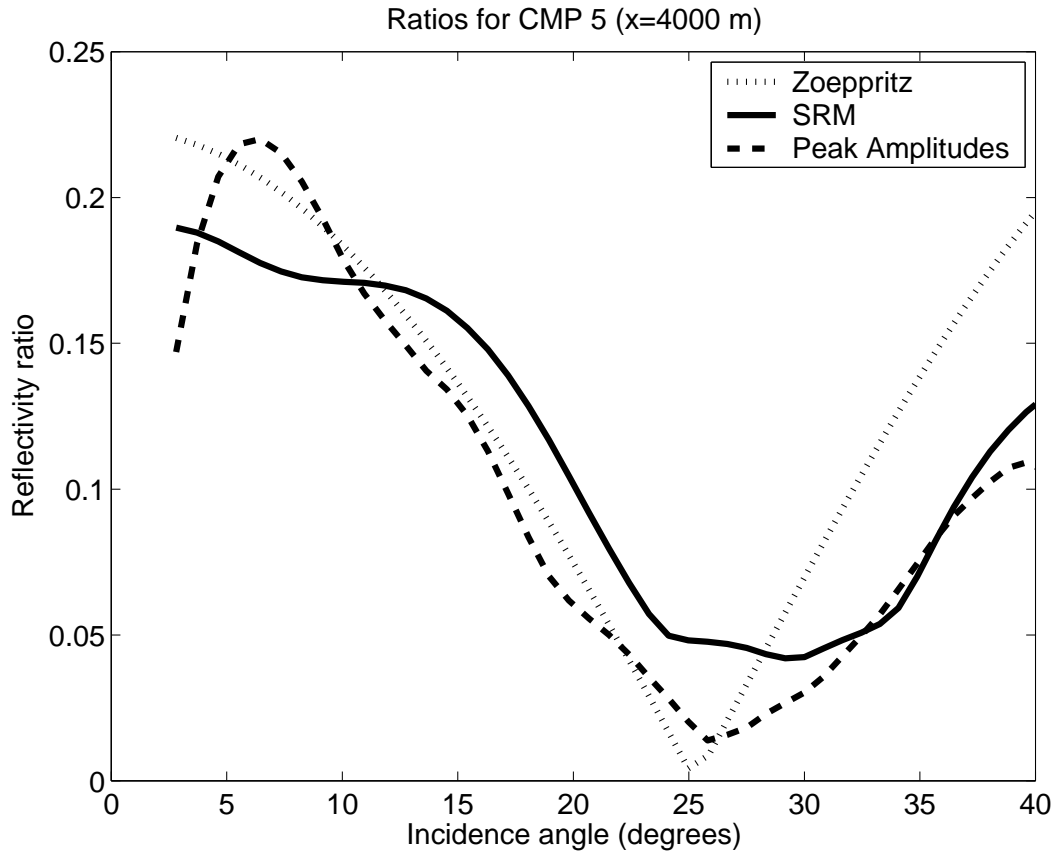
between the ratios computed with the spectral ratio method (black line) and from the peak amplitudes (gray line). Both spectral ratio and peak amplitude data differ slightly from theoretical reflectivity ratios computed from the elastic model (Table 1) with Zoeppritz equations (dotted line). This may be due to interfering wavefields that were not entirely removed by f-k filtering. In addition it looks like the computed incidence angles are too large, possibly as a result of incorrect migration or reflector curvature.

Figure 14 show calculated ratios of reflectivity for a constant angle of incidence. Here, we observe that the ratios computed with the spectral ratio method (black line) are closer to the theoretical values (dotted line) than the ratios computed from peak amplitudes (gray line). The explanation for the discrepancy may be that the peak amplitude data were not smoothed. However, the interfering wavefield may result in differences, since we attempt to suppress the influence of this with f-k filtering before applying the spectral ratio method.

In order to quantify the time-lapse changes in elastic parameters from the ratio of reflectivity data, we use equation (7) with the assumption that we know the reflection coefficient at the time of the baseline survey. The reflection coefficient at the time of the monitor survey is then computed. However, since we are only able to compute the absolute value of the ratio of reflectivity, we need to check the polarity of both the monitor



**Figure 12:** Ratios of reflectivity (a) and phase difference (b) for the top reservoir reflector in the synthetic experiment.



**Figure 13:** Ratios of reflectivity vs. incidence angle for the top reservoir interface for cmp 5. The solid black line represent data computed with the spectral ratio method; the solid grey line is computed with peak amplitudes; and the dotted line are theoretical values computed with zoeppritz equations.

and reference reflected waves to get the correct sign. Observe that for near offsets ( $\lesssim 1200$  m), the polarity of the top reservoir reflector for the monitor survey is reversed compared to the baseline survey. This means that the ratio of reflectivity has a negative sign for these offsets. Hence, we multiply the ratio data for the near offsets by -1. Figure 15 shows the polarity-corrected ratio of reflectivity vs. angle (solid line) compared to the theoretical ratio (dotted line).

From the calculated reflection coefficients for the monitor survey, and the assumed known reflection coefficients for the monitor survey, we computed the change in avo intercept,  $\Delta R_0$ , and in avo gradient,  $\Delta G$ . The values were obtained by linear least squares fitting of the data. Figure 16 shows a cross-plot of  $\Delta R_0$  vs.  $\Delta G$ , obtained from the spectral ratio method (black squares) and the peak amplitudes (gray triangles). Note that the values of  $\Delta R_0$  agree well, but that the values of  $\Delta G$  differ significantly. It is clear that the values computed from peak amplitudes correspond best to the theoretical value (black circle), which is obtained from equation (9).

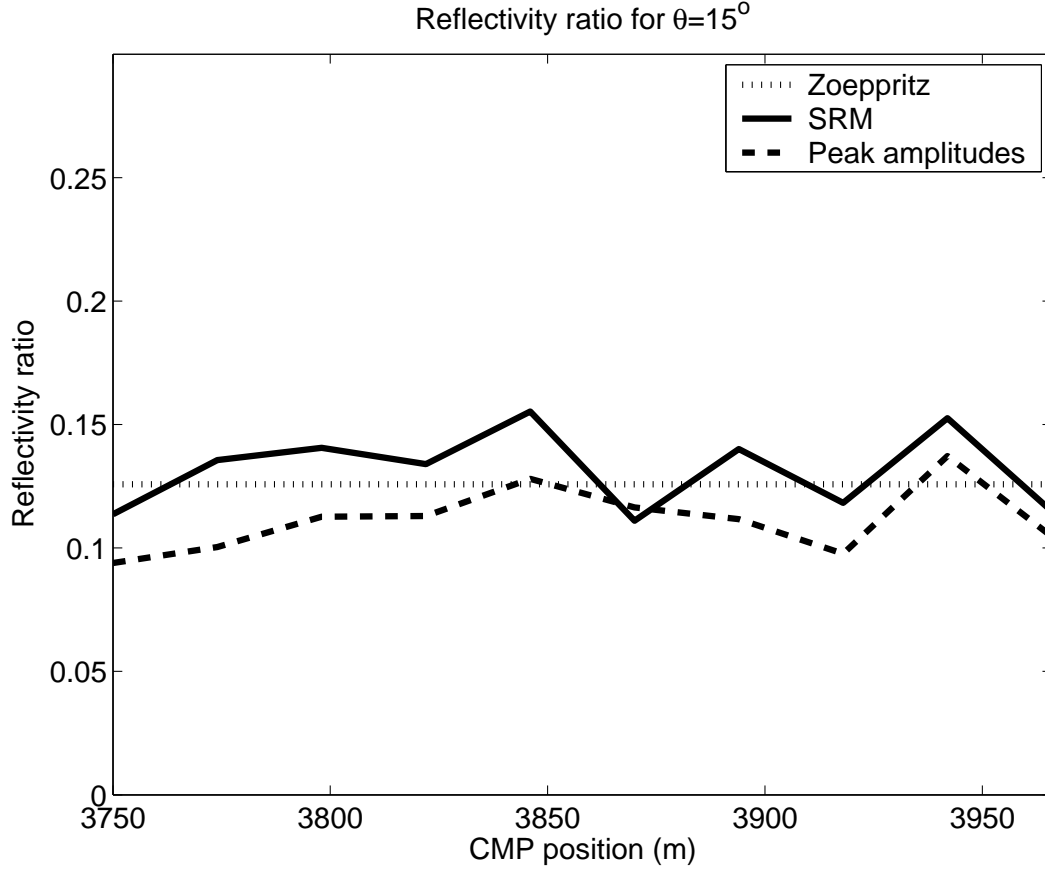


**Figure 14:** Ratios of reflectivity for CMP 1-10. The incidence angle is  $16^\circ$ . The solid black line represent data computed with the spectral ratio method; the solid grey line is computed with peak amplitudes; and the dotted line are theoretical values computed with zoeppritz equations.

The analysis indicate that peak amplitudes are better suited for quantification of time-lapse changes in elastic parameters than data obtained from the spectral ratio method. This is related to the nonlinear nature of the ratio data. Consider the values for reflectivity ratios at  $20^\circ$  in Figure 13. The value obtained from the spectral ratio method is approximately 0.1, while the theoretical value is 0.075. Thus, using equation (7) to estimate the value for the reflection coefficient gives

$$R_B = \frac{R_A}{0.1} = 0.75 \frac{R_A}{0.075}. \quad (10)$$

I.e., 25% lower than the true value. Using peak amplitudes, we do not encounter this problem, since the values obtained from  $R_B$  in this case are independent of the values obtained for  $R_A$ , except for a global scaling factor.

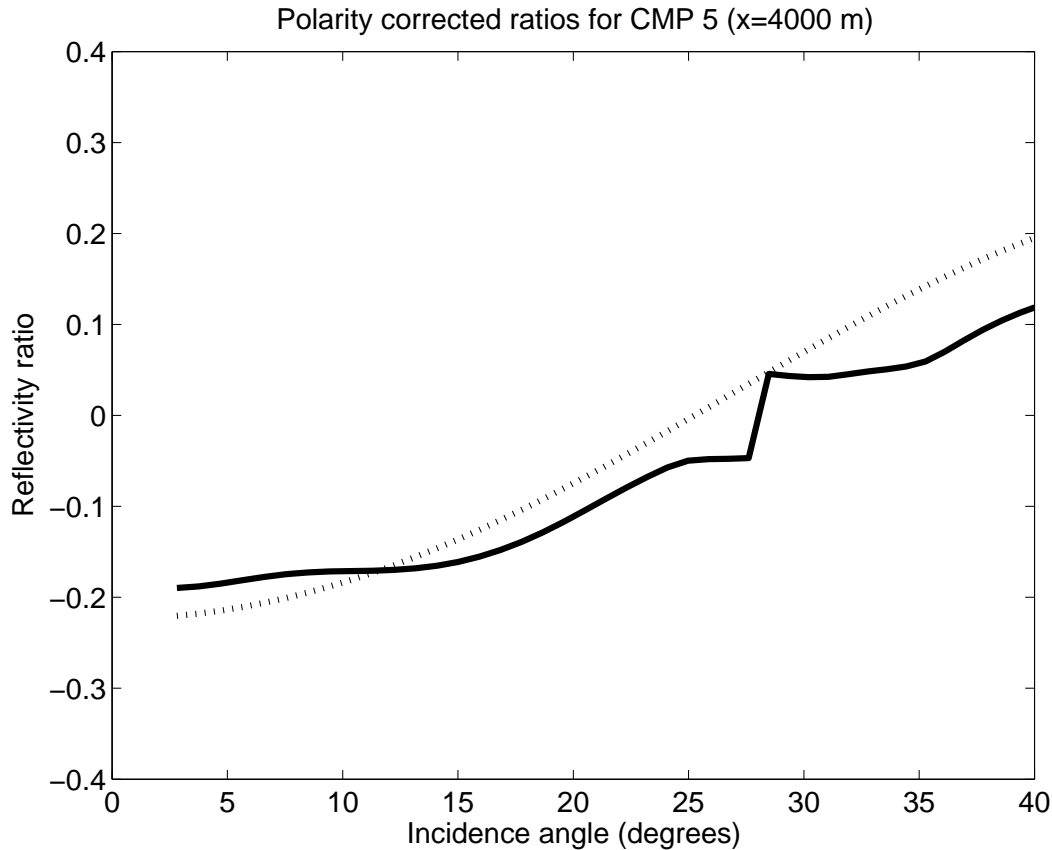


**Figure 15:** Ratios of reflectivity vs. incidence angle for the top reservoir interface for cmp 5, corrected for polarity shifts in the data. The solid black line represent data computed with the spectral ratio method; the dotted line represent theoretical values computed with zoeppritz equations.

### 3.2 Gullfaks data

For the Gullfaks data, we used the upper interpreted reflector in Figure 1 for source wavelet substitution.. By visual inspection, 31 CMP's with good S/N ratio were selected from the dataset. For these CMP's, the Top Cook and the Top Statfjord reflectors were isolated and reflectivity ratios and time shifts were calculated for both interfaces. As for the synthetic data, we extracted peak amplitudes for comparison of the results.

First, we consider stacked traces in order to test the validity of the spectral ratio method for this dataset. The observed ratios of reflectivity for the Top Cook interface, averaged over 8 traces from inline 2761 is shown in Figure 17 (solid line). Standard deviations are shown as dotted lines. Note that the observed ratios are uniformly less than 1, indicating a time-lapse change of the reflection coefficient at this interface. However, we observe considerable fluctuations with frequency. As for the synthetic case we attempt to



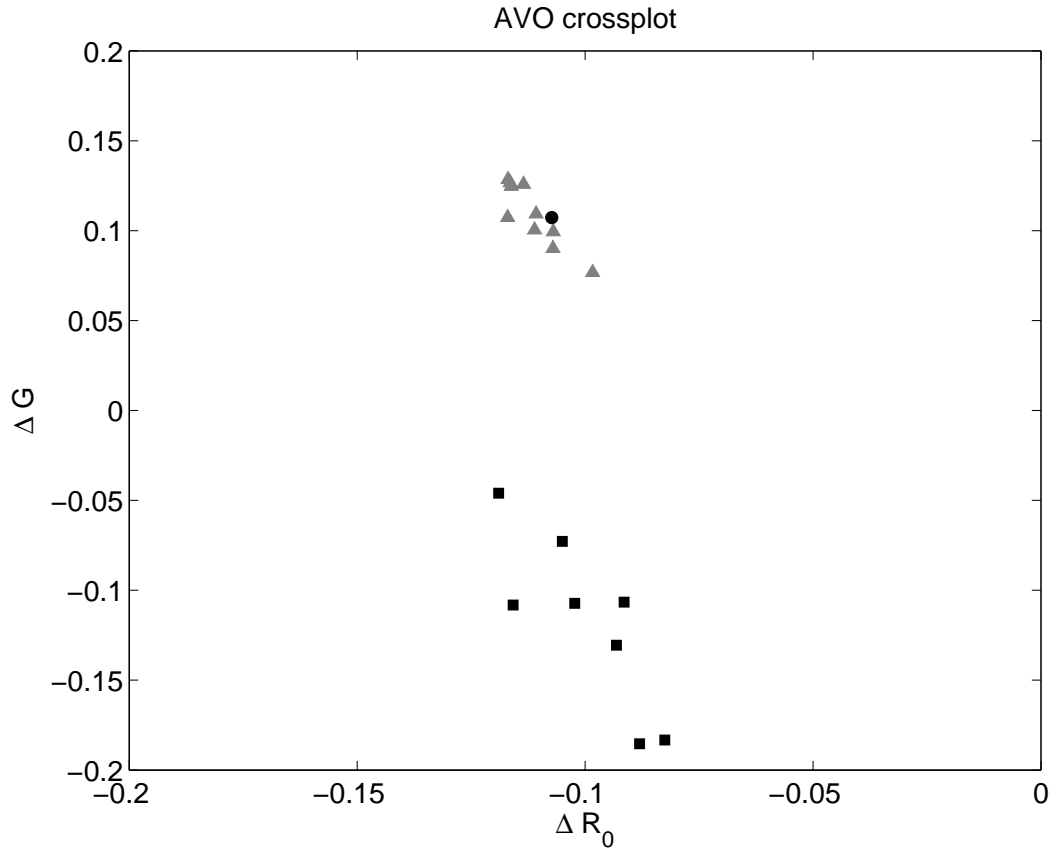


**Figure 16:** Crossplot of  $\Delta R_0$  vs  $\Delta G$ . The black squares represent data obtained from the spectral ratio method, the grey triangles represent values obtained from peak amplitudes, and the black circle represent the theoretical value.

compensate for this by averaging over the dominant frequencies.

Since we are working with real data, it is possible that the windowed reflection that we use for source wavelet substitution in equation (5) does not represent the shape of the true source wavelet. Further, effects of fine layering may distort the signal from the horizon used for source wavelet substitution as well as for the horizon that we wish to monitor. Thus, we need to consider both reflections when finding an appropriate frequency range for the spectral ratio method. Figure 18 shows the normalized amplitude spectra of the nominator (black line) and the denominator (gray line) of the left hand side of equation (5) for one of the traces. Note that frequencies between approximately 20 Hz and 35 Hz dominate. Consequently, we average over this frequency band to find an estimate for the ratio of reflection coefficients for this trace. Similarly, we average over dominant frequencies for the other traces. Table 2 summarizes the observed amplitude ratios and time shifts for the Top Cook and Top Statfjord interfaces. The data are averaged over 8 traces from inline 2761. Note that the observed ratios of reflectivity are comparable with the results obtained from peak amplitudes. However, there are large uncertainties in the

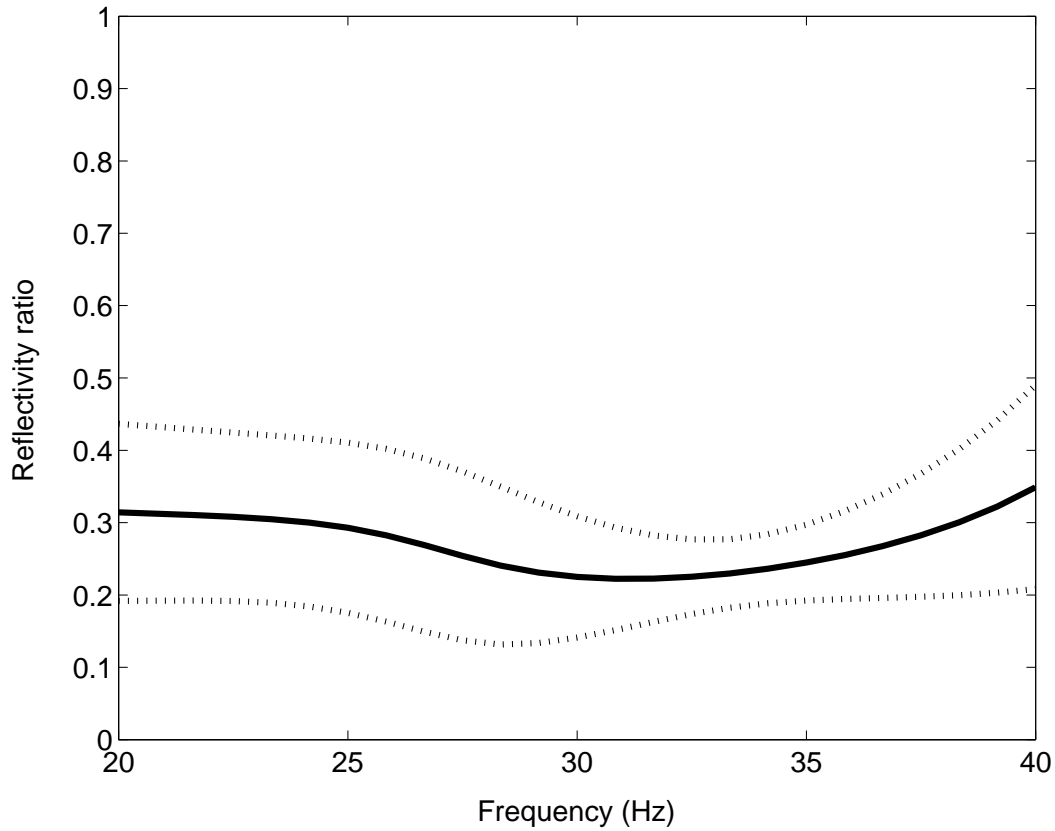


**Figure 17:** Ratios of reflectivity vs. frequency for the Top Cook interface, averaged over 8 traces from inline 2761. The dotted lines correspond to one standard deviation and indicate the spread in the data.

**Table 2:** Reflectivity ratios and time shifts from analysis of 8 stacked traces of inline 2761.

	$R_A/R_B$ , Top Cook	Time shift, Top Cook (ms)	$R_A/R_B$ , Top Statfj.	Time shift, Top Statfj. (ms)
Spectral ratio	$0.28 \pm 0.1$	$-2 \pm 8$	$1.1 \pm 0.4$	$4 \pm 3$
Peak ampl.	$0.30 \pm 0.06$	$-1 \pm 10$	$1.28 \pm 0.6$	$10 \pm 2$

time shift data computed with the spectral ratio method.

The observed time-lapse change at the Top Cook interface was examined further by applying the spectral ratio method to prestack seismic data. Figure 19 shows the reflectivity ratios for the Top Cook interface vs. incidence angle, averaged over all CMP's. Note that there is good correspondence between the data obtained from the spectral ratio method

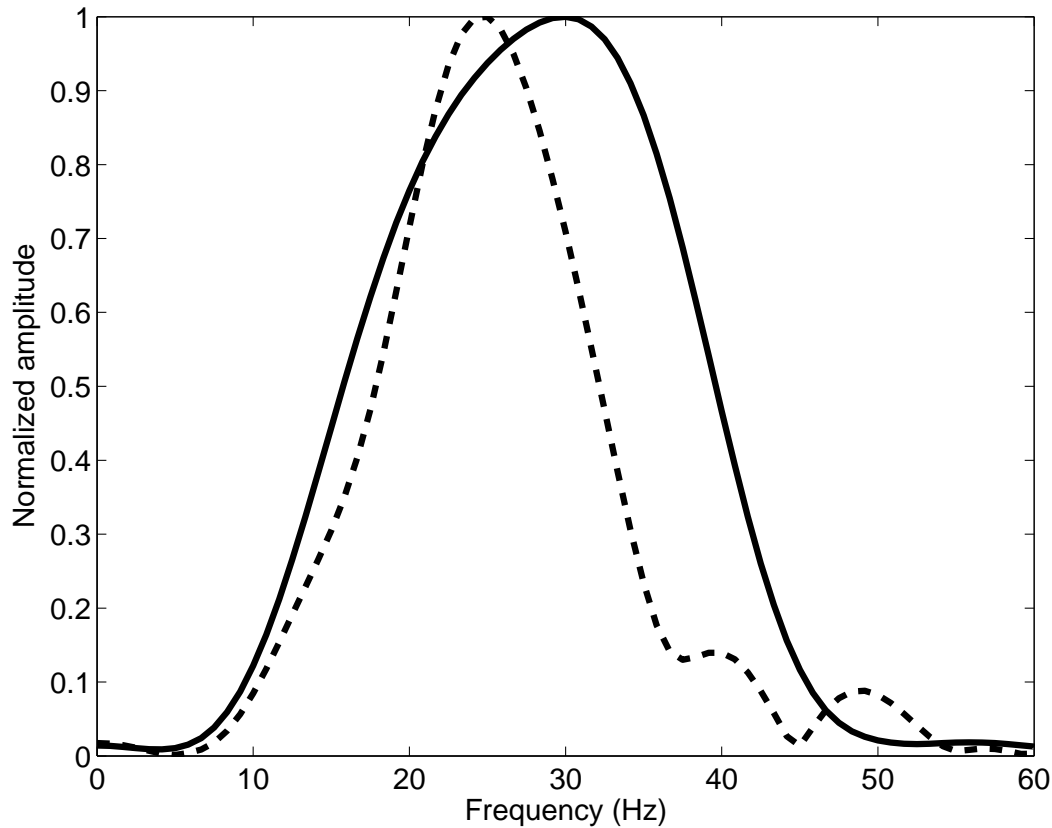


**Figure 18:** Normalized amplitude spectra for the nominator (black line) and denominator (grey line) of the left hand side of equation (5), computed for the Top Cook interface.

(black solid line) and the data obtained from peak amplitudes (gray solid line). The dotted lines indicate the spread in the data obtained with the spectral ratio method (one standard deviation). The ratios of reflectivity for the Top Cook interface are significantly different from 1, which is a clear indication of time lapse changes. This can be verified by visual inspection of Figures 1a and 1b.

The reflectivity model for the Top Cook interface (Table 3), used for computing the reflection coefficient at the time of the monitor survey was taken from a nearby well log. No S-wave log was available, so S-wave velocities were calculated assuming that the  $V_p/V_s$  ratio at this depth is 1.8.

Based on the reflectivity model and the amplitude ratio data, values for  $\Delta R_0$  and  $\Delta G$  were calculated. Figure 20 shows a plot of  $\Delta R_0$  vs  $\Delta G$  obtained from the spectral ratio method (black squares) and peak amplitudes (gray triangles). Note that there is good agreement. However, the data calculated from peak amplitudes are better confined than the data calculated from the reflectivity ratio data.

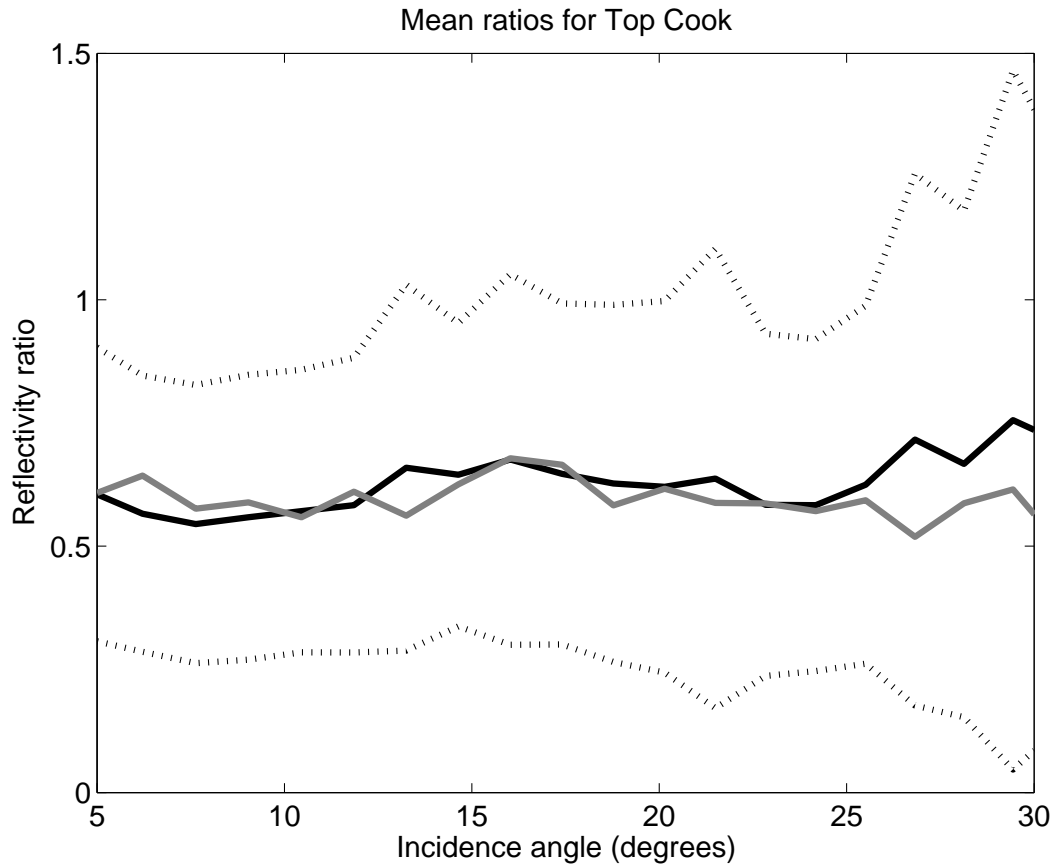


**Figure 19:** Ratios of reflectivity vs. incidence angle for the Top Cook, averaged over all CMP's. The solid black line represent data computed with the spectral ratio method; the grey line represent data obtained from peak amplitudes; and the dotted lines represent one standard deviation from the spectral ratio data.

**Table 3:** Elastic model used to compute reflection coefficients for top Cook interface.

	$V_p$ (m/s)	$V_s$ (m/s)	$\rho$ (kg/m <sup>3</sup> )
Cap rock	2580	1180	2300
reservoir	2630	1340	2350

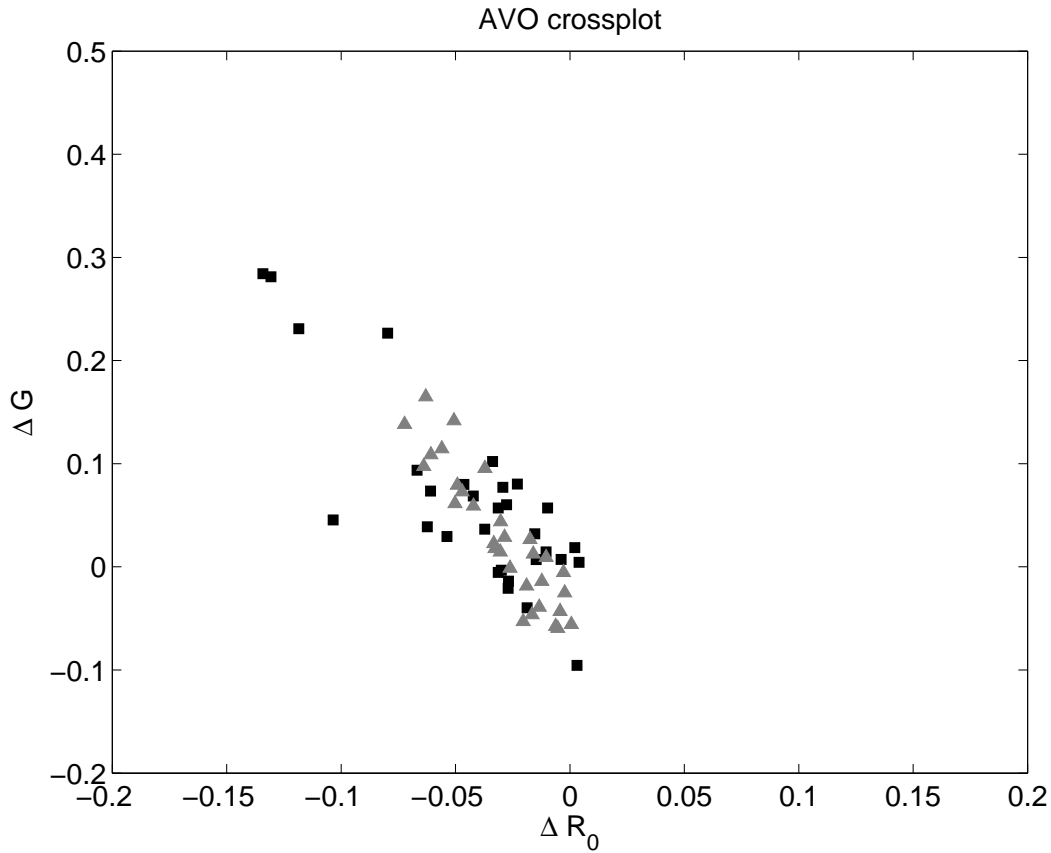


**Figure 20:** Crossplot of  $\Delta R_0$  vs  $\Delta G$  for Top Cook interface. The squares represent data obtained from the spectral ratio method, the triangles represent values obtained from peak amplitudes.

## 4 Discussion

The method described here aims to detect and quantify changes in the subsurface from repeated seismic data. A simple 1D example showed that the method, in theory, compensates for variations in source wavelet between the surveys. However, there are many sources of errors in time-lapse seismic data which are not properly addressed with this method. For instance, if the source and receiver positions are not repeated sufficiently well in the monitor seismic survey, this will cause artificial differences in the time-lapse seismic data. This effect will be significant in cases with small-scale velocity anomalies in the overburden, causing the recorded wavefield from similar offsets to have different character (referance). However, these are errors that are hard to remove with processing. Instead, it is important to have a feeling for the limitations of a time-lapse seismic dataset. Fortunately, for the Gullfaks data, this does not represent a severe problem.

Equation (5) states that reflectivity ratios and time shifts computed with the spectral ratio method are constants with frequency. However, application of this method to synthetic and real stacked seismic data show that this is not the case. We have demonstrated that fluctuation with frequency may be caused by tuning effects. However, in the synthetic case, it is more likely that the geometry in the model is the cause. It is possible that geometry also may be of significance for the Gullfaks data.

In a time-lapse setting, it is often of interest to monitor changes in thin zones, sometimes much thinner than the dominant wavelength. In this case, the time-lapse differences themselves are effects of fine-layering, and is only visible as tuning effects on amplitudes. In this case, we can not expect the spectral ratio method to give satisfactory results, since this may affect the frequency content of the reflected signal.

Another complicating factor is time-lapse changes in absorption. Ultrasonic measurements (Tokoz et al., 1979) show that the quality factor is a function of both saturation and pore pressure. If this effect is significant, the seismic amplitude will change independent of changes in the reflection coefficient. However, we have no reason to believe that this effect will cause more errors with the spectral ratio approach than any other method of time-lapse seismic monitoring.

The results from the synthetic and real studies show that time-lapse AVO analysis based on peak amplitudes is more stable than time-lapse AVO analysis based on spectral ratio data. This is related to the nonlinear nature of the spectral ratio data, which are more sensitive to noise than amplitude data. We observed larger uncertainties in the results for spectral ratio data. For the synthetic data case, we obtained an erroneous value for the change in AVO gradient  $\Delta G$ . However, the results overall agree well with results obtained from analysis of peak amplitudes, indicating that the reflectivity ratios contain information on time-lapse changes in elastic parameters.

## 5 Conclusions

Analysis of both synthetic and real seismic data show that the spectral ratio approach presented here gives ratios of reflectivity that agree well with those obtained from peak amplitude analysis. For the synthetic case, we also were able to obtain good estimates for the time shifts, but in the real data case, there were large uncertainties.

The nonlinear nature of the reflectivity ratio introduces uncertainties in the prestack AVO analysis. Computed changes in AVO intercept,  $R_0$ , and gradient,  $G$ , show significantly more spread than when computed from peak amplitudes. However, the results for  $R_0$  are in agreement with results obtained from peak amplitudes.

The advantage of this method is that it is able to suppress time-lapse differences in the source wavelet. For conventional time-lapse AVO analysis, this must be taken care of by wavelet processing of both datasets (e.g., spiking deconvolution). The real data example does not demonstrate this advantage of the spectral ratio method, since spiking deconvolution was applied to the data.

In a time-lapse setting, this methodology could serve as a relatively fast, but less accurate, alternative than more conventional AVO analysis methods (peak amplitudes, AVO inversion).

## **6 Acknowledgements**

Statoil ASA and their license partners at Gullfaks, Norsk Hydro ASA and Petoro AS are acknowledged for permission to show the data. Alexey Stovas is acknowledged for help with the fine layered modeling.

## Chapter 7

# Discrimination between Phase and Amplitude Attributes in Time-Lapse Seismic Streamer Data

Jesper Spetzler<sup>1</sup> and Øyvind Kvam<sup>2</sup>

<sup>1</sup>*Department of Geotechnology, TU Delft  
P.O. Box 5028, NL-2600 GA Delft the Netherlands.*

<sup>2</sup>*Department of Petroleum Engineering and Applied Geophysics  
Norwegian University of Science and Technology  
S.P. Andersens vei 15A, 7491 Trondheim, Norway*

**ABSTRACT:** In time-lapse seismic experiments, one wants to obtain information about production related effects in hydrocarbon reservoirs to increase the recovery percentage. However, non-repeatability problems such as acquisition differences, overburden effects and noise are often significantly stronger than the imprint of production changes in time-lapse seismic data sets. Consequently, it is very difficult to appraise the changes in the petrophysical reservoir parameters over time. We introduce a 4D monitoring approach that is based on the spectral ratio method. Thereby, it is possible to monitor production reservoirs for time-lapse effects in the two seismic attributes that are phase and amplitude, while simultaneously correcting for the major causes of non-repeatability in repeated surveys. The time-lapse method is applicable to structurally simple overburden and reservoirs. In addition, the monitoring algorithm is validated using a synthetic time-lapse streamer data set and is as well applied on real time-lapse prestack streamer data from the Troll West Gas Province in the North Sea.



# 1 Introduction

The success of time-lapse (also known as 4D) reservoir monitoring depends heavily on the suppression of non-repeatability effects. Examples of problems with non-repeatability effects in marine 4D seismic experiments are differences in the airgun-hydrophone response, differences in the source-receiver positions in the vertical and horizontal direction, seasonal changes in the water temperature (e.g., a temperature shift of 10 to 15 degrees from summer to winter resulting in different sound speeds), tidal differences, changes in the elastic wavefield parameters in the overburden above the producing reservoir due to subsidence and/or compaction, random noise in the recording units and coherent noise such as free surface multiples. All these non-repeatability effects may introduce phase and amplitude changes of reflected wavefields in the time-lapse experiment which can be much stronger than the signature of production related 4D differences. It is therefore important to take non-repeatability effects into account when monitoring a reservoir over time.

Several time-lapse monitoring experiments and methods are reported in the literature. Sønneland et al. (1997) and Boyd-Gorst et al. (2001) perform a time-lapse monitoring of the Nelson field and the Gullfaks field, respectively, both in the North Sea using synthetic wavefield modelling combined with a reservoir simulation model. Biondi et al. (1998) show an example of reservoir monitoring in which they correctly recognize that time-lapse seismics is a multidisciplinary study using all available reservoir data. Lumley (2001) discusses the concept of 4D seismic reservoir monitoring and possible approaches to tackle problems with non-repeatability effects in time-lapse experiments. Landrø (2001) makes use of PP AVO data to distinguish between pore-pressure and saturation changes. Kragh and Christie (2002) discuss the meaning of seismic repeatability in terms of normalised rms (Nrms) and predictability. Laws and Kragh (2002) investigate the effect of rough sea in 4D seismic experiments, and find that a 2 meter difference in sea state height changes the 4D Nrms from 5% to 10%. Bertrand and MacTeth (2003) focus on the non-repeatability problem with sea water velocity variations in real-time reservoir monitoring. By using data processing such as deterministic tidal time shift correction and regularisation of irregularly sampled streamer data, Eiken et al. (2003) are able to reduce the Nrms value to 12% for a deep, structurally complex field and 6% for a shallow, structurally simple field.

The spectral ratio approach (Aki and P, 1980; Mavko et al., 1998) permits to define a monitoring method that separates amplitude and phase related to time-lapse changes in reflected waves. Thereby time-lapse changes are evaluated at reservoir level in the reflection coefficient and traveltimes shift of seismic wavefields. At the same time, the 4D monitoring approach takes the non-repeatability effects inherent to source wavelet variability and to changes in the overburden during production into account. We performed a detailed literature research to look for other stable 4D seismic monitoring methods which separate the amplitude and phase information of time-lapse signals while simultaneously

correcting for these two significant non-repeatability causes. The current time-lapse methods are cross-correlation and differencing of cross-equalised wavefields. Cross-correlation methods will provide information about differences in travel times only. The difference of cross-equalised wavefields (e.g., Nrms-predictability cross-plotting processing schemes, (Kragh and Christie, 2002), or match-filters) includes a mix of phase and amplitude information. In addition, cross-correlation methods and difference wavefield based approaches are strongly sensitive to differences in the source-receiver coupling and to overburden effects.

In our time-lapse monitoring approach, the reference and monitor wavefields from a reflecting interface above the producing reservoir are combined with the reflected wavefield from the reservoir level in a convolution-deconvolution operation. Thereby, it is possible to perform the automatic correction for source-receiver coupling variability and overburden differences while appraising the 4D production effects in the amplitude and phase of the time-lapse data. In addition, it turns out that amplitude information as 4D attribute is little sensitive to the non-repeatability problem with misposition of source-receiver locations. We test the time-lapse monitoring method on synthetic prestack data before and after migration. The 2D lateral variant elastic model includes many important non-repeatability problems. Also, the 4D monitoring approach is applied on one subline of prestack streamer data from the Troll West Gas Province.

First, the time-lapse monitoring method using the phase and amplitude attribute of reflected wavefields separately is explained. Next, the synthetic time-lapse experiment with major causes of non-repeatability effects is demonstrated. Then, the real data example from the Troll field is presented. Finally, conclusions are drawn.

## **2 Time-lapse changes in phase and amplitude attributes of reflected wavefields**

In this section, we present the reservoir monitoring method that applies the 4D seismic attributes phase and amplitude of reflected wavefields in a time-lapse data set. The 4D monitoring algorithm makes use of convolution and deconvolution of wavefields, hence we choose to work in the frequency domain where convolution and deconvolution of wavefields simply are multiplication and division operations.

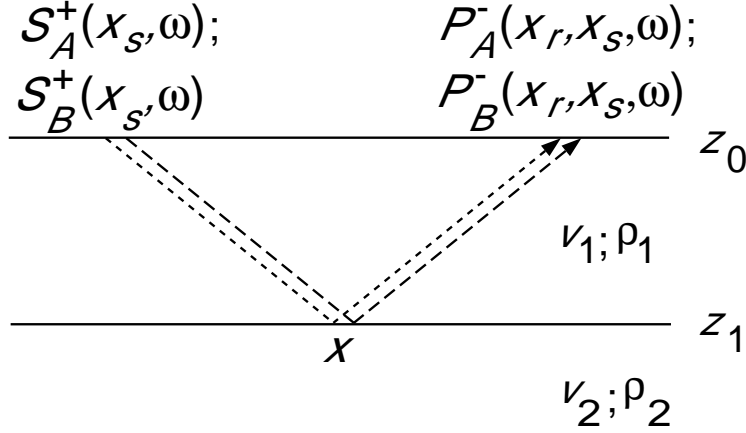


**Figure 1:** Definition of the one-layer model for reflected wavefields in the reference survey *A* (dotted line) and monitor survey *B* (dashed line).

## 2.1 Discrimination between phase and amplitude

We start by analysing the most simple configuration. In Figure 1, a 4D experiment using a one-layer model for a reference survey (*A*) and a monitor survey (*B*) is illustrated for a wavefield that is reflected at the interface at depth  $z_1$ . The terminology for one-way wavefields is applied here. Down-going and up-going wavefields are denoted with a plus- and minus-sign, respectively, in the superscript, while the subscript refers to the reference and monitor survey. In addition, we assume that the source and receiver positions are identical in the two surveys. The problem with mispositioning of source-receiver geometry will be discussed in the last part in the theory section.

For the configuration in Figure 1, the source wavelets  $S_A^+(x_s, \omega)$  and  $S_B^+(x_s, \omega)$  at the angular frequency  $\omega$  in the two surveys are equal to the down-going wavefields at the source position  $x_s$ , hence

$$P_A^+(x_s, \omega) = S_A^+(x_s, \omega) \quad \text{and} \quad P_B^+(x_s, \omega) = S_B^+(x_s, \omega). \quad (1)$$

The up-going wavefields that are reflected at the specular reflection point  $x$  and then recorded at the receivers at position  $x_r$  in the reference and monitor survey are given by

$$P_A^-(x_r, x_s, \omega) = A_A(x_r, x_s, \omega) W_A^-(x_r, x) R_{A,1}(x) W_A^+(x, x_s) S_A^+(x_s, \omega), \quad (2)$$

and

$$P_B^-(x_r, x_s, \omega) = A_B(x_r, x_s, \omega) W_B^-(x_r, x) R_{B,1}(x) W_B^+(x, x_s) S_B^+(x_s, \omega), \quad (3)$$

where the reflection coefficient is denoted by  $R(x)$  and the phase propagators  $W^+(x, x_s, \omega)$  and  $W^-(x_r, x, \omega)$  are equal to  $\exp(-i\omega t(x_r, x_s))$  with the time parameter  $t(x_r, x_s)$  denoting

the two-way traveltime (Wapenaar and Berkhout, 1989). The complex amplitude factor  $A(x_r, x_s, \omega)$  includes geometrical spreading and transmission effects due to layering.

For the moment, we assume that the source wavelets  $S_A^+(x_s, \omega)$  and  $S_B^+(x_s, \omega)$  are known. To correct for source wavelet variations between the reference and monitor survey, the up-going reference wavefield is convolved with the down-going monitor wavefield and vice versa. Then the ratio between  $P_A^- P_B^+$  and  $P_A^+ P_B^-$  at position  $x_r$  is computed (i.e. a deconvolution operation), hence for precritical surface data

$$\begin{aligned} \frac{P_A^- P_B^+}{P_A^+ P_B^-}(x_r, x_s, \omega) &= \frac{A_A(x_r, x_s, \omega) W_A^-(x_r, x) R_{A,1}(x) W_A^+(x, x_s) S_A^+(x_s, \omega) S_B^+(x_s, \omega)}{S_A^+(x_s, \omega) A_B(x_r, x_s, \omega) W_B^-(x_r, x) R_{B,1}(x) W_B^+(x, x_s) S_B^+(x_s, \omega)} \\ &\approx \frac{R_{A,1}}{R_{B,1}}(x) e^{-i\omega \delta t_1(x_r, x_s)}, \end{aligned} \quad (4)$$

where the ratio of phase operators  $(W_A^-(x_r, x) W_A^+(x, x_s)) / (W_B^-(x_r, x) W_B^+(x, x_s))$  is equal to  $\exp(-i\omega \delta t_1(x_r, x_s))$ , and the two-way traveltime shift  $\delta t_1(x_r, x_s)$  equals  $t_{A,1}(x_r, x_s) - t_{B,1}(x_r, x_s)$  in layer one. The ratio  $A_A(x_r, x_s, \omega) / A_B(x_r, x_s, \omega)$  is close to unity in 4D seismic experiments, hence the approximation sign. By combining phase and modulus of equation (4), the time delay  $\delta t_1(x_r, x_s)$  and the ratio of reflection coefficients  $R_{A,1}/R_{B,1}(x)$  at frequency-component  $\omega$  are estimated in separate terms. Let the complex number  $c(x_r, x_s, \omega)$  be equal to  $P_A^- P_B^+ / P_A^+ P_B^- (x_r, x_s, \omega)$ , then we obtain that

$$\delta t_1(x_r, x_s) = -\frac{\angle c(x_r, x_s, \omega)}{\omega} \quad \text{and} \quad \frac{R_{A,1}}{R_{B,1}}(x) = \text{sgn}(\text{pol}) \|c(x_r, x_s, \omega)\|, \quad (5)$$

where  $\angle c(x_r, x_s, \omega)$  and  $\|c(x_r, x_s, \omega)\|$  are the phase and modulus, respectively. Notice that the complex norm  $\|c(x_r, x_s, \omega)\|$  always returns an absolute number, thus  $\|c(x_r, x_s, \omega)\|$  in the ratio of reflectivity formula is multiplied by the operator  $\text{sgn}(\text{pol})$  that accounts for changes in polarisation between the reference and monitor wavefield.

Instead of estimating time shifts and ratios of reflection coefficients at a single frequency as in expression (5), we propose to evaluate  $\delta t_1(x_r, x_s)$  and  $R_{A,1}/R_{B,1}(x)$  over a frequency-band from  $\omega_c - \Delta\omega$  to  $\omega_c + \Delta\omega$  for which the signal-to-noise (S/N) ratio is high.

According to expression (5), the time-lapse two-way traveltime shift and ratio of reflection coefficient are equal to zero and one, respectively, when there are no time-lapse differences in the one-layer model shown in Figure 1. On the other hand, with significant 4D changes in the one-layer model, the two-way traveltime shift and the ratio of reflection coefficients deviate considerably from zero and one. Hence, by inspecting these two seismic attributes, we can monitor the subsurface for 4D changes in wavefield parameters.

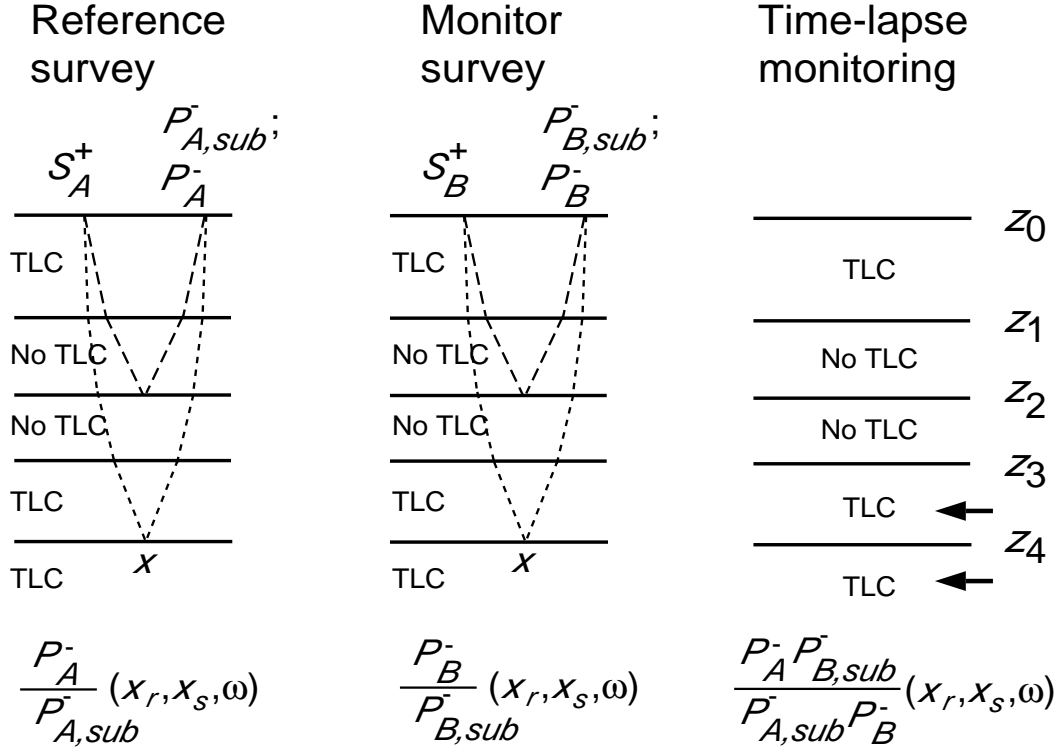


**Figure 2:** Definition of the multi-layer model for reflected wavefields. There are no time-lapse changes in layers 2 and 3, while there may be time-lapse changes in layer 1, 4 and 5. The reference wavefield  $P_{A,sub}^-(x_r, x_s, \omega)$  and monitor wavefield  $P_{B,sub}^-(x_r, x_s, \omega)$  used for the source-receiver response and overburden function correction in the time-lapse experiment are indicated with the dashed line, respectively. To monitor time-lapse changes in phase and amplitude above and below interface at depth  $z_4$ , the reference  $P_A^-(x_r, x_s, \omega)$  and monitor reflected wavefield  $P_B^-(x_r, x_s, \omega)$  are applied (dotted lines). The sketch illustrates the physical effect of the wavefield ratio.

## 2.2 Correction for source-receiver response and overburden differences

It is often very difficult to estimate accurately the source wavelet in seismic exploration. In addition, overburden effects can corrupt the production related signal considerably. However, by replacing the down-going wavefields in equation (4) with reflected wavefields from regions where no time-lapse changes exist, the differences in source-receiver response and in the overburden between the reference and monitor survey can be taken into account.

The multi-layer model in Figure 2 illustrates how a source-receiver response and overbur-

den function correction in a 4D experiment can be performed by substituting down-going wavefields  $P_A^+(x_s, \omega)$  and  $P_B^+(x_s, \omega)$  with the upgoing reference and monitor wavefields  $P_{A,sub}^-(x_r, x_s, \omega)$  and  $P_{B,sub}^-(x_r, x_s, \omega)$ , respectively. In Figure 2, the layers 1,2 and 3 represent the overburden that includes time-lapse changes (TLC) in layer 1. The layers 4 and 5 are the target zone for 4D monitoring. There can be time-lapse changes in layer 4 and 5. The reference and monitor wavefields  $P_{A,sub}^-(x_r, x_s, \omega)$  and  $P_{B,sub}^-(x_r, x_s, \omega)$ , respectively, are reflected at the interface at depth  $z_2$ , and the wavefields  $P_A^-(x_r, x_s, \omega)$  and  $P_B^-(x_r, x_s, \omega)$  in the 4D data are reflected at the interface at depth  $z_4$ . To compensate for differences in the source-receiver coupling and overburden in the time-lapse data set, we make the substitution for the source terms in equation (4), thus

$$S_A^+(x_s, \omega) \mapsto P_{A,sub}^-(x_r, x_s, \omega) = A_{A,sub}(x_r, x_s, \omega) W_A^-(x_r, z_0, z_1) W_A^-(z_1, z_2) R_{A,2} \times W_A^+(z_2, z_1) W_A^+(x_s, z_1, z_0) S_A^+(x_s, \omega), \quad (6)$$

and

$$S_B^+(x_s, \omega) \mapsto P_{B,sub}^-(x_r, x_s, \omega) = A_{B,sub}(x_r, x_s, \omega) W_B^-(x_r, z_0, z_1) W_B^-(z_1, z_2) R_{B,2} \times W_B^+(z_2, z_1) W_B^+(x_s, z_1, z_0) S_B^+(x_s, \omega), \quad (7)$$

where  $\times$ -symbol means a multiplication in the frequency-domain.  $A_{sub}(x_r, x_s, \omega)$  denotes the amplitude factor. In expression (6) and (7), the reflection coefficients  $R_{A,2}$  and  $R_{B,2}$  are identical. For simplicity and without loss of generality, we include receiver function changes (e.g., due to different recording units) in the source wavelet term  $S^+(x_s, \omega)$ . The reflected wavefields inherent to the interface at depth  $z_4$  in the reference and monitor survey are given by

$$P_A^-(x_r, x_s, \omega) = A_A(x_r, x_s, \omega) W_A^-(x_r, z_0, z_1) W_A^-(z_1, z_2) W_A^-(z_2, z_3) W_A^-(x, z_3, z_4) R_{A,4}(x) \times W_A^+(x, z_4, z_3) W_A^+(z_3, z_2) W_A^+(z_2, z_1) W_A^+(x_s, z_1, z_0) S_A^+(x_s, \omega), \quad (8)$$

and

$$P_B^-(x_r, x_s, \omega) = A_B(x_r, x_s, \omega) W_B^-(x_r, z_0, z_1) W_B^-(z_1, z_2) W_B^-(z_2, z_3) W_B^-(x, z_3, z_4) R_{B,4}(x) \times W_B^+(x, z_4, z_3) W_B^+(z_3, z_2) W_B^+(z_2, z_1) W_B^+(x_s, z_1, z_0) S_B^+(x_s, \omega). \quad (9)$$

By constructing the ratio of the reflected wavefield from interface  $z_4$  and the one from interface  $z_2$  in one survey, the source-receiver response and the effect of the overburden (above interface  $z_2$ ) cancel out. Hence, for the reference survey the deconvolution of the wavefield in equation (8) with the wavefield in equation (6) gives that

$$\frac{P_A^-}{P_{A,sub}^-}(x_r, x_s, \omega) = \frac{A_A(x_r, x_s, \omega)}{A_{A,sub}(x_r, x_s, \omega)} \frac{R_{A,4}(x)}{R_{A,2}} e^{-i\omega(t_{A,3}(x_r, x_s) + t_{A,4}(x_r, x_s))}. \quad (10)$$

In a similar vein, it follows for the monitor survey that

$$\frac{P_B^-}{P_{B,sub}^-}(x_r, x_s, \omega) = \frac{A_B(x_r, x_s, \omega)}{A_{B,sub}(x_r, x_s, \omega)} \frac{R_{B,4}(x)}{R_{B,2}} e^{-i\omega(t_{B,3}(x_r, x_s) + t_{B,4}(x_r, x_s))}, \quad (11)$$

where  $W^+W^-(x_r, x_s, z_4, z_2) = \exp(-i\omega(t_3(x_r, x_s) + t_4(x_r, x_s)))$ . In Figure 2, the effect of the wavefield deconvolution is illustrated for the reference and monitor survey. By dividing the wavefield ratio for survey A in equation (10) with the one for survey B in equation (11), the time-lapse differences in phase and the ratio of reflectivity are derived. Hence, for precritical surface data

$$\frac{P_A^- P_{B,sub}^-}{P_{A,sub}^- P_B^-}(x_r, x_s, \omega) \approx \frac{R_{A,4}}{R_{B,4}}(x) e^{-i\omega \delta t_4(x_r, x_s)}, \quad (12)$$

which has the same form as the expression (4), since  $t_{A,3}(x_r, x_s) = t_{B,3}(x_r, x_s)$  and  $R_{A,2} = R_{B,2}$ . The ratio of amplitude factors  $A_A A_{B,sub}/A_B A_{A,sub}(x_r, x_s, \omega)$  is close to unity in 4D experiments, therefore the approximation sign in equation (12). The two-way time shift  $\delta t_4(x_r, x_s)$  is generated by time-lapse changes in the velocity of layer 4, and the ratio of reflection coefficients  $R_{A,4}/R_{B,4}(x)$  is measured at interface depth  $z_4$ . In Figure 2, the physics of equation (12) is illustrated. The arrows point out the layers 4 and 5 which are monitored for 4D changes in the phase and amplitude attribute.

## 2.3 Limitation of time-lapse monitoring algorithm

The time shift  $\delta t(x_r, x_s)$  is correctly obtained only when

$$-\frac{\pi}{\omega} \leq \delta t(x_r, x_s) \leq \frac{\pi}{\omega}, \quad (13)$$

since the arithmetic arc-tangents function with values between  $\pm\pi$  is applied. Notice from equation (13) that the time-lapse monitoring algorithm of traveltimes shifts allows the largest 4D changes in the phase for low-frequency waves. The time-lapse monitoring algorithm using amplitude information of reflected waves is not restricted by any means.

## 2.4 The effect of mispositioning on the traveltimes shift and reflectivity ratio

Until now it was assumed that the source and receiver geometry is same in the reference and monitor survey. However, it is generally acknowledged (e.g., Ebrom et al., 1997; Kragh and Christie, 2002; Calvert and Charles, 2002; Curtis et al., 2002; Eiken et al., 2002) that the non-repeatability effect due to mispositioning of the source-receiver locations in the repeated survey can be more significant than the production induced effect in the 4D seismic signal. We investigate analytically the non-repeatability effect due to source-receiver mispositioning on the traveltimes shift and reflectivity ratio as 4D seismic attributes. In appendix A, the traveltimes delay and the reflection coefficient difference

as function of misposition error  $\Delta x$  are derived for the one-layer model in Figure 1. Notice for media with a complex overburden including large-scale structures (i.e. compared to the wavelength) like gas chimneys and turbidities the presented criteria for mispositioning must be modified. The basic idea behind this analysis is that the 4D production induced time-lapse effect must be bigger than the non-repeatability effect inherent to mispositioning problems with the source and receiver location in order to identify the production imprint in the 4D signal.

The traveltime residual  $\Delta t$  for a zero-offset data point inherent to the mispositioning  $\Delta x$  is given by

$$\Delta t(\Delta x) \approx \frac{(\Delta x)^2}{4hv_1}, \quad (14)$$

where the layer thickness  $h = z_1 - z_0$ , and the constant velocity in layer one is denoted  $v_1$  in Figure 1. According to Kragh and Christie (2002), the production related traveltime delay  $\Delta t_{prod}$  is on the order of a few msec for a receiver with a good recovery. For instance, say  $\Delta t_{prod} = 2$  msec for a P-wave reflected at the lower interface of a reservoir at  $h = 1500$  m depth and the overburden velocity is  $v_1 = 2000$  m/s. For

$$\Delta t(\Delta x) \ll \Delta t_{prod} \quad \Rightarrow \quad \Delta x \ll 2\sqrt{hv_1\Delta t_{prod}} \quad (15)$$

to hold requires that  $\Delta x \ll 155$  m. The misposition of the repeated source-receiver geometry should not be larger than a certain fraction of the estimated misposition limit. For this specific example, the mispositioning should not be more than a few times the standard bin-size to be able to see a production effect in the traveltime delay on the order of 2 msec.

In a similar vein, the analysis of non-repeatability effect due to mispositioning on the offset dependent reflection coefficient is carried out. In appendix A, it is shown that the reflectivity change  $\Delta R(x_{sr}, \Delta x)$  for the offset  $x_{sr}$  and mispositioning  $\Delta x$  is given by

$$\Delta R(x_{sr}, \Delta x) = \begin{cases} 0 & \text{if } x_{sr} \ll h \\ \frac{2G}{5h}\Delta x & \text{if } x_{sr} \approx h. \end{cases} \quad (16)$$

The offset  $x_{sr} = x_r - x_s$  between the source and receiver position and  $G$  is the AVO gradient (Mavko et al., 1998). It is clear that the sensitivity inherent to misposition in the reflection coefficient is negligible for near-offset data. In addition, by inserting the reservoir parameters for the Gullfaks field as indicated in appendix B of Landrø (2001), one find that  $\Delta R(x_{sr}, \Delta x) \ll \Delta R_{prod}$  for intermediate offset data. Consequently, the reflectivity ratio  $R_a/R_b \approx 1 - \Delta R/R_a$  in the near and intermediate offset range is remarkably unaffected by mispositioning problems. On the other hand, the traveltime delay has a much stronger dependence on the mispositioning of source-receiver geometries on the order of the bin-size.



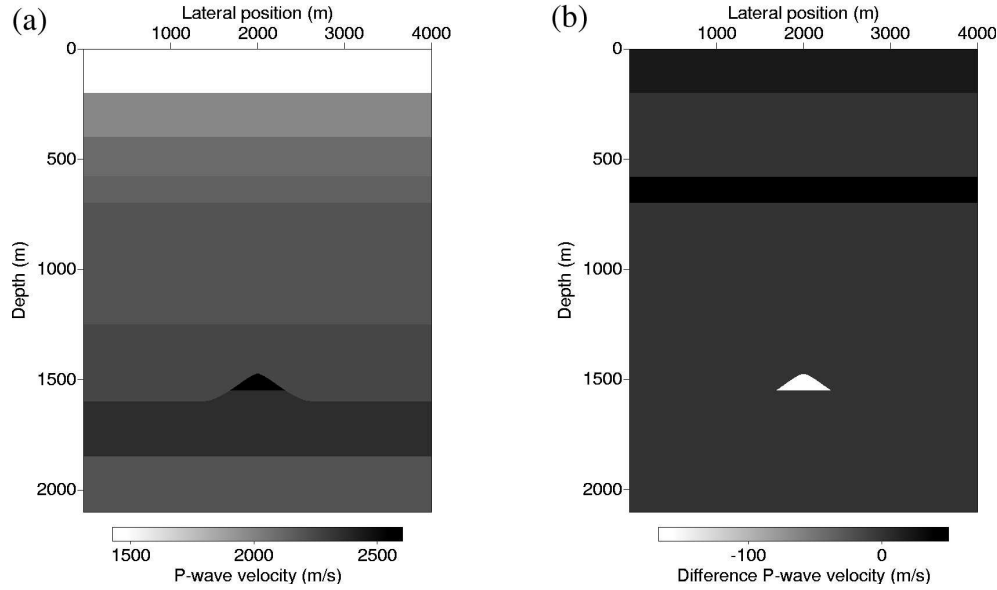


**Figure 3:** Illustration of the synthetic time-lapse experiment. (a) The P-wave velocity structure in one survey. (b) The difference model of the P-wave velocity structure. Notice the overburden effects in the water layer and in the layer above the anticline structure. The producing reservoir is located in the volume below the anticline.

### 3 Synthetic modelling of a time-lapse marine experiment

The time-lapse monitoring method is validated using a synthetic 4D data set from a marine experiment. First, the petrophysical time-lapse model is presented, then the modelling of the synthetic marine surveys is explained, and finally results from the 4D monitoring method applied on the synthetic time-lapse streamer data set are given.

#### 3.1 Petrophysical time-lapse model

For the synthetic experiment, we use a petrophysical model where a reservoir with the shape of an anticline is buried under several horizontal layers (see Figure 3a). The properties of each layer (i.e., P- and S-wave velocities and density) are selected in such a way that they represent typical macro velocity values from the North Sea. The elastic parameters for the reference and monitor model are given in Table 1 and 2, respectively. We assume a reservoir with 80% oil saturation in the reference model. In the monitor model we assume that the oil saturation has dropped to 20% due to production. Assuming a 20% porosity sandstone reservoir with quartz grains, we use the Biot-Gassmann equations to obtain values for velocities and density, see Mavko et al. (1998).

To test the overall robustness of the 4D monitoring method, we introduce an overburden effect in layer 0 and 3. This effect may be due to seasonal changes of the water temperature (layer 0) and subsidence of the overburden (layer 3). Subsidence near the top of the reservoir may be greater than subsidence at the seafloor, and consequently the overburden is stretched. This will lead to a decrease in the effective stress in the overburden, and hence a decrease in the seismic velocities (Mavko et al., 1998). It should be mentioned that no physical model is used to obtain the lowered velocities for layer 3 in the monitor model. In Figure 3b, the difference P-wave velocity model is illustrated in which both overburden and production time-lapse changes are clearly visible.

**Table 1:** Elastic parameters in synthetic streamer time-lapse experiment for the reference model.

Layer number	$v_p$ (m/s)	$v_s$ (m/s)	$\rho$ (kg/m <sup>3</sup> )
0 (Water)	1500	0	1000
1	1980	790	1800
2	2100	830	2030
3 (Overburden effect)	2180	1150	2090
4	2200	1100	2100
5	2250	1040	2140
6 (Reservoir)	2393	1447	2197
7	2360	1170	2300
8	2200	1000	2200

**Table 2:** Elastic parameters in synthetic streamer time-lapse experiment for the monitor model.

Layer number	$v_p$ (m/s)	$v_s$ (m/s)	$\rho$ (kg/m <sup>3</sup> )
0 (Water)	1480	0	1000
1	1980	790	1800
2	2100	830	2030
3 (Overburden effect)	2140	1105	2070
4	2200	1100	2100
5	2250	1040	2140
6 (Reservoir)	2550	1437	2228
7	2360	1170	2300
8	2200	1000	2200

Figure 4 illustrates difference common-offset gathers for the elastic 4D model in Figure

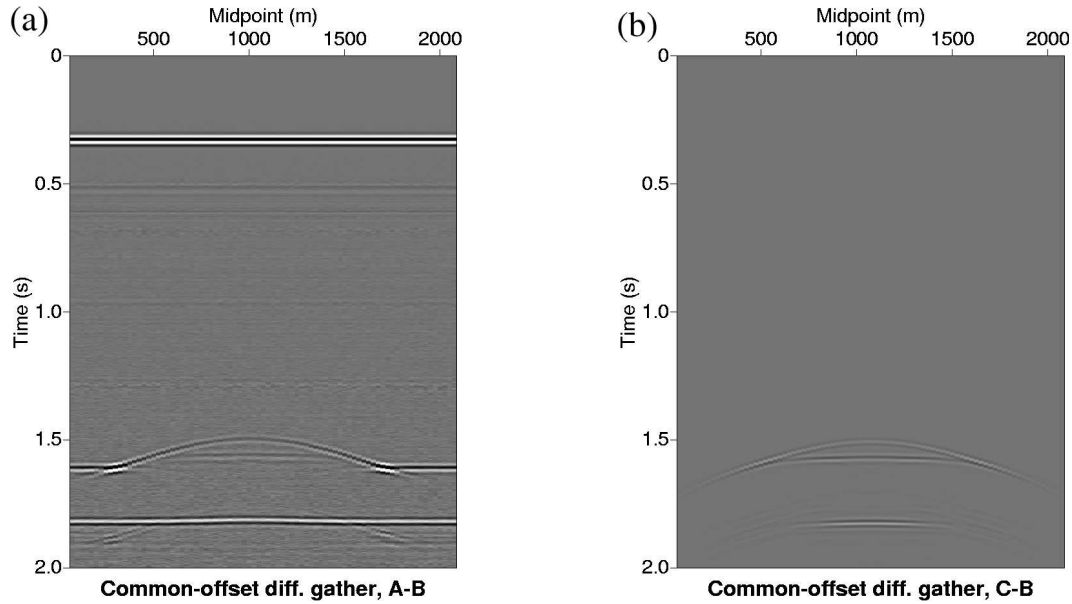


**Figure 4:** Difference plots of common-offset gathers. (a) Difference A - B, including production and non-repeatability effects. (b) C - B, only pure production effects.

3. To generate this figure, an elastic forward modelling of two distinct time-lapse experiments have been carried out. In one 4D experiment, the reference model (A) and the monitor model (B) (as shown in Figure 3) include the production and non-repeatability effects (see also the next section for a detailed explanation). The difference common offset gather in Figure 4a is generated by using a match-filter to the overburden reflections to remove non-repeatability effects. The observed difference wavefield from the reservoir is the accumulated result of both production and non-repeatability effects. On the other hand, the clear difference wavefields outside the anticline reservoir are due to non-repeatability effects only which can not be compensated by the match-filter. In the other time-lapse experiment the only 4D changes are located at reservoir level, while the acquisition parameters are kept constant in the two surveys. Consequently, the monitor model (B) is compared to another 'reference' model (C) only with 4D elastic properties differences in the reservoir. The difference near-offset gather in Figure 4b shows the 4D imprint related to the pure production only. From these two examples of difference gathers, it is clearly seen that the time-lapse non-repeatability effects are more dominant than the production signature in the 4D data.

### 3.2 Forward modelling of time-lapse streamer experiment

We use a 2D elastic finite-difference code (van Vossen et al., 2002) to generate synthetic marine surveys for the two models; each survey results in 81 common shotgathers with

the source-position ranging between  $\pm 1$  km from the centre of the anticline model. The source separation is 25 m, while the receiver array consists of 114 hydrophones with a separation of 12.5 m. The offset between the source and first receiver is 150 m. The full elastic wave equations are used, hence amplitude losses due to mode conversions at the interfaces and geometrical spreading are accounted for. The model for the elastic parameters is divided into grid cells of 2 by 1.5 meters, and proper care is taken to diminish unwanted modelling effects like grid dispersion and backscattering from the boundaries. We introduce several common causes of non-repeatability effects in the time-lapse data

**Table 3:** Causes of non-repeatability effects in time-lapse seismics. Symbol notation;  $\star$ : included in synthetic experiment, and  $\oplus$ : relevant in Troll data set.

Acquisition:	Different source-receiver coupling ( $\star, \oplus$ )
	Different source-receiver positions ( $\star, \oplus$ )
	Different sail directions ( $\oplus$ )
	Missing data
Noise:	Uncorrelated noise ( $\star, \oplus$ )
	Coherent noise ( $\star, \oplus$ )
Other factors:	Different water temperature ( $\star, \oplus ?$ )
	Overburden effects ( $\star, \oplus ?$ )
	Tidal differences ( $\oplus$ )

set (see Table 3). In the reference survey, the source and array of receivers are at 10 m depth, while in the monitor survey the source and receivers are at 5 m depth. To include the problem with mispositioning of source-receiver locations, all repeated receiver positions are shifted 60 meter (i.e. several times the standard bin-size) compared to the reference one. Two different source wavelets are chosen for the reference and monitor surveys. For the reference survey, we use a Ricker wavelet with a central frequency of 28 Hz and in the monitor survey the central frequency is increased to 32 Hz. Reflections from the sea surface are allowed, so the seismic data contain free surface multiples. In addition, strong random noise is added to the data. An example of a single shotgather from the synthetic surveys is shown in Figure 5a where the source position is located at the middle of the anticline structure.

### 3.3 Preprocessing of synthetic time-lapse streamer data

Before applying the time-lapse monitoring method on the synthetic 4D data sets, several preprocessing steps are carried out to correct for non-repeatability effects. In Figure 6, the flow-diagram indicates the preprocessing operations starting from the common shot

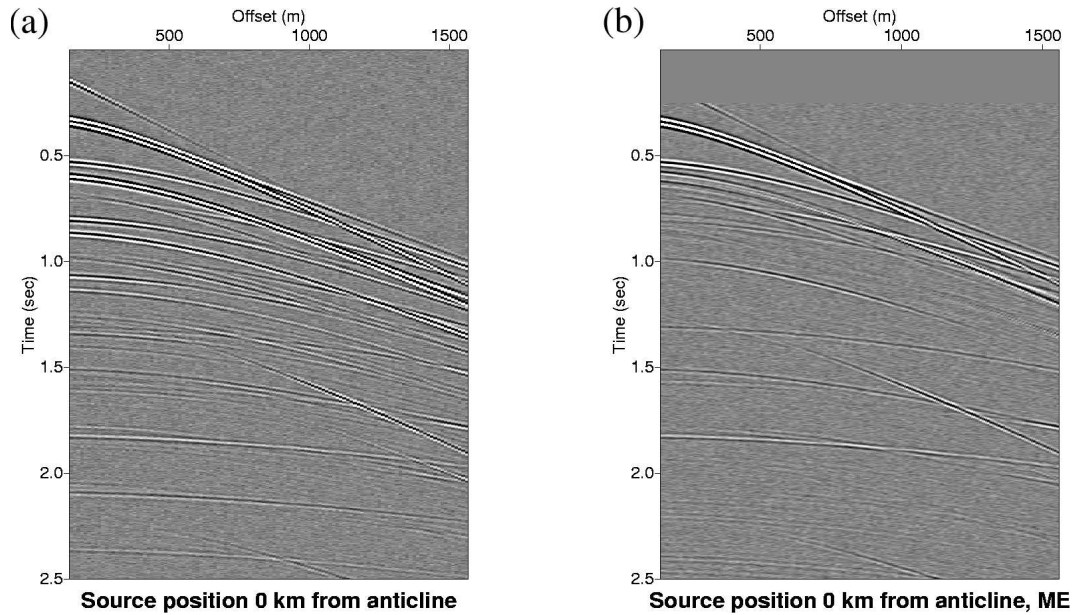


**Figure 5:** Example of common shot gathers computed in the synthetic time-lapse experiment. (a) The source position is at the middle of the anticline structure (i.e. lateral position equal to 2000 m in Figure 3a) before free surface multiple elimination. (b) Like in Figure 5a but after free surface multiple elimination. Notice that the reflected wavefields from the reservoir interfaces are much more clear after multiple removal.

gathers and finishing with the time-lapse monitoring analysis using common-offset gathers and/or CMP-gathers. The preprocessing sequence includes the following steps; 1) Missing traces (for instance due to dead hydrophones) are recovered with a wavefield reconstruction method (e.g. Sconeville, 2000; Zwartjes and Hindriks, 2001). Note that neither the synthetic nor the real time-lapse data set need to be corrected for missing traces. For examples of wavefield reconstruction using real data, see Sconeville (2000) and Zwartjes and Hindriks (2001). 2) Coherent noise such as free surface multiples are removed with a surface related multiple elimination method (e.g. Verschuur et al., 1992). See Figure 5b for an example of free surface multiple elimination in a synthetic common shotgather. 3) The preprocessed shotgathers are sorted into common-offset gathers and CMP-gathers in which PP-reflections are identified for the source-receiver response and overburden function correction and for 4D monitoring of the producing hydrocarbon reservoir. 4) The interpreted PP-reflections are filtered in the frequency-wavenumber (f-k) domain to remove interfering wavefields and high-frequency random noise.

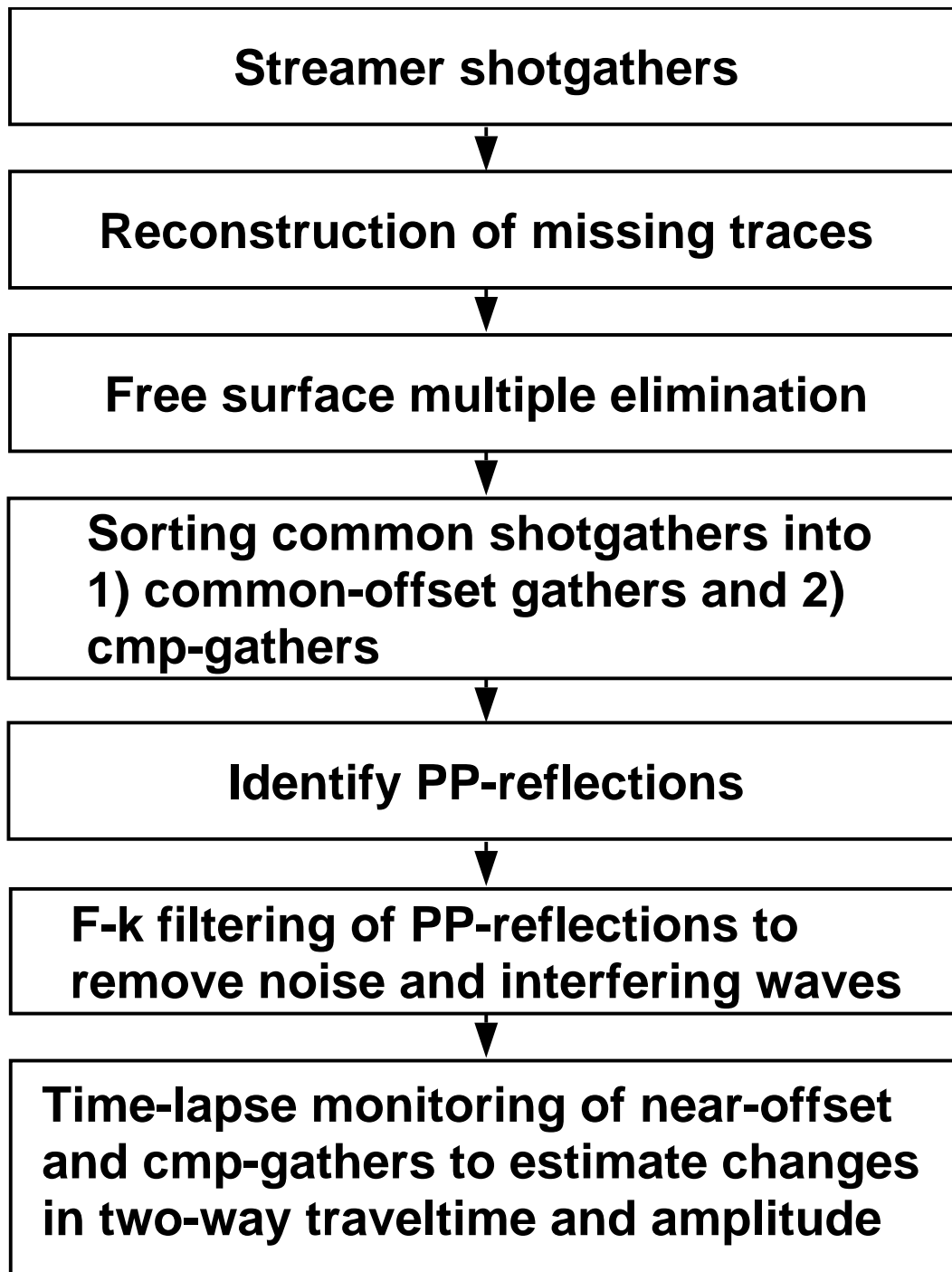


**Figure 6:** Flow-diagram of preprocessing steps carried out on prestack streamer data to reduce the effects of non-repeatability in time-lapse seismic experiments. The processing sequence is applied on the synthetic, as well as the real streamer data sets except for the reconstructing operation of missing data.

### 3.4 Result of synthetic time-lapse monitoring

The results of the synthetic time-lapse experiment are presented in the common offset domain and in the CMP domain. We show one example of a 4D common-offset gather, and another example of a time-lapse CMP-gather with the CMP-position located at the centre position of the anticline model. In addition, the 4D monitoring method is applied on prestack depth migrated data.

First, we consider the 4D monitoring analysis of the common-offset gathers from which we extract information about changes in the two-way travel time and the ratio of reflectivity. In Figure 7a, we see the reference common-offset gather of filtered reflected wavefields from interface 5, 6, 7 and 8. The anticline structure of the producing reservoir illustrated in Figure 3a is clearly visible in the common-offset gather at the wavefields labeled with *interface 6 and 7*. The reference and monitor wavefields with the label *interface 5* are applied for the source-receiver coupling substitution in the equations (6) and (7), while the time-lapse wavefields reflected at interface 6, 7 and 8 correspond to equation (8) and (9). Hence, by performing the deconvolution operation of convolved wavefields on the left-handside of equation (12), the two-way traveltimes shift and the reflectivity ratio of the wavefields reflected at reservoir level are determined. The frequency-integration of the phase and modulus term in equation (5) are carried out between 25 Hz to 55 Hz. Thus, according to equation (13) with a maximum frequency of 55 Hz the estimated traveltimes shifts must be within  $\pm 9$  msec to be estimated correctly. This is several times larger than the production related time delay in the anticline between interface 6 and 7. To calculate the two-way traveltimes shift of the wavefield twice going through the producing reservoir (thus expecting time-lapse changes distinctly different from zero), we have applied the reflected wavefield labeled *interface 8*. The observed traveltimes shift for this wavefield is shown with the black solid line, while the true values of the travel time difference due to production in the reservoir are illustrated with the grey dotted line. According to equation (15), the horizontal mispositioning of the source-receiver geometry (i.e.,  $\Delta x = 60$  m) introduces a timeshift of a few msec which is on the order of the production induced travel time delay. However, the anticline structure acts as a focussing lens of the wavefield reflected at interface 8. This is the physical reason for the clear agreement between the observed and true two-way travel time delay for the reflected wavefield from interface 8 though the synthetic time-lapse experiment is influenced by repeatability effects due to mispositioning and other important acquisition differences (see table 3).

The time-lapse monitoring analysis of amplitude changes of the reflected wavefield for interface 6 and 7 in the common-offset gathers are shown in Figure 7c. The observed and true values of the ratio of reflection coefficients are shown with the black solid and grey dotted lines, respectively, of variable line width. The length of the grey dotted lines for the true values of the reflectivity ratio for interface 6 and 7 indicates the horizontal extension of the anticline model. Interface 6 and 7 correspond to the top and bottom of the producing reservoir, hence the reflectivity ratio at these two interfaces differ significantly

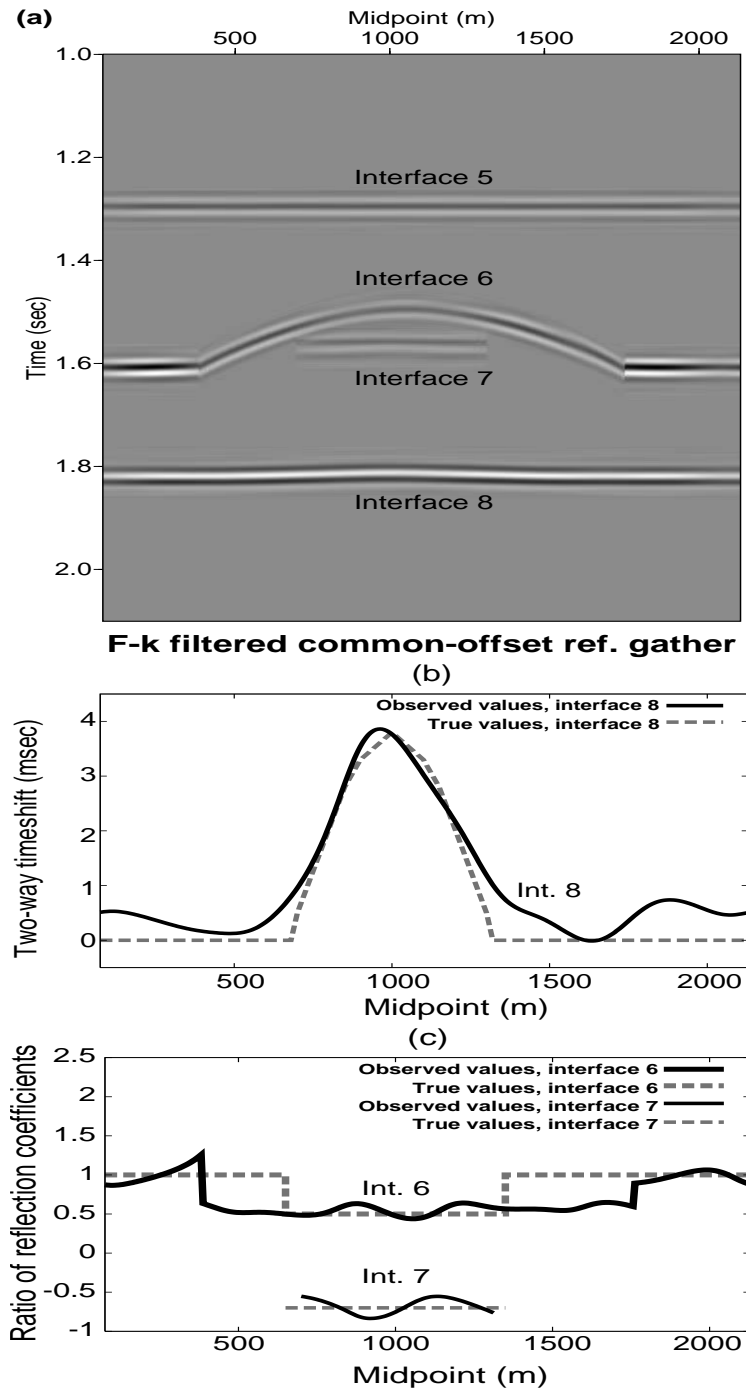


**Figure 7:** Time-lapse monitoring of two-way traveltime shift and amplitude of reflected waves using the synthetic common-offset gathers. The true values for the traveltime delay and reflectivity ratio are indicated with grey dotted lines. (a) The filtered reflected wavefields from interface 5 to 8. (b) 4D monitoring of two-way traveltime using the wavefield reflected at interface 8 that propagates twice through the reservoir. (c) Time-lapse monitoring of the amplitude attribute using the wavefields that are reflected at the top of the reservoir (interface 6), the bottom of the reservoir (interface 7).



from the value one which is clearly demonstrated in the figure. In general, there is a good agreement between the observed and theoretical values of time-lapse amplitude changes except for the lateral extension of the anticline. This latter point is related to the geometrical structure of the anticline model that is poorly resolved with non-migrated data. A migration operation of the seismic data reveals the correct horizontal length of the anticline structure. This is shown in Figure 8b.

The example of 4D monitoring using a filtered CMP-gather is illustrated in Figure 8a for the CMP-position at the middle of the anticline structure. We look for time-lapse changes in the reflectivity ratio only, since 4D monitoring of amplitude changes of reflected wavefields, unlike two-way traveltime shift, is unaffected of non-repeatability effects in the overburden. The AVO-behaviour of the reflectivity ratios (i.e. frequency-integrated between 25 Hz and 55 Hz) are shown with the black solid lines of different line width, while the true values of the ratio of reflectivity are indicated in the figures with grey dotted lines of variable line width. For the CMP-gather in Figure 8a, we expect clear indications of 4D changes in the producing reservoir because the CMP-position is at the centre of the anticline structure. Undoubtedly, we see for interface 6 and 7 (the top and bottom of the reservoir, respectively) significant deviations from the value one indicating that the reflection coefficient changes from the reference survey to the monitor survey. For interface 6, the observed values of the AVO-behaviour of the ratio of reflectivity agree well with theoretical values computed with Zoeppritz' equations. Notice in Figure 8a that the observed AVO-curve for interface 7 shows significant discrepancies from the true AVO-curve for offsets larger than 500 m because of the strong lateral 2-D structure of the anticline model which results in a vanishing wavefield at large offsets.

The purpose of migration is to bring the recorded data from the surface to the reflecting interface level. The phase and amplitude operators in the recorded reference and monitor wavefields in equation (8) and (9) are compensated for during the migration process. Hence in the ideal case of an accurate velocity input model, the migrated reference and monitor wavefields are reduced to the product of the reflection coefficient and the source wavelet. By performing the source wavelet substitution method described in the theory section using the migrated data, one again ends up with the right-handside of equation (12). Figure 8b shows an example of the reflectivity ratio estimated from prestack depth migrated data. The shotgathers after the free surface multiple elimination operation were prestack migrated in the  $(x-\omega)$ -domain using a correlation function as imaging condition (Thorbecke, 1997). The source-wavelet substituting convolution-deconvolution method was applied on the image gathers from which the reflectivity ratios for the top reservoir reflector (interface 6) and bottom reservoir reflector (interface 7) were extracted. The observed ratios of reflection coefficient from the migrated data are indicated with the black solid line, while the ones from the pre-migrated data (same curve as in Figure 7c) are shown with the black dotted line. The true value of the reflection ratio and the extension of the anticline structure is given by the grey dotted line. It is clear from this example that the migration process improves significantly the lateral resolution of the time-lapse signal inherent to the producing reservoir at interface 6. The migrated

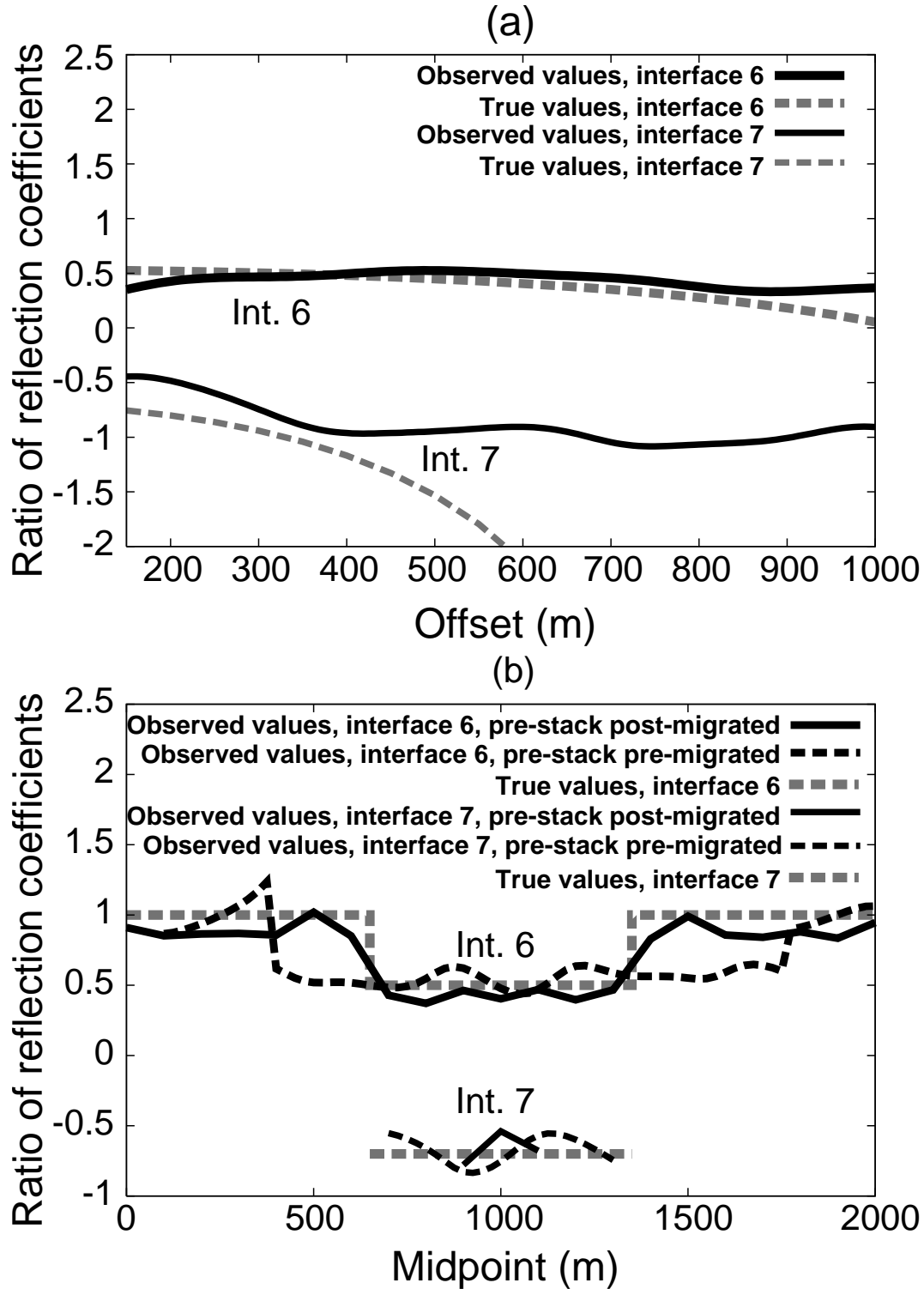


**Figure 8:** (a) Time-lapse monitoring of amplitude using synthetic CMP-gathers. The CMP-position is at the midpoint position of the anticline structure (i.e., lateral position equal 2000 m in Figure 3a). (b) The reflection ratio estimated from prestack migrated data.

wavefield for the bottom reservoir reflector at interface 7 is very weak at the reservoir edges so no reflectivity ratios are estimated at those points.

## **4 Example of time-lapse monitoring of a real streamer time-lapse data set**

The time-lapse monitoring method explained above was applied to a time-lapse seismic dataset from the Troll Field which is a giant oil and gas field located in the Northern North Sea, offshore Norway. The field is divided in two main hydrocarbon bearing structures, Troll West and Troll East. An estimated 2/3 of the gas reserves are located in Troll East. Troll West is further divided into two structures, the Troll West Oil Province (western part), and the Troll West Gas Province (eastern part). Good reservoir sandstones are found in the Late Jurassic Sognefjord Formation at approximately 1500-1600 m burial depth. A thin layer of oil-bearing sand exists below the gas column. In the Troll West Oil Province, this layer is about 25 meters thick and has been under production since 1995. Oil is also being produced in the Gas Province, where the oil column is 10-15 meters thick. At Troll East the oil column is too thin to be of any commercial interest. Gas has been produced from Troll East since 1996.

In this example, we focus on a section of the Troll West Gas Province where production started in may 2000. The time-lapse seismic data are from the inline 1070. The reference survey is from 1998 and the monitor survey is from 2001. In Table 3, actual and possible (denoted with a question mark) non-repeatability effects in the Troll 4D data are stated. The sail direction of the reference survey is opposite to the one in the monitor survey which is accounted for in the time-lapse monitoring analysis by using source-receiver reciprocity to interchange the source and receiver positions in the reference survey. The raw common shotgathers had only been seis/navy-merge corrected before they were pre-processed following the processing flow-diagram in Figure 6.

Figure 9a illustrates the migrated 2D section of the reservoir in 1998 and 2001. The Gas Province is located under the two clear reflecting interfaces at about 1480-1550 m, while the weak but still visible gas-fluid contact is indicated with the white dashed line at about 1620 m. In 3D prestack depth migrated data the gas-fluid contact is much more clear. Since the oil-column is thin in this area, there must be interference with the oil-water contact. The gas-fluid contact is therefore probably due to the contrast between gas and water. A match filter was applied to compensate for source-receiver variability and overburden effects between the two migrated sections in Figure 9a. The difference stack between these two match-filtered 2D sections is shown in Figure 9b. Notice the strong contrasts at the top reservoir level and at the gas-fluid contact. The source wavelet substitution method in equation (12) was used in CMP-gathers, where the wavefield for

compensation of source-wavelet variability and overburden effects is from a reflector at about 750-800 m depth (not shown here). The top and lower reflector at the top reservoir between 1480 m and 1550 m are both monitored for changes in reflectivity. Hereby the CMP-gathers were filtered for a broad frequency band (i.e. 20-80 Hz) with a high S/N-ratio, before the reflectivity ratio curves for midpoints between 1000 m and 3000 m were estimated from the near-offset traces. The curves with the reflectivity ratio for the top and lower reflectors are shown in Figure 9c. Both reflectivity ratio curves oscillate closely around the value one. This is an indication that no significant time-lapse changes are present in the top part of the reservoir of the Troll West Gas Province during 1998 and 2001.

Production history tells that it is possible that the gas-fluid contact was moved downwardly between 1998 and 2001. We have tested this idea for several production scenarios that the gas-fluid contact is shifted 5, 10, 15 and 20 m vertically down. First log-data from a nearby well about 500 m from the seismic subline was modified using a simplified version of the Biot-Gassmann equations (see Mavko et al., 1998, page 167) to simulate new logs for the four production cases. The reference and monitor logs for the P-wave velocity and density are shown in Figure 10a. Notice that the P-wave velocity is most sensitive to the gas-fluid contact movement. Then a seismic trace for the reference log and each modified logs was computed by convolving a wavelet with the reflectivity series obtained from the sonic and density logs. Finally the reflectivity ratio at the gas-fluid contact level was estimated with expression (12). The ratio of reflection coefficients is approximately 0.95, 0.92, 0.915 and 0.91 for the 5, 10, 15 and 20 m, respectively, displacement of the gas-fluid interface. Similarly, we applied the convolution-deconvolution method in Eq. (12) to estimate the reflectivity ratio for the observed gas-fluid contact in the prestack Troll data as function of midpoint position. The curve with the ratio of reflection coefficients is illustrated in Figure 10b. On average, the observed reflectivity ratio is on the order of 0.9 to 1.0 with lower values on the left handside and higher values on the right handside. It does not seem plausible that the gas-fluid contact is lateral variant. Instead, the observed reflectivity ratio shows a possible indication that the gas-fluid contact has moved downwardly. It is however impossible to assess accurately how much the gas-fluid interface was shifted between 1998 and 2001. A displacement of the gas-fluid contact on the order of 10-20 is very likely as estimated from the injection-production records at nearby wells.

## 5 Conclusions and discussion

A time-lapse seismic monitoring methodology based on the spectral ratio technique is developed. By computing the ratio of time-windowed reflected wavefields from the reference and monitor survey, we inspect separately the time-lapse phase and reflectivity changes related to reservoir production effects. The 4D approach accounts for several

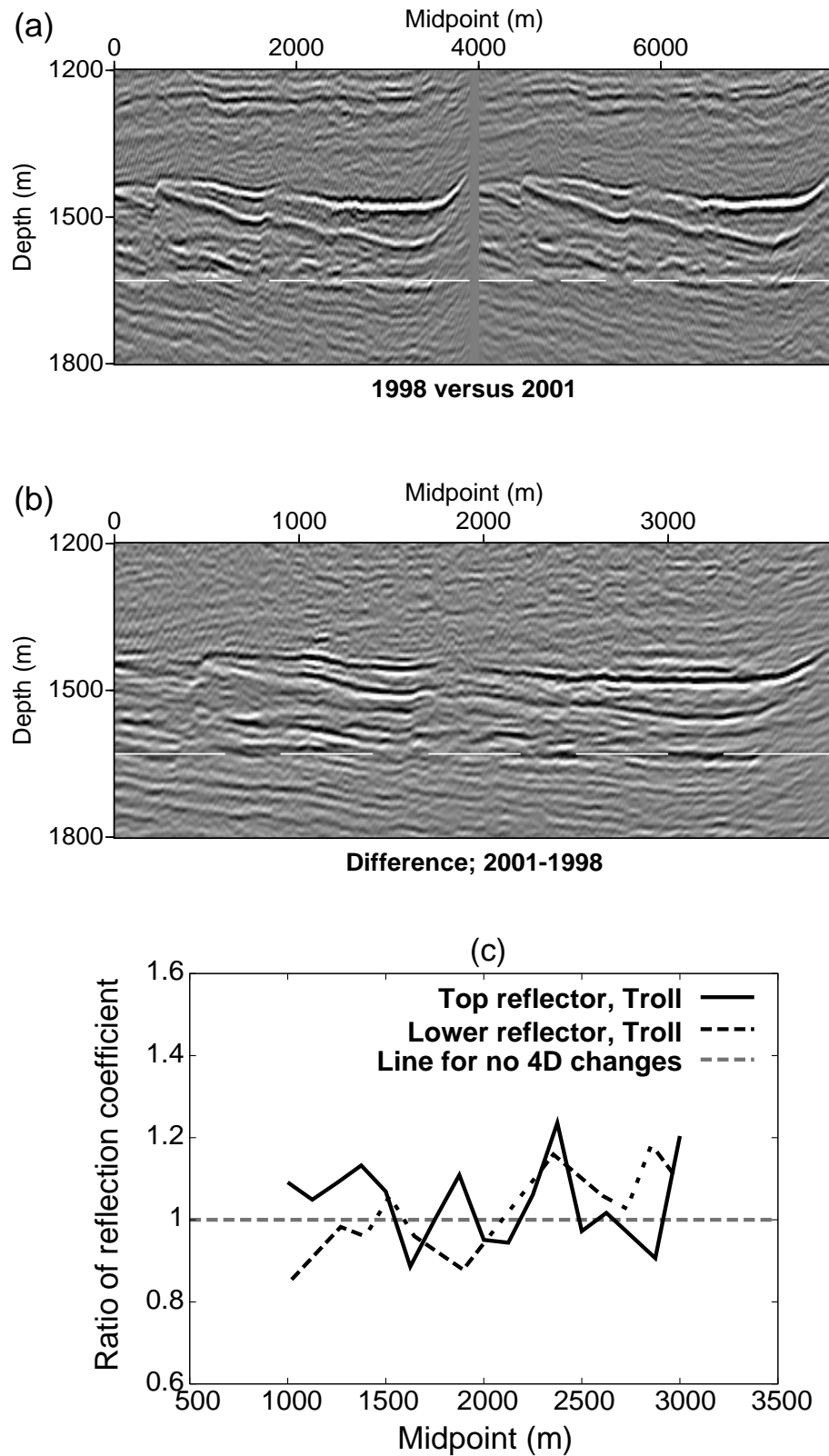


**Figure 9:** 4D seismic monitoring of Troll west. (a) The migrated section of the reservoir in year 1998 and 2001. The white dotted line indicate the gas-fluid contact. (b) The difference section of the two stacks in Figure 9a. (c) Reflection ratio curves of the two strong reflectors between 1480 m and 1550 m. (Courtesy of Norsk Hydro.)

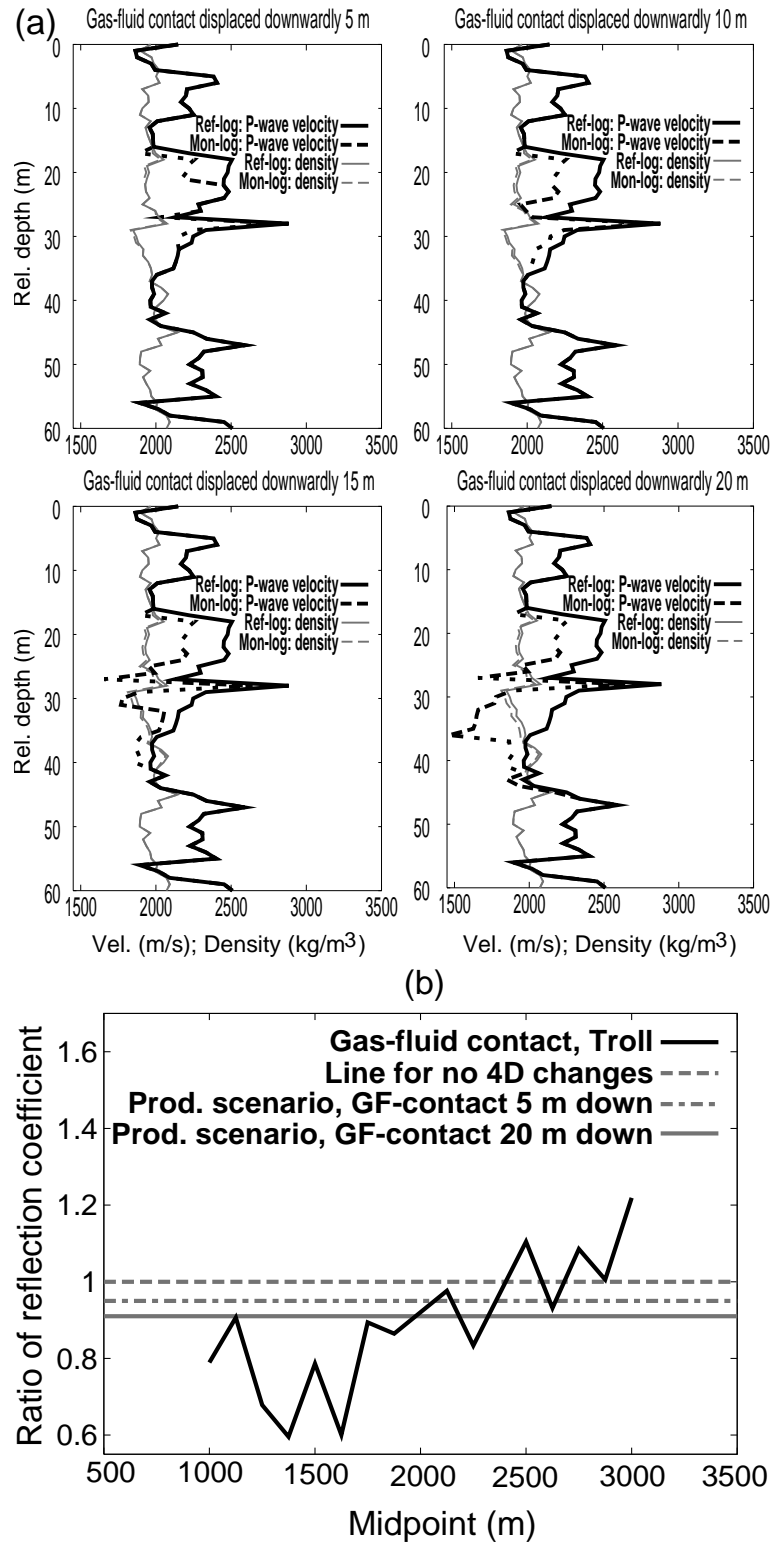


**Figure 10:** 4D seismic monitoring of Troll west. (a) Well-log data for four production scenarios. The fluid-gas contact is moved downwardly by 5, 10, 15 and 20 m. (b) Reflection ratio curve of the gas-fluid contact in the Troll data set. (Courtesy of Norsk Hydro.)

major causes of non-repeatability effects due to differences in acquisition, overburden and noise (e.g., random and coherent noise). The time-lapse phase attribute is sensitivity to mispositioning problems of source-receiver configurations on the order of the standard bin-size. On the other hand, the 4D reflectivity attribute is insensitive to mispositioning problems in source-receiver configurations for near-offset and intermediate offset data. The time-lapse methodology is successfully validated in a synthetic time-lapse streamer data experiment including non-repeatability causes inherent to differences in acquisition, overburden and noise distribution. With this synthetic example, it is shown that the 4D monitoring method is applicable to prestack common-offset gathers, prestack CMP-gathers and image gathers of prestack migrated data.

In the case of the Troll West Gas Province, the physical conditions in the reservoir had changed because of a vertical movement of the fluid contact on the order of 5-15 m. The time-lapse monitoring method described here failed to detect this change from seismic amplitude data. This is no surprise, since this method measures the relative change in reflection coefficient at a reflecting interface. A vertical movement of the fluid contact is not likely to give a significant change in the reflection strength of the fluid contact.

The validity of the time-lapse approach depends on the complexity of the overburden and the production effect on the seismic parameters at reservoir level. For a simple structural overburden with small lateral variation and dipping interfaces the proposed 4D method works well. On the other hand, for a strongly heterogeneous overburden with for instance turbidites or a gas-chimney non-linear ray bending effects leads to a severe distortion of the amplitude of the recorded wavefield so that a time-lapse evaluation at reservoir level is very difficult. At reservoir level, any production-related variation must result in a significant change in seismic velocity and/or density. This is possible if there has been a significant change in fluid saturation, pore pressure or temperature (Wang et al., 1991). Changes in fluid saturation and pore pressure depend on communication in the reservoir and will not act across sealing interfaces. A fluid saturation or pressure change in the proximity of a seismic reflector that acts as a seal may be detectable on time-lapse seismic data. For example, Landrø and Strønen (2003) successfully recognized amplitude differences as result of a fluid saturation change below a dipping top reservoir interface. Also, fluid saturation and temperature changes as a result of steam injection have been found to have significant impact on time-lapse seismic data (Jenkins et al., 1997b). Seismic velocities depend on pore pressure through the effective pressure. However, velocities are more sensitive to a pore pressure increase than a pore pressure decrease (see e.g. Christensen and Wang, 1985). Increasing pore pressure as a result of water injection have been seen in time-lapse seismic data (Landrø, 2001).

The proposed 4D method can be used for more than just monitoring of production related reservoirs. The output-data of the time-lapse reservoir monitoring scheme can serve as input-data in a lithological inversion to estimate the elastic reservoir differences, as well as changes in saturation and pore-pressure over time. In addition, the method is not limited to streamer data experiments, but one can naturally generalise the approach to

OBC - (e.g., to include both P-to-P and P-to-S wave conversion) and land seismics.

## **6 Acknowledgements**

This manuscript is sponsored by the European Community through the Atlass project, no. NNE5-1999-20211. Kees Wapenaar, Eric Verschuur, Jan Thorbecke, Robbert van Vossen, Ivar Andreas Sandrø, Sture Leiknes and Ole-André Eikeberg are acknowledged for constructive discussions which helped us to complete the manuscript. We thank Norsk Hydro for the permission to use the Troll data set.



## A The effect of mispositioning on traveltime and reflectivity changes

The analytical derivations for the effect of horizontal mispositioning of source-receiver geometry on the traveltime shift and the reflectivity coefficient are shown in this appendix. First, the zero-offset traveltime delay is investigated using the one-layer model in Figure 1. Let the layer thickness  $h = z_1 - z_0$  and the stationary velocity in layer one is denoted  $v_1$ . The reference traveltime  $t_{ref}$  for a zero-offset measurement is given by

$$t_{ref} = \frac{2h}{v_1}. \quad (17)$$

The monitor traveltime  $t_{mon}$  is recorded at the offset position  $\Delta x$  indicating a mispositioning of the repeated source-receiver offset with respect to the reference one. According to Figure 1, the

$$\begin{aligned} t_{mon}(\Delta x) &= \frac{\sqrt{(\Delta x)^2 + (2h)^2}}{v_1} \\ &\approx \frac{2h}{v_1} \left( 1 + \frac{1}{2} \left( \frac{\Delta x}{2h} \right)^2 \right), \end{aligned} \quad (18)$$

where the mispositioning  $\Delta x \ll 2h$ . The traveltime delay  $\Delta t(\Delta x) = t_{mon}(\Delta x) - t_{ref}$  inherent to the offset difference then equals

$$\Delta t(\Delta x) \approx \frac{(\Delta x)^2}{4hv_1}. \quad (19)$$

Second, the effect of misposition on the offset-dependent PP wave reflectivity coefficient is estimated analytically. The offset  $x_{sr} = x_r - x_s$  between the source and receiver position. For the reference survey, the simplified form of the PP reflection coefficient in Aki and P (1980) and Shuey (1985) is given by

$$\begin{aligned} R_{ref}(x_{sr}) &= R_0 + G \sin^2(\theta) \\ &= R_0 + \frac{Gx_{sr}^2}{4h^2 + x_{sr}^2}, \end{aligned} \quad (20)$$

where  $R_0$  and  $G$  are respectively the normal incidence reflection coefficient and the AVO gradient (Mavko et al., 2003). The sine-function  $\sin(\theta) = x_{sr}/\sqrt{4h^2 + x_{sr}^2}$  in equation (20) for the one-layer model in Figure 1. In the monitor survey, the offset position of the recording is shifted by  $\Delta x$ . The monitor reflection coefficient is then given by

$$\begin{aligned} R_{mon}(x_{sr}, \Delta x) &= R_0 + \frac{G(x_{sr} + \Delta x)^2}{4h^2 + (x_{sr} + \Delta x)^2} \\ &\approx R_{ref}(x_{sr}) + \frac{2Gx_{sr}}{4h^2 + x_{sr}^2} \Delta x, \end{aligned} \quad (21)$$

for  $\Delta x \ll x_{sr}$ . For intermediate offset data (i.e.  $x_{sr} \approx h$ ), this means that the reflectivity change due to a mispositioning of  $\Delta x$  is

$$\begin{aligned}\Delta R(x_{sr}, \Delta x) &= R_{mon}(x_{sr}, \Delta x) - R_{ref}(x) \\ &\approx \frac{2G}{5h} \Delta x.\end{aligned}\tag{22}$$

For near-offset data (i.e.  $x_{sr} \ll h$  and  $\Delta x \ll h$ ), it is found from equation (21) that

$$\Delta R(x_{sr}, \Delta x) \approx 0.\tag{23}$$



# Chapter 8

## Closing remarks

As stated in the introduction for this thesis, research on pressure prediction is of great interest to the oil industry. This is reflected in the number of publications per year in the field of pore pressure prediction from seismic data which has increased steadily since the pioneering work of Pennebaker (1968), Reynolds (1970) and Eaton (1972). The field of pore pressure prediction from seismic data is very diverse, covering a range of topics from general seismic processing techniques to experimental core plug analysis. It has been necessary to constraint the focus of my work, meaning that only a few aspects of pore pressure prediction from seismic data are covered here.

In order to predict pore pressures from seismic velocities it is necessary to derive consistent and reliable velocity information from the seismic data. Although there exist advanced tools for this purpose, I have chosen to use well known and established techniques to derive the required velocities. It has not been my purpose to develop more accurate tools for velocity analysis. The focus of this work has been on the combined use of velocity analysis and amplitude analysis to detect anomalous pressures in thin, isolated zones. Repeated (time lapse) seismic data have been used for verification of the pressure effect.

The reason for using established techniques for investigating the impact of pore pressure on seismic data is partly practical, the software has been available and ready to use. In addition, the examined Gullfaks and Haltenbanken fields are characterized by severe overpressures. This increases the probability that a potential velocity effect on seismic data by conventional methods. However, the precision of these conventional methods is not the best. The results from the present study imply that conventional velocity analysis is inaccurate for pore pressure prediction purposes in thin reservoir zones. This illustrates that there is a need for better velocity analysis techniques. In the recent years, we have seen a large development in the field of velocity analysis. It would have been very in-

teresting to test some of these ideas on the data sets used in this study. It is my opinion that the increased focus on seismic parameters as predicting lithology, fluid and pressure indicators will encourage the industry to incorporate advanced velocity analysis methods as standard tools.

The results from the Gullfaks study (Paper 1) imply that abnormally high pore pressures may be detectable by the means of seismic amplitude analysis even though the thickness of the anomalous pressured zone is smaller than the resolution of conventional velocity analysis. This is not surprising, since seismic amplitudes have higher temporal resolution than a velocity field derived from semblance velocity analysis. However, it is a useful observation, since this is confirmation of pressure dependent velocities in situ. Seismic amplitude analysis is a promising tool for detecting overpressures in thin, isolated zones. However, it is not straightforward to use this knowledge for an exploration case, since seismic velocities are determined by a number of factors, which are more or less unknown in an exploration setting. In the Haltenbanken case, we used well data from the area to put constraints on the pore pressure vs. seismic velocity relationship. Integrating knowledge from several disciplines in this way might be helpful for understanding the cause of velocity variations in the subsurface.

Eaton based approaches for pore pressure prediction, where the velocity field is compared with a normal compaction trend has proven to work fairly well in many areas. In retrospect, I would have liked to test an Eaton based method for pore pressure prediction in the Haltenbanken case, or for another data set. The reason for not using an Eaton based approach for Haltenbanken is large uncertainties about the cause of overpressuring in this area. A prerequisite for such methods to work is that there is a fundamental correlation between porosity and pore pressure. While we observe such a correlation in the Haltenbanken sandstones, the shale porosities are essentially independent of pore pressure Hermanrud et al. (1998). This makes the use of normal compaction trends questionable.

In general, uncertainties in the relationship between seismic velocities and pore pressure is a major limitation for pore pressure prediction. The mechanisms that are involved are not very well understood. It is recognized that overpressured sediments generally have higher porosities, and hence lower velocities than normally pressured sediments, because water is prevented from escaping from the pore space. However, as we have seen at Haltenbanken, it is not always the case that porosity and pore pressure correlate. In the present work, I have explained the pressure-velocity relationship through microscopic mechanisms, allowing the seismic velocities to change, even though the porosity remains constant. It is known that for granular media, the stiffness of grain contacts change with pressure. In addition opening/closing of microscopic cracks are important, as is the mineralogy of the rock. It is possible to construct models for idealized cases, e.g., spherical grains. However, real rocks often consist of a mixture of mineralogies, and it is expected that both grain contacts and microcracks contribute to pressure dependent velocities. Because of the complexity of these mechanisms, the behaviour of seismic velocities with pore pressure is difficult to model. I think that there is a need for better understanding of

these mechanisms in order to make more reliable pressure predictions from seismic data, especially in areas where the cause of overpressuring is unknown.

In my opinion, pore pressure prediction from seismic data is a challenging topic with many aspects. It is important to understand that it is a multidisciplinary field. For the hydrocarbon industry, this means that projects which aim to predict pore pressure from seismic data requires the combined effort from a team of specialists in several disciplines.



# References

- Aki, K., and P. R., 1980, Quantitative seismology: W. H. Freeman & Co.
- Bertrand, A., and MacTeth, C., 2003, Seawater velocity variations and real-time reservoir monitoring: *The Leading Edge*, **22**, 351–356.
- Biondi, B., Mavko, G., Mukerji, T., Rickett, J., Lumley, D., C, D., Gundersø, R., and Thiele, M., 1998, Reservoir monitoring: a multidisciplinary feasibility study: *The Leading Edge*, **17**, 1404–1414.
- Borge, H., 2000, Fault controlled pressure modelling in sedimentary basins: Ph.D. thesis, Norwegian University of Science and Technology.
- Boyd-Gorst, J., Fail, P., and Pointing, L., 2001, 4-D time lapse reservoir monitoring of Nelson Field, central North Sea: successful use of an integrated rock physics model to predict and track reservoir production: *The Leading Edge*, **17**, 1336–1350.
- Calvert, R., and Charles, J., 2002, 4D acquisition geometry requirements and QA: *Eur. Ass. Geosci. Eng., Expanded Abstracts*, A017.
- Carcione, J. M., Helle, H. B., and T, Z., 1998, Effects of attenuation and anisotropy on reflection amplitude versus offset: *Geophysics*, **63**, 1652–1658.
- Carcione, J., Helle, H. B., Pham, N. H., and Toverud, T., 2003, Pore pressure estimation in reservoir rocks from seismic reflection data: *Geophysics*, **68**, 1569–1579.
- Castagna, J. P., Batzle, M. L., and L, E. R., 1985, Relationship between compressional-wave and shear-wave velocities in clastic silicate rocks: *Geophysics*, **50**, 571–581.
- Christensen, N. I., and Wang, H. F., 1985, The influence of pore pressure and confining pressure on dynamic elastic properties of berea sandstone: *Geophysics*, **50**, 207–213.
- Curtis, T., Smith, P., Combee, L., and Olafsen, W., 2002, Acquisition of highly repeatable seismic data using active streamer steering: 72nd Ann. Internat. Mtg. Soc. Expl. Geophys., *Expanded Abstracts*, 81-84.
- Domenico, S. N., 1977, Elastic properties of unconsolidated porous sand reservoirs: *Geophysics*, **42**, 1339–1368.



- Dutta, N. C., 1987, Geopressure:, Soc. Expl. Geophys. reprint series No. 7 Soc. Expl. Geophys.
- Dutta, N. C., 2002a, Geopressure detection using reflection seismic data and rock physics principles: Methodology and case histories from deepwater tertiary clastic basins: SPE Paper 77820, pages 2012–2041.
- 2002b, Geopressure prediction using seismic data: Current status and the road ahead.: Geophysics, **67**, 2012–2041.
- Dvorkin, J., Mavko, G., and Nur, A., 1991, The effect of cementation on the elastic properties of granular material: Mechanics of materials, **12**, 207–217.
- Eaton, B. A., 1972, The effect of overburden stress on geopressure prediction from well logs: J. Pet Tech., SPE paper 3719.
- Eberhart-Phillips, D., Han, D. H., and Zoback, M. D., 1989, Empirical relationships among seismic velocity, effective pressure porosity, and clay content in sandstone: Geophysics, **54**, 82–89.
- Ebrom, O., Purnell, G., and Krail, P., 1997, Repeatability of marine seismic streamer data for prestack analysis at the Orea basin: 67th Ann. Internat. Mtg., Soc. Expl. Geophys., Expanded Abstracts, 59-62.
- Eiken, O., Aronsen, H., Furre, A., Klefstad, L., and Nordby, L., 2002, Repeated seismic surveys from the Norwegian Sea using new streamer technology: 72nd Ann. Internat. Mtg., Soc. Expl. Geophys., Expanded Abstracts, 1700–1703.
- Eiken, O., Haugen, G. U., Schoneville, M., and Duijndam, A., 2003, A proven method for acquiring highly repeatable towed streamer seismic data: Geophysics, **68**, 1303–1309.
- Fertl, W. H., 1976, Abnormal formation pressures: Elsevier.
- Fjær, E., Holt, R., Horsrud, P., Raaen, A. M., and Risnes, R., 1989, Petroleum related rock mechanics: Elsevier.
- H, J. D., N, T. M., and A, T., 1979, Attenuation of seismic waves in dry and saturated rocks. ii: Mechanisms: Geophysics, **44**, 479–497.
- Han, D., Nur, A., and Morgan, D., 1986, Effects of porosity and clay content in sandstones: Geophysics, **51**.
- Hermanrud, C., Teige, G. M. G., Vik, E., Wensaas, L., and Nordgård Bolås, H. M., 1998, Overpressures in shales - do we know what they are and why they are there?: Bulletin du Centre de Recherches, Elf Exploration Production Memoir, **22**, 43–48.
- Hermanrud, C., Wensaas, L., Teige, G. M. G., Norgård Bolås, H. M., Hansen, S., and E, V., 1998b, Shale porosities from well logs on haltenbanken (offshore mid-norway) show no influence of overpressuring *in* Law, B. E., Ulmishek, G. F., and Slavin, V. I., Eds., Abnormal pressures in hydrocarbon environments:, 65–85.

## References

---

- Holberg, O., 1987, Computational aspects of the choice of operator and interval for numerical differentiation in large-scale simulation of wave-phenomena: *Geophys. Prosp.*, **35**, 629–655.
- Hornby, B. E., Johnson, C. D., and Cook, J. M., 1994, Ultrasonic measurements of the elastic properties of shales: 64th ann. internat. mtg., Soc. Expl. Geophys., expanded abstracts, pages 1117–1120.
- Huffmann, A. R., and Castagna, J. P., 2001, The petrophysical basis for shallow-water flow prediction using multicomponent seismic data: *The leading edge*, **20**, 1030–1052.
- Jack, I., 1998, Time-lapse seismic in reservoir management: *Soc. Expl. Geophys.*
- Jenkins, S. D., Waite, M. W., and Bee, M. F., 1997a, Time lapse monitoring of the Duri steamflood: A pilot and case study: *The leading edge*, **16**, 1267–1273.
- Jones, L. E. A., and Wang, H. F., 1981, Ultrasonic velocities in cretaceous shales from the williston basin: *Geophysics*, **46**, 288–297.
- Jonston, D. H., 1987, Physical properties of shale at temperature and pressure: *Geophysics*, **52**, 1391–1401.
- Khaksar, A., Griffiths, C. M., and McCann, C., 1999, Compressional- and shear-wave velocities as a function of confining stress in dry sandstones: *Geophys. Prosp.*, **47**, 487–508.
- Kragh, E., and Christie, P., 2002, Seismic repeatability, normalized rms and predictability: *The Leading Edge*, **21**, 640–647.
- Kvam, Ø., and Spetzler, J., 2003, Lithological inversion of time-lapse streamer data using reflectivity ratios: 73rd Ann. Internat. Mtg., Soc. Expl. Geophys., Expanded Abstracts, 1505-1508.
- L, A., and R, M., 1994, Estimation of phase velocities and q-factors from zero-offset, vertical seismic profile data: *Geophysics*, **59**, 500–517.
- Landrø, M., and Strønen, L. K., 2003, 4D study of fluid effects on seismic data in the Gullfaks Field: *Geofluids*, **3**, 233–244.
- Landrø, M., Solheim, O. A., Hilde, E., Ekren, B. O., and K, S. L., 1999, The gullfaks 4d seismic study: *Petr. Geosci.*, **5**, 213–226.
- Landrø, M., Digranes, P., and Strønen, L. K. , 2002, pressure effects on seismic data - possibilities and limitations:. Paper presented at the NPF biannual conference in Kristiniansand, Norway, 11-13 March, 2002.
- Landrø, M., 2001, Discrimination between pressure and fluid saturation changes from time-lapse seismic data: *Geophysics*, **66**, 836–844.

- Landrø, M., 2002, Uncertainties in quantitative time-lapse seismic analysis: *Geophys. Prosp.*, **50**, 527–538.
- Laws, R., and Kragh, E., 2002, Rough seas and time-lapse seismic: *Geophys. Prosp.*, **50**, 195–195.
- Lumley, D., 2001, Time-lapse seismic reservoir monitoring: *Geophysics*, **66**, 50–53.
- Mavko, G., Mukerji, T., and Dvorkin, J., 1998, *The rock physics handbook*: Cambridge University Press.
- Mindlin, R. D., and Deresiewicz, H., September 1953, Elastic spheres in contact under varying oblique forces: *J. App. Mech.*, pages 327–344.
- Nes, O. M., Holt, R. M., and Fjær, E., 2000, The reliability of core data as input to seismic reservoir monitoring studies: SPE 65180.
- NOU(1986:16), 1986, Uncontrolled blowout on the West Vanguard platform october 6, 1985 (in Norwegian), Public report: Norwegian ministry of justice.
- Pennebaker, E. S., 1968, Seismic data indicate depth, magnitude of abnormal pressures: *World Oil*, **166**, 73–78.
- Reynolds, E. B., 1970, Predicting overpressured zones with seismic data: *World Oil*, **171**, 78–82.
- Rickett, J. E., and Lumley, D., 2001, Cross-equalization data processing for time-lapse seismic monitoring: A case study from the gulf of mexico: *Geophysics*, **66**, 1015–1025.
- Sayers, C. M., M, J. G., and G, D., 2002, Predrill pore pressure prediction using seismic data: *Geophysics*, **67**, 1286–1292.
- Sconeille, M., 2000, Fourier reconstruction of irregularly sampled seismic data: Ph.D. thesis, TU-Delft.
- Shuey, R. T., 1985, A simplification of the zoeppritz equations: *Geophysics*, **50**, 609–614.
- Smith, G. C., and Gidlow, P. M., 1987, Weighted stacking for rock property estimation and detection of gas: *Geophys. Prosp.*, **35**, 993–1014.
- Smith, J. E., 1971, The dynamics of shale compaction and evolution of pore-fluid pressures: *Mathematical Geology*, **3**, 239–263.
- Sønneland, L., Veire, H. H., Benoit, R., Signer, C., Pedersen, L., Ryan, S., and Colin, S., 1997, Seismic reservoir monitoring on gullfaks: *The Leading Edge*, **16**, 1247–1253.
- Spetzler, J., and Kvam, Ø., 2003, Time-lapse seismic monitoring in the prestack domain: 73rd Ann. Internat. Mtg., Soc. Expl. Geophys., Expanded Abstracts, 1414-1417.

## References

---

- Thorbecke, J., 1997, Common focus point technology: Ph.D. thesis, TU-Delft.
- Tokoz, M. N., Johnston, D. H., and Timur, A., 1979, Attenuation of seismic waves in dry and saturated rocks: I. laboratory measurements: *Geophysics*, **44**, 681–690.
- van Vossen, R., Robertsson, J. O. A., and Chapman, C. H., 2002, Finite-difference modeling of wave propagation in a fluid-solid configuration: *Geophysics*, pages 618–624.
- Vernik, L., 1997, Predicting porosity from acoustics in siliciclastics: A new look: *Geophysics*, **62**, 118–128.
- Verschuur, D. J., Berkhout, A. J., and Wapenaar, P. A., 1992, Adaptive surface-related multiple elimination: *Geophysics*, **57**, 1166–1177.
- Walton, K., 1987, The effective elastic moduli of a random packing of spheres: *J. Mech. Phys. Solids*.
- Wapenaar, C. P. A., and Berkhout, A. J., 1989, Elastic wavefield extrapolation, redatuming of single- and multi-component seismic data: Elsevier.
- Yilmaz, O., 2001, *Seismic data analysis*, second edition: SEG.
- Zwartjes, P. M., and Hindriks, C. O. H., 2001, Regularising 3d data using fourier reconstruction and sparse inversion: 70th Ann. Internat. Mtg., Soc. Expl. Geophys., pages 2162–2165.